BRNO UNIVERSITY OF TECHNOLOGY
VYSOKÉ UČENÍ TECHNICKÉ V BRNĚ

FACULTY OF ELECTRICAL ENGINEERING AND COMMUNICATION
FAKULTA ELEKTROTECHNIKY A KOMUNIKAČNÍCH TECHNOLOGIÍ

DEPARTMENT OF CONTROL AND INSTRUMENTATION
ÚSTAV AUTOMATIZACE A MĚŘICÍ TECHNIKY

MODELING AND CONTROL OF ELECTRIC AND THERMAL FLOWS IN FULLY ELECTRIC VEHICLES
MODELOVÁNÍ A ŘÍZENÍ TOKŮ ELEKTRICKÉ A TEPELNÉ ENERGIE V PLNĚ ELEKTRICKÝCH AUTOMOBILECH

DOCTORAL THESIS
DISERTAČNÍ PRÁCE

AUTHOR
AUTOR PRÁCE

Ing. Jan Glos

ADVISOR
ŠKOLITEL

prof. Ing. Pavel Václavek, Ph.D.

BRNO 2020

ABSTRACT

In fully electric vehicles a systematic control of thermal and electric flows is becoming very important as there is not enough waste heat for cabin heating. To avoid vehicle driving range decrease under winter condition it is necessary to employ devices allowing minimization of energy needed for cabin heating (e.g. heat pump, thermal energy storage). It is required to implement control algorithms for such devices to ensure their optimal operation. In summer conditions it is also necessary to control thermal flows to avoid excessive battery discharge due to vehicle thermal management. This work deals with control algorithms design as well as with the development of decision controller allowing routing of thermal flows.

KEYWORDS

fully electric vehicle, FEV, automotive, thermal model, thermal flows control, heat pump control, vapor compression refrigeration system control, VCRS, electronic expansion valve, EXV, vehicle thermal management system, VTMS, hybrid model predictive control, HMPC, non-linear model predictive control, NMPC, air quality control, virtual sensors, thermal energy storage, TES

ABSTRAKT

Systematické řízení tepelných a elektrických toků v plně elektrických automobilech se stává velmi důležitým, protože v těchto typech automobilů není k dispozici dostatek odpadního tepla pro vytápění kabiny. Aby v zimním období nedocházelo ke snížení dojezdu, je nutné použití technologií, které umožní snížení spotřeby energie nutné k vytápění kabiny (např. tepelné čerpadlo, zásobník tepla). Je také zapotřebí vytvořit řídicí algoritmy pro tato zařízení, aby byl zajištěn jejich optimální provoz. V letním období je nezbytné řídit tepelné toky v rámci elektromobilu tak, aby nedocházelo k nadměrnému vybíjení baterie kvůli chlazení kabiny a dalších částí. Tato práce řeší jak návrh řídicích algoritmů, tak i vývoj rozhodovacího algoritmu, který zajistí směřování tepelných toků.

KLÍČOVÁ SLOVA

plně elektrický automobil, tepelný model, řízení tepelných toků, řízení tepelného čerpadla, řízení chladicích systémů, elektronické expanzní ventily, tepelný management vozidla, hybridní prediktivní řízení, nelineární prediktivní řízení, řízení kvality vzduchu, virtuální snímače, zásobník tepelné energie

GLOS, Jan. *Modeling and Control of Electric and Thermal Flows in Fully Electric Vehicles*. Brno, 2020, 207 p. Doctoral thesis. Brno University of Technology, Faculty of Electrical Engineering and Communication, Department of Control and Instrumentation. Advised by prof. Ing. Pavel Václavek, Ph.D.

DECLARATION

I declare that I have written the Doctoral Thesis titled "Modeling and Control of Electric and Thermal Flows in Fully Electric Vehicles" independently, under the guidance of the advisor and using exclusively the technical references and other sources of information cited in the thesis and listed in the comprehensive bibliography at the end of the thesis.

As the author I furthermore declare that, with respect to the creation of this Doctoral Thesis, I have not infringed any copyright or violated anyone's personal and/or ownership rights. In this context, I am fully aware of the consequences of breaking Regulation § 11 of the Copyright Act No. 121/2000 Coll. of the Czech Republic, as amended, and of any breach of rights related to intellectual property or introduced within amendments to relevant Acts such as the Intellectual Property Act or the Criminal Code, Act No. 40/2009 Coll., Section 2, Head VI, Part 4.

Brno ....

author's signature

ACKNOWLEDGMENT

I would like to thank my advisor, prof. Ing. Pavel Václavek, Ph.D., for guidance, consultations, patience and useful ideas to this work. I also appreciate him for the opportunity to conduct research on this interesting and current topic and the possibility to finalize the test bench assembly and complete this thesis.

Many thanks also belong to prof. František Šolc, who was my closest collaborator within this work. He helped me with dynamic modeling of thermal systems (including refrigeration circuit), the simulations of those systems and results analysis. He also provided me assistance with the test bench physical assembling and commissioning. Together we studied hybrid systems theory, model predictive control of these systems and we found a new approach of thermal mode selection. However, the endless discussions, detailed analysis of my thoughts and proposed approaches including their constructive criticism were the most beneficial aspects of our collaboration.

I would also like to thank Petr Blaha for his advice in the field of control theory and help with test bench realization.

Matúš Kozovský helped me in the field of motor control algorithms, which were used for compressor speed control and complemented by another compressor related software (LIN communication, power computation, etc.). We spent long hours in the laboratory by testing the compressor control algorithms and I'd like to express gratitude to him.

I would like to thank Lukáš Otava for help with control hardware, especially for the design of fan PCB, help with AURIX memory management and other advice (including discussions about sensors wiring, control algorithms design, etc.). He was my neighbor in the office, so he was the first in the row, who I asked for help if necessary and he never refused.

Petr Petyovský helped me by preparing a suitable LIN interface for HVAC flaps, whose software was developed by him and Matúš within the 3Ccar project. Thanks to his involvement it was possible to use the flaps at our test bench.

Then I would like to thank Libor Veselý for printing the coolant pump holder. Thanks also belong to Zdeněk Havránek, Jiří Fialka and their colleagues from Measurement technology group, who helped me by measuring the characteristics of temperature sensors. I would like to thank Jan Vodička for his support in the field of mechanical assembly of the test bench and fixing the parts of it.

As this work is connected with the OSEM-EV project, the project partners were important to achieve practical results. First of all, I'd like to thank Infineon Technologies AG, especially Reiner John for coordinating this interesting and complicated project, Christopher Roemmelmayer for design and production of control units hardware (PCBs). AVL List GmbH contributed by the design of the vehicle thermal management system, I'd like to highlight the collaboration with Ernst Sumann, Mihai Nica, Matthias Hütter

and Jianbo Tao. I'd like to also thank all others, who were involved in the OSEM-EV project and are not listed above.

Finally, I would like to thank my family, especially my wife Eliška and my son Lukáš, for their support and patience during my long-lasting research and thesis preparation period.

This research was carried out under the project H2020 653514 OSEM-EV - Optimised and Systematic Energy Management in Electric Vehicles.

This research was carried out under the project LQ1601 CEITEC 2020.

The research was supported by the research infrastructure of CEITEC - Central European Institute of Technology.

The research results were verified in simulation using AVL CRUISE M simulation SW provided by AVL within University Partnership Program.

Brno ....

author's signature

Contents

List of Figures

List of Tables

Listings

Introduction

Fully electric vehicles (FEV) require special approaches for cabin heating, as the classical solution adapted from an internal combustion engine (ICE) vehicles is not satisfactory from the perspective of energy consumption. ICE vehicles utilize waste heat from the ICE for cabin heating. The ICE's tank-to-wheel efficiency is usually 20 % to 30 %, and approximately 30 % of total energy can be used for cabin heating [1, 2]. If we consider petrol ICE, the energy density is $34.2\,\mathrm{MJ\,l^{-1}}$. For city driving with an average speed of $40\,\mathrm{km\,h^{-1}}$ and average fuel consumption of 8 l/100km, there is an available thermal flow of 9 kW on average for cabin heating.

On the other hand, the electric vehicle (EV) powertrain has a much higher overall efficiency (67 % to 82 %), with approx. 10 % to 25 % converted to waste heat [3]. As a result, the EV generates a maximum waste heat flow rate of approx. 0.85 kW to 2 kW under the same conditions as for the ICE vehicle above. Moreover, part of this thermal flow is from a low potential source, as the batteries temperature can not be higher than approx. 30 °C to 40 °C. Thus, the coolant temperature will be even lower and the use of this heat for cabin heating is quite complicated. Since the batteries temperature can not exceed approx. 30 °C to 40 °C, the waste heat recovery makes sense in combination with the use of a heat pump system, which would elevate the temperature for cabin heating. Thermal energy storage (TES) could be also used to support heating and cooling.

It needs to be mentioned that the use of the TES and waste heat recovery is not state-of-the-art technology for EVs, and there is no common understanding among the manufacturers. Current EVs use positive temperature coefficient (PTC) heaters, air to water heat pumps, or their combination, as a heat source [4].

Regardless of the heat source, a cabin heating system needs to be powered from batteries and the power consumption negatively influences the mileage of the EV. An extremely unpleasant choice can occur when the user needs to decide if the EV will heat the cabin or reach its destination.

The cabin heating system is the most significant consumer of battery energy and thus it was taken as an example above. However, even a cabin cooling system, battery cooling/heating system and E-Drive cooling system needs to be also powered from batteries and thus might reduce the EV range. As the EV subsystems can be both the heat sink and source, a systematic approach of energy routing is necessary to achieve energy optimal vehicle operation.

This thesis proposes a partial solution to this problem, especially from a control perspective. The basic goal is to keep the range of the EV as long as possible, which means to minimize the energy needed for vehicle auxiliaries - cabin, battery, and E-Drive heating and cooling.

Considering cabin heating and cooling as the most problematic auxiliary, this target can be achieved by multiple methods and preferably by their combination

- minimizing the cabin thermal losses through walls and windows (insulation etc.)
- minimizing the thermal losses through cabin ventilation
- improvement of the heat source (e.g. from a PTC heater with a coefficient of performance (COP) of 1.0, to a heat pump with a COP of 1.5 to 3)
- waste heat recovery from the electric motor, power electronics, and battery
- utilization of thermal energy storage (based on phase-change material)

The first item needs to be solved during the vehicle design and control algorithms are not connected with this area. The second bullet point can be solved by proper control of cabin Heating, Ventilation and Air Conditioning (HVAC) system as proposed in Section 4.2. The remaining three points are a challenge, as they require suitable control algorithms in combination with a decision-making algorithm for mode switching.

This thesis provides innovative control techniques of energetic flows within a fully electric vehicle based on an integrated and systematic approach. The core of that approach is an algorithm called Model Predictive Thermal Decision Controller, which is proposed for decision-making tasks (i.e. transfer heat from here to there). This core algorithm is complemented with the Non-linear Model Predictive Control algorithm for cabin comfort (combined temperature with air quality), which minimizes the thermal losses caused by vehicle cabin ventilation. The third important part deals with model-based vapor compression refrigeration system control, as this system is the backbone of the whole vehicle thermal management system. These leading topics are completed by other supportive components (dynamic models, virtual sensors, graphical user interface, etc.).

1 State-of-the-Art

This chapter describes the current State-of-the-Art (SOA) of relevant parts of the Vehicle Thermal Management System (VTMS) for a passenger vehicle. A disadvantage of today's fully electric vehicles (FEV) is the weather-dependent range, which means that under cold ambient temperatures the range of vehicles dramatically decreases [5] down to less than half of their nominal range. This issue partially depends on increased high-voltage (HV) battery internal resistance under cold conditions [6]. Secondly, this issue is caused also by Heating, Ventilation and Air Conditioning (HVAC) system, which needs to be powered from HV battery. Especially the cabin heating can decrease the vehicle range by $\sim$20 % at an ambient temperature of $-7\,°C$ [7] and even worse for lower temperatures.

A Mercedes-Benz B-class (W242.890) vehicle was used as an SOA example. This car is a fully electric vehicle (FEV) based on the internal combustion engine (ICE) platform.

A comprehensive overview of different possible VTMS approaches for EVs can be found for example in [4].

1.1 Vehicle thermal management system

ICE vehicles usually use a quite simple VTMS layout. There are two main goals - control the cabin temperature and cool the ICE. The cabin cooling is ensured by independent and simple Vapor Compression Refrigeration System (VCRS). The cabin heating is accomplished using waste heat of ICE, eventually by an additional gas or electric heater. The ICE is cooled by rejecting excessive heat using a coolant loop with a water-to-air heat exchanger (HX) into the ambient air and/or into the cabin.

FEV requires a more complicated VTMS layout. Compared to ICE vehicles a High-Voltage Battery temperature needs to be controlled and Electric Motor (EM) with Power Electronics (PE) needs to be cooled. Moreover, the amount of waste heat of power-train is much lower, thus it is not sufficient to use only the power-train waste heat for cabin heating and separate (electric) heater needs to be used.
This VTMS layout brings some issues:

- FEV mileage decrease under cold ambient conditions
- High dependency of FEV range on HVAC (especially if cabin heating is active)
- A high number of VTMS components (heat exchangers, pumps, etc.)

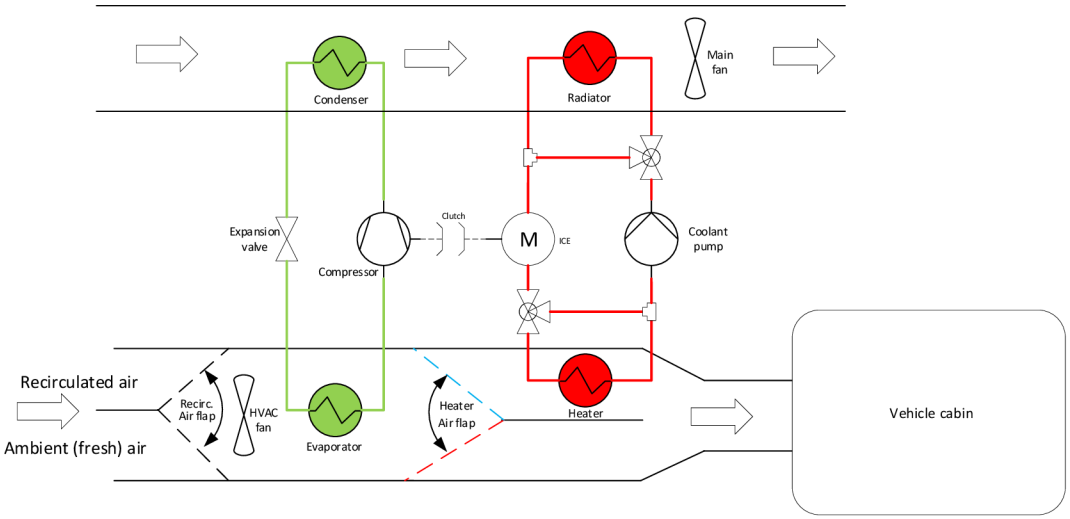

Fig. 1.1: Example of VTMS for ICE vehicle

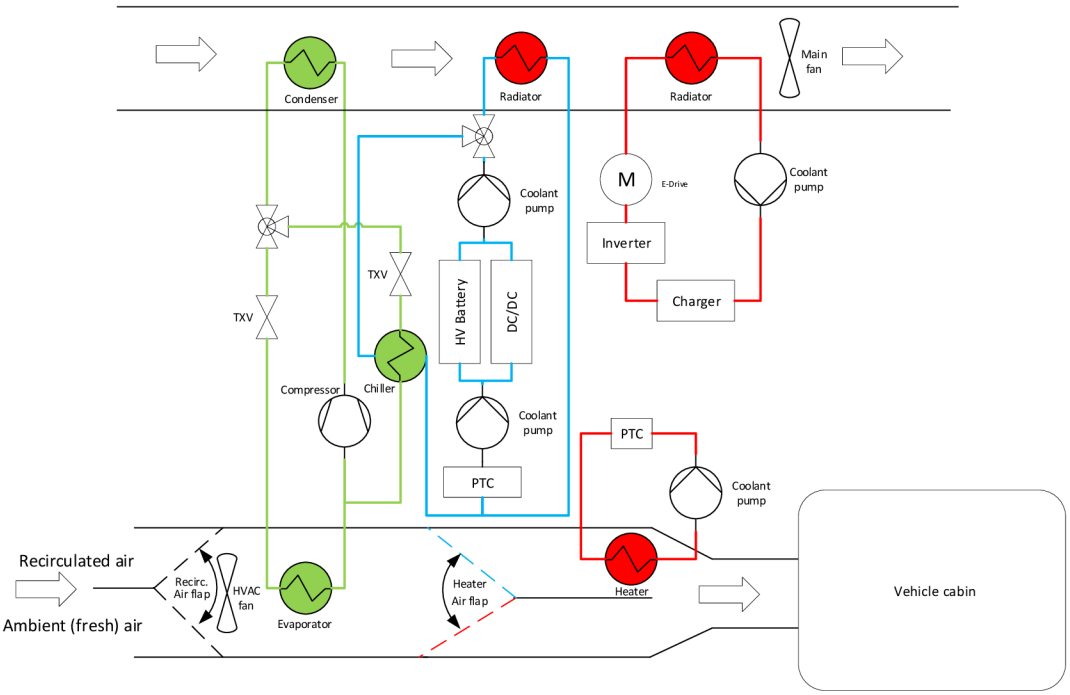

Fig. 1.2: Example of VTMS for fully electric vehicle

1.2 VCRS control

Considering the VCRS system, there are two main configurations possible, a system with a high-pressure receiver complemented by evaporator superheat control and a system with a low-pressure accumulator with a fixed orifice.

The SOA for EXV control is the application of a PI or PID controller for superheat control [8]. The PID control, fuzzy control, and artificial neural network control were implemented for superheat control in [9]. There are also applications of Model Predictive Control (MPC) for VCRS control [10, 11, 12, 13]. A more exhaustive overview of possible approaches can be found in [14].

The control algorithms for a VCRS in ICE vehicles are usually quite simple. The compressor is driven by ICE (via the clutch) and VCRS capacity control is realized by a compressor on/off control or variable displacement control (both based on evaporation pressure) [15]. The Thermal Expansion Valve (TXV) is used as a throttling device and it autonomously controls the refrigerant superheat degree at the evaporator outlet. Auxiliary devices (evaporator and condenser fans) are controlled based on cabin cooling demand and condensing pressure respectively.

In FEV (B-Class) the approach is similar to ICE vehicle, but it comes with some changes and improvements. Due to missing ICE, the electric compressor is used and variable speed controlled to match the current cooling request. For HV Battery cooling a chiller was added as the second evaporator. The chiller is equipped with a TXV and solenoid shut-off valve (SOV). The second SOV was added to allow evaporator enabling or disabling.

Both the ICE and FEV (B-class) VCRS include a liquid receiver and are operated as superheat controlled (the TXV meters the refrigerant flow rate to the evaporator to keep the defined refrigerant superheat degree at evaporator outlet and compressor suction).

1.3 Thermal control units HW/SW

In ICE vehicles the number of control units involved in VTMS can be quite low (for example two - the first one for ICE cooling and the second one for VCRS control). The exact number of ECU and their responsibilities depend on the manufacturer and vehicle.

In the case of FEV (B-class), the VTMS is much more complicated and the system is controlled by multiple ECUs. Firstly, Automatic Air Conditioning ECU is responsible for cabin heating and cooling. Secondly, Thermal Management Control Unit takes care of HV Battery and E-Drive cooling and heating. Powertrain Control Unit and Battery Management System Control Unit are partly involved in VTMS

by monitoring the parts and indicating cooling or heating requests. Also, the PTC heater and HV Compressor are recognized as ECUs.

The E-Drive and HV Battery waste heat recovery is not implemented, thus there is no need for extensive cooperation of ECUs.

2 Goals

The goals of this thesis were partially formulated by the OSEM-EV project proposal and the rest of them appeared during the project solution. In general, this work should give a set of novel modeling and control approaches related to electric vehicle (EV) thermal management. Specifically, the methods were originally developed and applied on fully (battery) electric vehicles (FEV or BEV), but it is partially or even fully applicable for other EV types, like plug-in hybrid electric vehicle (PHEV) or fuel cell electric vehicle (FCEV).

The basic and general goal of the OSEM-EV project was an increase of the FEV range, especially under adverse ambient conditions (cold winter or very hot summer). Fulfillment of this goal requires the cooperation of different FEV subsystems, e.g. energy-efficient powertrain and batteries, HVAC system, overall thermal management system with low heat losses, etc. The optimality can be only achieved if the subsystems are properly designed, realized and then controlled.

The main goal of this thesis was the research and development of control algorithms ensuring energy-efficient FEV operation. These algorithms can be divided into several groups:

- Low-level control algorithms (compressor motor control, flaps control, fan speed control, etc.)
- High-level control algorithms (HVAC control, VCRS control, HvBat and E-Drive temperature control, etc.)
- Vehicle energy flow routing (Thermal Decision Controller)

The models and algorithms were developed in general form, but in some cases, the specific values of variables were necessary for intelligibility. The specific values were measured on test bench (mass flow rates, heat exchanger dimensions, etc.), gained from data sheets (compressor displacement, etc.) or computed based on known variables (cycles in ph diagram, etc.). The proposed VTMS and VCRS were intended for installation into Mercedes-Benz B-class, thus all the specific values of variables are linked to this vehicle and proposed systems.

2.1 Vehicle thermal management system

This thesis focuses in particular on FEV thermal management and HVAC subsystems control, but also some parts of these subsystems had to be designed. A completely new vehicle thermal management system (VTMS) layout in Fig. 2.1 was designed by AVL List in cooperation with OSEM-EV project partners (including BUT).

This layout enables E-Drive and HV Battery waste heat recovery, cabin heating by VCRS and also incorporates thermal energy storage (TES). The designed VTMS is a little bit more complicated (from circuit and valves perspective), but it also saves some components (fewer pumps and heat exchangers).

The routing of thermal flows is based on the VCRS circuit in combination with coolant loops. As the VCRS circuit is quite complicated, Electronic Expansion Valves (EXV) had to be used instead of Thermal Expansion Valves (TXV). This innovative approach (in automotive applications) allow VCRS reversing (or more precisely different operating modes as true reversing is not suitable for this application).

The goal was to complete the proposed VTMS with suitable control algorithms for both the simulations and real operation. The algorithms should assure compliance of constraints (like HV Battery and ED temperature range, etc.) and also regulation to defined references (cabin temperature).

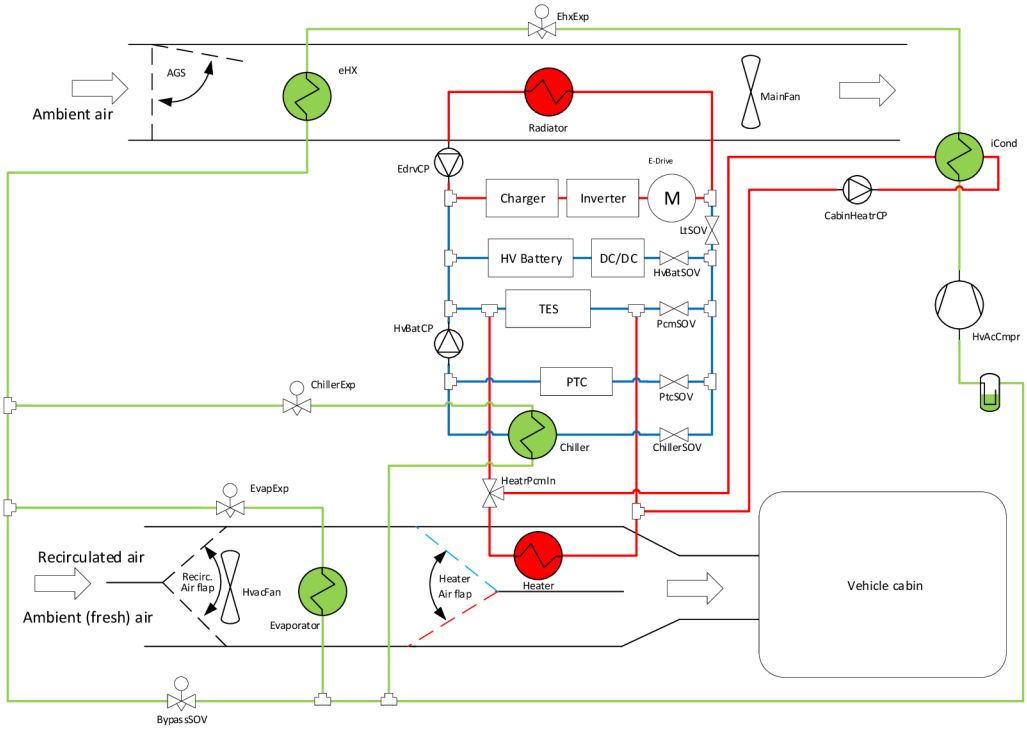

Fig. 2.1: VTMS for a fully electric vehicle from OSEM-EV project

2.2 VCRS control

The OSEM-EV proposed solution includes a suction line accumulator, which ensures pure vapor (no liquid) refrigerant at compressor suction and also serves as a

refrigerant reservoir. The EXVs are used to control the condenser subcooling to achieve the best performance of the VCRS.

It was found in [16] that condenser subcooling (SC) has a significant influence on the Coefficient of Performance (COP) and several methods of optimal SC determination were introduced in [17, 18, 19].

In contrast to SOA VCRS control, the OSEM-EV VCRS circuit requires a much more sophisticated control approach and also allows system efficiency improvement. The goal was to design the control algorithms concerning all possible operating modes, e.g. heating and cooling with different heat sources and sinks configuration.

2.3 Thermal control units HW/SW

The HW for control units was designed by Infineon according to system layout and the software requirements formulated by BUT.

An innovative approach has been used during thermal control unit development. The VTMS was originally controlled by several control units (B-class) with limited cooperation. All the control units were merged into a single and highly integrated Thermo-Electric Management Control Unit (TEMCU). To save space and costs the TEMCU was placed into HV Compressor housing and all parts of VTMS are controlled from this point. This approach enables the cooperation of heat sources and sinks, waste heat recovery, utilization of heat storage and effective energy using and reusing. On the other hand, more complicated and sophisticated control algorithms are required to take full advantage of the improved VTMS layout.

TEMCU is intended to control the whole of the thermal management system shown in Fig. 2.1. In Tab. 2.1, Tab. 2.2 and Tab. 2.3 physical sensors, virtual sensors, and actuators are shown respectively. From these tables, it is evident that VTMS for FEV is a highly complex system, which needs to be appropriately controlled to achieve the lowest possible power consumption of HVAC and other auxiliary systems. The sensors and actuators, which are installed within the test bench, are highlighted by bold style in sensors and actuators tables.

The sensors are directly wired to TEMCU as most of them are negative temperature coefficient (NTC) thermistors. On the other hand, most of the actuators are connected to TEMCU via LIN bus, which allows both the actuator control and its feedback (including fault detection, power consumption, etc. as supported by LIN slave). The overview of LIN topology is shown in Fig. 2.2. All of the three LIN clusters were described by the LIN description file (LDF), which were then used for TEMCU LIN driver automatic code generation and also for LIN bus traffic analysis.

The goal was to implement the control algorithms into developed HW and complete them by necessary software packages (real-time operating system, communica-

tion drivers, virtual sensors, fault detection, safety functionalities, manual control, etc.).

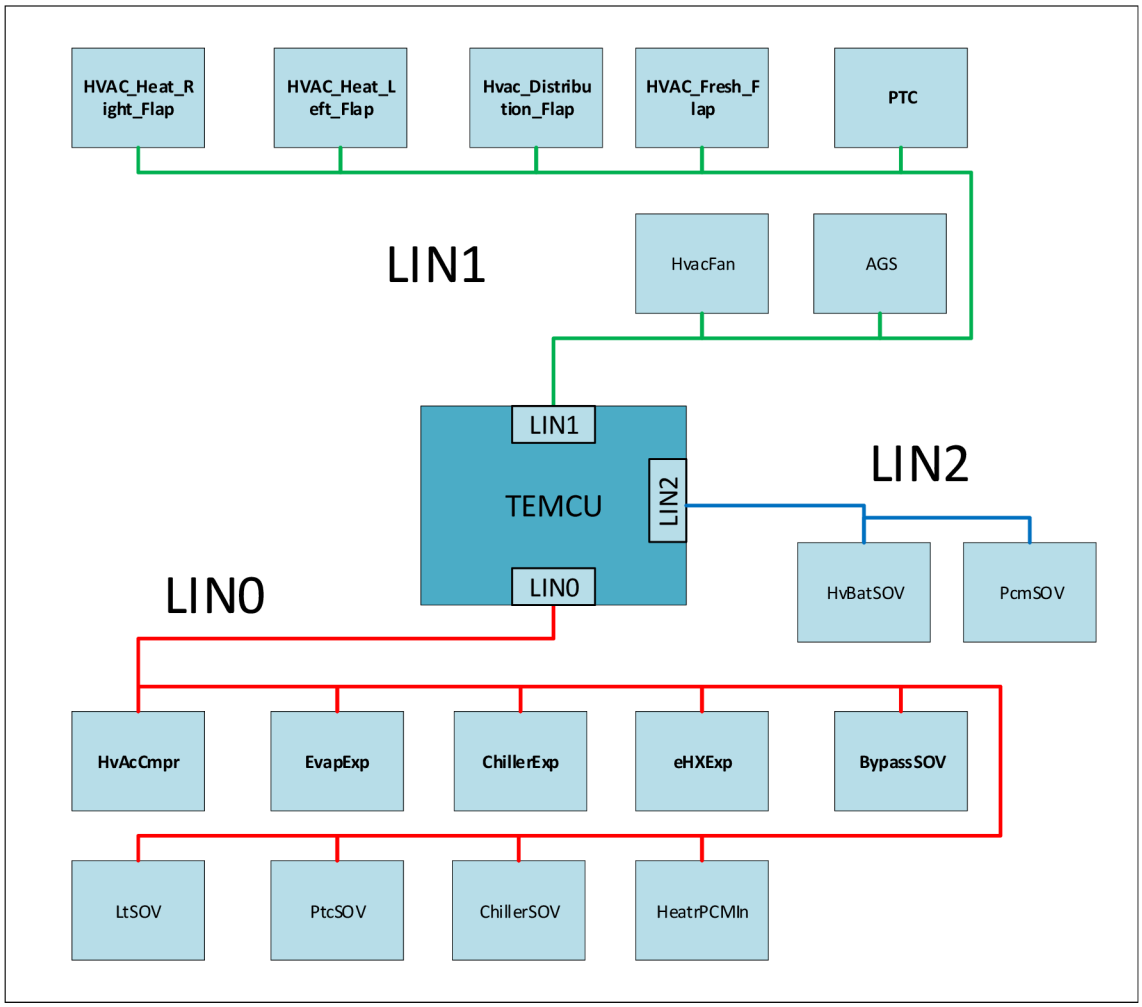

Fig. 2.2: TEMCU LIN buses topology

Tab. 2.1: TEMCU physical sensors

Identifier	Unit	Description
T_CoLtHxOut	K	Coolant temperature at LT HX outlet
T_CoHvBatIn	K	Coolant temperature at HvBat inlet
T_CoICondOut	K	Coolant temperature at iCond outlet
T_CoPcmOut	K	Coolant temperature at TES (PCM) outlet
T_CoPtcOut	K	Coolant temperature at PTC outlet
T_CoPeIn	K	Coolant temperature at PE inlet
T_CoChillerOut	K	Coolant temperature at Chiller outlet
T_RefICondOut	K	Refrigerant temperature at iCond outlet
T_RefEhxOut	K	Refrigerant temperature at eHX outlet
T_RefCmprOut	K	Refrigerant temperature at HvAcCmpr outlet
T_RefChillerIn	K	Refrigerant temperature at Chiller inlet
T_RefEvapIn	K	Refrigerant temperature at Evaporator inlet
T_Amb	K	Ambient air temperature
T_AirLtHxIn	K	Air temperature at LT HX inlet
T_AirChOut	K	Air temperature at Cabin Heater outlet
T_AirCabin	K	Cabin air temperature
T_AirEvapOut	K	Air temperature at evaporator outlet
p_RefHigh	Pa	Refrigerant high pressure
p_RefLow	Pa	Refrigerant low pressure
p_RefEhxOut	Pa	Refrigerant pressure at eHX outlet
T_Pcm	K	TES (PCM) internal temperature
T_RefHvAcCmprIn	K	Refrigerant temperature at compressor inlet
T_RefAccuIn	K	Refrigerant temperature at accumulator inlet

Tab. 2.2: TEMCU virtual sensors

Identifier	Unit	Description
SC_RefEhxOut	K	Refrigerant subcooling at eHX outlet
SC_RefICondOut	K	Refrigerant subcooling at iCond outlet
PCM_status	%	TES (PCM) current status (heat charge)
HvAcCmpr_mdot	$\mathrm{kg\,s^{-1}}$	HV compressor refrigerant mass flow rate
ChillerExp_mdot	$\mathrm{kg\,s^{-1}}$	Chiller EXV refrigerant mass flow rate
COP	-	Coefficient of performance
COP_overall	-	Overall coefficient of performance
SH_HvAcComprIn	K	Refrigerant superheat at HV compressor inlet
SH_AccuIn	K	Refrigerant superheat at accumulator inlet

Tab. 2.3: TEMCU actuators

Identifier	Description	Range
PTC	PTC heater	0..6 kW
HvacFan	HVAC fan speed	0..3000 rpm
MainFan	Main Fan speed	0..2500 rpm
EvapExp	Evaporator EXV	0..2.95 mm^2
BypasSOV	Refrigerant bypass valve	closed/open
EhxExp	External HX EXV	0..3.95 mm^2/open
HeatrPcmIn	3WV Heater/TES (PCM)	A/B
ChillerExp	Chiller EXV	0..3.95 mm^2
PcmSOV	TES (PCM) coolant valve	closed/open
PtcSOV	PTC heater coolant valve	closed/open
ChillerSOV	Chiller coolant valve	closed/open
LtSOV	Low temp. coolant valve	closed/open
HvBatSOV	HV battery coolant valve	closed/open
HvBatCP	HV battery coolant pump	0..20 l min^{-1}
EdrvCP	E-Drive coolant pump	0..20 l min^{-1}
CabinHeatrCP	Cabin heater coolant pump	0..20 l min^{-1}
HvAcCmpr	HV compressor	0..8000 rpm
HVAC_Fresh_Flap	Recirculated/fresh air flap	0..1
HVAC_Heat_Left_Flap	Heater left flap	0..1
HVAC_Heat_Right_Flap	Heater right flap	0..1
HVAC_Distribution_Flap	Air distribution flap	4 positions
AGS	Air grill shutter	closed/open

3 Electro-thermal modeling

Several dynamic and static models of FEV and its components, mainly thermal and electrical parts, were developed and assembled.

The first of them was an overall B-class vehicle model (including the OSEM-EV VTMS solution). The model contains all the relevant VTMS parts of FEV, like vehicle cabin, HVAC system, VCRS, E-Drive, HV Battery, cooling system, etc. This model was developed mainly by AVL, some parts were adjusted by responsible OSEM-EV partners and the model was equipped with a controller by BUT. The cabin model was prepared in Kuli, the VCRS model was assembled in Dymola, the powertrain model was developed in Cruise and the cooling system was prepared in Cruise M. These model components were complemented by the control algorithms model developed in MATLAB/Simulink. The overall simulation of all the models was possible using Model.CONNECT tool, which is designed for integrated simulation of models developed in different environments. The resulting model is highly complex and accurate and by its simulation, it is possible to predict the real FEV behavior for example during WLTC.

The second group comprises several Dymola models focused on VCRS modeling, which are arranged into the Modelica library. These models are based on commercial Dymola libraries, whose components were utilized during models assembly. The Dymola libraries `ThermalSystems` and `ThermalSystems Mobile AC` were used during assembling the VCRS, HVAC, and EV cabin models. The resulting models are very complex (approx. 30 000 state variables) and accurate. Thus they are suitable for dynamic behavior investigations and control algorithms evaluation, testing and verification. On the other hand, they are not appropriate for control algorithms design and real-time computations, because of their high complexity. Screenshots of assembled Dymola models are presented in Appendix H.

The third part contains a few VCRS models, which were developed from scratch. Their purpose is to enable real-time VCRS simulations for different purposes (fault detection, virtual sensors, state estimation, etc.).

The fourth model describes thermal parts of FEV in simplified form. The aim of this model is control algorithms design and the basis for the derived models for real-time decision making tasks in terms of thermal and electric energy routing inside FEV.

All the models from the third and fourth groups are based on basic equations and laws, which are shown in Appendix E.

3.1 VCRS model

The assembled VCRS model is shown in Fig. 3.1 and described by the following set of differential and algebraic equations. The derivation of the equations is shown in Appendix F.

The model state variables are refrigerant pressures p, refrigerant specific enthalpies h and outlet air temperatures T, all of them for the condenser (with the subscript "c,m") and evaporator (with the subscript "e,m"), where "m" stands for medium ("r" for refrigerant, "a" for the air). Complementary variables include mass m, mass flow rate $\dot{m}$, volume V, volumetric mass density ρ, heat flow rate $\dot{Q}$ and others, which are described in detail in Appendix F.

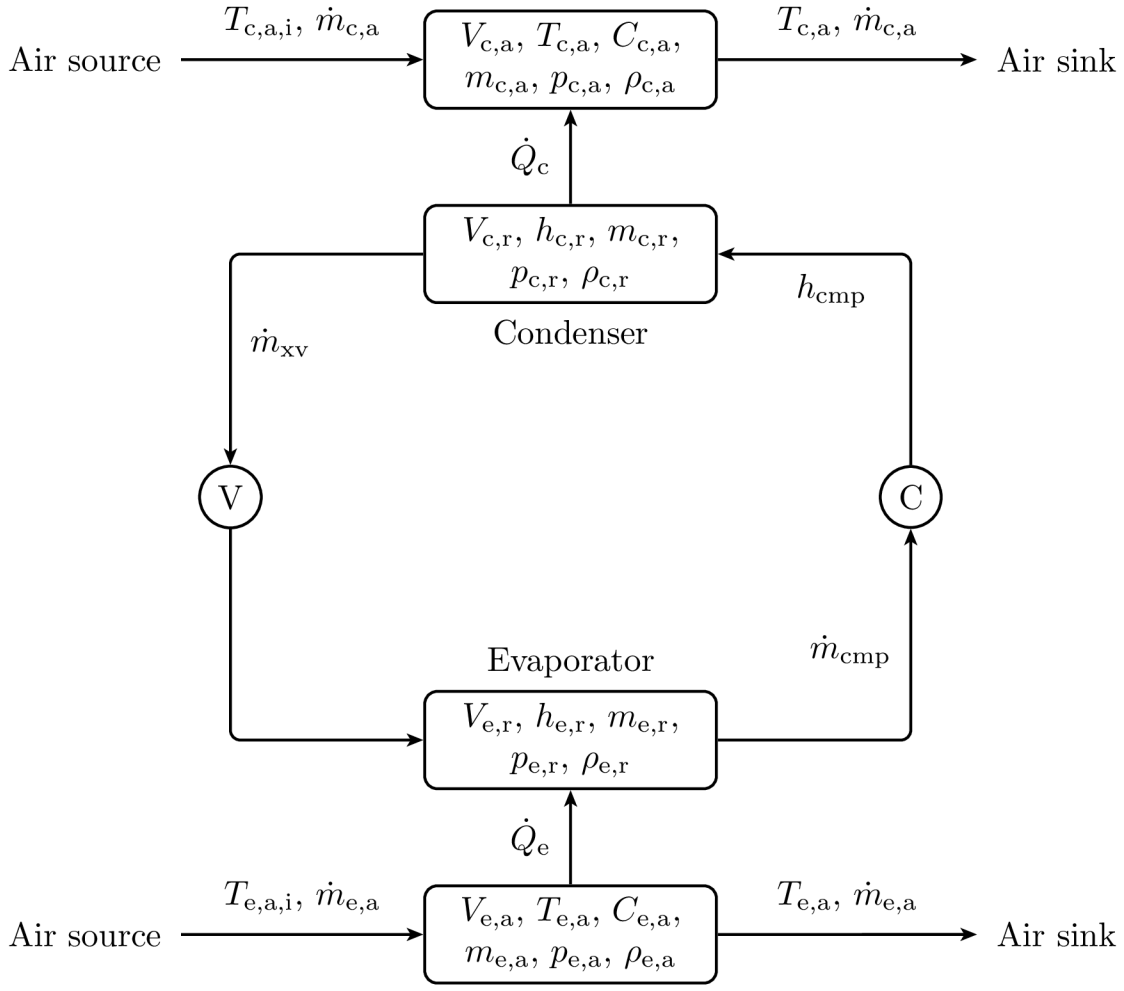

Fig. 3.1: VCRS model

$$\frac{\mathrm{d}p_{c,r}}{\mathrm{d}t} = \frac{m_{c,r}(\dot{m}_{cmp} - \dot{m}_{xv}) - V_{c,r}\left(\frac{\partial\rho}{\partial h}\right)_p \left(-\dot{Q}_c + \dot{m}_{cmp}(h_{cmp} - h_{c,r})\right)}{V_{c,r}\left(m_{c,r}\left(\frac{\partial\rho}{\partial p}\right)_h + V_{c,r}\left(\frac{\partial\rho}{\partial h}\right)_p\right)}, \tag{3.1}$$

$$\frac{\mathrm{d}p_{\mathrm{e,r}}}{\mathrm{d}t} = \frac{m_{\mathrm{e,r}}(\dot{m}_{\mathrm{xv}} - \dot{m}_{\mathrm{cmp}}) - V_{\mathrm{e,r}}\left(\frac{\partial\rho}{\partial h}\right)_p\left(\dot{Q}_{\mathrm{e}} + \dot{m}_{\mathrm{xv}}(h_{\mathrm{c,r}} - h_{\mathrm{e,r}})\right)}{V_{\mathrm{e,r}}\left(m_{\mathrm{e,r}}\left(\frac{\partial\rho}{\partial p}\right)_h + V_{\mathrm{e,r}}\left(\frac{\partial\rho}{\partial h}\right)_p\right)}, \tag{3.2}$$

$$\frac{\mathrm{d}h_{\mathrm{c,r}}}{\mathrm{d}t} = \frac{\left(\frac{\partial\rho}{\partial p}\right)_h\left(-\dot{Q}_{\mathrm{c}} + \dot{m}_{\mathrm{cmp}}(h_{\mathrm{cmp}} - h_{\mathrm{c,r}})\right) + \dot{m}_{\mathrm{cmp}} - \dot{m}_{\mathrm{xv}}}{m_{\mathrm{c,r}}\left(\frac{\partial\rho}{\partial p}\right)_h + V_{\mathrm{c,r}}\left(\frac{\partial\rho}{\partial h}\right)_p}, \tag{3.3}$$

$$\frac{\mathrm{d}h_{\mathrm{e,r}}}{\mathrm{d}t} = \frac{\left(\frac{\partial\rho}{\partial p}\right)_h\left(\dot{Q}_{\mathrm{e}} + \dot{m}_{\mathrm{xv}}(h_{\mathrm{c,r}} - h_{\mathrm{e,r}})\right) + \dot{m}_{\mathrm{xv}} - \dot{m}_{\mathrm{cmp}}}{m_{\mathrm{e,r}}\left(\frac{\partial\rho}{\partial p}\right)_h + V_{\mathrm{e,r}}\left(\frac{\partial\rho}{\partial h}\right)_p}, \tag{3.4}$$

$$h_{\mathrm{cmp}} = h_{\mathrm{e,r}} + \frac{h_{\mathrm{cmp,ie}} - h_{\mathrm{e,r}}}{\eta_{\mathrm{ie}}\eta_{\mathrm{m}}\eta_{\mathrm{mot}}}, \tag{3.5}$$

$$h_{\mathrm{cmp,ie}} = \mathrm{h}(p_{\mathrm{c,r}}, s_{\mathrm{e,r}}), \tag{3.6}$$

$$\dot{m}_{\mathrm{cmp}} = \frac{\omega}{2\pi}\rho_{\mathrm{e,r}}V_{\mathrm{cmp}}\eta_{\mathrm{vol}}, \tag{3.7}$$

$$\dot{m}_{\mathrm{xv}} = C_{\mathrm{d}}A\sqrt{2\rho_{\mathrm{c,r}}\left(p_{\mathrm{c,r}} - p_{\mathrm{e,r}}\right)}, \tag{3.8}$$

$$\frac{\mathrm{d}T_{\mathrm{c,a}}}{\mathrm{d}t} = \frac{1}{C_{\mathrm{c,a}}}\left[\dot{m}_{\mathrm{c,a}}c_{\mathrm{p,a}}(T_{\mathrm{c,a,i}} - T_{\mathrm{c,a}}) + \dot{Q}_{\mathrm{c}}\right], \tag{3.9}$$

$$\frac{\mathrm{d}T_{\mathrm{e,a}}}{\mathrm{d}t} = \frac{1}{C_{\mathrm{e,a}}}\left[\dot{m}_{\mathrm{e,a}}c_{\mathrm{p,a}}(T_{\mathrm{e,a,i}} - T_{\mathrm{e,a}}) - \dot{Q}_{\mathrm{e,a}}\right], \tag{3.10}$$

$$\dot{Q}_{\mathrm{c}} = U_{\mathrm{c}}A_{\mathrm{c}}\Delta T_{\mathrm{c}}, \tag{3.11}$$

$$\dot{Q}_{\mathrm{e}} = \dot{Q}_{\mathrm{e,a}} + \dot{Q}_{\mathrm{e,v}}, \tag{3.12}$$

$$\dot{Q}_{\mathrm{e,a}} = U_{\mathrm{e}}A_{\mathrm{e}}\Delta T_{\mathrm{e}}, \tag{3.13}$$

$$\dot{Q}_{\mathrm{e,v}} = 0.622\dot{m}_{\mathrm{e,a,i}}L\left[\frac{\phi_{\mathrm{e,i}}p^*_{\mathrm{V}}(T_{\mathrm{e,a,i}})}{p - \phi_{\mathrm{e,i}}p^*_{\mathrm{V}}(T_{\mathrm{e,a,i}})} - \frac{p^*_{\mathrm{V}}(T_{\mathrm{e,r}})}{p - p^*_{\mathrm{V}}(T_{\mathrm{e,r}})}\right], \tag{3.14}$$

$$p^*_{\mathrm{V}}(T_{\mathrm{e,a,i}}) = p_0\exp\left\{\left[\frac{h_{\mathrm{fg}}}{R}\left(\frac{1}{T_0} - \frac{1}{T_{\mathrm{e,a,i}}}\right)\right]\right\}, \tag{3.15}$$

$$p^*_{\mathrm{V}}(T_{\mathrm{e,r}}) = p_0\exp\left\{\left[\frac{h_{\mathrm{fg}}}{R}\left(\frac{1}{T_0} - \frac{1}{T_{\mathrm{e,r}}}\right)\right]\right\}, \tag{3.16}$$

$$\Delta T_{\mathrm{e}} = \frac{\Delta T_1 - \Delta T_2}{\ln\frac{\Delta T_1}{\Delta T_2}} = \frac{(T_{\mathrm{e,a,i}} - T_{\mathrm{e,r}}) - (T_{\mathrm{e,a}} - T_{\mathrm{e,r}})}{\ln\frac{(T_{\mathrm{e,a,i}} - T_{\mathrm{e,r}})}{(T_{\mathrm{e,a}} - T_{\mathrm{e,r}})}}, \tag{3.17}$$

$$\Delta T_{\mathrm{c}} = \frac{\Delta T_1 - \Delta T_2}{\ln\frac{\Delta T_1}{\Delta T_2}} = \frac{(T_{\mathrm{c,r}} - T_{\mathrm{c,a,i}}) - (T_{\mathrm{c,r}} - T_{\mathrm{c,a}})}{\ln\frac{(T_{\mathrm{c,r}} - T_{\mathrm{c,a,i}})}{(T_{\mathrm{c,r}} - T_{\mathrm{c,a}})}}, \tag{3.18}$$

$$T_{\mathrm{c,r}} = \mathrm{T}_{\mathrm{sat}}(p_{\mathrm{c,r}}), \tag{3.19}$$

$$T_{\mathrm{e,r}} = \mathrm{T}_{\mathrm{sat}}(p_{\mathrm{e,r}}), \tag{3.20}$$

$$m_{\mathrm{c,r}} = V_{\mathrm{c,r}}\boldsymbol{\rho}(\bar{h}_{\mathrm{c,r}}, p_{\mathrm{c,r}}), \tag{3.21}$$

$$m_{\mathrm{e,r}} = V_{\mathrm{e,r}}\boldsymbol{\rho}(\bar{h}_{\mathrm{e,r}}, p_{\mathrm{e,r}}). \tag{3.22}$$

3.2 Simple thermal FEV models

These models were derived from basic laws and equations from Appendix E. Their purpose is to plainly describe the modeled parts and assemble the simplest possible model, which can be then used for real-time computations, controller design, and other related tasks.

3.2.1 FEV HVAC thermal model

A vehicle cabin (complemented with an HVAC system) is quite complicated to be modeled from a thermal point of view. It consists of a high number of materials, including both the thermal insulants (foam, plastics, etc.) and thermal conductors (metal, glass, etc.). There are also a lot of other influences on cabin thermal behavior, such as the radiative thermal flow from the sun, passenger thermal flow, forced convection during driving, ventilation using windows, etc.

Thus, the model describing all the above-mentioned effects, and reflecting all the heat transfer types (conduction, convection, and radiation), would be very complicated and not useful for control design. Therefore, the structure of the model was simplified to represent a grey-box model, where the structure is fixed and the parameters are guessed, or identified, and can be considered as lumped (e.g. the thermal flow through the cabin walls are represented by single thermal conductance G_{c1}, which has no representation in a real system, but is used as a cumulative variable).

The simplified HVAC system in Fig. 3.2 can be described by the following set of equations

$$C_{\mathrm{h1}}\frac{\mathrm{d}T_{\mathrm{h1}}}{\mathrm{d}t} = \dot{Q}_{\mathrm{h7}} + \dot{Q}_{\mathrm{h5}} - \dot{Q}_{\mathrm{h6}}, \tag{3.23}$$

$$C_{\mathrm{h3}}\frac{\mathrm{d}T_{\mathrm{h3}}}{\mathrm{d}t} = \dot{Q}_{\mathrm{h9}} - \dot{Q}_{\mathrm{h8}} - \dot{Q}_{\mathrm{h7}}, \tag{3.24}$$

$$C_{\mathrm{h4}}\frac{\mathrm{d}T_{\mathrm{h4}}}{\mathrm{d}t} = \dot{Q}_{\mathrm{h8}} - \dot{Q}_{\mathrm{h9}} + \dot{Q}_{\mathrm{h10}}, \tag{3.25}$$

where C denotes thermal capacity, T stands for thermodynamic temperature, and $\dot{Q}$ is a general thermal flow rate. The subscript meanings can be found in Fig. 3.2.

Heat exchanger 1 (HX1) is used as a condenser and the refrigerant is rejecting heat into the coolant, which is circulated by the coolant pump (P1). HX1 and the heat flow rate $\dot{Q}_{\mathrm{h10}}$ could be replaced by another heat source (PTC etc.) for a different application. The air is heated by the coolant in HX2 and then supplied to the vehicle cabin. The air from the cabin can be exhausted outside or reused by operating a fresh air flap. The air movement is assured by the HVAC fan (F1).

We assume that the fan and pump speeds can be controlled and the heat flow rate $\dot{Q}_{\mathrm{h10}}$ can be adjusted by compressor speed control (or, in general, by heat source control for a Positive Temperature Coefficient (PTC) heater, etc.).

The heat flows from Fig. 3.2 can be expressed as

$$\dot{Q}_{\mathrm{h5}} = \dot{m}_{\mathrm{h1}} c_{\mathrm{h}} T_{\mathrm{h2}}, \tag{3.26}$$
$$\dot{Q}_{\mathrm{h6}} = \dot{m}_{\mathrm{h1}} c_{\mathrm{h}} T_{\mathrm{h1}}, \tag{3.27}$$
$$\dot{Q}_{\mathrm{h7}} = G_{\mathrm{h7}} (T_{\mathrm{h3}} - T_{\mathrm{h1}}), \tag{3.28}$$
$$\dot{Q}_{\mathrm{h8}} = \dot{m}_{\mathrm{h5}} c_{\mathrm{co}} T_{\mathrm{h3}}, \tag{3.29}$$
$$\dot{Q}_{\mathrm{h9}} = \dot{m}_{\mathrm{h5}} c_{\mathrm{co}} T_{\mathrm{h4}}. \tag{3.30}$$

After substitution of (3.26)-(3.30) to (3.23)-(3.25), and minor modifications, a new set of equations can be obtained

$$\frac{\mathrm{d}T_{\mathrm{h1}}}{\mathrm{d}t} = \frac{1}{C_{\mathrm{h1}}} [G_{\mathrm{h7}} (T_{\mathrm{h3}} - T_{\mathrm{h1}}) + \dot{m}_{\mathrm{h1}} c_{\mathrm{h}} (T_{\mathrm{h2}} - T_{\mathrm{h1}})], \tag{3.31}$$
$$\frac{\mathrm{d}T_{\mathrm{h3}}}{\mathrm{d}t} = \frac{1}{C_{\mathrm{h3}}} [\dot{m}_{\mathrm{h5}} c_{\mathrm{co}} (T_{\mathrm{h4}} - T_{\mathrm{h3}}) - G_{\mathrm{h7}} (T_{\mathrm{h3}} - T_{\mathrm{h1}})], \tag{3.32}$$
$$\frac{\mathrm{d}T_{\mathrm{h4}}}{\mathrm{d}t} = \frac{1}{C_{\mathrm{h4}}} [\dot{m}_{\mathrm{h5}} c_{\mathrm{co}} (T_{\mathrm{h3}} - T_{\mathrm{h4}}) + \dot{Q}_{\mathrm{h10}}], \tag{3.33}$$
$$T_{\mathrm{h2}} = \varphi T_{\mathrm{h5}} + (1 - \varphi) T_{\mathrm{c1}}, \tag{3.34}$$

with G being the thermal conductance (subscript referring to thermal flow index), $\dot{m}_{\mathrm{h1}}$ stands for the air mass flow rate caused by the HVAC fan, c_{h} is the air specific thermal capacity, φ is the fresh air flap status (0 to 1), $\dot{m}_{\mathrm{h5}}$ is the coolant mass flow rate caused by the coolant pump, and c_{co} is the coolant specific thermal capacity.

The cabin model in Fig. 3.2 is described in detail in the following section.

Cabin thermal model

The cabin model overview can be found in Fig. 3.3. The model can be in general described by the following equations

$$C_{\mathrm{c1}} \frac{\mathrm{d}T_{\mathrm{c1}}}{\mathrm{d}t} = \dot{Q}_{\mathrm{c1}} + \dot{Q}_{\mathrm{c2}} + \dot{Q}_{\mathrm{c5}} + \dot{Q}_{\mathrm{c4}} + \dot{Q}_{\mathrm{c3}} - \dot{Q}_{\mathrm{c6}}, \tag{3.35}$$
$$C_{\mathrm{c2}} \frac{\mathrm{d}T_{\mathrm{c2}}}{\mathrm{d}t} = -\dot{Q}_{\mathrm{c3}}, \tag{3.36}$$
$$C_{\mathrm{c3}} \frac{\mathrm{d}T_{\mathrm{c3}}}{\mathrm{d}t} = -\dot{Q}_{\mathrm{c1}} + \dot{Q}_{\mathrm{c7}} + \dot{Q}_{\mathrm{c8}}, \tag{3.37}$$
$$C_{\mathrm{c4}} \frac{\mathrm{d}T_{\mathrm{c4}}}{\mathrm{d}t} = -\dot{Q}_{\mathrm{c2}} + \dot{Q}_{\mathrm{c9}}, \tag{3.38}$$

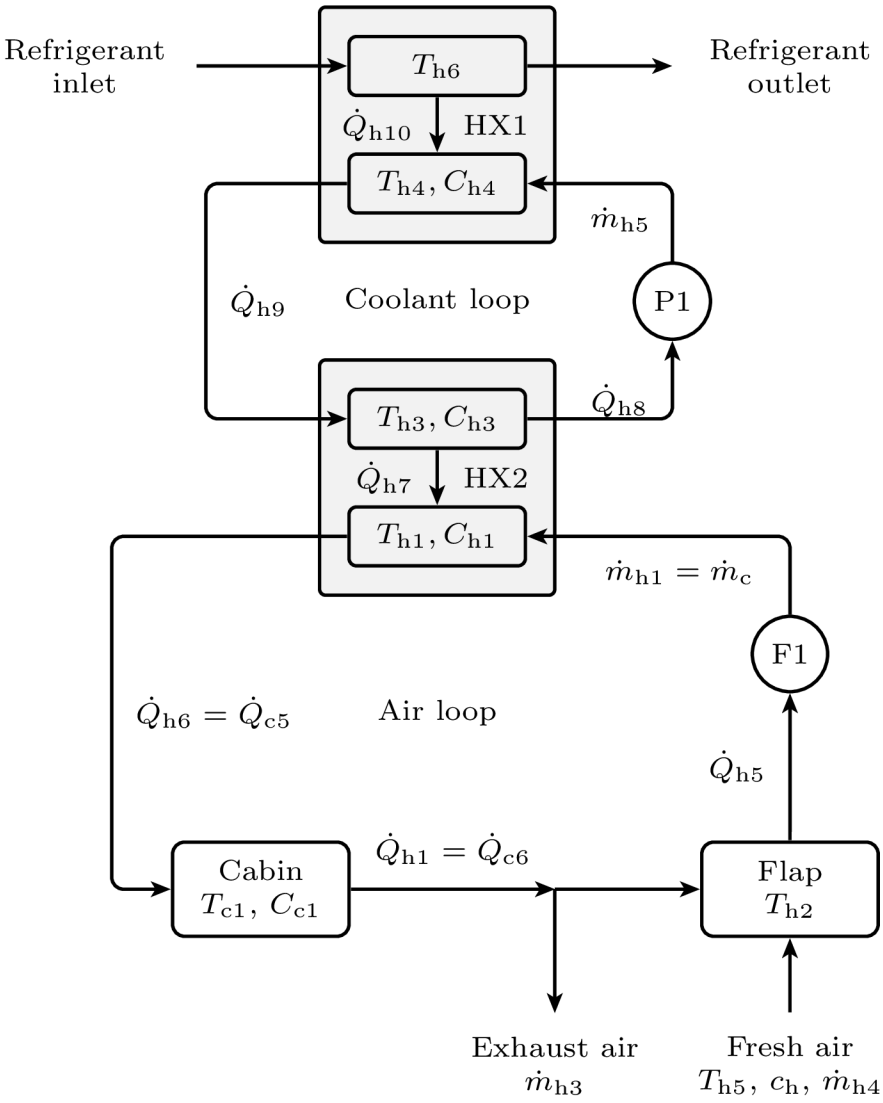

Fig. 3.2: FEV HVAC model

which can be then modified to the substituted form

$$\frac{\mathrm{d}T_{c1}}{\mathrm{d}t} = \frac{1}{C_{c1}}[G_{c1}(T_{c3} - T_{c1}) + G_{c2}(T_{c4} - T_{c1}) + \dot{m}_c c_c(T_{h1} - T_{c1}) + \dot{Q}_{c4} + G_{c3}(T_{c2} - T_{c1})], \tag{3.39}$$

$$\frac{\mathrm{d}T_{c2}}{\mathrm{d}t} = \frac{1}{C_{c2}}[-G_{c3}(T_{c2} - T_{c1})], \tag{3.40}$$

$$\frac{\mathrm{d}T_{c3}}{\mathrm{d}t} = \frac{1}{C_{c3}}[-G_{c1}(T_{c3} - T_{c1}) + \dot{Q}_{c7} + G_{c8}(T_{c5} - T_{c3})], \tag{3.41}$$

$$\frac{\mathrm{d}T_{c4}}{\mathrm{d}t} = \frac{1}{C_{c4}}[-G_{c2}(T_{c4} - T_{c1}) + G_{c9}(T_{c5} - T_{c4})], \tag{3.42}$$

where $\dot{m}_c = \dot{m}_{h1}$ and stands for the air mass flow rate through the cabin (caused by the HVAC fan), $c_c = c_h$ and is the air specific thermal capacity, $\dot{Q}_{c7}$ is the solar heat flow rate and $\dot{Q}_{c4}$ is the passenger heat flow rate. The subscript meanings for the rest of the variables are apparent from Fig. 3.3.

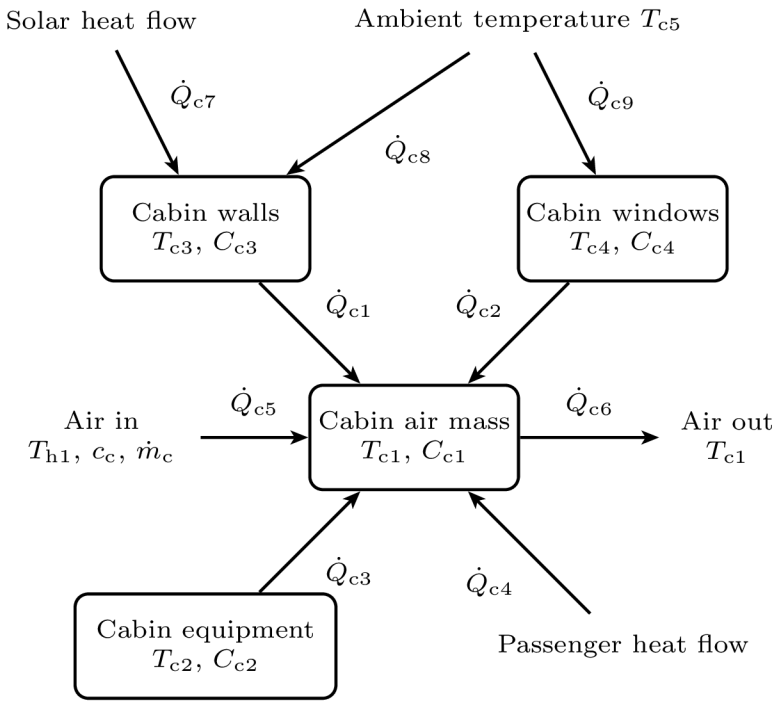

Fig. 3.3: FEV cabin thermal model

Air quality model

We can define the air quality in the most used form [20], i.e. as a ratio of CO_2 volume to the total vehicle cabin volume. The air quality can be expressed in percent or ppm (commonly used for indoor air quality evaluation [21, 20]).

The behavior of air quality inside a vehicle cabin can be described by

$$V\frac{\mathrm{d}\kappa}{\mathrm{d}t} = n_{\mathrm{pas}}\dot{V}_{\mathrm{res}}(\kappa_{\mathrm{ex}} - \kappa) + \varphi\dot{V}_{\mathrm{HVAC}}(\kappa_{\mathrm{amb}} - \kappa), \tag{3.43}$$

where κ is cabin air quality, κ_{ex} the exhaled air quality, κ_{amb} the ambient air quality, $\dot{V}_{\mathrm{res}}$ is the respiratory volume flow rate, $\dot{V}_{\mathrm{HVAC}}$ the volume flow rate of the HVAC, n_{pas} is the number of passengers in the vehicle, φ is the fresh air flap state ($\varphi = 1$: only fresh air, $\varphi = 0$: only recirculated air) and V is the cabin volume.

Respiratory volume flow rate can be computed as

$$\dot{V}_{\mathrm{res}} = f_{\mathrm{res}}V_{\mathrm{res}}, \tag{3.44}$$

where $f_{\mathrm{res}} = 0.25\,\mathrm{Hz}$ is the respiratory frequency and $V_{\mathrm{res}} = 0.0005\,\mathrm{m}^3$ is respiratory volume [22], which leads to

$$\frac{\mathrm{d}\kappa}{\mathrm{d}t} = \frac{1}{V}\left[n_{\mathrm{pas}} f_{\mathrm{res}} V_{\mathrm{res}}(\kappa_{\mathrm{ex}} - \kappa) + \varphi \frac{\dot{m}_{\mathrm{c}}}{\rho_{\mathrm{c}}}(\kappa_{\mathrm{amb}} - \kappa)\right], \tag{3.45}$$

where $\dot{m}_{\mathrm{c}}$ is the air mass flow rate defined above and ρ_{c} stands for cabin air mass density.

3.2.2 E-Drive model

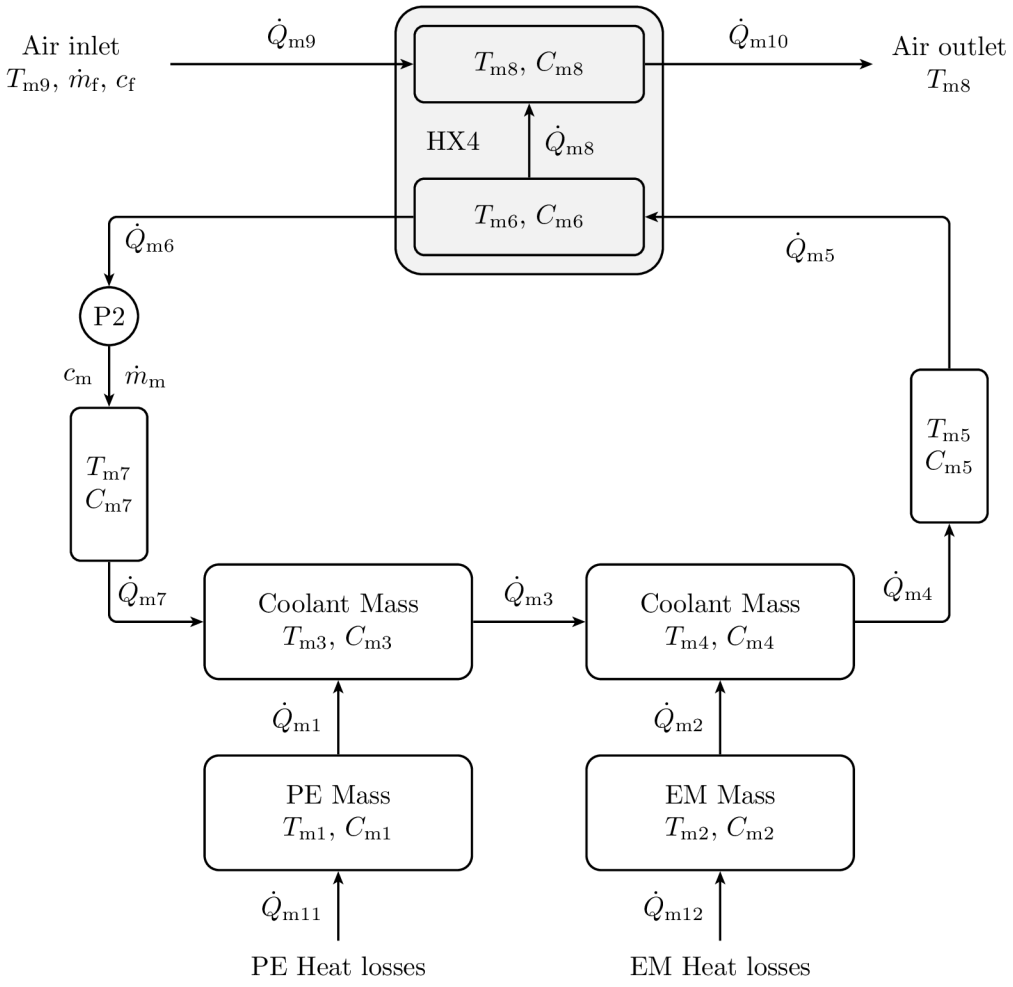

Fig. 3.4: Electric motor cooling circuit model

The Electric Motor (EM) and Power Electronics (PE) model is shown in Fig. 3.4 and it consists of heat exchanger HX4, which is used for coolant cooling by the air from the vehicle front-end. A pump P2 is incorporated to circulate the coolant through the EM and PE coolers and also through two pipes. EM and PE have also

defined thermal capacity, which is used to model the dynamic behavior of EM and PE parts.

The model can be described by the following system of equations

$$C_{\mathrm{m1}}\frac{\mathrm{d}T_{\mathrm{m1}}}{\mathrm{d}t} = \dot{Q}_{\mathrm{m11}} - \dot{Q}_{\mathrm{m1}}, \tag{3.46}$$
$$C_{\mathrm{m2}}\frac{\mathrm{d}T_{\mathrm{m2}}}{\mathrm{d}t} = \dot{Q}_{\mathrm{m12}} - \dot{Q}_{\mathrm{m2}}, \tag{3.47}$$
$$C_{\mathrm{m3}}\frac{\mathrm{d}T_{\mathrm{m3}}}{\mathrm{d}t} = \dot{Q}_{\mathrm{m7}} + \dot{Q}_{\mathrm{m1}} - \dot{Q}_{\mathrm{m3}}, \tag{3.48}$$
$$C_{\mathrm{m4}}\frac{\mathrm{d}T_{\mathrm{m4}}}{\mathrm{d}t} = \dot{Q}_{\mathrm{m3}} + \dot{Q}_{\mathrm{m2}} - \dot{Q}_{\mathrm{m4}}, \tag{3.49}$$
$$C_{\mathrm{m5}}\frac{\mathrm{d}T_{\mathrm{m5}}}{\mathrm{d}t} = \dot{Q}_{\mathrm{m4}} - \dot{Q}_{\mathrm{m5}}, \tag{3.50}$$
$$C_{\mathrm{m6}}\frac{\mathrm{d}T_{\mathrm{m6}}}{\mathrm{d}t} = \dot{Q}_{\mathrm{m5}} - \dot{Q}_{\mathrm{m6}} - \dot{Q}_{\mathrm{m8}}, \tag{3.51}$$
$$C_{\mathrm{m7}}\frac{\mathrm{d}T_{\mathrm{m7}}}{\mathrm{d}t} = \dot{Q}_{\mathrm{m6}} - \dot{Q}_{\mathrm{m7}}, \tag{3.52}$$
$$C_{\mathrm{m8}}\frac{\mathrm{d}T_{\mathrm{m8}}}{\mathrm{d}t} = \dot{Q}_{\mathrm{m8}} + \dot{Q}_{\mathrm{m9}} - \dot{Q}_{\mathrm{m10}}, \tag{3.53}$$

which can be rewritten as

$$\frac{\mathrm{d}T_{\mathrm{m1}}}{\mathrm{d}t} = -\frac{G_{\mathrm{m1}}}{C_{\mathrm{m1}}}T_{\mathrm{m1}} + \frac{G_{\mathrm{m1}}}{C_{\mathrm{m1}}}T_{\mathrm{m3}} + \frac{\dot{Q}_{\mathrm{m11}}}{C_{\mathrm{m1}}}, \tag{3.54}$$
$$\frac{\mathrm{d}T_{\mathrm{m2}}}{\mathrm{d}t} = -\frac{G_{\mathrm{m2}}}{C_{\mathrm{m2}}}T_{\mathrm{m2}} + \frac{G_{\mathrm{m2}}}{C_{\mathrm{m2}}}T_{\mathrm{m4}} + \frac{\dot{Q}_{\mathrm{m12}}}{C_{\mathrm{m2}}}, \tag{3.55}$$
$$\frac{\mathrm{d}T_{\mathrm{m3}}}{\mathrm{d}t} = \frac{G_{\mathrm{m1}}}{C_{\mathrm{m3}}}T_{\mathrm{m1}} - \frac{G_{\mathrm{m1}} + \dot{m}_{\mathrm{m}}c_{\mathrm{m}}}{C_{\mathrm{m3}}}T_{\mathrm{m3}} + \frac{\dot{m}_{\mathrm{m}}c_{\mathrm{m}}}{C_{\mathrm{m3}}}T_{\mathrm{m7}}, \tag{3.56}$$
$$\frac{\mathrm{d}T_{\mathrm{m4}}}{\mathrm{d}t} = \frac{G_{\mathrm{m2}}}{C_{\mathrm{m4}}}T_{\mathrm{m2}} + \frac{\dot{m}_{\mathrm{m}}c_{\mathrm{m}}}{C_{\mathrm{m4}}}T_{\mathrm{m3}} - \frac{G_{\mathrm{m2}} + \dot{m}_{\mathrm{m}}c_{\mathrm{m}}}{C_{\mathrm{m4}}}T_{\mathrm{m4}}, \tag{3.57}$$
$$\frac{\mathrm{d}T_{\mathrm{m5}}}{\mathrm{d}t} = \frac{\dot{m}_{\mathrm{m}}c_{\mathrm{m}}}{C_{\mathrm{m5}}}T_{\mathrm{m4}} - \frac{\dot{m}_{\mathrm{m}}c_{\mathrm{m}}}{C_{\mathrm{m5}}}T_{\mathrm{m5}}, \tag{3.58}$$
$$\frac{\mathrm{d}T_{\mathrm{m6}}}{\mathrm{d}t} = \frac{\dot{m}_{\mathrm{m}}c_{\mathrm{m}}}{C_{\mathrm{m6}}}T_{\mathrm{m5}} - \frac{G_{\mathrm{m8}} + \dot{m}_{\mathrm{m}}c_{\mathrm{m}}}{C_{\mathrm{m6}}}T_{\mathrm{m6}} + \frac{G_{\mathrm{m8}}}{C_{\mathrm{m6}}}T_{\mathrm{m8}}, \tag{3.59}$$
$$\frac{\mathrm{d}T_{\mathrm{m7}}}{\mathrm{d}t} = \frac{\dot{m}_{\mathrm{m}}c_{\mathrm{m}}}{C_{\mathrm{m7}}}T_{\mathrm{m6}} - \frac{\dot{m}_{\mathrm{m}}c_{\mathrm{m}}}{C_{\mathrm{m7}}}T_{\mathrm{m7}}, \tag{3.60}$$
$$\frac{\mathrm{d}T_{\mathrm{m8}}}{\mathrm{d}t} = \frac{G_{\mathrm{m8}}}{C_{\mathrm{m8}}}T_{\mathrm{m6}} - \frac{G_{\mathrm{m8}} + \dot{m}_{\mathrm{f}}c_{\mathrm{f}}}{C_{\mathrm{m8}}}T_{\mathrm{m8}} + \frac{\dot{m}_{\mathrm{f}}c_{\mathrm{f}}}{C_{\mathrm{m8}}}T_{\mathrm{m9}}. \tag{3.61}$$

The coolant mass flow rate $\dot{m}_{\mathrm{m}}$ is described by another equation

$$\dot{m}_{\mathrm{m}} = \mathrm{P}_2(n_{\mathrm{P2}}), \tag{3.62}$$

where P_2 is a function to compute $\dot{m}_{\mathrm{m}}$ from pump revolutions n_{P2}.

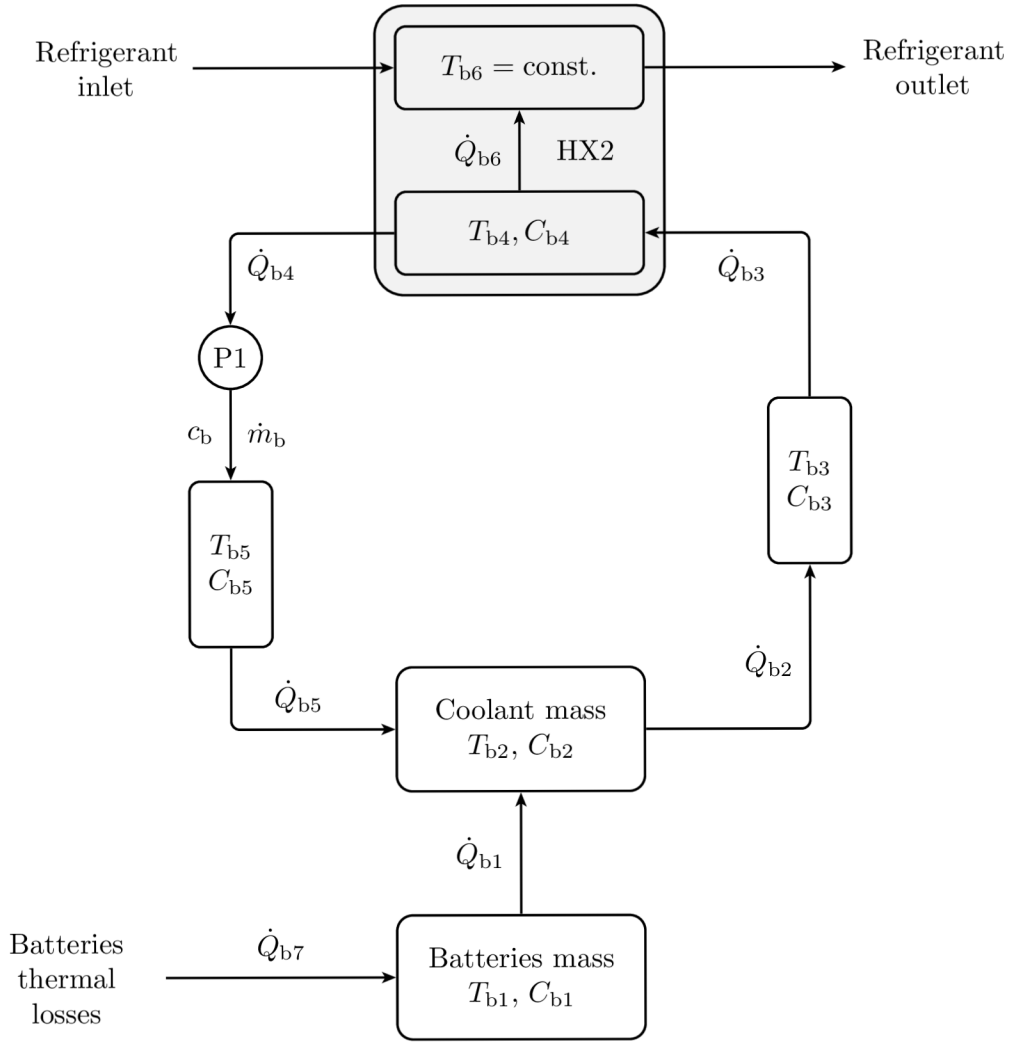

Fig. 3.5: FEV HV batteries thermal model

3.2.3 HV Battery model

The basic battery thermal model equations according to Fig. 3.5 are

$$C_{b1}\frac{dT_{b1}}{dt} = \dot{Q}_{b7} - \dot{Q}_{b1}, \tag{3.63}$$

$$C_{b2}\frac{dT_{b2}}{dt} = \dot{Q}_{b1} + \dot{Q}_{b5} - \dot{Q}_{b2}, \tag{3.64}$$

$$C_{b3}\frac{dT_{b3}}{dt} = \dot{Q}_{b2} - \dot{Q}_{b3}, \tag{3.65}$$

$$C_{b4}\frac{dT_{b4}}{dt} = \dot{Q}_{b3} - \dot{Q}_{b4} - \dot{Q}_{b6}, \tag{3.66}$$

$$C_{b5}\frac{dT_{b5}}{dt} = \dot{Q}_{b4} - \dot{Q}_{b5} \tag{3.67}$$

and can be modified to

$$\frac{\mathrm{d}T_{\mathrm{b1}}}{\mathrm{d}t} = -\frac{G_{\mathrm{b1}}}{C_{\mathrm{b1}}}T_{\mathrm{b1}} + \frac{G_{\mathrm{b1}}}{C_{\mathrm{b1}}}T_{\mathrm{b2}} + \frac{\dot{Q}_{\mathrm{b7}}}{C_{\mathrm{b1}}}, \tag{3.68}$$

$$\frac{\mathrm{d}T_{\mathrm{b2}}}{\mathrm{d}t} = \frac{G_{\mathrm{b1}}}{C_{\mathrm{b2}}}T_{\mathrm{b1}} - \frac{G_{\mathrm{b1}} + \dot{m}_{\mathrm{b}}c_{\mathrm{b}}}{C_{\mathrm{b2}}}T_{\mathrm{b2}} + \frac{\dot{m}_{\mathrm{b}}c_{\mathrm{b}}}{C_{\mathrm{b2}}}T_{\mathrm{b5}}, \tag{3.69}$$

$$\frac{\mathrm{d}T_{\mathrm{b3}}}{\mathrm{d}t} = \frac{\dot{m}_{\mathrm{b}}c_{\mathrm{b}}}{C_{\mathrm{b3}}}T_{\mathrm{b2}} - \frac{\dot{m}_{\mathrm{b}}c_{\mathrm{b}}}{C_{\mathrm{b3}}}T_{\mathrm{b3}}, \tag{3.70}$$

$$\frac{\mathrm{d}T_{\mathrm{b4}}}{\mathrm{d}t} = \frac{\dot{m}_{\mathrm{b}}c_{\mathrm{b}}}{C_{\mathrm{b4}}}T_{\mathrm{b3}} - \frac{\dot{m}_{\mathrm{b}}c_{\mathrm{b}} + G_{\mathrm{b6}}}{C_{\mathrm{b4}}}T_{\mathrm{b4}} + \frac{G_{\mathrm{b6}}}{C_{\mathrm{b4}}}T_{\mathrm{b6}}, \tag{3.71}$$

$$\frac{\mathrm{d}T_{\mathrm{b5}}}{\mathrm{d}t} = \frac{\dot{m}_{\mathrm{b}}c_{\mathrm{b}}}{C_{\mathrm{b5}}}T_{\mathrm{b4}} - \frac{\dot{m}_{\mathrm{b}}c_{\mathrm{b}}}{C_{\mathrm{b5}}}T_{\mathrm{b5}}. \tag{3.72}$$

The refrigerant temperature T_{b6} is assumed to be constant to simplify the model. The coolant mass flow rate $\dot{m}_{\mathrm{b}}$ is described by another equation

$$\dot{m}_{\mathrm{b}} = \mathrm{P}_1(n_{\mathrm{P1}}), \tag{3.73}$$

where P_1 is a function to compute $\dot{m}_{\mathrm{b}}$ from pump revolutions n_{P1}.

4 Control of electro-thermal flows

Control algorithms were prepared for whole the VTMS shown in Fig. 2.1. The algorithms were incorporated into the overall control model in Fig. 4.1 in the form of three blocks in the middle of the figure. Each of them represents HVAC, HV

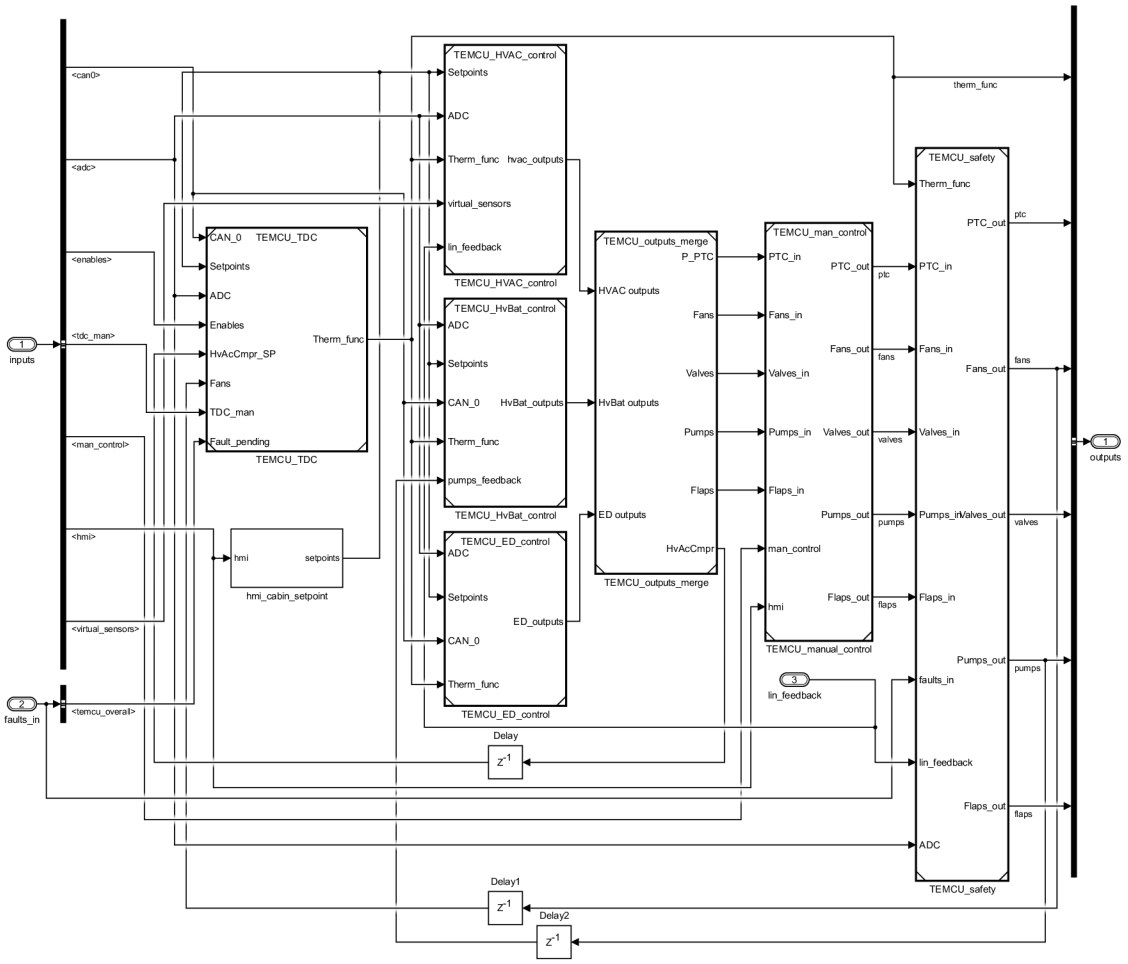

Fig. 4.1: TEMCU overall control model

Battery, and ED control algorithms and is internally divided into several control models, which defines the control within each of the Thermal Functions. These sets of algorithms are based on PI controllers, so the detailed description is omitted as these approaches are generally known. For selected parts of VTMS, innovative algorithms were designed and their description is included within this chapter.

The algorithms (both the basic and advanced) were tested on the overall Dymola model and also they were partially tested on the assembled test bench.

4.1 VCRS model-based EXV control

Compressor speed (and thus cooling/heating power) can be quite easily controlled (PI controller, optionally with gain scheduling based on evaporator air mass flow rate and/or chiller coolant mass flow rate) to defined pressure reference (usual pressure of 3..4 bar for refrigerant R1234yf). EXV control is much more tricky - in Vapor Compression Refrigeration System (VCRS) with suction accumulator the EXV should ensure defined condenser subcooling (e.g. 5..10 K; representing optimal COP). Issues of a simple PI controller approach are:

1. Reduced VCRS performance during startup - EXV is almost closed due to low or even none subcooling (will be discussed later), thus the low-side pressure goes below the defined pressure reference and compressor speed is significantly reduced by its speed control.
2. Subcooling (SC) measurement - subcooling is defined and measurable (computable) only for positive values (even if the refrigerant is far in the two-phase region, the subcooling sensor always reports 0 K). If SC setpoint is 5 K then maximum control error is +5 K and for refrigerant of quality $\xi \in (0, 1)$ will be always the same. Despite that SC should be positive during the whole operation, the decrease to 0 K can easily happen during startup or fast condenser air mass flow rate change.

If we consider VCRS startup, we can observe zero or low SC values during the first tenths seconds of operation. This phenomenon is caused by SC's definition and its properties, especially the dependence on high-side pressure. The blue line in Fig. 4.2 shows a maximal theoretical value of SC for different pressure values under the assumption that the refrigerant is cooled down exactly to ambient temperature in the condenser. As this assumption usually does not hold for a real condenser, two characteristics were added into Fig. 4.2. The symbol ΔT_{HX} represents the temperature difference between ambient temperature and refrigerant temperature at the condenser outlet. If we consider the worse presented case ($\Delta T_{\mathrm{HX}} = 10\,\mathrm{K}$), the SC value is equal to zero for pressure below 9 bar and then it gradually rises. Thus the classical approach with PI controller would restrict the EXV refrigerant mass flow rate (e.g. it will see zero or low SC until reaching 11 bar for SC reference of 7 K).

As it was found that the more advanced control approach is desirable, we need to define its goals. First of all, the EXV should be controlled to keep the refrigerant subcooled (to avoid refrigerant flow reduction due to vapor bubbles), then the SC value should track the SC reference and the whole VCRS should provide desired cooling capacity (even during startup). We identified several possible solutions, which would satisfy some or all of the goals.

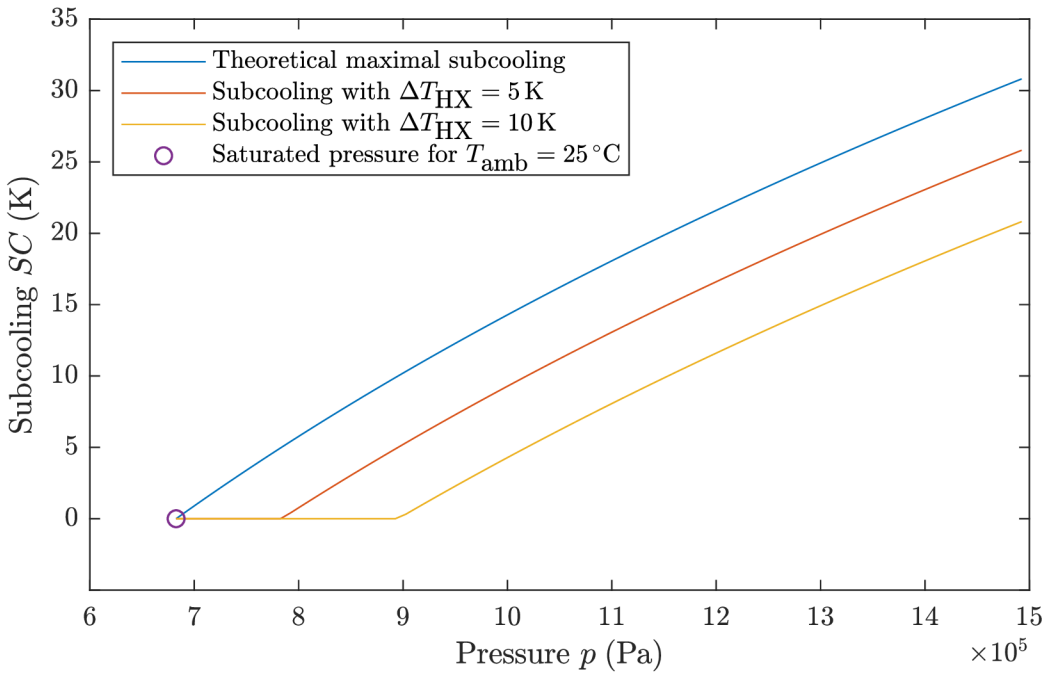

Fig. 4.2: Dependency of condenser subcooling on refrigerant pressure (R1234yf) for ambient temperature $T_{amb} = 25\,°C$

1. Compressor startup by ramp - ramp final value needs to be defined, some switching to controller needed, very low suction pressure, still quite low performance (due to low refrigerant mass flow rate in the evaporator).
2. EXV startup value - the value and the validity time needs to be defined, probably dependent on operating conditions and compressor speed.
3. Higher low limit of EXV opening - depends on operating conditions, would need to be adjusted (probably online), could lead to no SC (if more closed EXV required).
4. EXV control based on refrigerant mass flow rate computation - low pressure not dropping so much, performance not reduced, dependent on the accuracy of $\dot{m}$ guess value ("open-loop").
5. EXV control based on the VCRS model - EXV can be controlled to specific enthalpy instead of SC (valid also in the two-phase area), more precise $\dot{m}$ computation.

The fourth method was selected as it should fulfill the defined goals and it is quite easily implementable and tunable. The fifth method would also provide the required performance, but the deployment would be much more complicated, so it could be the next step in our research activities.

4.1.1 EXV refrigerant mass flow rate computation

Using (F.1) we can compute the expected refrigerant mass flow rate of the compressor and by employing (F.19) we can get the mass flow rate through the EXV.

In steady-state we suppose that these refrigerant mass flow rates are equal

$$\dot{m}_{\mathrm{xv}} = \dot{m}_{\mathrm{cmp}}. \tag{4.1}$$

By combining (F.19) and (F.1) and by some reordering we can get an equation for estimated EXV effective area needed for steady-state VCRS operation

$$A = \frac{\frac{\omega}{2\pi}\rho_{\mathrm{cmp,i}} V_{\mathrm{cmp}} \eta_{\mathrm{vol}}}{C_{\mathrm{d}}\sqrt{2\rho_{\mathrm{xv,i}}\left(p_{\mathrm{c}} - p_{\mathrm{e}}\right)}}. \tag{4.2}$$

We know almost all of the variables used, but particularly refrigerant volumetric mass densities at the compressor and EXV inlet are not precisely known.

Regarding the compressor inlet refrigerant density, the situation is quite clear. If we measure the evaporator pressure (suction pressure), we can then get the refrigerant mass density from refrigerant tables as a function

$$\rho_{\mathrm{cmp,i}} = \mathrm{\rho}(p_{\mathrm{e}}, h_{\mathrm{e}}). \tag{4.3}$$

The VCRS circuit is equipped with a suction line accumulator, which ensures no liquid refrigerant in compressor suction (i.e. the quality of refrigerant is always equal 1 or even superheated). Then we can simplify (4.3) as a function of a single variable

$$\rho_{\mathrm{cmp,i}} = \mathrm{\rho}_{\mathrm{sv}}(p_{\mathrm{e}}), \tag{4.4}$$

where $\rho_{\mathrm{sv}}(p_{\mathrm{e}})$ is a function returning refrigerant mass density based on refrigerant pressure p at saturated vapor line. We neglect the changes of refrigerant mass density caused by possible refrigerant superheating in the evaporator or pipe between the accumulator and compressor, but it is evident from Fig. 4.3 that it has a negligible impact on refrigerant mass density (under usual operating conditions).

The second unknown variable is the refrigerant mass density at EXV inlet. In this case, we need to investigate the possibilities in more detail. Under fixed pressure (we can measure) we can get dependency of refrigerant density on specific enthalpy (Fig. 4.4) and this would give us the best possible results

$$\rho_{\mathrm{xv,i}} = \mathrm{\rho}(p_{\mathrm{c}}, h_{\mathrm{c}}), \tag{4.5}$$

but the specific enthalpy can not be directly measured or simply computed. In mentioned Fig. 4.4 the refrigerant mass density for saturated liquid is highlighted by a small circle. The only measurable variable - subcooling - can be computed

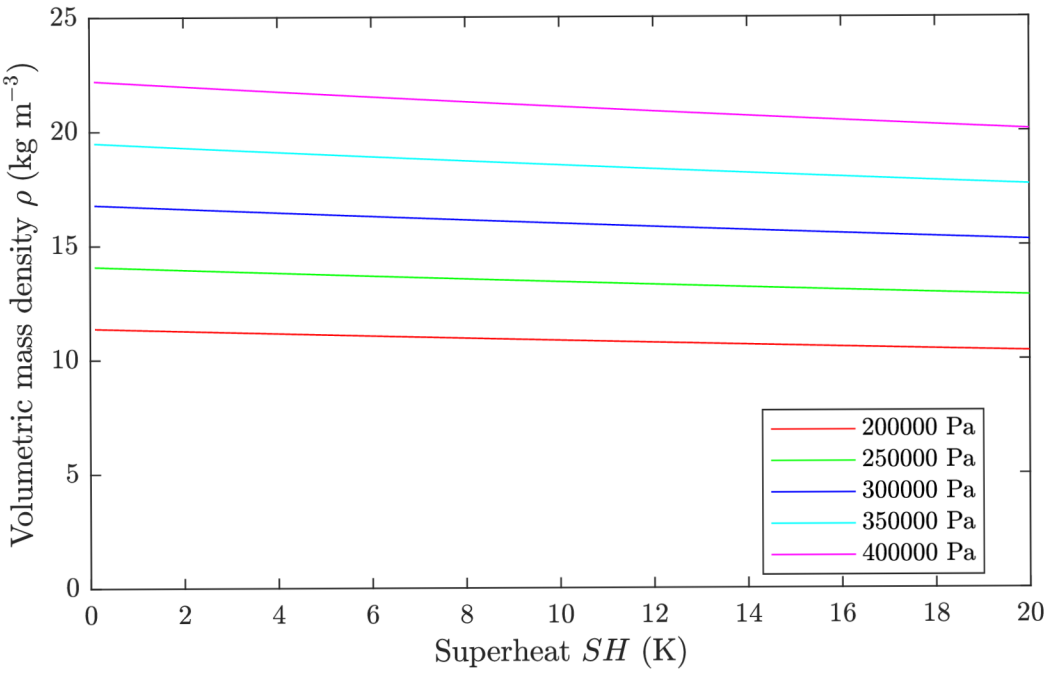

Fig. 4.3: R1234yf volumetric mass density dependency on superheat for different evaporator pressure levels

using

$$SC = \mathrm{T_{sl}}(p_\mathrm{c}) - T_\mathrm{ref}, \tag{4.6}$$

where $\mathrm{T_{sl}}(p)$ is a function returning refrigerant temperature based on its pressure on the saturated liquid line and T_ref is measured refrigerant temperature at condenser outlet.

If we investigate the volumetric mass density dependency on subcooling in Fig. 4.5, we can simplify the (4.5) to the function of a single variable, as the density variation due to subcooling can be neglected for reasonable values of subcooling

$$\rho_\mathrm{xv,i} = \mathrm{\rho_{sl}}(p_\mathrm{c}), \tag{4.7}$$

where $\rho_\mathrm{sl}(p)$ is a function returning the refrigerant density based on its pressure at the saturated liquid line. We could also omit this neglection and compute the mass density as

$$\rho_\mathrm{xv,i} = \mathrm{\rho}(p_\mathrm{c}, SC), \tag{4.8}$$

but the accuracy improvement would not be significant.

On the other hand, the simplification in (4.7) can not be extended to the two-phase region, as the refrigerant mass density is strongly dependent on refrigerant quality. This dependency is illustrated in Fig. 4.6.

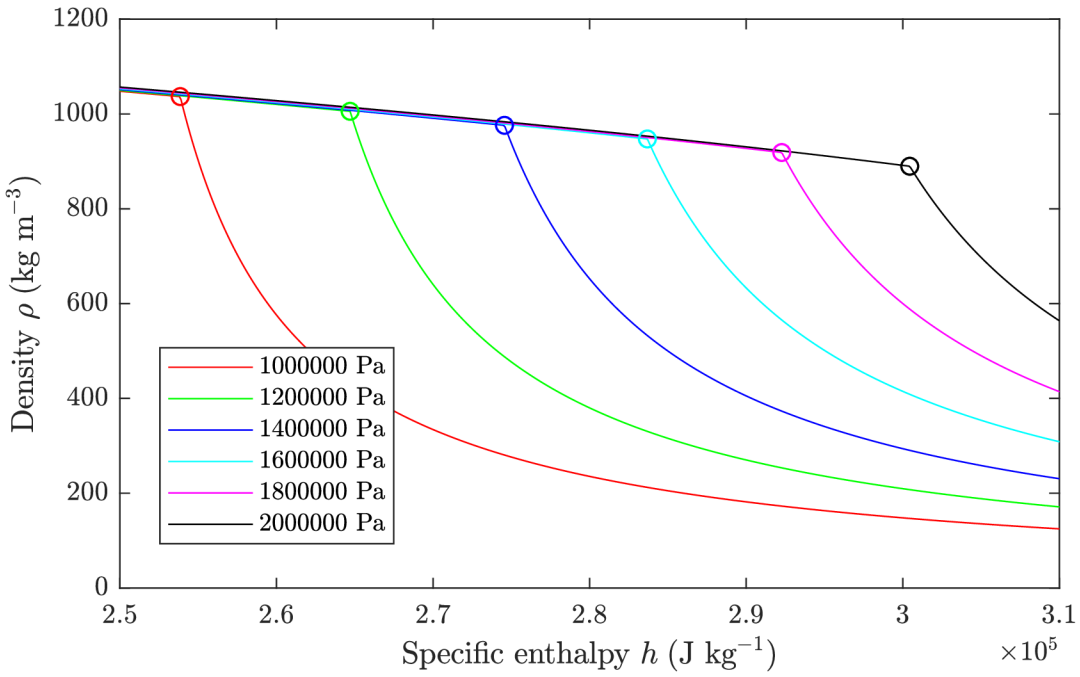

Fig. 4.4: R1234yf volumetric mass density dependency on specific enthalpy for different condenser pressure levels

Then, there are two possibilities of EXV mass density computation. The first one presumes subcooled refrigerant throughout whole the operation and this approach was used within this work. The second one requires the value of specific enthalpy, which can be obtained by executing the VCRS model during its operation. This approach can be the direction of future research and developments.

We recall (4.2) and substitute functions for refrigerant mass density

$$A = \frac{\frac{\omega}{2\pi}\rho_{\mathrm{sv}}(p_{\mathrm{e}})V_{\mathrm{cmp}}\eta_{\mathrm{vol}}}{C_{\mathrm{d}}\sqrt{2\rho_{\mathrm{sl}}(p_{\mathrm{c}})\,(p_{\mathrm{c}}-p_{\mathrm{e}})}} \tag{4.9}$$

and using this equation we can compute the estimated effective flow area of EXV. As some simplifications were made (neglecting the influence of superheat and subcooling on refrigerant mass density), there will be some error. It might be also caused by inaccurate EXV model, disturbances and other influences.

An additional PI controller was proposed to ensure disturbance rejection and to control the subcooling to optimal reference value with no steady-state error as shown in Fig. 4.7. This method does not require any additional sensors compared to the standard sensor equipment (two pressures and refrigerant temperature at the condenser outlet).

The CoolProp library [23] was used in the text above to obtain refrigerant state variables and other properties.

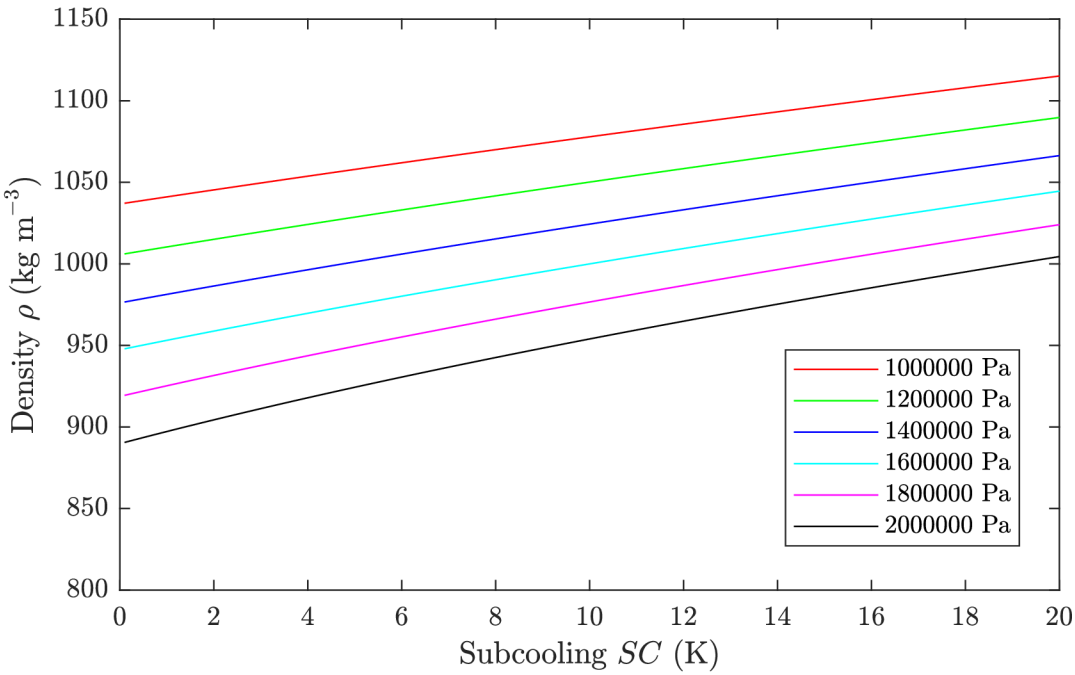

Fig. 4.5: R1234yf mass density dependency on refrigerant subcooling for different condenser pressure levels

This approach of EXV control was implemented into Thermo-Electric Management Control Unit (TEMCU) and evaluated on the test bench with results presented in Fig. 4.8. It is evident that this control approach gives great results in terms of subcooling reference tracking and substantially improves the VCRS system startup. The first plot shows the refrigerant pressures including a low-pressure setpoint. It was reached after approx. 150 s from the compressor start and this time is caused by the conservative setting of the compressor controller (to prevent any oscillations) and by different time constants (caused by e.g. evaporator heat capacity). From the second plot, we can see that VCRS is capable to cool the air and the performance is not limited (even at startup). The evaporator superheat and condenser subcooling are presented in the next plot. The subcooling reference is reached approx. 30 s after compressor startup and it needs some additional time for settling, but then the reference is tracked without any substantial deviation. The last two plots show the manipulated inputs, the compressor speed, and the EXV opening ratio.

The presented method of EXV SC control could be (with minor changes) also applied to VCRS EXV superheat control.

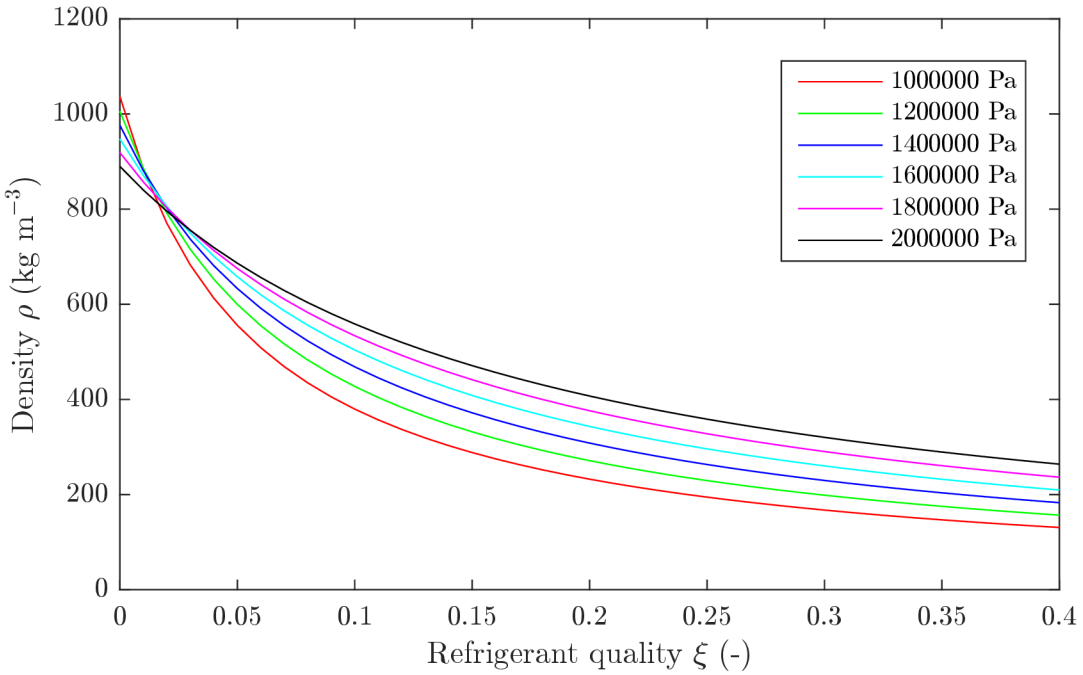

Fig. 4.6: R1234yf mass density dependency on refrigerant quality for different condenser pressure levels

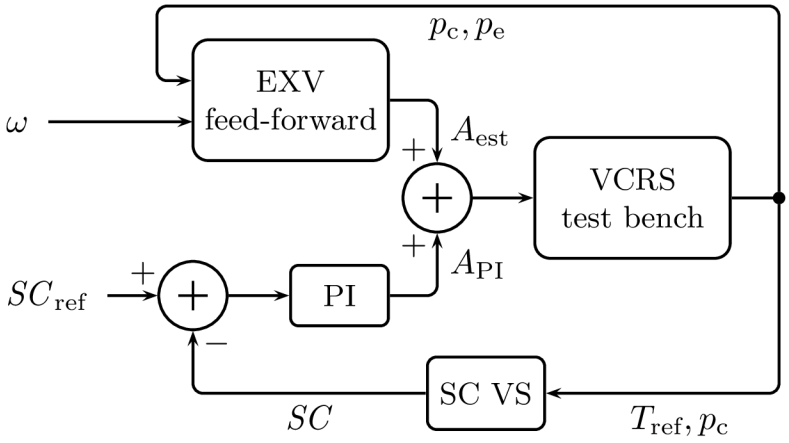

Fig. 4.7: Model-based VCRS EXV control loops.

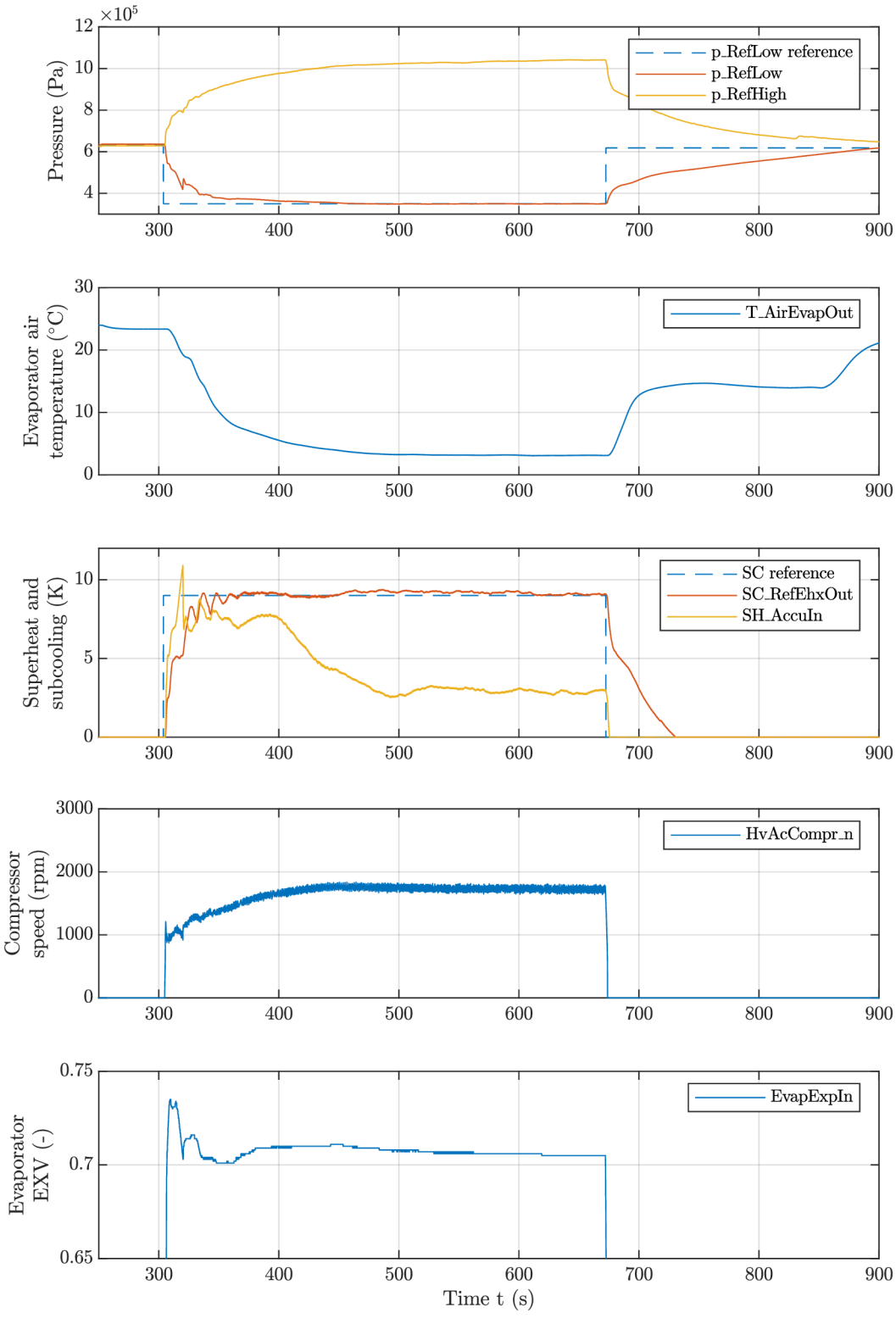

Fig. 4.8: Test bench measurements of model-based EXV control

4.2 Cabin temperature control

This section aims to design energy-efficient control of cabin air temperature. Vehicle cabin needs to be ventilated, but the exhausted air carries out heated or conditioned air, which leads to substantial energy losses. As this issue is more significant in winter during cabin heating, we will consider this case. The summer operation would be very similar when considering cooling efficiency.

It is obvious that with full cabin air recirculation, minimal heat requirements would be achieved. Nevertheless, this approach can not be used, as no fresh air will be supplied to the cabin and thus the air quality will be deteriorated in terms of a higher carbon dioxide (CO_2) concentration. High concentrations of CO_2 can lead to driver (and also passenger) fatigue [24]. Moreover, the cabin air humidity can increase and under some conditions windows can get fogged, leading to a limited driver view. Both these problems can negatively influence the driver's comfort and attention, which could in the worst case cause an accident.

In this section, the C-segment passenger car (or its equivalent, like the US compact car) is considered to have a cabin compartment volume of 3000 l and a length of approx. 4.5 m.

As a first preview of the required thermal flows for vehicle cabin heating, we performed a set of simulations, whose results are presented in Fig. 4.9 and 4.10. These simulations were executed in Dymola, based on the model described in section 4.2.1, with constant controls (apart from the heat source and fresh air flap) and ambient conditions, defined in Table 4.1.

Tab. 4.1: Actuators and conditions for basic cabin thermal flow simulations

Actuator/condition name	Symbol	Value
Coolant mass flow rate	$\dot{m}_{\mathrm{h5}}$	$0.4\,\mathrm{kg\,s^{-1}}$
Air mass flow rate	$\dot{m}_{\mathrm{c}}$	$0.07\,\mathrm{kg\,s^{-1}}$
Thermal flow to coolant	$\dot{Q}_{\mathrm{h10}}$	dependent
Fresh air flap	φ	independent
Cabin air quality	κ	dependent
Number of passengers	n_{pas}	2
Ambient temperature	T_{c5}	$-10\,^{\circ}\mathrm{C}$
Cabin temperature reference	T_{c1}	$20\,^{\circ}\mathrm{C}$

In Fig. 4.9, there is the heat required for cabin heat build-up during a 30-minute drive presented. All the vehicle parts were initially at the ambient temperature and then we started heating up the cabin, and this process was repeated for different

settings of the fresh air flap

$$\varphi \in \{0, 10, 25, 50, 75, 100\} \quad (\%). \tag{4.10}$$

This setting was kept constant during the individual simulation runs and the results for the dependent variables of all the runs are shown in Fig. 4.9. Both the required heat and the resulting cabin air quality are strongly dependent on the fresh air flap setting. Then, two important conclusions can be obtained from Fig. 4.9:

1. The fresh air flap - needs to be kept above approx. 25 % to achieve satisfactory cabin air quality (considering 2 passengers and HVAC fan air mass flow rate $\dot{m}_c = 0.07\,\mathrm{kg\,s^{-1}}$; with possible short-term lower values of the fresh air ratio)
2. A heat source in the order of kW (e.g. 4..8 kW) is needed for cabin heat build-up (note: even all the waste heat from an EV powertrain is not sufficient).

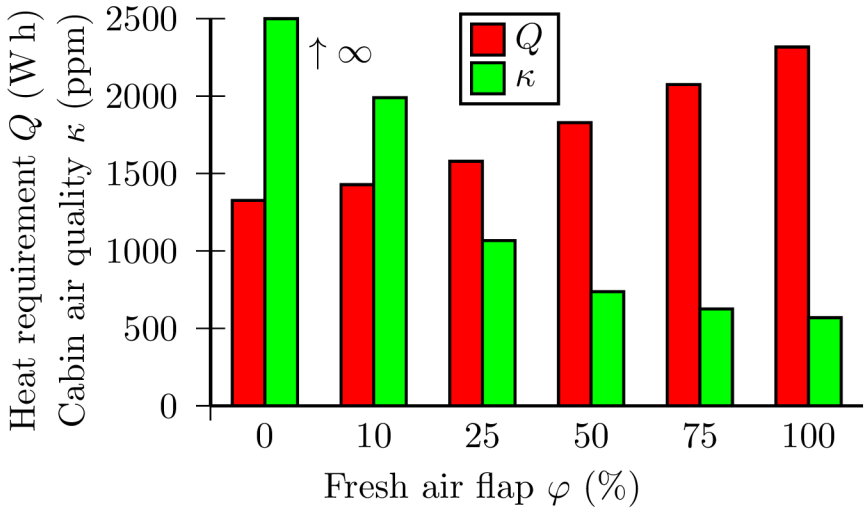

Fig. 4.9: Heat required by a heating system for cabin heat build-up during a 30-minute drive (conditions defined in Tab. 4.1)

Furthermore, Fig. 4.10 presents the steady-state heat flow rate dependency on the fresh air flap setting. It is evident that the fresh air flap can not be entirely closed (full recirculation) and that the heat flow rate is highly dependent on its value.

Regarding the influence of cabin heating on vehicle range, in the worst-case (under conditions defined in Tab. 4.1), the heat source would consume approx. 2.3 kW h per cabin heat build-up and 3 kW h per each hour of driving, with a higher air mass flow rate the power consumption would be also higher. For a mid-size EV (such as a Mercedes-Benz B-class, Nissan Leaf) that means a loss of mileage by 7.6 % due to cabin heat build-up and 10 % per each hour of operation. This model case didn't take into account the power consumption of the fan and coolant pump,

a possible lower ambient temperature, heat losses in the engine compartment, and other influences that might make the range loss even higher. The conclusion from this analysis is that cabin heating can have a strong negative influence on the EV range.

At this point, we should summarize the requirements on cabin environment control:

1. Temperature - keep it at a (user) defined reference
2. Air quality - keep it at a reasonable value (approx. 600..1000 ppm, short time up to 1500 ppm)
3. Power consumption - minimize the power of the heat source, fan, and coolant pump
4. Noise - keep the fan speed as low as possible

The controlled system's manipulated variables are constrained, moreover, its internal states and outputs are constrained too (e.g. supply air temperature should not exceed 60 °C, coolant temperature 90 °C, etc.).

Considering the above requirements, one of the preferable control approaches is Non-linear Model Predictive Control (NMPC). The traditional control approaches introduce a high number of additional control references, switching between control scenarios (e.g. heat build-up, steady-state, etc.), and complicated state constraints compliance. Moreover, the system has four inputs, two outputs, significant cross-couplings between inputs, and outputs and power consumption optimization is required. In the end, the traditional control system would become overcomplicated, thus the NMPC approach is preferable from our perspective.

NMPC applied to Plug-in Hybrid Electric Vehicle (PHEV) thermal management (battery, charger and power electronics cooling) was successfully tested in a Software in the Loop (SIL) simulation [25] and then tested in the real environment [26]. Model predictive on-off control for cabin heating in ICE vehicles was developed and implemented in [27]. The HVAC system, including the heat pump, was successfully controlled by NMPC in [28] with NMPC running on an Intel i5 2.6 GHz quad-core processor of a laptop. There are also several papers on cabin air quality and ventilation, such as [29, 30], but none of them links the air quality with power consumption for heating. The indoor air quality control is quite often used in building environment control, in combination with MPC, reported, for example by [31]. The authors of [32] proposed linear MPC for vehicle cabin heating, and in conclusion they call for considering cabin air recirculation in an MPC control strategy.

Model predictive control is also widely used in different automotive applications, especially for fuel consumption reduction [33, 34, 35, 36], path tracking [37, 38] and cruise control [39, 40, 41].

As far as we at best know, there is no implementation of NMPC in an automotive-

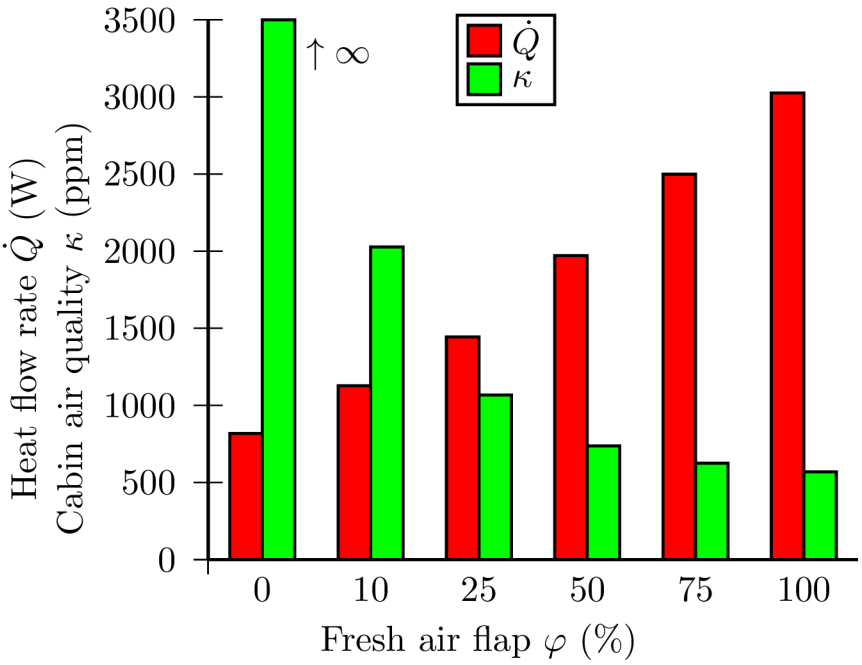

Fig. 4.10: Heat flow rate needed for cabin heating in a steady-state (conditions defined in Tab. 4.1)

grade processor in series production for EV cabin heating concerning cabin air quality.

The dynamic model of the FEV cabin and HVAC was prepared as a combination of the equations (3.31)-(3.33), (3.39)-(3.42) and (3.45)

$$\dot{\mathbf{x}} = \mathbf{f}(\mathbf{x}, \mathbf{u}), \tag{4.11}$$

$$\mathbf{z} = \mathbf{h}(\mathbf{x}), \tag{4.12}$$

with state ($\mathbf{x}$), input ($\mathbf{u}$) and output ($\mathbf{z}$) vectors

$$\mathbf{x} = \begin{bmatrix} T_{\mathrm{c1}} & T_{\mathrm{c2}} & T_{\mathrm{c3}} & T_{\mathrm{c4}} & T_{\mathrm{h1}} & T_{\mathrm{h3}} & T_{\mathrm{h4}} & \kappa \end{bmatrix}^{\mathsf{T}}, \tag{4.13}$$

$$\mathbf{u} = \begin{bmatrix} \dot{m}_{\mathrm{h5}} & \dot{m}_{\mathrm{c}} & \dot{Q}_{\mathrm{h10}} & \varphi \end{bmatrix}^{\mathsf{T}}, \tag{4.14}$$

$$\mathbf{z} = \begin{bmatrix} z_{T_{\mathrm{c1}}} & z_{T_{\mathrm{h1}}} & z_{T_{\mathrm{h4}}} & z_{\kappa} \end{bmatrix}^{\mathsf{T}}, \tag{4.15}$$

$\mathbf{f}(\cdot)$ stands for the right-hand sides of (3.31)-(3.33), (3.39)-(3.42) and (3.45) and $\mathbf{h}(\cdot)$ is a vector of the output functions. The output functions are linear, thus we can write

$$\mathbf{z} = \mathbf{h}(\mathbf{x}) = \mathbf{H}\mathbf{x}, \tag{4.16}$$

where

$$\mathbf{H} = \begin{bmatrix} 1 & 0 & 0 & 0 & 0 & 0 & 0 & 0 \\ 0 & 0 & 0 & 0 & 1 & 0 & 0 & 0 \\ 0 & 0 & 0 & 0 & 0 & 0 & 1 & 0 \\ 0 & 0 & 0 & 0 & 0 & 0 & 0 & 1 \end{bmatrix}. \tag{4.17}$$

4.2.1 Cabin and HVAC reference model in Dymola

A reference model of the FEV cabin and HVAC system was set up in Dymola using the `ThermalSystems` library, which was extended to suit the requirements (air quality modeling, additional temperature measurements). The model was exported into a Functional Mockup Unit (FMU), which was then imported into the MATLAB Simulink environment using the FMUtoolbox [88]. The FMU represents a black-box model of the cabin and HVAC system and is used as a substitution of a real FEV cabin and HVAC system.

An overview of the Dymola model is in Fig. 4.11, where the connectors were intentionally omitted to increase the clarity of the figure.

4.2.2 NMPC problem formulation

At each time step of the NMPC algorithm, an optimal control problem (OCP) needs to be solved [42]

$$\min J_N(\mathbf{x_0}, \mathbf{u}(\cdot)) = \sum_{k=0}^{N-1} \|\mathbf{l}(\mathbf{x}_k, \mathbf{u}_k) - \mathbf{r}_k\|^2_{\mathbf{Q}} + \|\mathbf{l}_N(\mathbf{x}_N) - \mathbf{r}_N\|^2_{\mathbf{Q}_N}, \tag{4.18}$$

subject to

$$\mathbf{x}_0 = \hat{\mathbf{x}}_0, \tag{4.19}$$

$$\mathbf{x}_{k+1} = \mathbf{f}(\mathbf{x}_k, \mathbf{u}_k), \tag{4.20}$$

$$\mathbf{x}_k^{\text{lo}} \leq \mathbf{x}_k \leq \mathbf{x}_k^{\text{up}}, \tag{4.21}$$

$$\mathbf{u}_k^{\text{lo}} \leq \mathbf{u}_k \leq \mathbf{u}_k^{\text{up}}, \tag{4.22}$$

where $\mathbf{l}(\cdot)$ and $\mathbf{l}_N(\cdot)$ are vectors of penalized variables, $\mathbf{r}_k$ and $\mathbf{r}_N$ stand for time-varying and final references, $\mathbf{Q}$ and $\mathbf{Q}_N$ are weighting matrices. Then $\mathbf{x}$ denotes the discrete states, $\mathbf{u}$ the control input. Both the states and control inputs can be constrained by (4.21) and (4.22).

To allow constraints on control changes and their penalization, the model was slightly modified. The controls $\mathbf{u} = \begin{bmatrix} \dot{m}_{\text{h5}} & \dot{m}_{\text{c}} & \dot{Q}_{\text{h10}} & \varphi \end{bmatrix}^{\mathsf{T}}$ are now considered as additional states and we use a new controls vector $\Delta\mathbf{u} = \begin{bmatrix} \Delta\dot{m}_{\text{h5}} & \Delta\dot{m}_{\text{c}} & \Delta\dot{Q}_{\text{h10}} & \Delta\varphi \end{bmatrix}^{\mathsf{T}}$

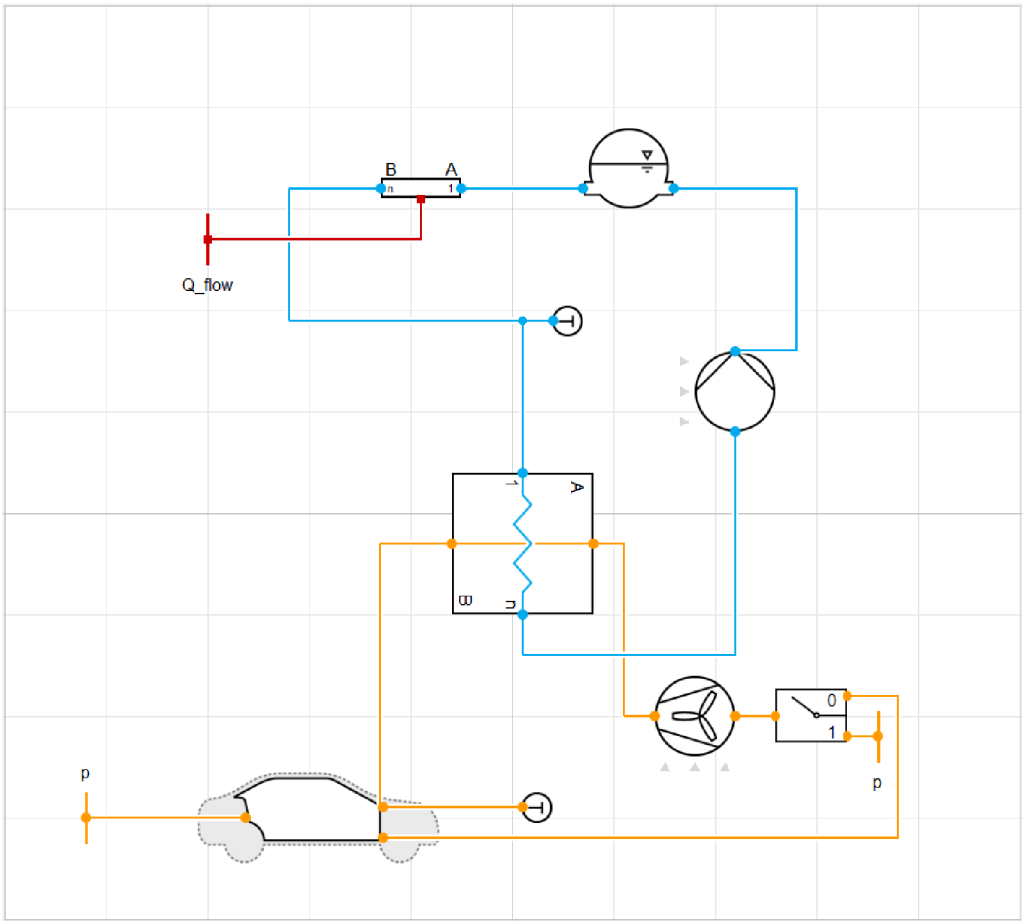

Fig. 4.11: NMPC reference model of the cabin and HVAC in Dymola

and the additional set of differential equations

$$\frac{\mathrm{d}}{\mathrm{d}t}\begin{bmatrix}\dot{m}_{\mathrm{h5}}\\ \dot{m}_{\mathrm{c}}\\ \dot{Q}_{\mathrm{h10}}\\ \varphi\end{bmatrix} = \begin{bmatrix}\Delta\dot{m}_{\mathrm{h5}}\\ \Delta\dot{m}_{\mathrm{c}}\\ \Delta\dot{Q}_{\mathrm{h10}}\\ \Delta\varphi\end{bmatrix}. \tag{4.23}$$

This approach allows us to define constraints on control input changes, which is important when considering real actuators such as the air flap, coolant pump, etc., which have a limited control input change rate. Moreover, it is possible to introduce the penalization of these changes, as fast changes are not convenient (especially for mechanical actuators).

The previously described change of control variables also ensures a zero steady-state error (offset free tracking), as shown, for example, in [43].

The model of the HVAC fan and coolant pump was calibrated on a test bench (Fig. 4.13) with real components by measurement of their characteristics (with a

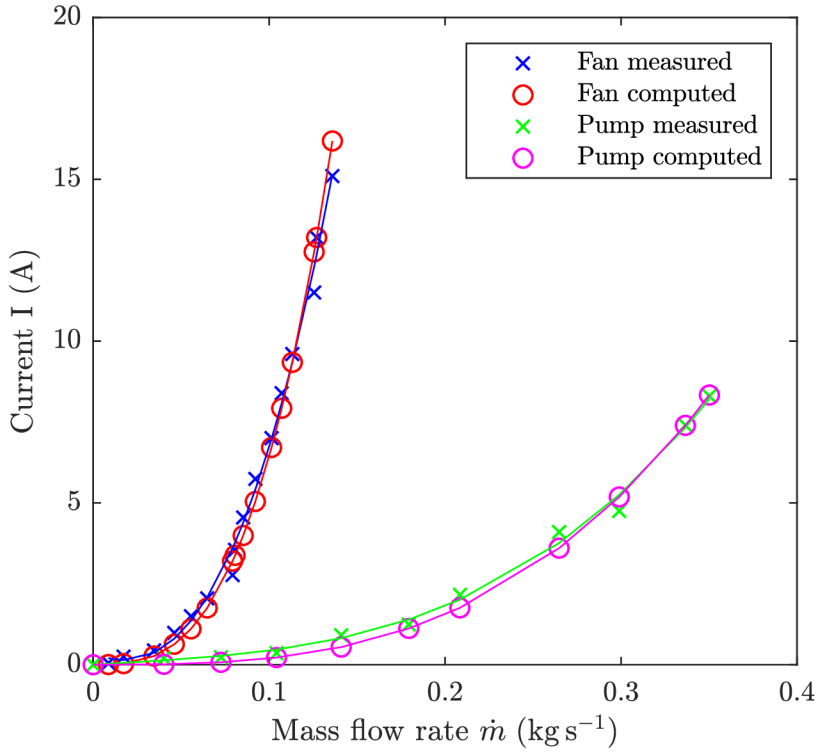

Fig. 4.12: HVAC fan and coolant pump current measurements and approximations

focus on power consumption). The resulting data are shown in Fig. 4.12 (labeled as "measured").

Then a formula describing the dependency of electric current on mass flow rate was found for each of these actuators, to allow their comparison (under a constant input voltage $U = 12\,\mathrm{V}$). Both the fan and pump employ a fan load characteristic, which means that motor torque is dependent on the squared angular speed, and the input power (and thus current) depends on the third power of angular speed. The volumetric flow rate and mass flow rate are approximately linearly dependent on the fan/pump motor angular speed. The HVAC fan electric current can be written as

$$I_{\mathrm{fan}} = a_{\mathrm{fan}}(\dot{m}_{\mathrm{fan}})^3, \tag{4.24}$$

where I_{fan} is the electric current of the HVAC fan, a_{fan} is a constant characterizing the fan and HVAC air distribution box (in our case, $a_{\mathrm{fan}} = 6443$). Then $\dot{m}_{\mathrm{fan}}$ is the air mass flow rate through the fan.

The coolant pump electric current can be described by

$$I_{\mathrm{pump}} = a_{\mathrm{pump}}(\dot{m}_{\mathrm{pump}})^3, \tag{4.25}$$

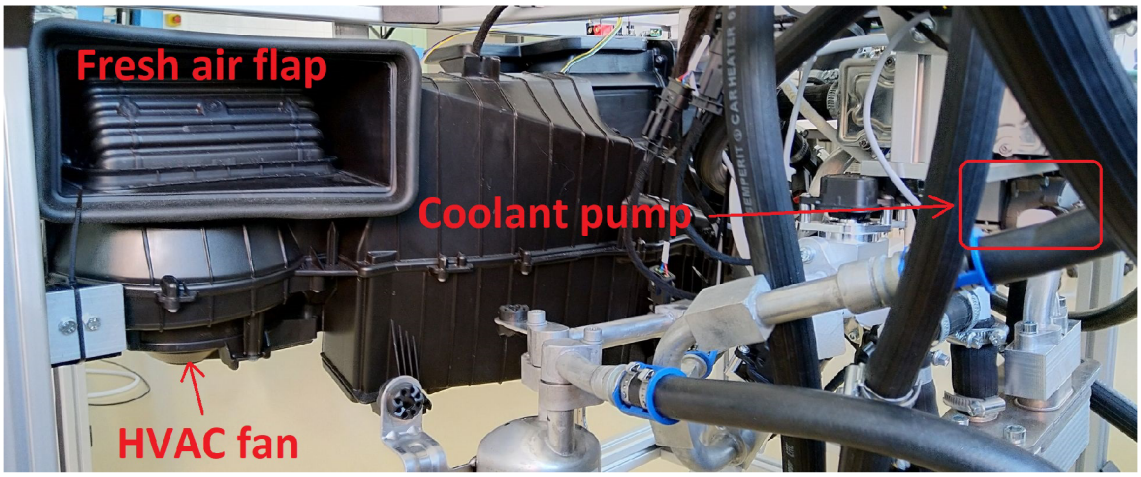

Fig. 4.13: FEV HVAC test bench

where I_{pump} is the electric current of the coolant pump, a_{pump} is a pump and pipes constant (in our case, $a_{\text{pump}} = 194$), and $\dot{m}_{\text{pump}}$ is the coolant mass flow rate caused by the pump.

The specific values of the fan and pump constants (a_{fan} and a_{pump}) were acquired by fitting the general formulae with a measured electric current. The comparison of measured values and results from (4.24) and (4.25) are in Fig. 4.12, and the correspondence is satisfactory.

From (4.24) and (4.25) it is evident that the penalization of the HVAC fan should be approximately thirty times higher compared to the coolant pump to ensure comparability of power consumption.

To accomplish the basic goal of energy-efficient control, the overall power consumption needs to be minimized. This can be computed as

$$P_{\text{el}} = P_{\text{fan}} + P_{\text{pump}} + P_{\text{heat}}, \tag{4.26}$$

where P_{el} is overall electric power consumption, P_{fan} and P_{pump} are electric power consumptions of HVAC the fan and pump respectively, and P_{heat} stands for electric power consumption of the heat source utilized to provide heat flow $\dot{Q}_{\text{h10}}$. After minor modifications and substitutions, we can write

$$P_{\text{el}} = U[a_{\text{fan}}(\dot{m}_{\text{c}})^3 + a_{\text{pump}}(\dot{m}_{\text{h5}})^3] + \frac{\dot{Q}_{\text{h10}}}{COP}, \tag{4.27}$$

where $U = 12\,\text{V}$ is battery voltage and COP stands for coefficient of performance

$$COP = \frac{|Q|}{W}, \tag{4.28}$$

where Q is the heat supplied to the coolant and W is the work required for that. If we consider purely electric heating, $COP = 1$, for heat pump systems, we expect $COP \in (1.5, 3)$.

The contribution of actuators to overall electric power consumption is illustrated in Fig. 4.14 for maximal values of actuators speed (causing maximal power consumption). In this example, a heat pump system is considered, if the PTC heater was a heat source, its percentage would be much higher.

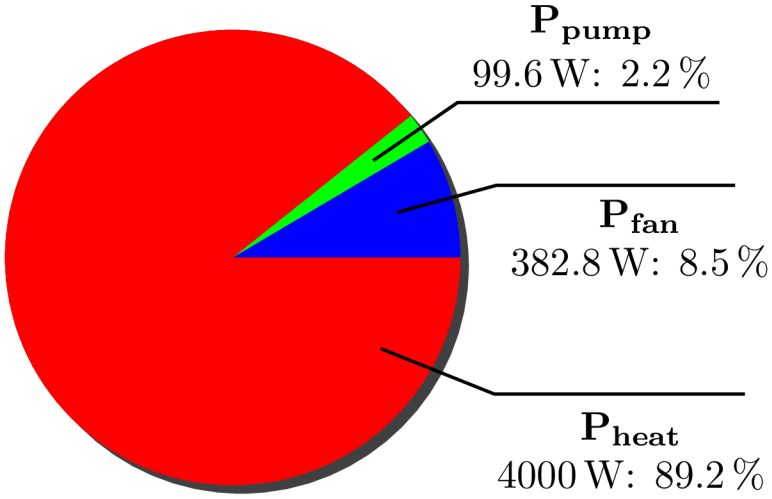

Fig. 4.14: Maximal power consumption of heating actuators, for a heat pump with $COP = 2$ and maximal thermal power $\dot{Q}_{\mathrm{h10}} = 8000\,\mathrm{W}$

The resulting vectors of penalized variables are

$$\mathbf{l}(\mathbf{x}_k, \mathbf{u}_k) = \begin{bmatrix} \mathbf{x}_\mathrm{l} \\ \mathbf{u}_\mathrm{l} \\ \Delta\mathbf{u}_\mathrm{l} \end{bmatrix}, \tag{4.29}$$

$$\mathbf{l}_N(\mathbf{x}_k) = \begin{bmatrix} \mathbf{x}_\mathrm{l} \\ \mathbf{u}_\mathrm{l} \end{bmatrix}, \tag{4.30}$$

where penalized state vector is

$$\mathbf{x}_\mathrm{l} = \mathbf{R}_x \mathbf{x}_k, \tag{4.31}$$

penalized controls vector

$$\mathbf{u}_\mathrm{l} = \mathbf{R}_u \mathbf{u}_k, \tag{4.32}$$

and penalized controls change vector

$$\Delta\mathbf{u}_\mathrm{l} = \mathbf{R}_{\Delta u} \Delta\mathbf{u}_k, \tag{4.33}$$

with $\mathbf{R}$ being the helper scaling matrices.

The weighting matrices $\mathbf{Q}$ and $\mathbf{Q}_N$ were initially set up with respect to (4.27), and then fine-tuned considering the user comfort point of view - the fan speed penalization was increased. Thus, the weighting matrices were slightly changed to fulfill all the requirements defined above in this section. As a result, the power consumption would probably not be optimal, but we can reach a satisfactory suboptimal trajectory of the system with the accomplishment of the user requirements.

The following set of state constraints was introduced

$$0 \leq T_{\mathrm{h4}} \leq 273.15 + 90 \qquad (\mathrm{K}), \tag{4.34}$$

$$0 \leq T_{\mathrm{h1}} \leq 273.15 + 60 \qquad (\mathrm{K}), \tag{4.35}$$

which represents the maximum allowed temperatures of coolant and supplied air respectively. The control constraints

$$0.04 \leq \dot{m}_{\mathrm{h5}} \leq 0.42 \qquad (\mathrm{kg\,s^{-1}}), \tag{4.36}$$

$$0.03 \leq \dot{m}_{\mathrm{c}} \leq 0.17 \qquad (\mathrm{kg\,s^{-1}}), \tag{4.37}$$

$$0 \leq \dot{Q}_{\mathrm{h10}} \leq 8000 \qquad (\mathrm{J\,s^{-1}}), \tag{4.38}$$

$$0 \leq \varphi \leq 1 \qquad (-), \tag{4.39}$$

respect the real possibilities of the considered system. The coolant and air mass flow rates were measured on our test bench (Fig. 4.13), the heat flow rate is a guessed value for a heat pump system and can be adjusted based on the heating device (heat pump, PTC, etc.). The fresh air ratio range is derived from its definition.

Then we also introduce constraints on the control changes

$$-0.05 \leq \Delta\dot{m}_{\mathrm{c}} \leq 0.05 \qquad (\mathrm{kg\,s^{-2}}), \tag{4.40}$$

$$-0.05 \leq \Delta\dot{m}_{\mathrm{h5}} \leq 0.05, \qquad (\mathrm{kg\,s^{-2}}) \tag{4.41}$$

$$-400 \leq \Delta\dot{Q}_{\mathrm{h10}} \leq 400 \qquad (\mathrm{J\,s^{-2}}), \tag{4.42}$$

$$-0.1 \leq \Delta\varphi \leq 0.1 \qquad (\mathrm{s^{-1}}), \tag{4.43}$$

which also respect the real system capabilities, such as maximum possible fan and pump acceleration, fresh flap speed, etc.

We introduce the reference vector

$$\mathbf{r} = \begin{bmatrix} \mathbf{r}_{\mathbf{x}}^{\intercal} & \mathbf{r}_{\mathbf{u}}^{\intercal} & \mathbf{r}_{\mathbf{\Delta u}}^{\intercal} \end{bmatrix}^{\intercal} \tag{4.44}$$

with state references $\mathbf{r}_{\mathbf{x}}$, controls references $\mathbf{r}_{\mathbf{u}}$ and controls change references $\mathbf{r}_{\mathbf{\Delta u}}$

$$\mathbf{r}_{\mathbf{x}} = \begin{bmatrix} r_{T_{\mathrm{c1}}} & 0 & 0 & 0 & 0 & 0 & r_{T_{\mathrm{h4}}} & 0 & r_{\kappa} \end{bmatrix}^{\intercal}, \tag{4.45}$$

$$\mathbf{r}_{\mathbf{u}} = \begin{bmatrix} 0 & 0 & 0 & 0 \end{bmatrix}^{\intercal}, \tag{4.46}$$

$$\mathbf{r}_{\mathbf{\Delta u}} = \begin{bmatrix} 0 & 0 & 0 & 0 \end{bmatrix}^{\intercal}, \tag{4.47}$$

where $r_{T_{c1}}$ is the cabin temperature reference, r_κ is the cabin air quality reference and, $r_{T_{h4}}$ is the coolant temperature reference.

The sampling rate was chosen as $T_s = 0.5\,s$ to cover the fastest dynamics in the controlled system. In combination with a prediction horizon $N = 20$, we get a prediction time of 10 s. The `ACADO toolkit` [44] (including MATLAB interface) was used for implementation in MATLAB/Simulink, and also for C/C++ code generation. A multiple shooting technique [45] was used for the discretization of the continuous-time model. A quadratic programming solver, `qpOASES` [46], employing an active-set method [47], was used to solve the optimization problem.

4.2.3 Extended Kalman Filter

The Extended Kalman Filter (EKF) from [48] was used to allow current system states estimation, as they are needed for NMPC computations.

A discrete-time system model

$$\mathbf{x}_k = \mathbf{f}(\mathbf{x}_{k-1}, \mathbf{u}_{k-1}) + \mathbf{w}_k, \tag{4.48}$$

$$\mathbf{z}_k = \mathbf{h}(\mathbf{x}_k) + \mathbf{v}_k, \tag{4.49}$$

is needed for both the phases (prediction and update) of the EKF. The model described above was discretized using the Euler method to get a discrete-time model of the vehicle cabin and HVAC system.

Then we use the following equations for the prediction phase of the EKF

$$\hat{\mathbf{x}}_k^- = \mathbf{f}(\mathbf{x}_{k-1}, \mathbf{u}_k, 0), \tag{4.50}$$

$$\mathbf{P}_k^- = \mathbf{F}_{k-1}\mathbf{P}_{k-1}\mathbf{F}_{k-1}^\intercal + \mathbf{Q}_{k-1}, \tag{4.51}$$

and the second set of equations for the update phase

$$\mathbf{K}_k = \mathbf{P}_k^-\mathbf{H}^\intercal(\mathbf{H}\mathbf{P}_k^-\mathbf{H}^\intercal + \mathbf{R})^{-1}, \tag{4.52}$$

$$\hat{\mathbf{x}}_k = \hat{\mathbf{x}}_k^- + \mathbf{K}_k(\mathbf{z}_k - \mathbf{H}\hat{\mathbf{x}}_k^-), \tag{4.53}$$

$$\mathbf{P}_k = (\mathbf{I} - \mathbf{K}_k\mathbf{H})\mathbf{P}_k^-, \tag{4.54}$$

where $\hat{\mathbf{x}}_k^-$ and $\hat{\mathbf{x}}_k$ are the a priori and a posteriori state estimates respectively, $\mathbf{P}_k^-$ and $\mathbf{P}_k$ are the a priori and a posteriori estimate error covariance matrices, $\mathbf{F}_{k-1}$ is the Jacobian of function $\mathbf{f}(\cdot)$, $\mathbf{Q}_{k-1}$ stands for the process noise covariance matrix, $\mathbf{K}_k$ is the Kalman gain, $\mathbf{R}$ is the measurement error covariance matrix. As the function $\mathbf{h}(\cdot)$ is linear, the last term in (4.53) was reduced to the product of matrix $\mathbf{H}$ and the a priori state estimate $\hat{\mathbf{x}}_k^-$ (compared with the standard $\mathbf{h}(\hat{\mathbf{x}}_k^-, 0)$ term).

The ambient temperature ($T_{h5} = T_{c5}$) can be considered as a measured disturbance since this variable behaves as an input to our models (can change in time, it

is not a constant, but we can not influence its value). Thus, we incorporate it as a measured state with a zero time derivative and its value is obtained by the EKF. The following equation was added to the set of the differential equations

$$\frac{\mathrm{d}T_{\mathrm{c5}}}{\mathrm{d}t} = 0, \tag{4.55}$$

where T_{c5} is the ambient temperature.

4.2.4 Simulations

The simulations described in this section were realized in the MATLAB/Simulink environment.

The cabin and HVAC model (described in section 4.2.1) was exported from Dymola into the Functional Mockup Unit (FMU) exchange format and then imported into Simulink using the `FMUtoolbox` [88], a self-developed FMU importing tool for MATLAB/Simulink.

Model in the loop

A Model in the Loop (MIL) simulation was the starting point during the NMPC algorithms tuning. As a first step, the NMPC algorithms were tested in a pure MATLAB environment (m-file script). This step was important for tuning the very base functionality - constraints, first guess of penalization matrices, etc.

The NMPC controller was connected to the same plant (cabin and HVAC) model that was used for the controller assembly. Thus the state observer was not necessary and the changes in the model and other settings are quite simple.

The main advantage of the MIL simulation is the speed of deployment, as C++ code generated based on an m-file script is automatically built into the mex-file and then simulated under the MATLAB environment with the possibility to easily plot the simulation results.

Software in the loop

Software in the Loop (SIL) simulation was performed in the MATLAB Simulink environment with usage of the C S-function. The `ACADO Code Generation tool` was used to export the highly efficient C-code for NMPC implementation.

As a plant model, the Dymola model of the cabin and HVAC was used. The model needs actuator values as inputs, but the controller provides only the changes in actuator values. The discrete integration of actuator values was added to the EKF algorithms.

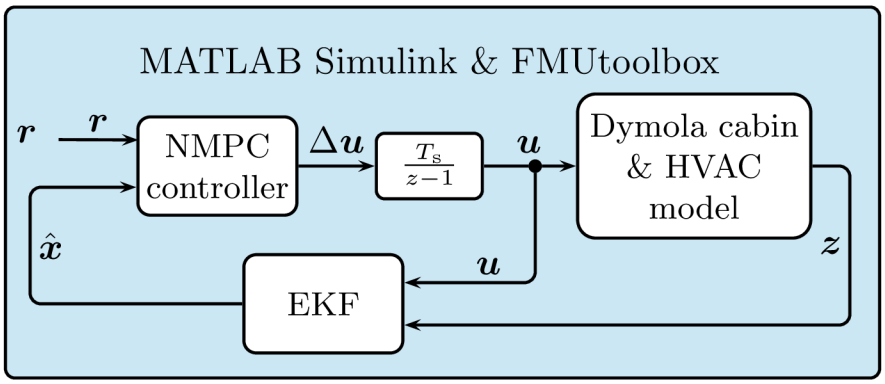

Fig. 4.15: NMPC SIL simulation diagram

Processor in the loop

The NMPC algorithms were successfully implemented on an Infineon AURIX Tricore TC299TF microcontroller unit (MCU), placed on the AURIX Starter Kit TC299. The MCU contains three cores running at 300 MHz, 8 MB FLASH (4x2 MB) and 728 kB RAM.

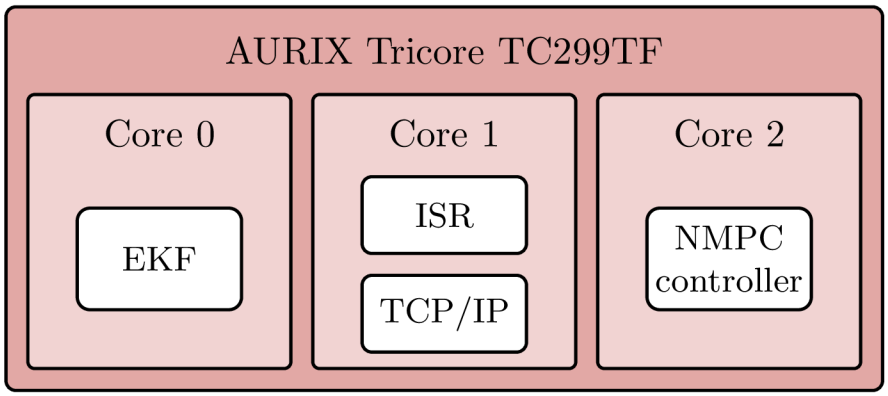

Fig. 4.16: NMPC AURIX Tricore tasks overview

The software tasks were divided between the MCU cores as shown in Fig. 4.16. Core 1 provides timing based on interrupts for the other cores (shown as an interrupt service routine (ISR) task), by setting the execution flags at a defined frequency. This core also ensures the TCP/IP communication with the MATLAB Simulink (illustrated in Fig. 4.17). Core 0 is responsible for EKF execution and the NMPC algorithms are running within Core 2.

In Fig. 4.17, there is a diagram of the Processor in the Loop (PIL) simulation. The references ($\mathbf{r}$) and measured outputs ($\mathbf{z}$) from the Dymola model (running under MATLAB/Simulink) are sent to the MCU via TCP/IP communication, and the

controls ($\mathbf{u}$) are sent from the MCU to the MATLAB Simulink and applied to the Dymola model. As mentioned before (SIL simulation), the controls from the NMPC controller have to be discretely integrated before applying them to the Dymola model.

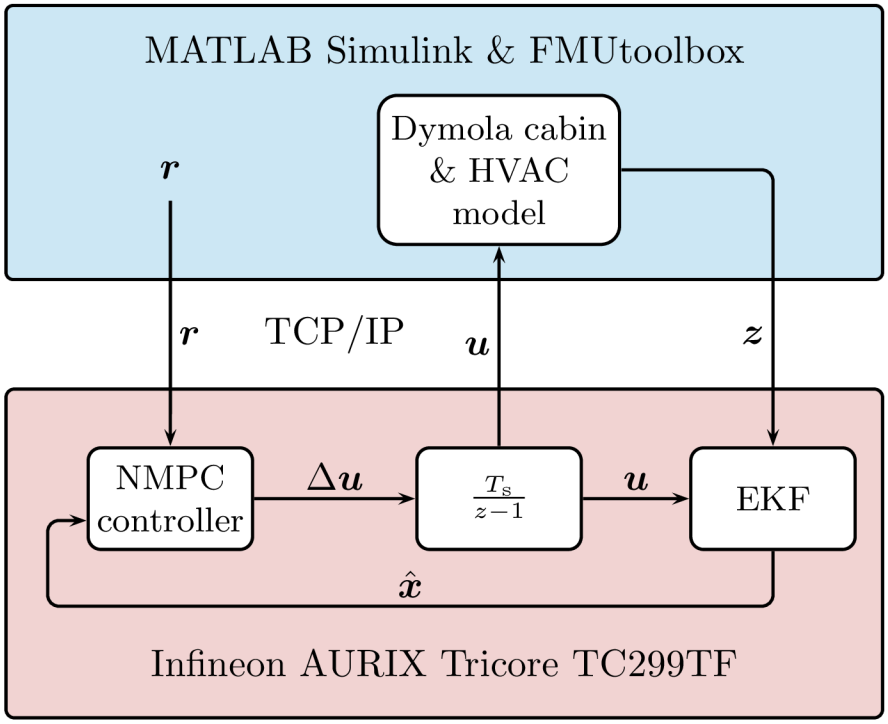

Fig. 4.17: NMPC PIL simulation diagram

In Fig. 4.18, there is a photo of the AURIX Starter Kit TC299 that was used as the target of the control algorithms described within this section. The board is connected via TCP/IP (see Fig. 4.17) with a PC, on which the MATLAB/Simulink environment and Dymola model are running. Moreover, there are debug and power lines.

FEV cabin heat build-up

In Fig. 4.19 there are results of a simulation of FEV cabin heat build-up. The simulation conditions were defined as an average winter day with an ambient temperature of $-10\,°\mathrm{C}$, and this temperature was also used as the initial temperature of the whole vehicle cabin and other equipment. Two passengers are considered, and no solar flow is present during the simulation.

The cabin temperature reference ($r_{T_{c1}} = 20\,°\mathrm{C}$) was achieved after approx. 200 s, which is quite an impressive value. This fast heat build-up is possible thanks to the fully closed fresh air flap, which has the drawback of slightly degraded air quality

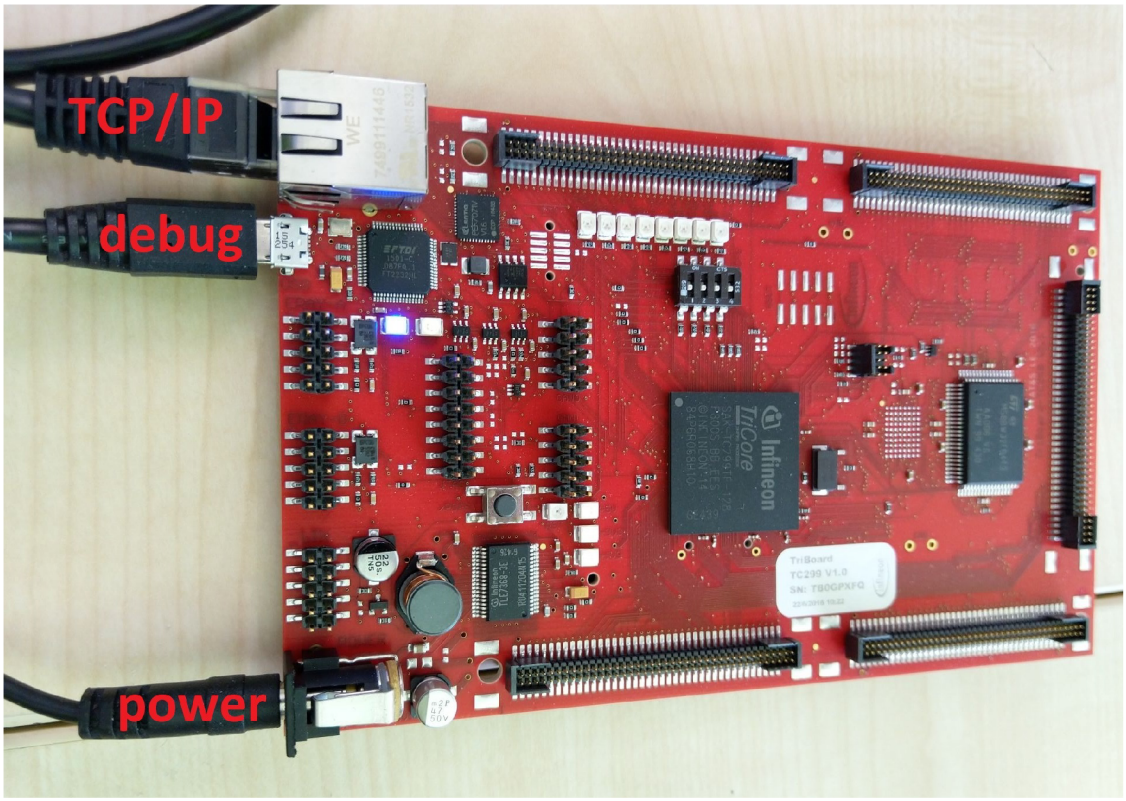

Fig. 4.18: NMPC PIL simulation target - Infineon AURIX TC299TF on the AURIX Starter Kit TC299

(above 1000 ppm; limited for a short time). The air quality is improved immediately after the cabin temperature settles and then it is kept approximately at the reference value of 900 ppm.

Temperature reference change

Fig. 4.20 presents the temperature reference change of 2 °C and the reaction of the NMPC algorithms to this change. The reference change occurred at the time of 600 s, and the new reference value of the cabin air temperature was reached after a very short time, which is possible by the coordination of all the actuators. Both the coolant pump and HVAC fan were speeded up, heat flow to the coolant was increased by 1200 W for a short time, and the fresh air flap was closed during the temperature increase. The benefits of NMPC are evident from this case, as multivariable control helps to reduce the time needed for the change of the cabin air temperature. Also, there is no overshoot and all of the variables are natively kept within the defined constraints.

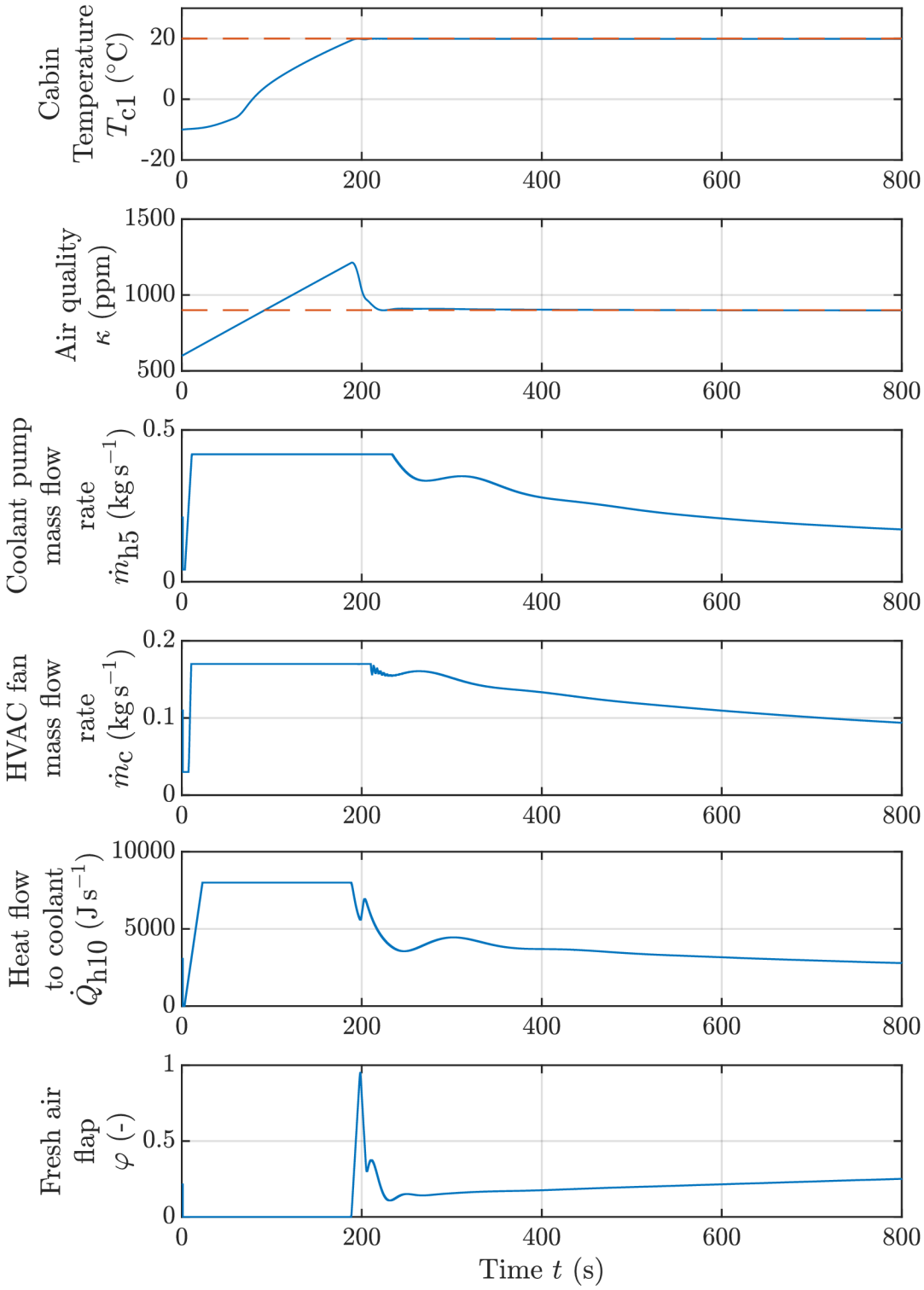

Fig. 4.19: NMPC PIL simulation of cabin heat build-up with ambient temperature $T_{c5} = -10\,°C$, two passengers inside the cabin and no solar heat flow

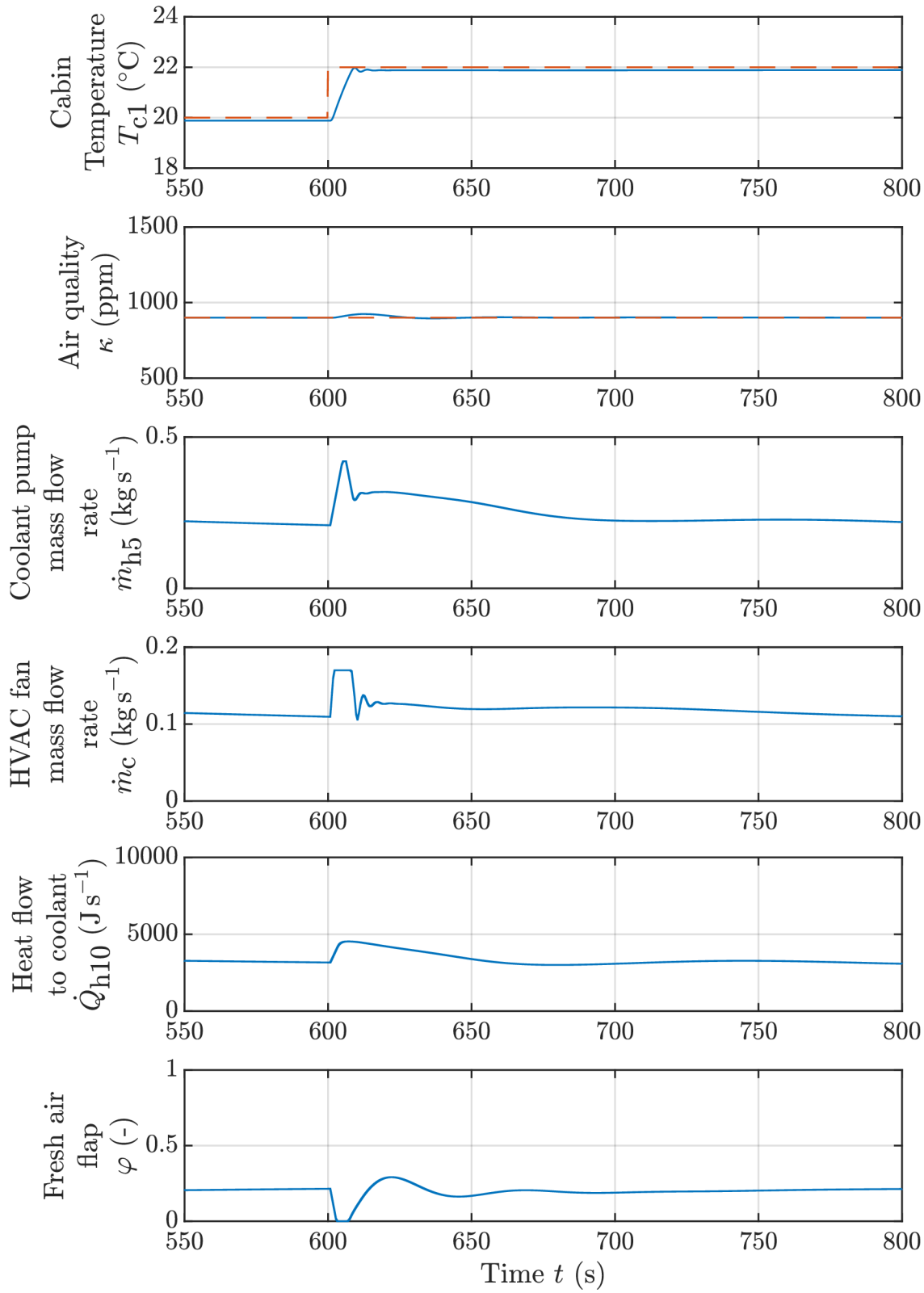

Fig. 4.20: NMPC PIL simulation of cabin temperature reference step response

Disturbance rejection

Two most common disturbances were selected for presentation. The first one is shown in Fig. 4.21, and was caused by increasing the number of passengers in the vehicle. Both the cabin air temperature and quality are affected by this change, and it can be seen that the temperature is kept approx. at the defined reference, the air quality got slightly worse, and there remains some steady-state error. This is caused by a conservative penalization value of the air quality, as it doesn't have to strictly track the reference, but it needs to be kept within a reasonable range (e.g. 800..1200 ppm). Thus, the steady-state error is the trade-off between the air quality and the power consumption needed for cabin heating. The fresh air flap position was moved from approx. 20 % to 50 % as an appropriate response to this disturbance.

The second disturbance is represented by ambient temperature change, which affects both the thermal losses through the cabin walls and the inlet fresh air temperature. In Fig. 4.22, there are results of the simulation with a step change of ambient temperature at the time of 600 s from −10 °C to 0 °C. Both the cabin temperature and air quality track the references, and only the decrease of the heat flow $\dot{Q}_{\mathrm{h10}}$ is perceptible.

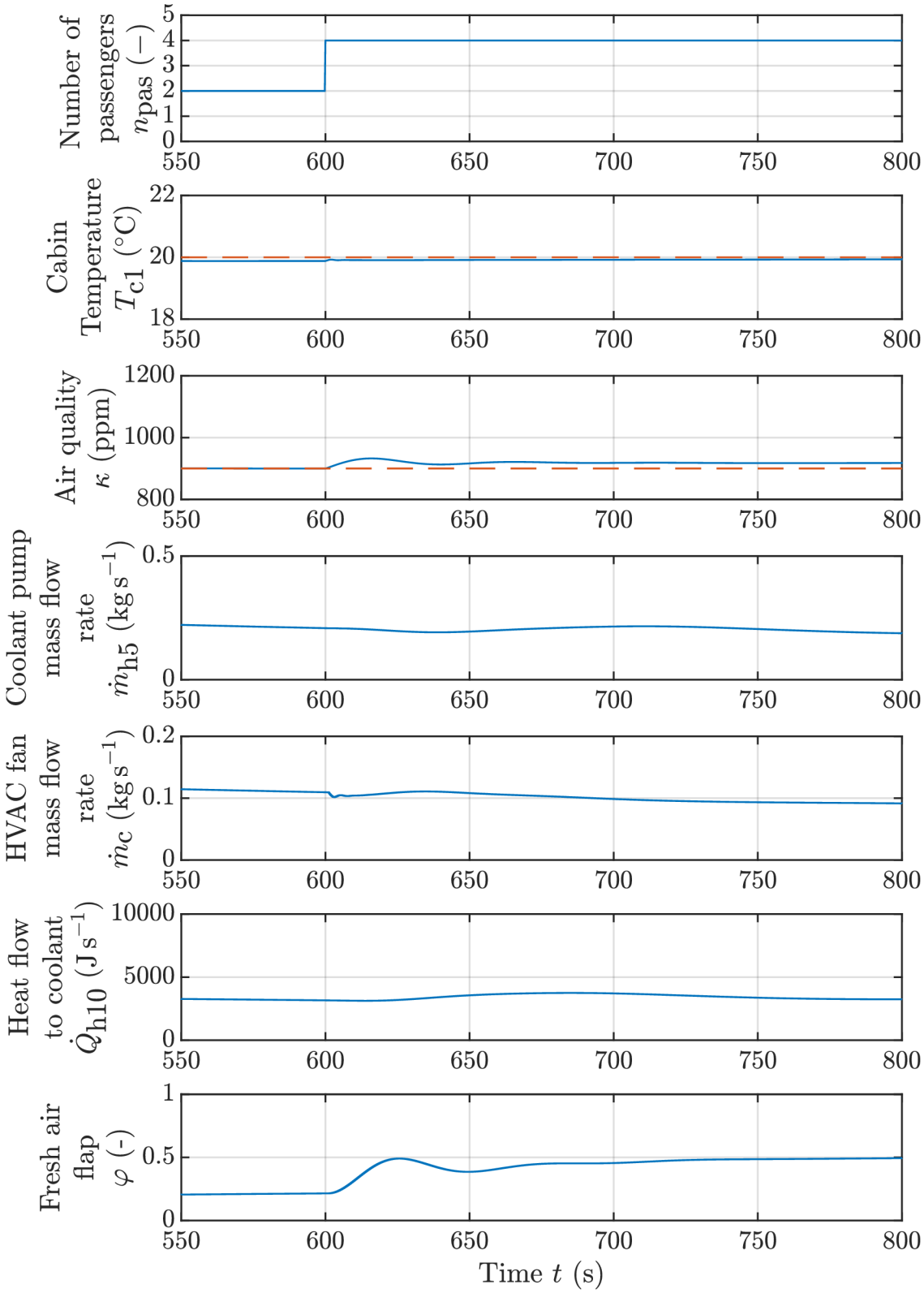

Fig. 4.21: NMPC PIL simulation of disturbance rejection - increase in the number of cabin passengers

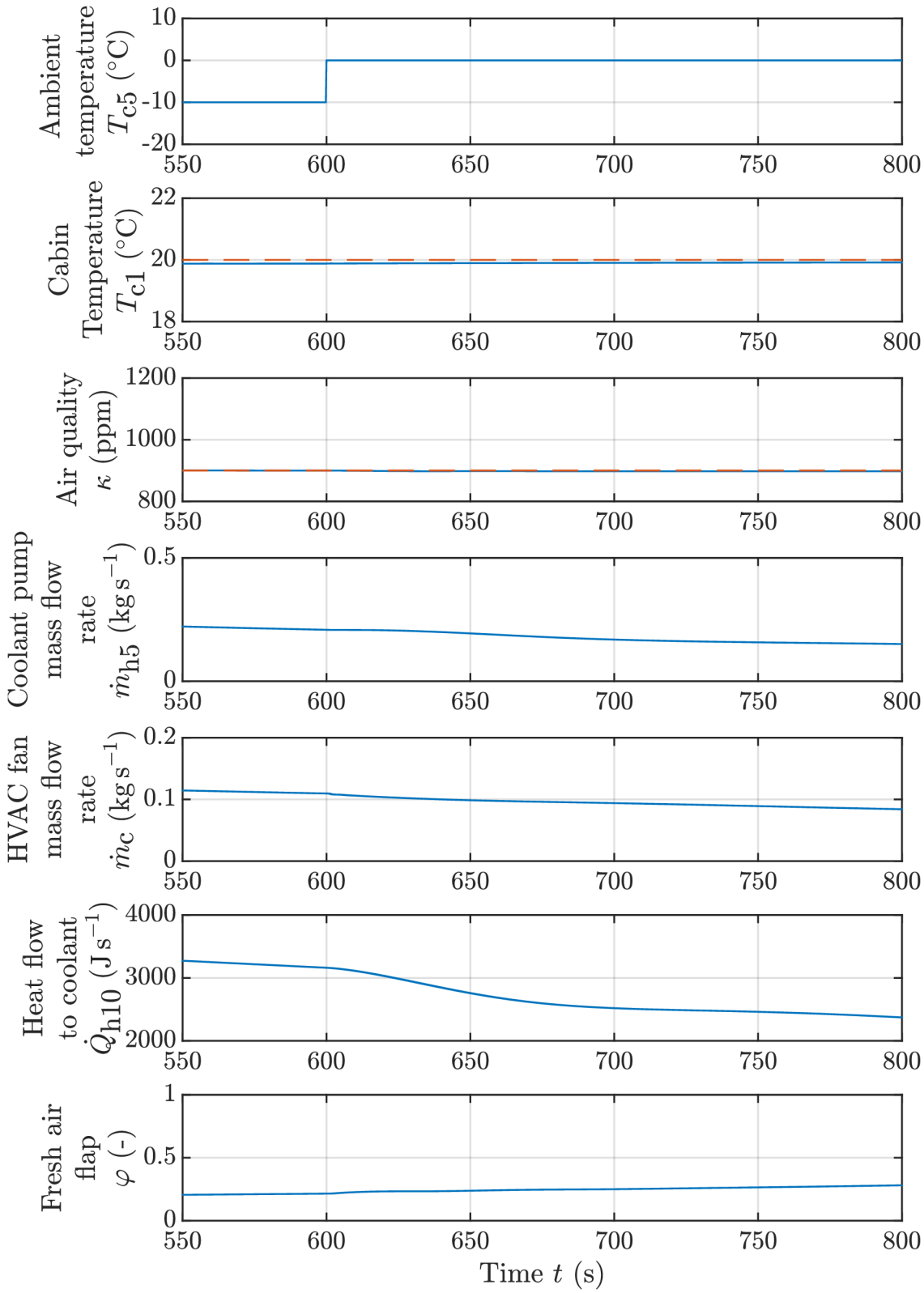

Fig. 4.22: NMPC PIL simulation of disturbance rejection - ambient temperature change

5 Electro-thermal flows optimization

The overall vehicle thermal system (Fig. 2.1) was divided into three subsystems: Heating, Ventilation and Air Conditioning (HVAC) (also includes Refrigeration (HVAC&R)), High-Voltage Battery (HvBat) and E-Drive (ED).

These subsystems are functionally interconnected together and changes of one subsystem (or its part – actuator) can influence the others. That is why all the actuators were assigned exclusively to one of these subsystems to assure a unique control source of the single actuator. There are four exceptions: High-Voltage Compressor (HvAcCmpr), MainFan, Air Grille Shutter (AGS) and Positive Temperature Coefficient Heater (PTC). These actuators are operated by multiple subsystems utilizing the maximum function.

5.1 Thermal Functions

Thermal Function (TF) is a term used for a set of actuators' values and control rules. Each TF is intended for different situations defined by ambient conditions, heating/cooling request and current values of VTMS states (TES status, coolant temperature, etc.).

Thermal Functions firstly define the values of two-state actuators, namely coolant shut-off valves and three-way valves and air grill shutter. Then also some values of continuously controlled actuators are defined, e.g. EXV fully opened or closed and completely disabled actuators (fans, pumps, compressor, etc.). For the rest of actuators, the control rules are defined, e.g. the compressor speed is controlled to keep the VCRS low side pressure at defined low side pressure reference (during cooling) or to keep the VCRS high side pressure at defined high side pressure reference (during heating).

The Thermal Functions were initially defined by AVL in descriptive form with schematics included. The original set of TFs was complemented by additional TFs (TF0 for all subsystems, HVAC TF5, HvBat TF7 and TF8, ED TF3 and TF4). The overview of all the TFs is shown in Table 5.1. For all the TFs the exact actuators' values or control rules were then defined and then used for the analysis of TF compatibility.

Thermal Decision Controller (TDC) is a name for a set of algorithms that are responsible for the selection of appropriate Thermal Function (TF). Two versions of TDC were developed, a Basic Thermal Decision Controller (BTDC) and a Model Predictive Thermal Decision Controller (MPTDC).

Tab. 5.1: VTMS Thermal Functions

Subsystem	Thermal Function	Description
HVAC	TF0	Disabled
HVAC	TF1	Cooling with ambient air
HVAC	TF2	VCRS cooling with TES and ambient air
HVAC	TF3	VCRS heating with waste heat and TES
HVAC	TF4	VCRS heating with ambient air
HVAC	TF5	VCRS cooling with the AC system
HvBat	TF0	Disabled
HvBat	TF1	VCRS Battery cooling with Chiller
HvBat	TF2	Battery cooling with ambient air
HvBat	TF3	Cooling with TES
HvBat	TF4	Heating with TES
HvBat	TF5	Heating with PTC
HvBat	TF6	Heating with E-Drive
HvBat	TF7	Cabin heating with battery waste heat
HvBat	TF8	TES charging using E-Drive
ED	TF0	Disabled
ED	TF1	E-drive cooling with ambient air
ED	TF2	Cooling with TES
ED	TF3	Using E-Drive waste heat
ED	TF4	Battery and E-Drive cooling with ambient air

5.2 Basic Thermal Decision Controller

BTDC selects appropriate TF for each subsystem to keep it in defined constraints (temperatures etc.). Usually, it is possible to achieve it using multiple TF. For example, under some conditions, it is possible to cool the HV battery by refrigeration system (requiring compressor power to cool the coolant) or it could be cooled using free cooling (the excessive heat is rejected from coolant to the air in the front heat exchanger). The second approach will be significantly more efficient as the compressor power will be higher than Main Fan power (which would also need to be operated for refrigerant cooling during vehicle standstill operation or slow movement).

The TFs for each subsystem were divided into two groups – cooling and heating (and only one group - cooling - for E-Drive TFs). Then the TFs were classified from the perspective of anticipated power consumption and overall efficiency. The PTC heater, Compressor, and Main Fan were identified as the main power consumers in a thermal management system with powers of 0..6000 W, 200..5000 W, and 0..600 W,

respectively. Other actuators have significantly lower power consumption (HvacFan 0..200 W, coolant pumps 0..100 W, valves and flaps are negligible). The order of consumers above (PTC, Compressor and Main Fan) was assembled based on power consumption and heating/cooling effectiveness starting with the worst (PTC produces heat purely from HV Battery, Compressor/heat pump can have 2-5 times better efficiency and free cooling using Main Fan have quite small power consumption).

With this knowledge the approach of efficient TF selection is quite clear – as long as possible the system must be operated in those TFs, in which all the three main power consumers are completely not active or only part of them are active while taking their order into account. Then default subsystem's TFs were selected for both the cooling and heating TF groups. For example, HVAC TF1 was selected as default TF for HVAC in cooling mode. Only HvacFan is operated in this TF and the cabin is cooled directly by the ambient air. This TF can be used only under certain ambient conditions, so if the ambient air temperature is too high or the cabin cooling demand is too high, another TF is automatically selected to ensure sufficient cabin cooling.

An overview of BTDC is presented in Appendix D and it is evident that the TF selection process is highly complicated and requires a lot of thresholds, additional conditions and emergency functions. In the end, the calibration is complicated and the developed instance of BTDC is hardly applicable to an even slightly different system. Therefore a more general and widely applicable approach of Thermal Function selection was requested and the proposed solution is described in the next section.

5.3 Model Predictive Thermal Decision Controller

This section describes an advanced algorithm for Thermal Function selection. The algorithm uses a Model Predictive Control (MPC) approach applied to the hybrid system - a dynamic system combined with discrete-valued variables or a state machine.

The theory of hybrid MPC is quite well established and in this thesis, it was used for the development of the decision-making algorithm. The system (or its simplified representation) and its modes are described by the PWA model and MPC is then used for the selection of optimal mode during system operation.

First of all, the MPC for Linear Time-Invariant (LTI) system is briefly described and the analogous approach is applied to the hybrid system. Then the concept of Decision Model Predictive Control (DMPC) is derived and followed by two examples. At the end of this section, an application of DMPC on the selection of operating mode (Thermal Function) of FEV VTMS is presented.

5.3.1 MPC for LTI systems

For Linear Time-Invariant (LTI) system described by a commonly used discrete-time state-space model [49]

$$\mathbf{x}_{k+1} = \mathbf{A}\mathbf{x}_k + \mathbf{B}\mathbf{u}_k, \tag{5.1}$$

$$\mathbf{y}_k = \mathbf{C}\mathbf{x}_k + \mathbf{D}\mathbf{u}_k, \tag{5.2}$$

$$\mathbf{x}_0 \quad \text{given} \tag{5.3}$$

we search the future control sequence

$$\hat{\mathbf{u}} = \begin{bmatrix} \mathbf{u}_k^\intercal & \mathbf{u}_{k+1}^\intercal & \dots & \mathbf{u}_{k+N-1}^\intercal \end{bmatrix}^\intercal \tag{5.4}$$

on prediction horizon N, which will minimize the objective function (in the simple form for clarity)

$$J_N(\mathbf{x}_0, \hat{\mathbf{u}}) = \frac{1}{2} \sum_{k=0}^{N-1} \left(\mathbf{x}_k^\intercal \mathbf{Q} \mathbf{x}_k + \mathbf{u}_k^\intercal \mathbf{R} \mathbf{u}_k \right), \tag{5.5}$$

$$\text{subject to} \tag{5.6}$$

$$\mathbf{x}_{k+1} = \mathbf{A}\mathbf{x}_k + \mathbf{B}\mathbf{u}_k. \tag{5.7}$$

The prediction equations can be written [50] as

$$\underbrace{\begin{bmatrix} \mathbf{x}_{k+1} \\ \mathbf{x}_{k+2} \\ \mathbf{x}_{k+3} \\ \vdots \\ \mathbf{x}_{k+N} \end{bmatrix}}_{\hat{\mathbf{x}}} = \underbrace{\begin{bmatrix} \mathbf{A} \\ \mathbf{A}^2 \\ \mathbf{A}^3 \\ \vdots \\ \mathbf{A}^N \end{bmatrix}}_{\mathbf{P}_x} \mathbf{x}_0 + \underbrace{\begin{bmatrix} \mathbf{B} & \mathbf{0} & \mathbf{0} & \dots \\ \mathbf{AB} & \mathbf{B} & \mathbf{0} & \dots \\ \mathbf{A}^2\mathbf{B} & \mathbf{AB} & \mathbf{B} & \dots \\ \vdots & \vdots & \vdots & \ddots \\ \mathbf{A}^{N-1}\mathbf{B} & \mathbf{A}^{N-2}\mathbf{B} & \mathbf{A}^{N-3}\mathbf{B} & \dots \end{bmatrix}}_{\mathbf{H}_x} \hat{\mathbf{u}}, \tag{5.8}$$

$$\underbrace{\begin{bmatrix} \mathbf{y}_k \\ \mathbf{y}_{k+1} \\ \mathbf{y}_{k+2} \\ \vdots \\ \mathbf{y}_{k+N-1} \end{bmatrix}}_{\hat{\mathbf{y}}} = \underbrace{\begin{bmatrix} \mathbf{C} \\ \mathbf{CA} \\ \mathbf{CA}^2 \\ \vdots \\ \mathbf{CA}^{N-1} \end{bmatrix}}_{\mathbf{P}} \mathbf{x}_0 + \underbrace{\begin{bmatrix} \mathbf{D} & \mathbf{0} & \mathbf{0} & \dots \\ \mathbf{CB} & \mathbf{D} & \mathbf{0} & \dots \\ \mathbf{CAB} & \mathbf{CB} & \mathbf{D} & \dots \\ \vdots & \vdots & \vdots & \ddots \\ \mathbf{CA}^{N-2}\mathbf{B} & \mathbf{CA}^{N-3}\mathbf{B} & \mathbf{CA}^{N-4}\mathbf{B} & \dots \end{bmatrix}}_{\mathbf{H}} \hat{\mathbf{u}}, \tag{5.9}$$

then rewritten to

$$\hat{\mathbf{x}} = \mathbf{P}_x \mathbf{x}_0 + \mathbf{H}_x \hat{\mathbf{u}}, \tag{5.10}$$

$$\hat{\mathbf{y}} = \mathbf{P}\mathbf{x}_0 + \mathbf{H}\hat{\mathbf{u}} \tag{5.11}$$

and beneficially used in transforming objective function to a quadratic programming problem

$$J_N(\mathbf{x}_0, \hat{\mathbf{u}}) = \frac{1}{2}\left[(\mathbf{P}_x\mathbf{x}_0 + \mathbf{H}_x\hat{\mathbf{u}})^\intercal\tilde{\mathbf{Q}}(\mathbf{P}_x\mathbf{x}_0 + \mathbf{H}_x\hat{\mathbf{u}}) + \hat{\mathbf{u}}^\intercal\mathbf{R}'\hat{\mathbf{u}}\right], \tag{5.12}$$

$$J_N(\mathbf{x}_0, \hat{\mathbf{u}}) = \frac{1}{2}\hat{\mathbf{u}}^\intercal\underbrace{\left(\mathbf{R}' + \mathbf{H}_x^\intercal\tilde{\mathbf{Q}}\mathbf{H}_x\right)}_{\mathbf{G}}\hat{\mathbf{u}} + \mathbf{x}_0^\intercal\underbrace{\left(\mathbf{P}_x^\intercal\tilde{\mathbf{Q}}\mathbf{H}_x\right)}_{\mathbf{F}^\intercal}\hat{\mathbf{u}}, \tag{5.13}$$

$$J_N(\mathbf{x}_0, \hat{\mathbf{u}}) = \frac{1}{2}\hat{\mathbf{u}}^\intercal\mathbf{G}\hat{\mathbf{u}} + \mathbf{x}_0^\intercal\mathbf{F}^\intercal\hat{\mathbf{u}}, \tag{5.14}$$

what conforms the common form of quadratic programming

$$\min f(\mathbf{x}) = \frac{1}{2}\mathbf{x}^\intercal\mathbf{Q}\mathbf{x} + \mathbf{q}^\intercal\mathbf{x}, \tag{5.15}$$

subject to

$$\mathbf{A}\mathbf{x} = \mathbf{a}, \tag{5.16}$$

$$\mathbf{B}\mathbf{x} \leq \mathbf{b}, \tag{5.17}$$

$$\mathbf{x} \geq 0, \tag{5.18}$$

which can be solved by numerous algorithms, e.g.

- active set methods [47]
- interior-point methods [51]
- sequential quadratic programming methods [52]

and others.

5.3.2 MLD, PWA, and other hybrid systems

In [53] it was shown that five classes of hybrid systems: mixed logical dynamical (MLD) systems, linear complementarity (LC) systems, extended linear complementarity (ELC) systems, piecewise affine (PWA) systems and max-min-plus-scaling (MMPS) systems are equivalent and the conversion between them is possible. Then it was shown in [54] that MLD systems can be successfully controlled by MPC and thus also PWA and other hybrid systems can be controlled using this technique.

We will focus only on MLD and PWA systems, as the others are not interesting for this work. MLD system [55] is usually written as

$$\mathbf{x}_{k+1} = \mathbf{A}\mathbf{x}_k + \mathbf{B}_1\mathbf{u}_k + \mathbf{B}_2\boldsymbol{\delta}_k + \mathbf{B}_3\mathbf{z}_k, \tag{5.19}$$

$$\mathbf{y}_k = \mathbf{C}\mathbf{x}_k + \mathbf{D}_1\mathbf{u}_k + \mathbf{D}_2\boldsymbol{\delta}_k + \mathbf{D}_3\mathbf{z}_k, \tag{5.20}$$

$$\mathbf{E}_1\mathbf{x}_k + \mathbf{E}_2\mathbf{u}_k + \mathbf{E}_3\boldsymbol{\delta}_k + \mathbf{E}_4\mathbf{z}_k \leq \mathbf{g}, \tag{5.21}$$

where $\mathbf{x}_k = \begin{bmatrix}\mathbf{x}_k^\mathrm{r} & \mathbf{x}_k^\mathrm{b}\end{bmatrix}^\intercal$ is state vector consisting of real $\mathbf{x}_k^\mathrm{r} \in \mathbb{R}^{n_\mathrm{r}}$ and binary $\mathbf{x}_k^\mathrm{b} \in \{0,1\}^{n_\mathrm{b}}$ states. Input $\mathbf{u}_k$ and output $\mathbf{y}_k$ vectors have a structure similar to the state vector and $\mathbf{z}_k \in \mathbb{R}^{r_\mathrm{r}}$ and $\boldsymbol{\delta}_k \in \{0,1\}^{r_\mathrm{b}}$ are auxiliary variables.

PWA system can be described [56] by

$$\mathbf{x}_{k+1} = \mathbf{A}_i \mathbf{x}_k + \mathbf{B}_i \mathbf{u}_k + \mathbf{f}_i^{\mathrm{c}}, \tag{5.22}$$

$$\mathbf{y}_k = \mathbf{C}_i \mathbf{x}_k + \mathbf{D}_i \mathbf{u}_k + \mathbf{g}_i^{\mathrm{c}}, \tag{5.23}$$

$$\text{for } \begin{bmatrix} \mathbf{x}_k \\ \mathbf{u}_k \end{bmatrix} \in \mathbf{\Omega}_i, \tag{5.24}$$

where $\mathbf{x}_k \in \mathbb{R}^n$, $\mathbf{u}_k \in \mathbb{R}^m$, and $\mathbf{y}_k \in \mathbb{R}^l$ denote the states, inputs and outputs vectors respectively. $\mathbf{\Omega}_i$ denotes convex polyhedra in the combined input-state space. $\mathbf{f}_i^{\mathrm{c}}$ and $\mathbf{g}_i^{\mathrm{c}}$ are constant vectors. The subscript $i \in \{1, 2 \dots s\}$ denotes the mode of the PWA system with s modes altogether.

The conversion between MLD and PWA systems consists of the relation between δ_i binary variables and PWA system modes

$$[\delta_i = 1] \leftrightarrow \left[\begin{bmatrix} \mathbf{x} \\ \mathbf{u} \end{bmatrix} \in \mathbf{\Omega}_i \right], \tag{5.25}$$

$$\text{under condition } \oplus_{i=1}^{s} [\delta_i = 1] \tag{5.26}$$

and the conversion process is well described in [55], from where we extend the (4e) to other forms suitable for our needs

$$[f(x) \leq 0] \leftrightarrow [\delta = 1] \text{ is true } \iff \begin{cases} f(x) \leq M(1-\delta) \\ f(x) \geq \varepsilon + (m-\varepsilon)\delta \end{cases}, \tag{5.27}$$

$$[f(x) \leq c] \leftrightarrow [\delta = 1] \text{ is true } \iff \begin{cases} f(x) \leq M(1-\delta) + c\delta \\ f(x) \geq \varepsilon + (m-\varepsilon)\delta + c(1-\delta) \end{cases}, \tag{5.28}$$

$$[f(x) \geq 0] \leftrightarrow [\delta = 1] \text{ is true } \iff \begin{cases} f(x) \geq m(1-\delta) \\ f(x) \leq -\varepsilon + (M+\varepsilon)\delta \end{cases}, \tag{5.29}$$

$$[f(x) \geq c] \leftrightarrow [\delta = 1] \text{ is true } \iff \begin{cases} f(x) \geq m(1-\delta) + c\delta \\ f(x) \leq -\varepsilon + (M+\varepsilon)\delta + c(1-\delta) \end{cases}, \tag{5.30}$$

where m and M are minimal and maximal values of $f(x)$ respectively and $c \in \mathbb{R}$ is mode switching constant.

If the original PWA system is described in the format of (5.19)-(5.21), it can be easily incorporated into an objective function. We introduce prediction equation

(here shown only for states, outputs would be similar)

$$\underbrace{\begin{bmatrix}\mathbf{x}_{k+1}\\ \mathbf{x}_{k+2}\\ \mathbf{x}_{k+3}\\ \vdots\\ \mathbf{x}_{k+N}\end{bmatrix}}_{\hat{\mathbf{x}}} = \underbrace{\begin{bmatrix}\mathbf{A}\\ \mathbf{A}^2\\ \mathbf{A}^3\\ \vdots\\ \mathbf{A}^N\end{bmatrix}}_{\mathbf{P}} \mathbf{x}_0 + \underbrace{\begin{bmatrix}\mathbf{B}_1 & \mathbf{0} & \mathbf{0} & \dots\\ \mathbf{A}\mathbf{B}_1 & \mathbf{B}_1 & \mathbf{0} & \dots\\ \mathbf{A}^2\mathbf{B}_1 & \mathbf{A}\mathbf{B}_1 & \mathbf{B}_1 & \dots\\ \vdots & \vdots & \vdots & \ddots\\ \mathbf{A}^{N-1}\mathbf{B}_1 & \mathbf{A}^{N-2}\mathbf{B}_1 & \mathbf{A}^{N-3}\mathbf{B}_1 & \dots\end{bmatrix}}_{\mathbf{H}_1} \underbrace{\begin{bmatrix}\mathbf{u}_k\\ \mathbf{u}_{k+1}\\ \mathbf{u}_{k+2}\\ \vdots\\ \mathbf{u}_{k+N-1}\end{bmatrix}}_{\hat{\mathbf{u}}} +$$
$$\underbrace{\begin{bmatrix}\mathbf{B}_2 & \mathbf{0} & \mathbf{0} & \dots\\ \mathbf{A}\mathbf{B}_2 & \mathbf{B}_2 & \mathbf{0} & \dots\\ \mathbf{A}^2\mathbf{B}_2 & \mathbf{A}\mathbf{B}_2 & \mathbf{B}_2 & \dots\\ \vdots & \vdots & \vdots & \ddots\\ \mathbf{A}^{N-1}\mathbf{B}_2 & \mathbf{A}^{N-2}\mathbf{B}_2 & \mathbf{A}^{N-3}\mathbf{B}_2 & \dots\end{bmatrix}}_{\mathbf{H}_2} \underbrace{\begin{bmatrix}\boldsymbol{\delta}_k\\ \boldsymbol{\delta}_{k+1}\\ \boldsymbol{\delta}_{k+2}\\ \vdots\\ \boldsymbol{\delta}_{k+N-1}\end{bmatrix}}_{\hat{\boldsymbol{\delta}}} +$$
$$\underbrace{\begin{bmatrix}\mathbf{B}_3 & \mathbf{0} & \mathbf{0} & \dots\\ \mathbf{A}\mathbf{B}_3 & \mathbf{B}_3 & \mathbf{0} & \dots\\ \mathbf{A}^2\mathbf{B}_3 & \mathbf{A}\mathbf{B}_3 & \mathbf{B}_3 & \dots\\ \vdots & \vdots & \vdots & \ddots\\ \mathbf{A}^{N-1}\mathbf{B}_3 & \mathbf{A}^{N-2}\mathbf{B}_3 & \mathbf{A}^{N-3}\mathbf{B}_3 & \dots\end{bmatrix}}_{\mathbf{H}_3} \underbrace{\begin{bmatrix}\mathbf{z}_k\\ \mathbf{z}_{k+1}\\ \mathbf{z}_{k+2}\\ \vdots\\ \mathbf{z}_{k+N-1}\end{bmatrix}}_{\hat{\mathbf{z}}}, \tag{5.31}$$

$$\underbrace{\begin{bmatrix}\mathbf{E}_1 & \mathbf{0} & \dots & \mathbf{0}\\ \mathbf{0} & \mathbf{E}_1 & \dots & \mathbf{0}\\ \vdots & \vdots & \ddots & \mathbf{0}\\ \mathbf{0} & \mathbf{0} & \mathbf{0} & \mathbf{E}_1\end{bmatrix}}_{\tilde{\mathbf{E}}_1} \hat{\mathbf{x}} + \underbrace{\begin{bmatrix}\mathbf{E}_2 & \mathbf{0} & \dots & \mathbf{0}\\ \mathbf{0} & \mathbf{E}_2 & \dots & \mathbf{0}\\ \vdots & \vdots & \ddots & \mathbf{0}\\ \mathbf{0} & \mathbf{0} & \mathbf{0} & \mathbf{E}_2\end{bmatrix}}_{\tilde{\mathbf{E}}_2} \hat{\mathbf{u}} + \underbrace{\begin{bmatrix}\mathbf{E}_3 & \mathbf{0} & \dots & \mathbf{0}\\ \mathbf{0} & \mathbf{E}_3 & \dots & \mathbf{0}\\ \vdots & \vdots & \ddots & \mathbf{0}\\ \mathbf{0} & \mathbf{0} & \mathbf{0} & \mathbf{E}_3\end{bmatrix}}_{\tilde{\mathbf{E}}_3} \hat{\boldsymbol{\delta}}$$
$$+ \underbrace{\begin{bmatrix}\mathbf{E}_4 & \mathbf{0} & \dots & \mathbf{0}\\ \mathbf{0} & \mathbf{E}_4 & \dots & \mathbf{0}\\ \vdots & \vdots & \ddots & \mathbf{0}\\ \mathbf{0} & \mathbf{0} & \mathbf{0} & \mathbf{E}_4\end{bmatrix}}_{\tilde{\mathbf{E}}_4} \hat{\mathbf{z}} \leq \underbrace{\begin{bmatrix}\mathbf{g}\\ \mathbf{g}\\ \mathbf{g}\\ \vdots\\ \mathbf{g}\end{bmatrix}}_{\tilde{\mathbf{g}}}, \tag{5.32}$$

which can then be rewritten to

$$\hat{\mathbf{x}} = \mathbf{P}\mathbf{x}_0 + \mathbf{H}_1\hat{\mathbf{u}} + \mathbf{H}_2\hat{\boldsymbol{\delta}} + \mathbf{H}_3\hat{\mathbf{z}}, \tag{5.33}$$
$$\tilde{\mathbf{E}}_1\hat{\mathbf{x}} + \tilde{\mathbf{E}}_2\hat{\mathbf{u}} + \tilde{\mathbf{E}}_3\hat{\boldsymbol{\delta}} + \tilde{\mathbf{E}}_4\hat{\mathbf{z}} \leq \tilde{\mathbf{g}}. \tag{5.34}$$

We recall (5.5) and after plugging (5.33) into it we get

$$J_N(\mathbf{x}_0, \cdot) = \frac{1}{2}\Big[(\mathbf{P}\mathbf{x}_0 + \mathbf{H}_1\hat{\mathbf{u}} + \mathbf{H}_2\hat{\boldsymbol{\delta}} + \mathbf{H}_3\hat{\mathbf{z}})^\intercal \tilde{\mathbf{Q}}(\mathbf{P}\mathbf{x}_0 + \mathbf{H}_1\hat{\mathbf{u}} + \mathbf{H}_2\hat{\boldsymbol{\delta}} + \mathbf{H}_3\hat{\mathbf{z}}) + \hat{\mathbf{u}}^\intercal \mathbf{R}'\hat{\mathbf{u}}\Big] \tag{5.35}$$

and then by defining

$$\boldsymbol{\Psi} \triangleq \begin{bmatrix} \hat{\mathbf{u}} \\ \hat{\boldsymbol{\delta}} \\ \hat{\mathbf{z}} \end{bmatrix} \tag{5.36}$$

we get

$$J_N(\mathbf{x}_0, \boldsymbol{\Psi}) = \frac{1}{2}\boldsymbol{\Psi}^\intercal \mathbf{G}\boldsymbol{\Psi} + \mathbf{x}_0^\intercal \mathbf{F}^\intercal \boldsymbol{\Psi}, \tag{5.37}$$

$$\text{s.t.} \qquad \mathbf{S}_1\boldsymbol{\Psi} \leq \mathbf{S}_2 + \mathbf{S}_3\mathbf{x}_0, \tag{5.38}$$

where the matrices $\mathbf{G}, \mathbf{F}, \mathbf{S}_1, \mathbf{S}_2$, and $\mathbf{S}_3$ are properly constructed from penalization and state prediction matrices.

The objective function can be then minimized using available solvers, as it is in the format of mixed-integer quadratic (constrained) programming (MIQP or MIQCP). For such a class of problems, the solvers are usually based on branch and bound method (used e.g. by GUROBI optimizer). This approach is only applicable to online (implicit) MPC.

The other option of PWA optimal control is a multiparametric method by Borelli in [57], which doesn't employ the transition of the PWA system to the MLD system but solves the optimization problem backward in time of prediction horizon. This approach is applicable for offline (explicit) MPC.

Branch and bound

The first proposal of the branch and bound (BnB) algorithm can be found in [58], but then it was substantially improved in [59].

The method solves the linear optimization problem

$$\min f(\mathbf{x}) = \mathbf{q}^\intercal \mathbf{x}, \tag{5.39}$$

subject to

$$\mathbf{A}\mathbf{x} = \mathbf{a}, \tag{5.40}$$

$$\mathbf{B}\mathbf{x} \leq \mathbf{b}, \tag{5.41}$$

$$x_i \in \mathbb{Z}, \forall i \in \mathbf{I} \wedge x_j \in \mathbb{R}, \forall j \in \{1, 2 \ldots n\} \setminus \mathbf{I}, \tag{5.42}$$

with set $\mathbf{I}$ containing the indices of integer elements of $\mathbf{x}$.

The first step is to solve the problem with omitting the integral restrictions defined in (5.42) and the problem reduces to a linear programming problem. This step is called relaxation and can be solved with any method suitable for linear programming. We obtain a solution, which, if by chance all integrality restrictions are fulfilled, is also a solution for problem (5.39)-(5.42). If the integrality restrictions are not satisfied ($\exists x_i, i \in \mathbf{I}, x_i \notin \mathbb{Z}$, e.g. $x_i = 1.2$), the branching part of the algorithm starts. We divide the solution of (5.39)-(5.42) into two subproblems with additional constraints $x_i \geq 2$ and $x_i \leq 1$. Each subproblem is then solved and the better of them is used as a solution to the original problem (5.39)-(5.42). If there were more than one integer variable ($|\mathbf{I}| > 1$), it is necessary to repeat the branching for each of them to satisfy the integral constraints for all defined variables.

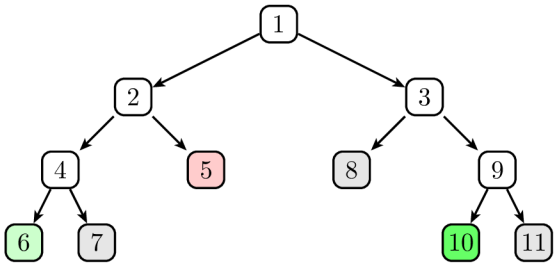

Fig. 5.1: Branch and bound algorithm overview

The BnB method is illustrated in Fig. 5.1. The nodes represent a single linear programming solution and the numbers denote possible evaluation order. The green color represents incumbent nodes (dark green represents the final incumbent - the solution of the problem). Grey color denotes the nodes marked as fathomed as their objective value is larger compared to the incumbent. Red color denotes the infeasible solution of the LP problem.

The method above can be also extended for quadratic integer problem even with quadratic constraints

$$\min f(\mathbf{x}) = \frac{1}{2}\mathbf{x}^\intercal \mathbf{Q}\mathbf{x} + \mathbf{q}^\intercal \mathbf{x}, \tag{5.43}$$

subject to

$$\mathbf{A}\mathbf{x} = \mathbf{a}, \tag{5.44}$$

$$\mathbf{B}\mathbf{x} \leq \mathbf{b}, \tag{5.45}$$

$$\frac{1}{2}\mathbf{x}^\intercal \mathbf{Q}_i\mathbf{x} + \mathbf{q}_i^\intercal \mathbf{x} \leq r_i \qquad \text{for } i = 1, 2 \ldots p \tag{5.46}$$

$$x_i \in \mathbb{Z}, \forall i \in \mathbf{I} \wedge x_j \in \mathbb{R}, \forall j \in \{1, 2 \ldots n\} \setminus \mathbf{I}, \tag{5.47}$$

which was reported in [60, 61, 62].

Explicit solvers for hybrid systems

There are two main possible approaches for offline hybrid MPC implementation. Both of them bring the possibility of precomputing the control laws, store them and then use them during real-time control instead of solving the optimization problem online.

The first of them use a combination of dynamic programming and multiparametric quadratic programming [57] for quadratic problems (called mp-MIQP) or combination of mp-LP and MILP solver [63] for 1-norm problems (called mp-MILP). This approach is used within the Hybrid toolbox.

The second possible way employs enumeration based PLCP solver [64]. The algorithm enumerates all bases, then prune the infeasible bases and for the rest of them returns critical regions and solutions of the problem within each region. This approach is implemented in the MPT toolbox.

5.3.3 DMPC for PWA systems

We propose to use MPC for selection of optimal control strategy of complex t-invariant non-linear system

$$\mathbf{x}_{k+1} = \mathbf{f}(\mathbf{x}_k, \mathbf{u}_k), \tag{5.48}$$

$$\mathbf{y}_k = \mathbf{h}(\mathbf{x}_k, \mathbf{u}_k), \tag{5.49}$$

with $\mathbf{x}$, $\mathbf{u}$ and $\mathbf{y}$ being the vector of states, inputs and outputs, $\mathbf{f}(\cdot)$ state update function and $\mathbf{h}(\cdot)$ the output function. Commonly, such a system has some binary $\mathbf{u}_k^{\mathrm{b}} \in \{0,1\}^{n_{\mathrm{b}}}$ and/or integral $\mathbf{u}_k^{\mathrm{i}} \in \mathbb{Z}^{n_{\mathrm{i}}}$ actuators (valves, switches, constant/step speed drives, etc.), which together form modes of the system. Under these modes, the system is operated and possibly continuously controlled by continuous inputs $\mathbf{u}_k^{\mathrm{r}} \in \mathbb{R}^{n_{\mathrm{r}}}$. Usually, the switching between modes is somehow constrained (switching frequency, etc.). Then the input vector can be written as

$$\mathbf{u}_k = \begin{bmatrix} \mathbf{u}_k^{\mathrm{b}} \\ \mathbf{u}_k^{\mathrm{i}} \\ \mathbf{u}_k^{\mathrm{r}} \end{bmatrix}. \tag{5.50}$$

We assume that we can find a simplified model of such a system in the form of a general high-level PWA dynamic model (incorporating e.g. generalized thermal flows, material flows, electric power flows, etc.). We define domain $\mathbb{U}_i^{\mathrm{b}}$ of i^{th} binary input variable u_i^{b} as

$$u_i^{\mathrm{b}} \in \mathbb{U}_i^{\mathrm{b}} \triangleq \{0,1\} \tag{5.51}$$

and similarly, the domain $\mathbb{U}_i^{\mathrm{i}}$ of i^{th} integral input variable u_i^{i} as

$$u_i^{\mathrm{i}} \in \mathbb{U}_i^{\mathrm{i}} \subset \mathbb{Z}, \tag{5.52}$$

with the assumption of reasonably constrained domains of integral variables. We then list all the binary and integral inputs combinations

$$\mathbf{M} = \prod_{i=1}^{n_{\mathrm{b}}} \mathbb{U}_i^{\mathrm{b}} \times \prod_{i=1}^{n_{\mathrm{i}}} \mathbb{U}_i^{\mathrm{i}} \tag{5.53}$$

and select their allowed combinations $\mathbf{M}_{\mathrm{a}} \subseteq \mathbf{M}$. Each item $m \in \mathbf{M}_{\mathrm{a}}$ is referred to as an *operating mode* and it is necessary to find an affine (or linear) dynamic description of the system within each operating mode. All the operating modes must have common vectors of inputs $\mathbf{u}^*$, states $\mathbf{x}^*$ and outputs $\mathbf{y}^*$, which, in general, will not be the same as the original vectors $\mathbf{u}$, $\mathbf{x}$ and $\mathbf{y}$ (they might be similar for simple systems). We suppose that all the operating modes share the same input and state constraints

$$\mathbf{E}\mathbf{x}_k^* + \mathbf{F}\mathbf{u}_k^* \leq \mathbf{G}, \tag{5.54}$$

which define the polyhedron

$$\mathcal{P} \subset \mathbb{R}^{n_{x^*}+n_{u^*}}. \tag{5.55}$$

Imagine that we succeed to find the dynamic description of i^{th} operating mode ($i = 1, 2 \ldots |\mathbf{M}_{\mathrm{a}}|$) in affine form as

$$\mathbf{x}_{k+1}^* = \mathbf{A}_i\mathbf{x}_k^* + \mathbf{B}_i\mathbf{u}_k^* + \mathbf{f}_i^{\mathrm{c}}, \tag{5.56}$$

$$\mathbf{y}_k^* = \mathbf{C}_i\mathbf{x}_k^* + \mathbf{D}_i\mathbf{u}_k^* + \mathbf{g}_i^{\mathrm{c}}, \tag{5.57}$$

$$\text{for } \begin{bmatrix} \mathbf{x}_k^* \\ \mathbf{u}_k^* \end{bmatrix} \in \mathcal{P}_i, \tag{5.58}$$

then several possibilities can happen:

- $\mathcal{P}_i = \mathcal{P}$ or $\mathcal{P}_i \supset \mathcal{P}$, which means that the current operating mode is also a *PWA system mode*
- $\mathcal{P}_i \subset \mathcal{P}$, which means that there exist at least two operating submodes within the current operating mode

In the second case, we denote the polyhedron $\mathcal{P}_i$ as $\mathcal{P}_{i1}$ and we need to find an affine dynamic model for $\mathcal{P}_{i2} \triangleq \mathcal{P} \backslash \mathcal{P}_{i1}$. We repeat this step and stop the searching if the condition

$$\bigcup_{j=1}^{s_i} \mathcal{P}_{ij} \supseteq \mathcal{P} \tag{5.59}$$

is fulfilled, which means that the whole constrained state-input space is covered by s_i submodes models. Each submode then becomes a new *PWA system mode*. This procedure is repeated for each operating mode (i.e. i is incremented and we try to find a model within this operating mode using the steps above).

Example. *Submodes could be useful if we consider a non-linear system with multiple functions (e.g. heating and cooling). We define two modes (for cooling and heating) and if the system has non-linear behavior within the mode, it can be described by several submodes (obtained e.g. by linearization).*

The distinction between operating modes is proposed based on dummy input $\tilde{u}$, which denotes the item $m \in \mathbf{M}_\mathrm{a}$. The input $\tilde{u}$ can be defined as needed, we propose $\tilde{u} \in \mathbb{N}$ and a single value of $\tilde{u}$ is assigned to each operating mode, for the i^{th} operating mode $\tilde{u} = i$.

The PWA system input vector $\mathbf{u}^*$ is extended by adding the dummy input $\tilde{u}$

$$\bar{\mathbf{u}} = \begin{bmatrix} \tilde{u} \\ \mathbf{u}^* \end{bmatrix} \tag{5.60}$$

and the polyhedron $\mathcal{P}$ has to be extended to

$$\mathcal{P}^* = \mathcal{P} \times \{1, 2 \dots |\mathbf{M}_\mathrm{a}|\}, \tag{5.61}$$

that is a polyhedral union of PWA system modes polyhedrons

$$\mathcal{P}^* = \bigcup_{i=1}^{|\mathbf{M}_\mathrm{a}|} \mathcal{P}_i^*, \tag{5.62}$$

where

$$\mathcal{P}_i^* = \begin{cases} \mathcal{P} \times i & \text{if } s_i = 1 \\ (\mathcal{P} \times i) \cap \bigcup_{j=1}^{s_i} \mathcal{P}_{ij}^* & \text{if } s_i > 1 \end{cases}, \tag{5.63}$$

where $i \in \{1, 2 \dots |\mathbf{M}_\mathrm{a}|\}$ and $\mathcal{P}_{ij}^* = \mathcal{P}_{ij} \times i$. For simplification of further text, we will denote $\mathcal{P}_i^*$ with no operating submodes as $\mathcal{P}_{i1}^*$. By recalling (5.22) - (5.24) and adjusting matrices $\mathbf{B}$ and $\mathbf{D}$ according to (5.60)

$$\mathbf{B}^* = \begin{bmatrix} \mathbf{0} & \mathbf{B} \end{bmatrix}, \qquad \mathbf{D}^* = \begin{bmatrix} \mathbf{0} & \mathbf{D} \end{bmatrix} \tag{5.64}$$

we get the description of the simplified system in PWA form

$$\mathbf{x}_{k+1}^* = \begin{cases} \mathbf{A}_{11}\mathbf{x}_k^* + \mathbf{B}_{11}^*\bar{\mathbf{u}}_k + \mathbf{f}_{11}^\mathrm{c} & \text{if } (\mathbf{x}_k^*, \bar{\mathbf{u}}_k) \in \mathcal{P}_{11} \\ \vdots & \vdots \\ \mathbf{A}_{|\mathbf{M}_\mathrm{a}|s_\mathrm{max}}\mathbf{x}_k^* + \mathbf{B}_{|\mathbf{M}_\mathrm{a}|s_\mathrm{max}}^*\bar{\mathbf{u}}_k + \mathbf{f}_{|\mathbf{M}_\mathrm{a}|s_\mathrm{max}}^\mathrm{c} & \text{if } (\mathbf{x}_k^*, \bar{\mathbf{u}}_k) \in \mathcal{P}_{|\mathbf{M}_\mathrm{a}|s_\mathrm{max}} \end{cases}, \tag{5.65}$$

$$\mathbf{y}_k^* = \begin{cases} \mathbf{C}_{11}\mathbf{x}_k^* + \mathbf{D}_{11}^*\bar{\mathbf{u}}_k + \mathbf{g}_{11}^\mathrm{c} & \text{if } (\mathbf{x}_k, \bar{\mathbf{u}}_k) \in \mathcal{P}_{11} \\ \vdots & \vdots \\ \mathbf{C}_{|\mathbf{M}_\mathrm{a}|s_\mathrm{max}}\mathbf{x}_k^* + \mathbf{D}_{|\mathbf{M}_\mathrm{a}|s_\mathrm{max}}^*\bar{\mathbf{u}}_k + \mathbf{g}_{|\mathbf{M}_\mathrm{a}|s_\mathrm{max}}^\mathrm{c} & \text{if } (\mathbf{x}_k^*, \bar{\mathbf{u}}_k) \in \mathcal{P}_{|\mathbf{M}_\mathrm{a}|s_\mathrm{max}} \end{cases}, \tag{5.66}$$

Tab. 5.2: Example of PWA system A matrix table. Each row represents one operating mode and cells within this row represent single operating submodes.

$\mathbf{A}_{11}$	$\mathbf{A}_{12}$	$\cdots$	$\mathbf{A}_{1s_{\max}}$
$\mathbf{A}_{21}$	$\mathbf{A}_{22}$	$\cdots$	$\mathbf{A}_{1s_{\max}}$
$\vdots$	$\vdots$	$\ddots$	$\vdots$
$\mathbf{A}_{\lvert\mathbf{M}_\mathrm{a}\rvert 1}$	$\mathbf{A}_{\lvert\mathbf{M}_\mathrm{a}\rvert 2}$	$\cdots$	$\mathbf{A}_{\lvert\mathbf{M}_\mathrm{a}\rvert s_{\max}}$

where

$$s_{\max} \triangleq \max_{i=1}^{|\mathbf{M}_\mathrm{a}|} s_i \tag{5.67}$$

denotes a maximal number of submodes over all the operating modes and $|\mathbf{M}_\mathrm{a}|$ is the cardinality of the set of allowed operating modes. The indexes of matrices, affine parts, and polyhedrons denote the coordinates in an appropriate table, an example for matrix $\mathbf{A}$ is in Tab. 5.2. It is allowed that some cells of the table are filled with zeros if for i^{th} operating mode if there is only one PWA mode or if the number of submodes s_i is lower than $s_{\max}$.

Usually, the PWA systems are used to describe the behavior of a real system concerning different dynamics for different operating points. Here we extend the usage for decision system, which can optimize system energy consumption with compliance to references and system constraints.

The modes of PWA system here represent different control strategies or different system configurations (for example heat pump source/sink configuration; cooling/ heating distinction for different systems; for HEV type of propulsion - petrol/electric etc.).

Then we propose to use MPC for selection of system mode and thus values of binary and integral actuators and at the same time the control strategy of the continuously controlled actuators (set of controllers etc.).

MPC is employed to find, which mode of system in (5.65) - (5.66) is optimal in terms of reference tracking, complying with the system constraints and power consumption minimization, all defined by cost function and model constraints. The cost function is used in the form

$$J_N(\mathbf{x}_0, \hat{\mathbf{u}}) = \sum_{k=0}^{N-1} \left[(\mathbf{x}_k - \mathbf{r}_k)^\intercal \mathbf{Q} (\mathbf{x}_k - \mathbf{r}_k) + \bar{\mathbf{u}}_k^\intercal \mathbf{R} \bar{\mathbf{u}}_k + \Delta \bar{\mathbf{u}}_k^\intercal \mathbf{S} \Delta \bar{\mathbf{u}}_k \right], \tag{5.68}$$

with $\mathbf{x}$ being the state vector, $\mathbf{r}$ the state references vector and $\bar{\mathbf{u}}$ the modified PWA system input vector. The matrices $\mathbf{Q}$, $\mathbf{R}$ and $\mathbf{S}$ are the penalization matrices for state error, inputs, and input change rate. The matrices $\mathbf{R}$ and $\mathbf{S}$ contain element related to input $\tilde{u}$ on position [1,1]

$$\mathbf{R} = \begin{bmatrix} R_{11} & \dots \\ \vdots & \ddots \end{bmatrix}, \qquad \mathbf{S} = \begin{bmatrix} S_{11} & \dots \\ \vdots & \ddots \end{bmatrix} \tag{5.69}$$

and these elements can be used for influencing the mode switching. Firstly, if we sort the operating modes from best to worst (from any perspective), using R_{11} the mode selection can be adjusted. Secondly, the mode switching rate can be penalized using S_{11}, which needs to be tuned to ensure the desired switching behavior.

Remark. *The cost function (5.68) is not used for optimizations in this form, as the PWA system (and also the penalization matrices) needs to be converted into MLD or LCP system to be usable with available solvers. However, the form of (5.68) is useful for its clearness and thus it is used for explanation of dummy input penalization.*

The result of the optimization of (5.68) (or its equivalent for MLD or LCP system) is a vector of predicted optimal inputs $\hat{\mathbf{u}}$. If we consider standard receding horizon control (RHC) on prediction horizon N, only the first step control values $\hat{\mathbf{u}}_k$ are applied on a controlled system and the rest of predicted values $(\hat{\mathbf{u}}_{k+1} \dots \hat{\mathbf{u}}_{k+N-1})$ are discarded. We can reuse this approach and extend it by discarding all the predicted inputs except $\tilde{u}_k$, which is used for operating mode selection.

The control of actuators is then managed by low-level algorithms, which ensure precise reference tracking, disturbance rejection, and other tasks. As this approach is aimed at a complex non-linear system (tens of inputs, up to tens of thousands of states), the MPC cannot be solved for every real input of the system because of high computational demands.

We refer to this approach of high-level system modes switching as the Decision Model Predictive Control (DMPC).

Remark. *The current inputs $\mathbf{u}_k^*$ could be also used for direct control of the system, but only if the system is simple enough. Another possibility is to use the inputs as high-level power inputs, e.g. to control the overall cooling/heating power of the heat pump system in the range of $\langle 0, 1 \rangle$, which is then realized by low-level control algorithms of compressor, expansion valve, fans, pumps, etc.*

5.3.4 Example of DMPC for heated element

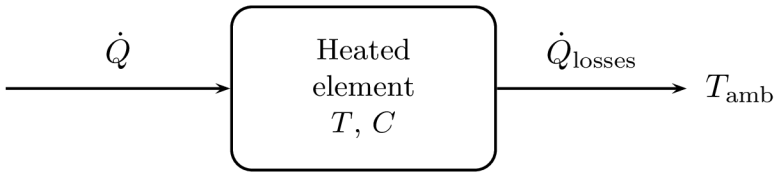

Fig. 5.2: Heated element example diagram

We consider a simple relay-controlled thermal system like iron, oven, etc.

$$\frac{\mathrm{d}T}{\mathrm{d}t} = -\frac{\dot{Q}_{\text{losses}}}{C} + \frac{\dot{Q}}{C} \tag{5.70}$$

and after substitutions of heat flows we get

$$\frac{\mathrm{d}T}{\mathrm{d}t} = -\frac{G}{C}(T - T_{\text{amb}}) + \frac{\dot{Q}^{\max}}{C}u \tag{5.71}$$

and after discretization with sampling period T_{s}

$$T_{k+1} = -\frac{GT_{\text{s}}}{C}(T_k - T_{\text{amb}}) + \frac{\dot{Q}^{\max}T_{\text{s}}}{C}u, \tag{5.72}$$

where T is the heated element temperature, C is its thermal capacity, T_{amb} is constant ambient temperature, G is thermal conductance and $\dot{Q}$ is thermal flow into the system. The thermal flow $\dot{Q}$ is a product of its constant maximal value $\dot{Q}^{\max}$ and the binary control input u (e.g. from the relay).

The set of allowed combinations of binary variables is equal to the set of all combinations of binary variables

$$\mathbf{M}_{\text{a}} = \mathbf{M} = \{0, 1\} \tag{5.73}$$

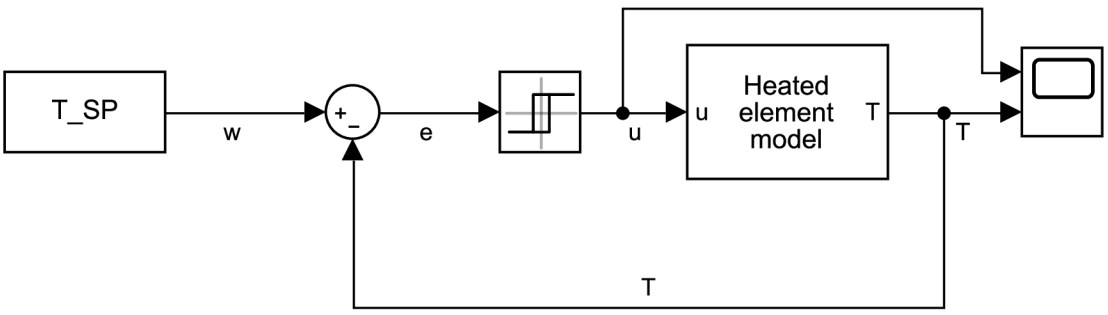

Fig. 5.3: Diagram of heated element relay control. Heated element modeled according to (5.72).

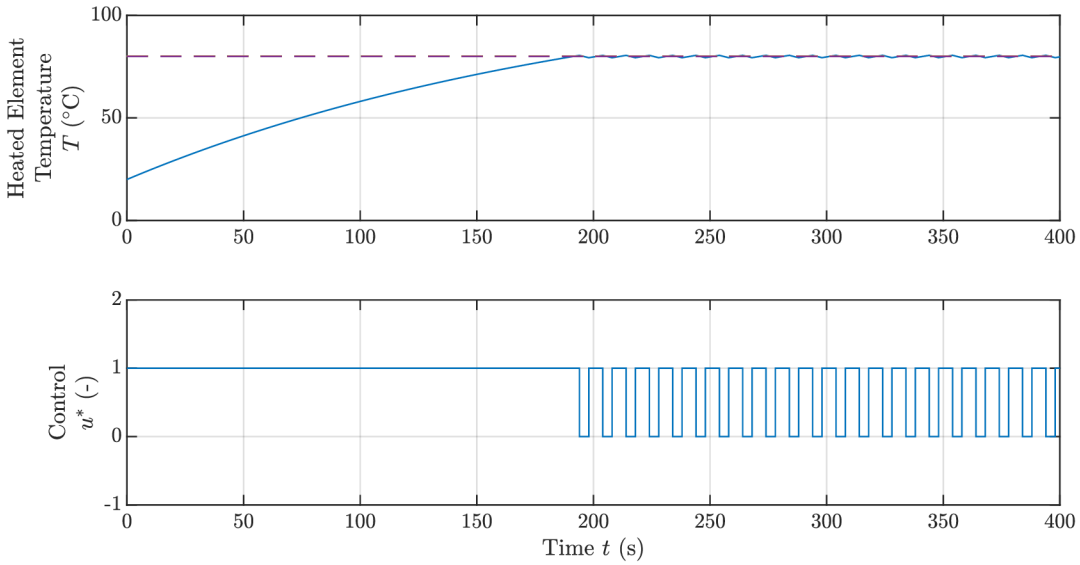

Fig. 5.4: Result of relay control of the heated element

and we then define the state constraints of the system

$$273.15 < T < 273.15 + 100 \qquad \text{(K)}, \tag{5.74}$$

which defines polyhedron $\mathcal{P}$ (in this example reduced to a line segment). Now we try to find the affine (or linear) model for operating modes with the following result

$$\text{for i=1:} \qquad T_{k+1} = -\frac{GT_\text{s}}{C}(T_k - T_\text{amb}), \tag{5.75}$$

$$\text{for i=2:} \qquad T_{k+1} = -\frac{GT_\text{s}}{C}(T_k - T_\text{amb}) + \frac{\dot{Q}^\text{max}T_\text{s}}{C} \tag{5.76}$$

and it is easy to see that the i^th model holds within the polyhedrons $\mathcal{P}_i^*$, thus these operating modes are also PWA system modes and there are no submodes. Then we can write the PWA system model as

$$\mathbf{x}_{k+1}^* = \begin{cases} \mathbf{A}_{11}\mathbf{x}_k^* + \mathbf{B}_{11}^*\bar{\mathbf{u}}_k + \mathbf{f}_{11}^\text{c} & \text{if } \tilde{u}_k = 1 \\ \mathbf{A}_{21}\mathbf{x}_k^* + \mathbf{B}_{21}^*\bar{\mathbf{u}}_k + \mathbf{f}_{21}^\text{c} & \text{if } \tilde{u}_k = 2 \end{cases}, \tag{5.77}$$

where

$$\mathbf{x}^* = \begin{bmatrix} T \end{bmatrix}, \qquad \bar{\mathbf{u}} = \begin{bmatrix} \tilde{u} \end{bmatrix}, \tag{5.78}$$

$$\mathbf{A}_{11} = \mathbf{A}_{21} = 1 - \frac{GT_\text{s}}{C}, \qquad \mathbf{B}_{11}^* = \mathbf{B}_{21}^* = 0, \tag{5.79}$$

$$\mathbf{f}_{11}^\text{c} = \frac{GT_\text{s}}{C}T_\text{amb} \qquad \mathbf{f}_{21}^\text{c} = \frac{GT_\text{s}}{C}T_\text{amb} + \frac{\dot{Q}^\text{max}T_\text{s}}{C}. \tag{5.80}$$

Translation to MLD system

The system in (5.77) is quite simple, thus we can easily rewrite it in the form of MLD system by reusing (5.30) and defining inequalities

$$u_k \geq m(1-\delta_k) + \delta_k, \tag{5.81}$$
$$u_k \leq -\varepsilon + (M+\varepsilon)\delta_k + 1 - \delta_k \tag{5.82}$$

and then by writing the MLD system in the matrix form

$$\mathbf{x}_{k+1} = \mathbf{A}\mathbf{x}_k + \mathbf{B}_2\boldsymbol{\delta}_k, \tag{5.83}$$
$$\mathbf{E}_2\mathbf{u}_k + \mathbf{E}_3\boldsymbol{\delta}_k \leq \mathbf{g}_5 \tag{5.84}$$

where

$$\mathbf{x} = \begin{bmatrix} T \\ T_{\text{amb}} \end{bmatrix}, \boldsymbol{\delta} = \begin{bmatrix} \delta \end{bmatrix}, \mathbf{u} = \begin{bmatrix} u \end{bmatrix}, \tag{5.85}$$
$$\mathbf{A} = \begin{bmatrix} \frac{C-GT_{\text{s}}}{C} & \frac{G}{C} \\ 0 & 0 \end{bmatrix}, \mathbf{B}_2 = \begin{bmatrix} \frac{\dot{Q}^{\max}}{C} \end{bmatrix}, \tag{5.86}$$
$$\mathbf{E}_2 = \begin{bmatrix} -1 \\ 1 \end{bmatrix}, \mathbf{E}_3 = \begin{bmatrix} 1-m \\ -M-\varepsilon+1 \end{bmatrix}, \mathbf{g}_5 = \begin{bmatrix} m \\ 1-\varepsilon \end{bmatrix}. \tag{5.87}$$

For prediction horizon $N = 2$ we can write prediction equations as

$$\underbrace{\begin{bmatrix} \mathbf{x}_{k+1} \\ \mathbf{x}_{k+2} \end{bmatrix}}_{\hat{\mathbf{x}}} = \underbrace{\begin{bmatrix} \mathbf{A} \\ \mathbf{A}^2 \end{bmatrix}}_{\mathbf{P}} \mathbf{x}_0 + \underbrace{\begin{bmatrix} \mathbf{B}_2 & 0 \\ \mathbf{A}\mathbf{B}_2 & \mathbf{B}_2 \end{bmatrix}}_{\mathbf{H}_2} \underbrace{\begin{bmatrix} \delta_k \\ \delta_{k+1} \end{bmatrix}}_{\hat{\boldsymbol{\delta}}}, \tag{5.88}$$
$$\begin{bmatrix} \mathbf{E}_2 & \mathbf{0} \\ \mathbf{0} & \mathbf{E}_2 \end{bmatrix} \begin{bmatrix} \mathbf{u}_k \\ \mathbf{u}_{k+1} \end{bmatrix} + \begin{bmatrix} \mathbf{E}_3 & \mathbf{0} \\ \mathbf{0} & \mathbf{E}_3 \end{bmatrix} \begin{bmatrix} \delta_k \\ \delta_{k+1} \end{bmatrix} \leq \begin{bmatrix} \mathbf{g}_5 \\ \mathbf{g}_5 \end{bmatrix} \tag{5.89}$$

and then plug them into the objective function

$$J_N(\mathbf{x}_0, \cdot) = \frac{1}{2}\left[(\mathbf{P}\mathbf{x}_0 + \mathbf{H}_2\hat{\delta})^\intercal \mathbf{Q}'(\mathbf{P}\mathbf{x}_0 + \mathbf{H}_2\hat{\boldsymbol{\delta}}) + \hat{\mathbf{u}}^\intercal \mathbf{R}'\hat{\mathbf{u}}\right], \tag{5.90}$$
$$\text{s.t.} \qquad \mathbf{S}_1\boldsymbol{\Omega} \leq \mathbf{S}_2 \tag{5.91}$$

and finally, we get

$$J_N(\mathbf{x}_0, \boldsymbol{\Omega}) = \frac{1}{2}\boldsymbol{\Omega}^\intercal \mathbf{G}\boldsymbol{\Omega} + \mathbf{x}_0^\intercal \mathbf{F}^\intercal \boldsymbol{\Omega}, \tag{5.92}$$
$$\text{s.t.} \qquad \mathbf{S}_1\boldsymbol{\Omega} \leq \mathbf{S}_2, \tag{5.93}$$

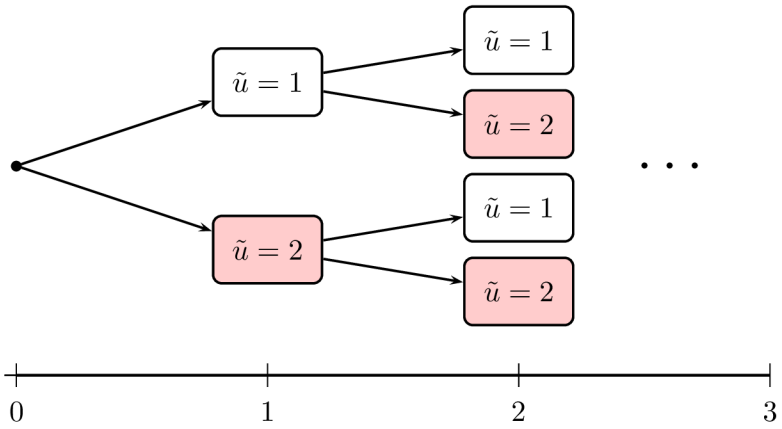

Fig. 5.5: Decision tree for heated element

where

$$\boldsymbol{\Omega} \triangleq \begin{bmatrix} \hat{\mathbf{u}} \\ \hat{\boldsymbol{\delta}} \end{bmatrix} = \begin{bmatrix} u_k \\ u_{k+1} \\ \delta_k \\ \delta_{k+1} \end{bmatrix}, \quad \mathbf{G} = \begin{bmatrix} \mathbf{R}' \\ \mathbf{H}_2^\intercal \mathbf{Q}' \mathbf{H}_2 \end{bmatrix}, \quad \mathbf{F}^\intercal = \begin{bmatrix} \mathbf{0} \\ \mathbf{P}^\intercal \mathbf{Q}' \mathbf{H}_2 \end{bmatrix}, \tag{5.94}$$

$$\mathbf{S}_1 = \begin{bmatrix} \mathbf{E}_2 & \mathbf{0} & \mathbf{E}_3 & \mathbf{0} \\ \mathbf{0} & \mathbf{E}_2 & \mathbf{0} & \mathbf{E}_3 \end{bmatrix}, \mathbf{S}_2 = \begin{bmatrix} \mathbf{g}_5 \\ \mathbf{g}_5 \end{bmatrix}. \tag{5.95}$$

This optimization problem can be then solved by MIQP solver, e.g. branch and bound method described before.

Simulations

The principle of the operation of the MPC controller in decision mode is illustrated in Fig. 5.5 (light red denotes the heating mode of the system). At step 0, there are two possibilities of decision for the next step - heating of the element or standby (and cooling with ambient). As we consider prediction horizon $N = 2$, in the second step there are four possible scenarios of system behavior. For all the possibilities the cost function is evaluated and then the optimal decision sequence for this system is selected. The first step of the decision sequence is applied to the controlled system and in the next step a new MPC decision operation is performed.

The implementation using MPTtoolbox [65] is in Listing 5.1. The result of MPC control is in Fig. 5.6 and it is similar to relay control result in Fig. 5.4.

Listing 5.1: Heated element MPC controller set up

```
% Dynamic model of the system
A = 1-G*Ts/C_h; B = [0]; C = [0]; D = 0;
f11 = G*Ts/C_h*T_amb;
f21 = G*Ts/C_h*T_amb + Qdot*Ts/C_h;

dyn1 = LTISystem('A', A, 'B', B, 'f', f11, 'C', C, 'D', D, 'Ts', Ts);
P1 = Polyhedron('A', [], 'b', [], 'Ae', 1, 'be', 1);
dyn1.setDomain('u', P1);

dyn2 = LTISystem('A', A, 'B', B, 'f', f21, 'C', C, 'D', D, 'Ts', Ts);
P2 = Polyhedron('A', [], 'b', [], 'Ae', 1, 'be', 2);
dyn2.setDomain('u', P2);

pwa = PWASystem([dyn1 dyn2]);

% Constraints
pwa.x.min = [273.15];
pwa.x.max = [273.15+100];
pwa.u.min = 0;
pwa.u.max = 2;

% References
pwa.x.with('reference');
pwa.x.reference = 'free';
xref = T_SP;

% Penalties
pwa.x.penalty = QuadFunction(100);
pwa.u.penalty = QuadFunction(1);
pwa.u.with('deltaPenalty');
pwa.u.deltaPenalty = QuadFunction(40);

% Controller
horizon = 2;
onl_ctrl = MPCController(pwa, horizon);

% Initialization
x0 = [T_amb];
u0 = 0;

% Simulation
Nsim = 800;
loop = ClosedLoop(onl_ctrl, pwa);
data = loop.simulate(x0, Nsim, 'x.reference', xref, 'u.previous', u0);
```

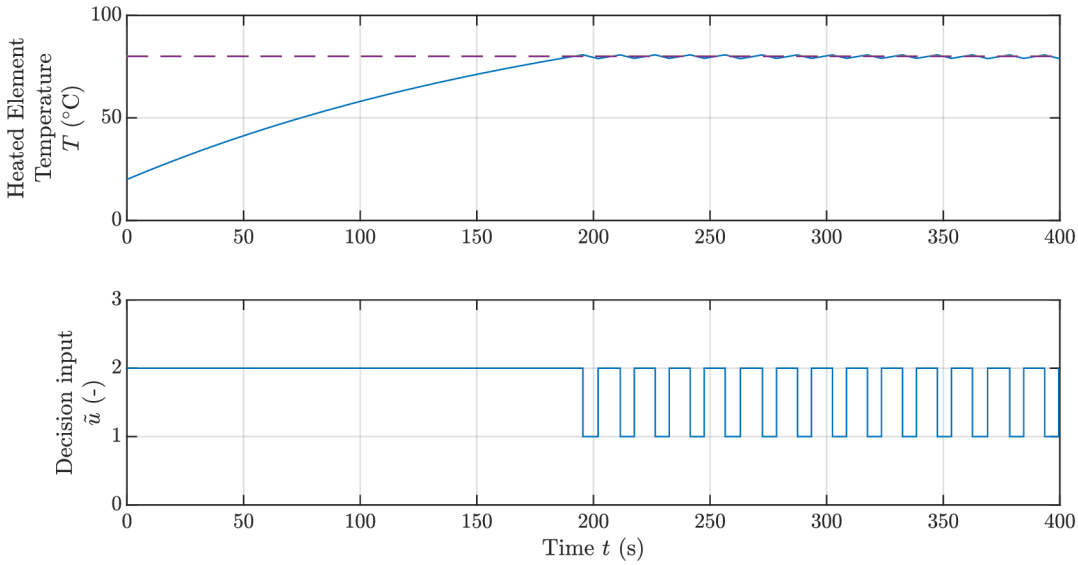

Fig. 5.6: Result of MPC control of heated element

5.3.5 Example of DMPC for vehicle cabin heating

As a second example, we introduce a simplified vehicle cabin, which is heated by a heat pump system with two different heat sources - ambient air and coolant (which ensures waste heat recovery from E-Drive and HV Battery). These modes are inspired by VCRS operating conditions in Section 5.3.6 and all the specific values of variables (such as *COP*, compressor power, heat flow rates, etc.) are also based on the condition's definition. The heat flow overview of the system is in Fig. 5.7 with following symbol meanings: T_{cab} is the cabin temperature, T_{co} is the temperature of the coolant, *TF* is a Thermal Function, $\dot{Q}_{\text{c}}$ is thermal flow from HV compressor, $\dot{Q}_{\text{loss}}$ stands for thermal losses of the cabin, $\dot{Q}_{\text{amb}}$ is heat pump thermal flow from ambient to the cabin and $\dot{Q}_{\text{co}}$ is heat pump thermal flow from the coolant to the cabin.

Suppose we have two evaporators, which are connected into a refrigerant circuit in parallel. Each evaporator has its shut-off valve (SOV) marked as v_1 and v_2. The performance of the heat pump is controlled by compressor speed (u_{c}). Then we can write the simple model of cabin heating as

$$\mathbf{x}_{k+1} = \mathbf{f}(\mathbf{x}_k, \mathbf{u}_k) \tag{5.96}$$

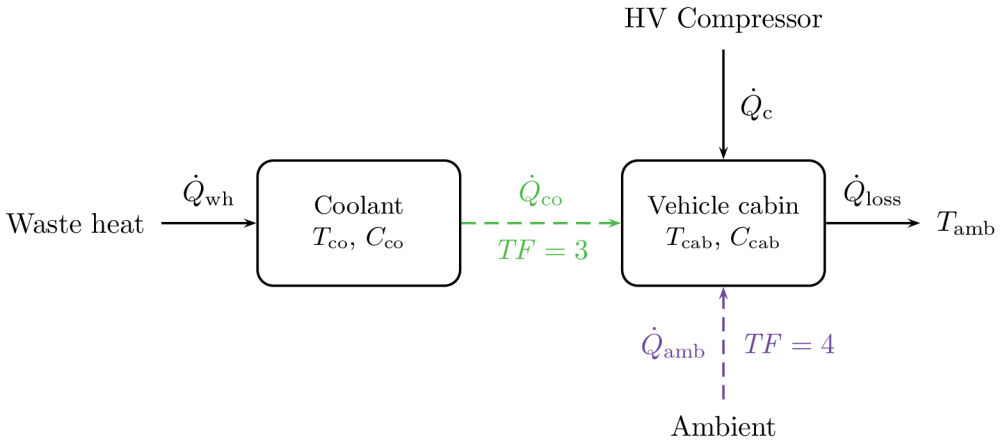

Fig. 5.7: Simple vehicle cabin heating

with

$$\mathbf{x} = \begin{bmatrix} T_{\text{cab}} \\ T_{\text{co}} \end{bmatrix}, \qquad \mathbf{u} = \begin{bmatrix} v_1 \\ v_2 \\ u_c \end{bmatrix}. \tag{5.97}$$

As there are two binary inputs (v_1 and v_2), all their possible combinations are

$$\mathbf{M} = \{00, 01, 10, 11\}, \tag{5.98}$$

but only two of them are allowed

$$\mathbf{M}_a = \{01, 10\}, \tag{5.99}$$

as both the SOV can not be closed or opened at the same time. Here we will violate the rule of denoting the operating modes from number 1, we will start from number 3 (as it is based on defined Thermal Function (TF)). So we mark the PWA system modes as TF 3 (heating with waste heat from coolant as a heat source) and TF 4 (heating with ambient air as a heat source).

Here we introduce the system constraints

$$273.15 - 20 < T_{\text{cab}} < 273.15 + 50 \qquad \text{(K)}, \tag{5.100}$$

$$273.15 + 5 < T_{\text{co}} < 273.15 + 40 \qquad \text{(K)}, \tag{5.101}$$

$$0 < u_{\text{c}} < 1 \qquad (-), \tag{5.102}$$

which describe the polyhedron $\mathcal{P}$.

In operating mode 3 (TF 3) the system overview is in Fig. 5.8 and it can be described by

$$C_{\text{cab}} \frac{\mathrm{d}T_{\text{cab}}}{\mathrm{d}t} = -\dot{Q}_{\text{loss}} + \dot{Q}_{\text{co}} + \dot{Q}_{\text{c}}, \tag{5.103}$$

$$C_{\text{co}} \frac{\mathrm{d}T_{\text{co}}}{\mathrm{d}t} = \dot{Q}_{\text{wh}} - \dot{Q}_{\text{co}} \tag{5.104}$$

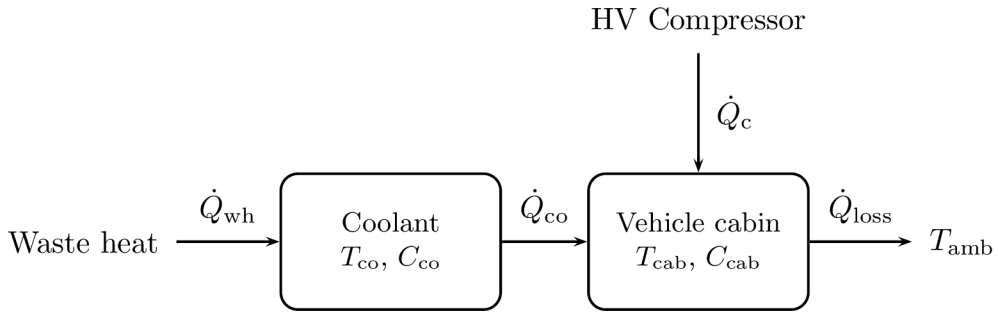

Fig. 5.8: Simple vehicle cabin heating - TF 3

and we evaluate

$$\dot{Q}_{\mathrm{c}} = P_{\mathrm{c,co}}^{\max} u_{\mathrm{c}}, \tag{5.105}$$

$$\dot{Q}_{\mathrm{co}} = (COP_{\mathrm{co}} - 1) u_{\mathrm{c}} P_{\mathrm{c,co}}^{\max}, \tag{5.106}$$

where $P_{\mathrm{c,co}}^{\max}$ is maximal compressor power for TF 3 (based on suction side refrigerant density and thus low side pressure). COP_{co} stands for Coefficient of Performance for a water-to-water heat pump. Then we get

$$C_{\mathrm{cab}} \frac{\mathrm{d}T_{\mathrm{cab}}}{\mathrm{d}t} = -G(T_{\mathrm{cab}} - T_{\mathrm{amb}}) + COP_{\mathrm{co}} u_{\mathrm{c}} P_{\mathrm{c,co}}^{\max}, \tag{5.107}$$

$$C_{\mathrm{co}} \frac{\mathrm{d}T_{\mathrm{co}}}{\mathrm{d}t} = \dot{Q}_{\mathrm{wh}} - (COP_{\mathrm{co}} - 1) P_{\mathrm{c,co}}^{\max} u_{\mathrm{c}}, \tag{5.108}$$

$$\frac{\mathrm{d}T_{\mathrm{cab}}}{\mathrm{d}t} = -\frac{G}{C_{\mathrm{cab}}} T_{\mathrm{cab}} + \frac{COP_{\mathrm{co}} P_{\mathrm{c,co}}^{\max}}{C_{\mathrm{cab}}} u_{\mathrm{c}} + \frac{G}{C_{\mathrm{cab}}} T_{\mathrm{amb}}, \tag{5.109}$$

$$\frac{\mathrm{d}T_{\mathrm{co}}}{\mathrm{d}t} = -\frac{(COP_{\mathrm{co}} - 1) P_{\mathrm{c,co}}^{\max}}{C_{\mathrm{co}}} u_{\mathrm{c}} + \frac{\dot{Q}_{\mathrm{wh}}}{C_{\mathrm{co}}} \tag{5.110}$$

and in discrete time with sampling period T_{s}

$$\mathbf{x}_{k+1} = \mathbf{A}_{31} \mathbf{x}(k) + \mathbf{B}_{31} \mathbf{u}^*(k) + \mathbf{f}_{31}^{\mathrm{c}}, \tag{5.111}$$

$$\mathbf{x} = \begin{bmatrix} T_{\mathrm{cab}} \\ T_{\mathrm{co}} \end{bmatrix}, \qquad \mathbf{u}^* = \begin{bmatrix} u_{\mathrm{c}} \end{bmatrix}, \tag{5.112}$$

$$\mathbf{A}_{31} = \begin{bmatrix} 1 - \frac{GT_{\mathrm{s}}}{C_{\mathrm{cab}}} & 0 \\ 0 & 1 \end{bmatrix}, \tag{5.113}$$

$$\mathbf{B}_{31} = \begin{bmatrix} \frac{COP_{\mathrm{co}} P_{\mathrm{c,co}}^{\max} T_{\mathrm{s}}}{C_{\mathrm{cab}}} \\ -\frac{(COP_{\mathrm{co}} - 1) P_{\mathrm{c,co}}^{\max} T_{\mathrm{s}}}{C_{\mathrm{co}}} \end{bmatrix}, \tag{5.114}$$

$$\mathbf{f}_{31}^{\mathrm{c}} = \begin{bmatrix} \frac{GT_{\mathrm{s}}}{C_{\mathrm{cab}}} T_{\mathrm{amb}} \\ \frac{\dot{Q}_{\mathrm{wh}} T_{\mathrm{s}}}{C_{\mathrm{co}}} \end{bmatrix}. \tag{5.115}$$

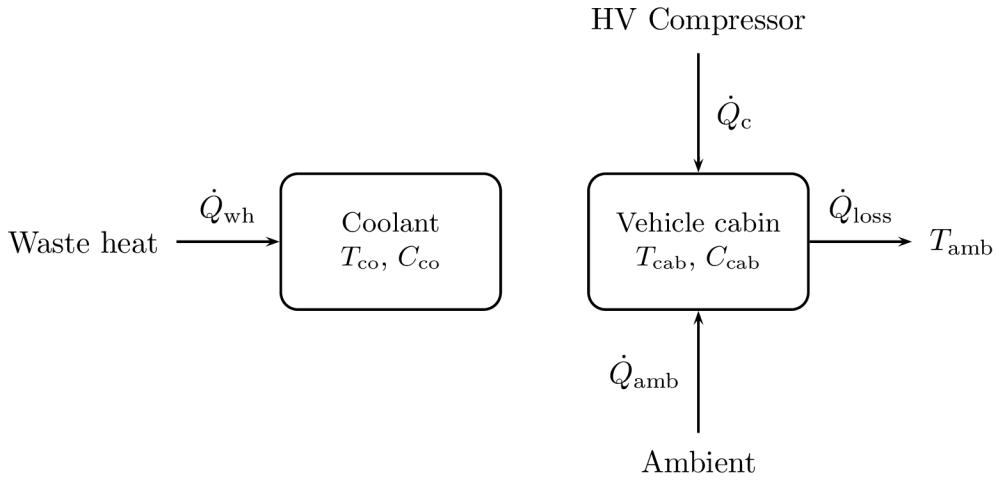

Fig. 5.9: Simple vehicle cabin heating - TF 4

In operating mode 4 (TF 4) the system overview is in Fig. 5.9 and it can be described by

$$C_{\mathrm{cab}}\frac{\mathrm{d}T_{\mathrm{cab}}}{\mathrm{d}t} = -\dot{Q}_{\mathrm{loss}} + \dot{Q}_{\mathrm{amb}} + \dot{Q}_{\mathrm{c}}, \tag{5.116}$$

$$C_{\mathrm{co}}\frac{\mathrm{d}T_{\mathrm{co}}}{\mathrm{d}t} = \dot{Q}_{\mathrm{wh}}, \tag{5.117}$$

we evaluate the heat flows and get

$$\dot{Q}_{\mathrm{c}} = P^{\max}_{\mathrm{c,amb}} u_{\mathrm{c}}, \tag{5.118}$$

$$\dot{Q}_{\mathrm{amb}} = (COP_{\mathrm{amb}} - 1) u_{\mathrm{c}} P^{\max}_{\mathrm{c,amb}}, \tag{5.119}$$

where $P^{\max}_{\mathrm{c,amb}}$ is maximal compressor power for TF 4 (based on suction side refrigerant density and thus low side pressure). COP_{amb} stands for Coefficient of Performance for an air-to-water heat pump. Then we get

$$C_{\mathrm{cab}}\frac{\mathrm{d}T_{\mathrm{cab}}}{\mathrm{d}t} = -G(T_{\mathrm{cab}} - T_{\mathrm{amb}}) + COP_{\mathrm{amb}} u_{\mathrm{c}} P^{\max}_{\mathrm{c,amb}}, \tag{5.120}$$

$$C_{\mathrm{co}}\frac{\mathrm{d}T_{\mathrm{co}}}{\mathrm{d}t} = \dot{Q}_{\mathrm{wh}}, \tag{5.121}$$

$$\frac{\mathrm{d}T_{\mathrm{cab}}}{\mathrm{d}t} = -\frac{G}{C_{\mathrm{cab}}}T_{\mathrm{cab}} + \frac{COP_{\mathrm{amb}} P^{\max}_{\mathrm{c,amb}}}{C_{\mathrm{cab}}} u_{\mathrm{c}} + \frac{G}{C_{\mathrm{cab}}} T_{\mathrm{amb}}, \tag{5.122}$$

$$\frac{\mathrm{d}T_{\mathrm{co}}}{\mathrm{d}t} = \frac{\dot{Q}_{\mathrm{wh}}}{C_{\mathrm{co}}} \tag{5.123}$$

and in discrete time with sampling period T_{s}

$$\mathbf{x}_{k+1} = \mathbf{A}_{41}\mathbf{x}_k + \mathbf{B}_{41}\mathbf{u}^*_k + \mathbf{f}^{\mathrm{c}}_{41}, \tag{5.124}$$

$$\mathbf{x} = \begin{bmatrix} T_{\mathrm{cab}} \\ T_{\mathrm{co}} \end{bmatrix}, \qquad \mathbf{u}^* = \begin{bmatrix} u_{\mathrm{c}} \end{bmatrix}, \tag{5.125}$$

$$\mathbf{A}_{41} = \begin{bmatrix} 1 - \frac{GT_{\mathrm{s}}}{C_{\mathrm{cab}}} & 0 \\ 0 & 1 \end{bmatrix}, \tag{5.126}$$

$$\mathbf{B}_{41} = \begin{bmatrix} \frac{COP_{\mathrm{amb}} P^{\max}_{\mathrm{c,amb}} T_{\mathrm{s}}}{C_{\mathrm{cab}}} \\ 0 \end{bmatrix}, \tag{5.127}$$

$$\mathbf{f}^{\mathrm{c}}_{41} = \begin{bmatrix} \frac{GT_{\mathrm{s}}}{C_{\mathrm{cab}}} T_{\mathrm{amb}} \\ \frac{\dot{Q}_{\mathrm{wh}} T_{\mathrm{s}}}{C_{\mathrm{co}}} \end{bmatrix}. \tag{5.128}$$

Now we suppose that the i^{th} model holds within the polyhedrons $\mathcal{P}^*_i$, thus these operating modes are also PWA system modes and there are no submodes. The overall model of vehicle cabin heating is

$$\mathbf{x}_{k+1} = \begin{cases} \mathbf{A}\mathbf{x}_k + \mathbf{B}_{31}\bar{\mathbf{u}}_k + \mathbf{f}^{\mathrm{c}} & \text{if } TF = 3 \\ \mathbf{A}\mathbf{x}_k + \mathbf{B}_{41}\bar{\mathbf{u}}_k + \mathbf{f}^{\mathrm{c}} & \text{if } TF = 4 \end{cases}, \tag{5.129}$$

where

$$\mathbf{x} = \begin{bmatrix} T_{\mathrm{cab}} \\ T_{\mathrm{co}} \end{bmatrix}, \qquad \bar{\mathbf{u}} = \begin{bmatrix} TF \\ u_{\mathrm{c}} \end{bmatrix}, \tag{5.130}$$

$$\mathbf{A} = \begin{bmatrix} 1 - \frac{GT_{\mathrm{s}}}{C_{\mathrm{cab}}} & 0 \\ 0 & 1 \end{bmatrix}, \tag{5.131}$$

$$\mathbf{B}^*_{31} = \begin{bmatrix} 0 & \frac{COP_{\mathrm{co}} P^{\max}_{\mathrm{c,co}} T_{\mathrm{s}}}{C_{\mathrm{cab}}} \\ 0 & -\frac{(COP_{\mathrm{co}} - 1) P^{\max}_{\mathrm{c,co}} T_{\mathrm{s}}}{C_{\mathrm{co}}} \end{bmatrix} \qquad \mathbf{B}^*_{41} = \begin{bmatrix} 0 & \frac{COP_{\mathrm{amb}} P^{\max}_{\mathrm{c,amb}} T_{\mathrm{s}}}{C_{\mathrm{cab}}} \\ 0 & 0 \end{bmatrix}, \tag{5.132}$$

$$\mathbf{f}^{\mathrm{c}} = \begin{bmatrix} \frac{GT_{\mathrm{s}}}{C_{\mathrm{cab}}} T_{\mathrm{amb}} \\ \frac{\dot{Q}_{\mathrm{wh}} T_{\mathrm{s}}}{C_{\mathrm{co}}} \end{bmatrix}. \tag{5.133}$$

The implementation using MPTtoolbox is shown in Listing 5.2.

This example was verified by simulation in MATLAB environment and the result is in Fig. 5.10. The MPC controller switches between TF 3 (heat pump with waste heat recovery) and TF 4 (heat pump with ambient air as a heat source) with satisfying the defined constraints (especially the coolant temperature) and the cabin temperature reference is also tracked successfully. This control problem could be also quite easily solved by some basic logic functions (or state diagram), but with increasing complexity (like VTMS in Fig. 2.1) it is not the preferable solution.

Listing 5.2: Simple vehicle cabin DMPC controller set up

```
% Dynamic model
A = [1-G*Ts/C_cab 0; 0 1];
B3 = [0 COP_co*Pco*Ts/C_cab; 0 -(COP_co-1)*Pco*Ts/C_co];
B4 = [0 COP_amb*Pamb*Ts/C_cab; 0 0];
C = [0 0]; D = [0 0];
f = [G*Ts/C_cab*T_amb; Qdot_wh*Ts/C_co];

dyn3 = LTISystem('A', A, 'B', B3, 'f', f, 'C', C, 'D', D, 'Ts', Ts);
P3 = Polyhedron('A', [0 1; 0 -1], 'b', [1;0], 'Ae', [1 0], 'be', [3]);
dyn3.setDomain('u', P3);

dyn4 = LTISystem('A', A, 'B', B4, 'f', f, 'C', C, 'D', D, 'Ts', Ts);
P4 = Polyhedron('A', [0 1; 0 -1], 'b', [1;0], 'Ae', [1 0], 'be', [4]);
dyn4.setDomain('u', P4);

pwa = PWASystem([dyn3 dyn4]);

% Constraints
pwa.x.min = [273.15-20 273.12+5];
pwa.x.max = [273.15+50 273.15+40];
pwa.u.min = [2 0];
pwa.u.max = [5 1];
pwa.x.with('softMax');
pwa.x.with('softMin');

% References
pwa.x.with('reference');
pwa.x.reference = 'free';
xref = [T_SP; 273.15+10];

% Penalties
pwa.u.with('deltaPenalty');
pwa.x.penalty = QuadFunction(diag([500 150]));
pwa.u.penalty = QuadFunction(diag([0.00001 300]));
pwa.u.deltaPenalty = QuadFunction(diag([3000 100]));

% Controller
horizon = 5;
onl_ctrl = MPCController(pwa, horizon);

% Initialization
x0 = [T_amb; 273.15+25];
u0 = [3;0];

% Simulation
Nsim = 400;
simulation_model = pwa;
loop = ClosedLoop(onl_ctrl, simulation_model);
data = loop.simulate(x0, Nsim, 'x.reference', xref, 'u.previous', u0);
```

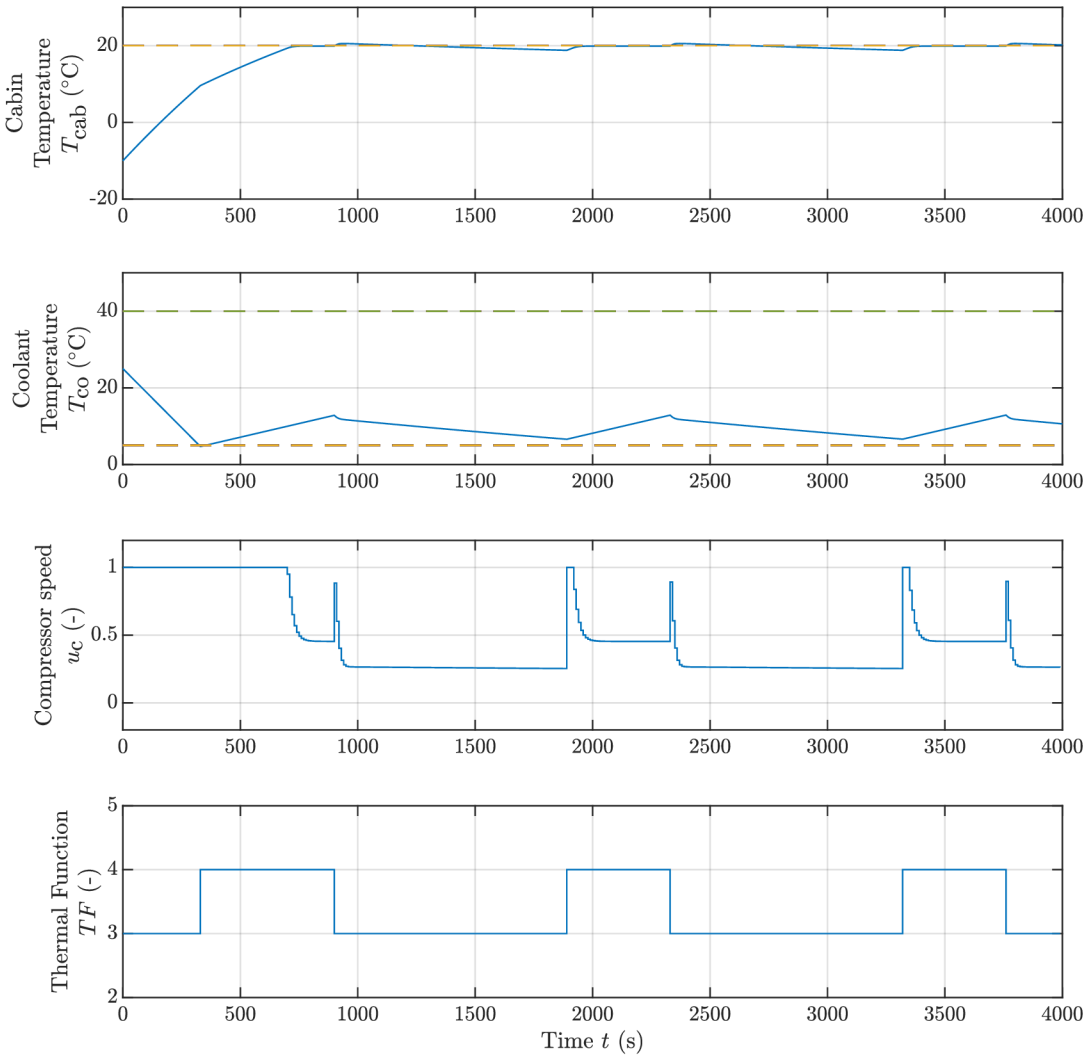

Fig. 5.10: Result of DMPC for simple vehicle cabin for $\dot{Q}_{\mathrm{wh}} = 1000\,\mathrm{W}$ and $T_{\mathrm{amb}} = -10\,^{\circ}\mathrm{C}$

Energy consumption optimality

Since there is a penalty on compressor speed (and not directly on the compressor power consumption), we need to discuss the energy optimality. We divide the discussion into two parts - cabin heat build-up and steady-state heating. The specific values of heat flow rates, power consumption, and COP come from VCRS operating conditions defined within Section 5.3.6.

During cabin heat build-up the compressor will run at maximal speed (to heat the cabin as fast as possible) and thus the resulting penalty of the compressor input

u_c will be maximal for both the TF. The power consumption will be

$$P_{\mathrm{c,co}}^{\max} = 2925\,\mathrm{J\,s^{-1}} \qquad \text{if } TF = 3, \tag{5.134}$$

$$P_{\mathrm{c,amb}}^{\max} = 2310\,\mathrm{J\,s^{-1}} \qquad \text{if } TF = 4 \tag{5.135}$$

and overall heat flow rate into the cabin

$$\dot{Q}_{\mathrm{cond,co}} = 8235\,\mathrm{J\,s^{-1}} \qquad \text{if } TF = 3, \tag{5.136}$$

$$\dot{Q}_{\mathrm{cond,amb}} = 5268\,\mathrm{J\,s^{-1}} \qquad \text{if } TF = 4 \tag{5.137}$$

with

$$COP_{\mathrm{co}} = 2.82, \tag{5.138}$$

$$COP_{\mathrm{amb}} = 2.28. \tag{5.139}$$

It is obvious, that 1 J of heat supplied to the cabin requires 0.35 W s and 0.44 W s of compressor power consumption for $TF = 3$ and $TF = 4$ respectively. Moreover, for $TF = 3$ much higher thermal flow is available and thus faster control error decrease is possible (but limited by the amount of heat removed from coolant).

Thus the value of cost function will be dependent especially on the cabin temperature control error and the MPC will select the TF, which will provide faster control error decrease over the prediction horizon.

During steady-state heating, only heat losses to ambient need to be compensated by heat pump heating. Considering heat losses $\dot{Q}_{\mathrm{loss}} = 1500\,\mathrm{J\,s^{-1}}$, we need the same thermal flow rate $\dot{Q}_{\mathrm{cond}} = \dot{Q}_{\mathrm{loss}}$ from the heat pump to keep the cabin temperature at the defined reference.

During $TF = 3$, the maximal heat flow to cabin is $\dot{Q}_{\mathrm{cond,co}} = 8235\,\mathrm{J\,s^{-1}}$, leading to $u_{\mathrm{c}} = \frac{1500}{8235} = 0.182$ with electric power consumption $P = P_{\mathrm{c,co}}^{\max} u_{\mathrm{c}} = 532.8\,\mathrm{W}$.

During $TF = 4$, the maximal heat flow to cabin is $\dot{Q}_{\mathrm{cond,amb}} = 5268\,\mathrm{J\,s^{-1}}$, leading to $u_{\mathrm{c}} = \frac{1500}{5268} = 0.285$ with electric power consumption $P = P_{\mathrm{c,amb}}^{\max} u_{\mathrm{c}} = 657.7\,\mathrm{W}$.

In general, if we consider the same discharge (high-side, head) pressure and different suction (low-side) pressures (due to different cold reservoir temperatures), we can say that with increasing suction pressure the COP increases too (due to the shape of saturated vapor line). This is quite obvious, for the ideal reversible cycle we can write

$$COP = \frac{T_{\mathrm{H}}}{T_{\mathrm{H}} - T_{\mathrm{C}}}, \tag{5.140}$$

where T_{C} and T_{H} are cold and hot reservoirs temperatures respectively. The difference between temperatures determines the theoretical COP maximum, the smaller the difference, the higher the COP. The pressures are connected with the temperatures of the reservoirs (if we had a heat exchanger of infinite size, the saturated

temperature would be the same as the reservoir temperature, otherwise there would be some thermal gradient). Equation (5.140) does not hold for real systems exactly, but the tendency is the same, as it is shown in Fig. 5.11 (includes isentropic efficiency).

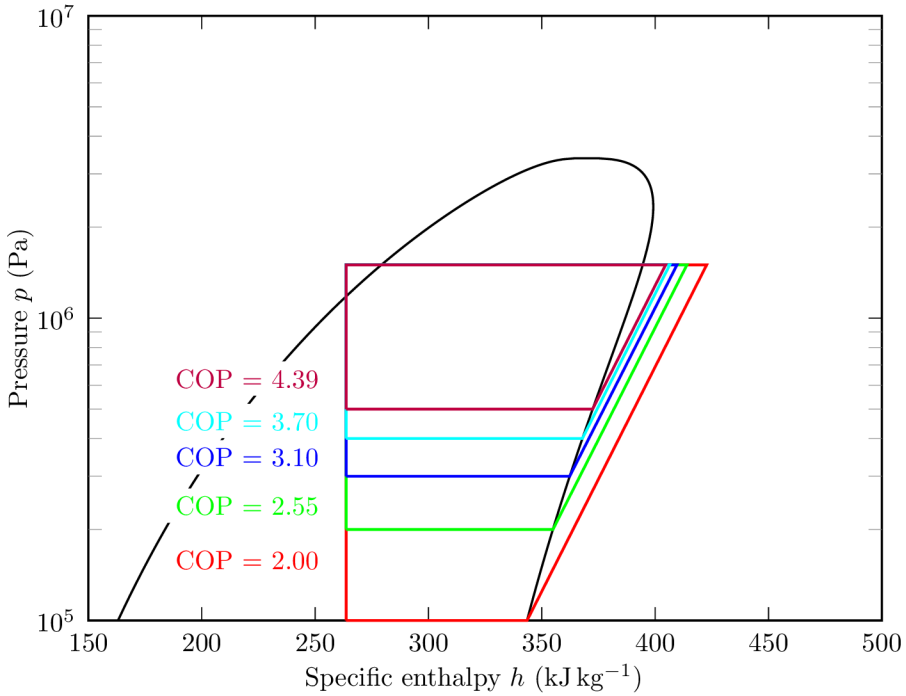

Fig. 5.11: ph diagram for different COP and suction pressures

We can write the current heat flow rate from the condenser as

$$\dot{Q}_{\text{cond}} = \dot{m}\Delta h, \tag{5.141}$$

where $\dot{m}$ is the refrigerant mass flow rate in the condenser and $\Delta h = h_{\text{i}} - h_{\text{o}}$ is condenser specific enthalpy difference with h_{i} and h_{o} being the condenser inlet and outlet specific enthalpy respectively. Now we neglect the changes of Δh (as the changes are negligible compared to mass flow rate changes: 11 % vs 470 % for suction pressures of 1 bar and 5 bar; under constant compressor speed) and we will concentrate on changes within $\dot{m}$

$$\dot{m} = u_{\text{c}} \frac{8000}{60} \rho V \eta_{\text{vol}}. \tag{5.142}$$

Then to keep the heat flow rate from condenser constant, the refrigerant mass flow rate must be also constant and we can write

$$u_{\text{c}} = \frac{1}{\rho} \frac{60\dot{m}}{8000 V \eta_{\text{vol}}} \tag{5.143}$$

and it is obvious that with increasing volumetric mass density ρ (caused by increasing suction pressure) the compressor speed input u_{c} is decreasing.

For minimal compressor speed u_{c} (decreases with increasing suction pressure) the COP is maximal (increases with increasing suction pressure) and thus for defined thermal flow to cabin $\dot{Q}$ the compressor power is

$$P = \frac{\dot{Q}}{COP} \tag{5.144}$$

and the compressor power is minimal for maximal possible COP. Then we can conclude that for the lowest possible compressor speed u_c (required to supply thermal flow rate needed to keep the cabin temperature at the defined reference) the compressor power consumption will be the lowest possible and it is sufficient to penalize the compressor speed in MPC problem formulation to achieve an optimal (minimal) compressor power consumption with sufficient penalty on its speed.

5.3.6 DMPC for FEV VTMS

Overview of a whole VTMS system is in Fig. 2.1 and for this system, there are many possible combinations of binary actuators. So, in this case, the procedure was slightly different from the theoretical procedure described above.

The system was divided into three subsystems - HVAC, HvBat and ED. For each subsystem, several Thermal Functions (TF) were defined to allow the required functionality(Table 5.1). Then compatibility of TFs between subsystems was analyzed and a table of compatible TFs was created. Still there remained a lot of possible combinations (approx. $20-30$), thus we assembled preferred combinations of TF for the subsystems and each combination is called Overall Thermal Function (OTF) and described by a number (124, 211, 224, 373, 463, 511, 524). The first position denotes HVAC TF, the second stands for HvBat TF and the third belongs to ED TF.

Example. *OTF 373 means a combination of HVAC TF3, HvBat TF7, and ED TF3.*

General assumptions for high-level VTMS modeling

1. Heat flow term $\dot{Q}_{\mathrm{loss}}$ contains all the cabin thermal losses (i.e. conductive, convective and ventilation) in simplified form
2. Thermal capacities (C_{x}) stand for generalized thermal capacities of EV parts (e.g. C_{cab} represents the thermal capacity of cabin air, cabin walls, cabin equipment, etc.)
3. Thermal losses (except cabin) are negligible (parts are well insulated)

4. The term $\dot{Q}_{\mathrm{cmpr}}$ stands for heat flow rate generated by the compressor itself (i.e. difference of condenser and evaporator heat flow)
5. The TES is considered as ideal latent heat storage with a melting temperature of 15 °C and a thermal capacity of 1 kW h.
6. The heat flow rate through evaporator consists of sensible and latent heat (air moisture condensation)

$$\dot{Q}_{\mathrm{e}} = \dot{Q}_{\mathrm{s}} + \dot{Q}_{\mathrm{l}}, \tag{5.145}$$

where $\dot{Q}_{\mathrm{e}}$ is evaporator heat flow rate, $\dot{Q}_{\mathrm{s}}$ and $\dot{Q}_{\mathrm{l}}$ are sensible and latent heat flow rates respectively. We define evaporator sensible heat ratio as

$$SHR = \frac{\dot{Q}_{\mathrm{s}}}{\dot{Q}_{\mathrm{e}}} \tag{5.146}$$

and its value depends on evaporator inlet air humidity with typical values $SHR \in \langle 0.4,\ 0.8 \rangle$.

VCRS operating conditions

We consider common parameters of the VCRS system:

- compressor overall efficiency $\eta_{\mathrm{o}} = 0.6$
- compressor volumetric efficiency $\eta_{\mathrm{vol}} = 0.9$
- condenser subcooling $SC = 10\,\mathrm{K}$
- compressor inlet superheat $SH = 0\,\mathrm{K}$

and then we introduce common equations, which are used to compute maximal power, heat flow, and COP values. Compressor outlet isentropic specific enthalpy can be computed as

$$h_{2,\mathrm{ie}} = \mathrm{h}(p_{\mathrm{c}}, \mathrm{s}(p_{\mathrm{e}}, h_1)), \tag{5.147}$$

where p_{c} is condensing pressure, p_{e} is evaporating pressure and h_1 stands for compressor inlet specific enthalpy. Then compressor outlet specific enthalpy is

$$h_2 = h_1 + \frac{h_{2,\mathrm{ie}} - h_1}{\eta_{\mathrm{o}}} \tag{5.148}$$

where overall efficiency

$$\eta_{\mathrm{o}} = \eta_{\mathrm{ie}} \eta_{\mathrm{m}} \eta_{\mathrm{mot}}, \tag{5.149}$$

is a product of isentropic, mechanical and motor efficiencies. The refrigerant mass flow rate through the compressor is

$$\dot{m}_{\mathrm{c}} = \frac{n}{60} \rho_1 V \eta_{\mathrm{vol}}, \tag{5.150}$$

where n (min^{-1}) is compressor speed, ρ_1 represents refrigerant density at the compressor inlet and V stands for compressor displacement. The compressor maximal power can be written as

$$P_{\mathrm{c}}^{\max} = \dot{m}_{\mathrm{c}}^{\max}(h_2 - h_1) \tag{5.151}$$

and coefficient of performance (COP)

$$COP_{\mathrm{c}} = \frac{h_2 - h_3}{h_2 - h_1}, \tag{5.152}$$

$$COP_{\mathrm{h}} = \frac{h_2 - h_1}{h_2 - h_1} \tag{5.153}$$

for cooling and heating respectively. Then maximal heat flow rate through the condenser is

$$\dot{Q}_{\mathrm{cond}}^{\max} = \dot{m}_{\mathrm{c}}^{\max}(h_2 - h_3) = COP_{\mathrm{h}} P_{\mathrm{c}}^{\max} = (COP_{\mathrm{c}} + 1) P_{\mathrm{c}}^{\max} \tag{5.154}$$

and maximal heat flow rate through the evaporator is

$$\dot{Q}_{\mathrm{evap}}^{\max} = \dot{m}_{\mathrm{c}}^{\max}(h_1 - h_3) = COP_{\mathrm{c}} P_{\mathrm{c}}^{\max} = (COP_{\mathrm{h}} - 1) P_{\mathrm{c}}^{\max}. \tag{5.155}$$

Considering the vapor compression refrigeration system (VCRS) circuit in Fig. 2.1 we can find four different VCRS operating conditions. They are distinguished by the combination of heat exchangers (which of them are used as evaporator(s) and condenser(s)) and consequently, there are a different heat sink and heat source temperatures with influence on condensing and evaporating pressures.

The VCRS operating conditions aim to be only samples, it might be useful to define additional conditions with different heat sink and source temperatures. However, the following VCRS conditions are designed to fit the usual application of the VCRS and are sufficient for the demonstration of the proposed approach.

Cooling with ambient air as a heat sink

Tab. 5.3: VCRS operating conditions for cooling with ambient air as a heat sink

Condensing pressure	p_c	$20\,\mathrm{bar}$
Evaporating pressure	p_e	$3.5\,\mathrm{bar}$
Compressor inlet density	ρ_1	$19.5\,\mathrm{kg\,m^{-3}}$
Refrigerant mass flow rate	$\dot{m}_\mathrm{c}$	$0.077\,22\,\mathrm{kg\,s^{-1}}$
Coefficient of performance - cooling	COP_c	1.633
Compressor maximal power	$P_\mathrm{c}^\mathrm{max}$	$3869\,\mathrm{W}$
Condenser maximal heat flow rate	$\dot{Q}_\mathrm{cond}^\mathrm{max}$	$10\,186\,\mathrm{J\,s^{-1}}$
Evaporator maximal heat flow rate	$\dot{Q}_\mathrm{evap}^\mathrm{max}$	$6318\,\mathrm{J\,s^{-1}}$

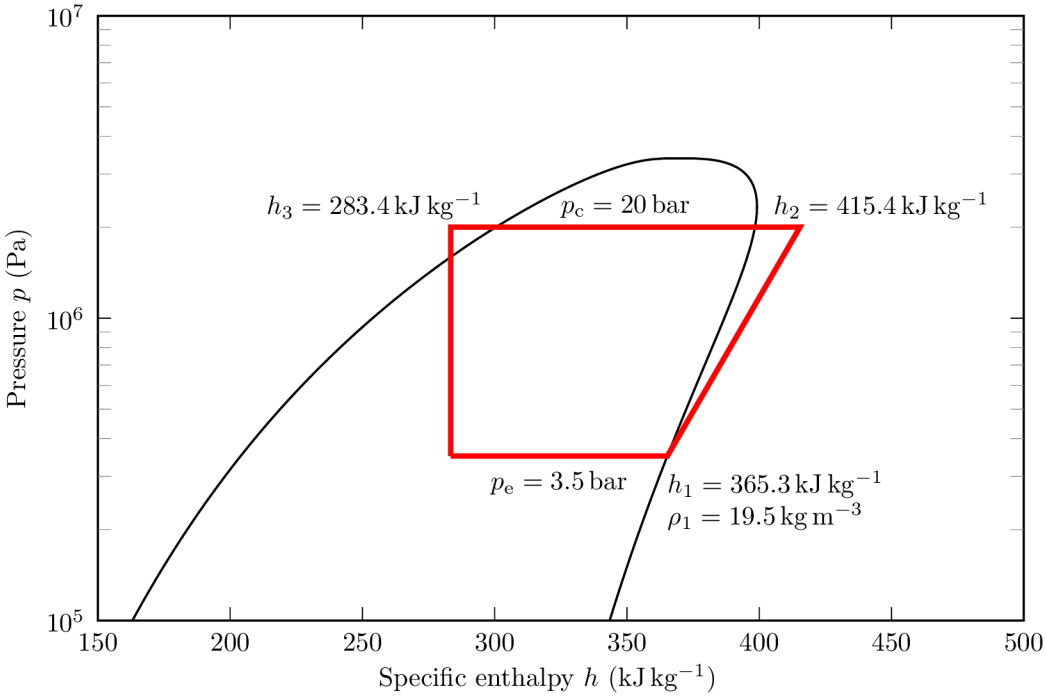

Fig. 5.12: ph diagram for cooling with ambient air as a heat sink

This VCRS mode is active for OTF 511 and OTF 524, so we define

$$COP_{511} = COP_{524} = 1.633, \tag{5.156}$$

$$P_{\mathrm{c},511}^\mathrm{max} = P_{\mathrm{c},524}^\mathrm{max} = 3869\,\mathrm{W} \tag{5.157}$$

for future usage.

Cooling with ambient and TES as heat sinks

Tab. 5.4: VCRS operating conditions for cooling with ambient and TES as heat sinks

Condensing pressure	p_c	13 bar
Evaporating pressure	p_e	3.5 bar
Compressor inlet density	ρ_1	$19.5\,\mathrm{kg\,m^{-3}}$
Refrigerant mass flow rate	$\dot{m}_\mathrm{c}$	$0.077\,22\,\mathrm{kg\,s^{-1}}$
Coefficient of performance - cooling	COP_c	2.864
Compressor maximal power	$P_\mathrm{c}^\mathrm{max}$	2982 W
Condenser maximal heat flow rate	$\dot{Q}_\mathrm{cond}^\mathrm{max}$	$11\,520\,\mathrm{J\,s^{-1}}$
Evaporator maximal heat flow rate	$\dot{Q}_\mathrm{evap}^\mathrm{max}$	$8538\,\mathrm{J\,s^{-1}}$

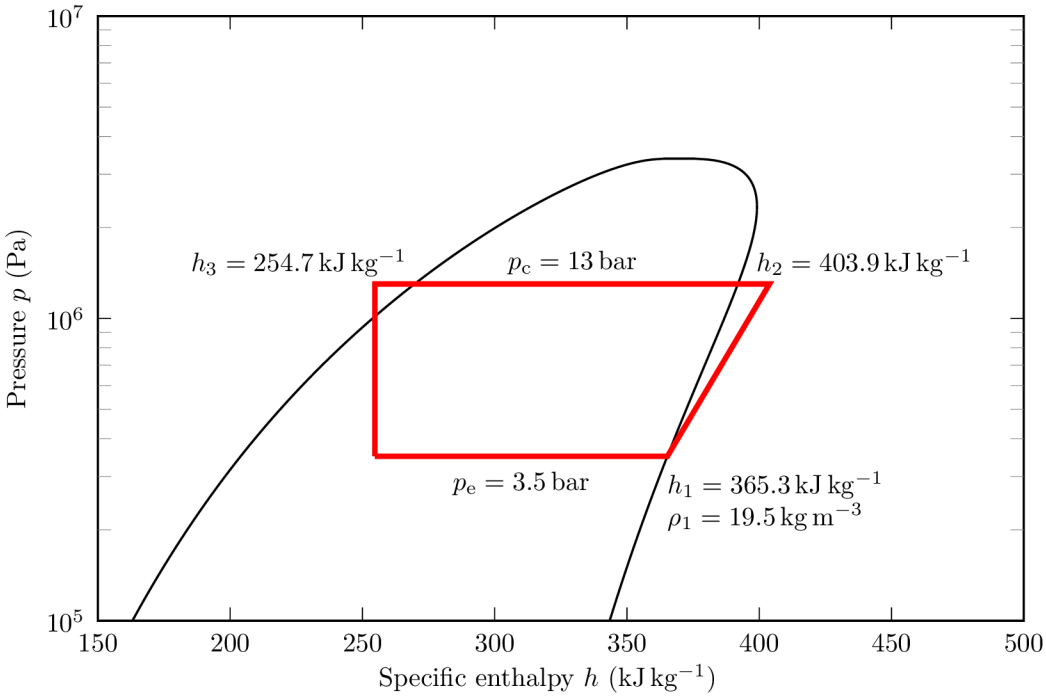

Fig. 5.13: ph diagram for cooling with ambient and TES as heat sinks

This VCRS mode is active for OTF 211 and OTF 224, so we define

$$COP_{211} = COP_{224} = 2.864, \tag{5.158}$$

$$P_{\mathrm{c},211}^\mathrm{max} = P_{\mathrm{c},224}^\mathrm{max} = 2982\,\mathrm{W} \tag{5.159}$$

for future usage.

Heating with ambient air as a heat source

Tab. 5.5: VCRS operating conditions for heating with ambient air as a heat source

Condensing pressure	p_c	15 bar
Evaporating pressure	p_e	1.5 bar
Compressor inlet density	ρ_1	$8.659\,\mathrm{kg\,m^{-3}}$
Refrigerant mass flow rate	$\dot{m}_\mathrm{c}$	$0.034\,29\,\mathrm{kg\,s^{-1}}$
Coefficient of performance - heating	COP_h	2.28
Compressor maximal power	$P_\mathrm{c}^\mathrm{max}$	2310 W
Condenser maximal heat flow rate	$\dot{Q}_\mathrm{cond}^\mathrm{max}$	$5268\,\mathrm{J\,s^{-1}}$
Evaporator maximal heat flow rate	$\dot{Q}_\mathrm{evap}^\mathrm{max}$	$2958\,\mathrm{J\,s^{-1}}$

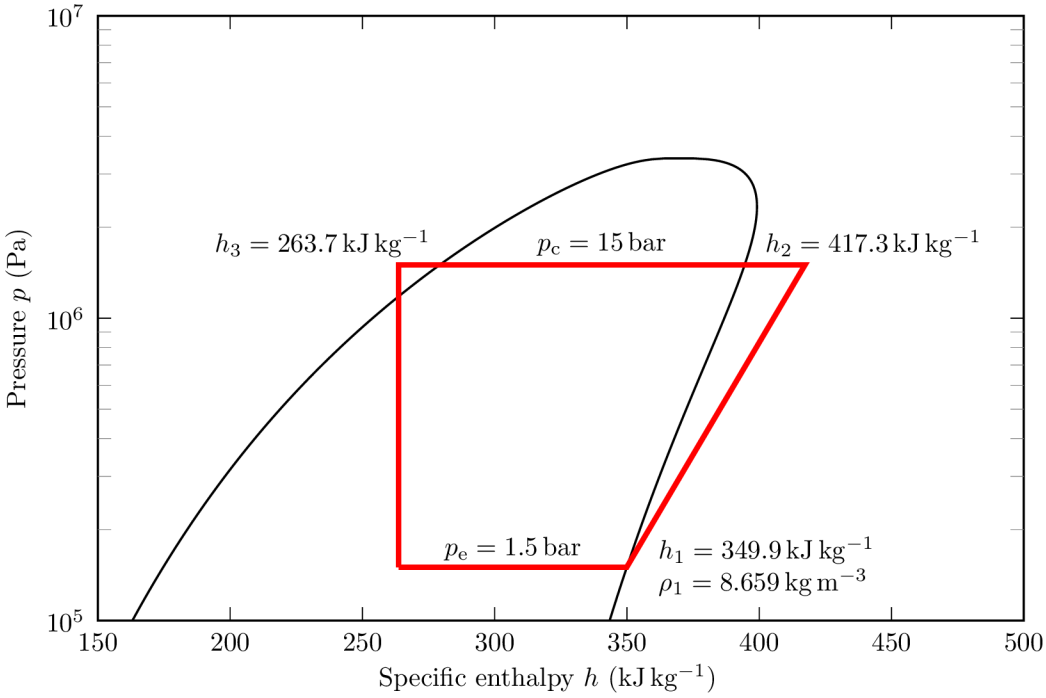

Fig. 5.14: ph diagram for heating with ambient air as a heat source

This VCRS mode is active for OTF 463, thus we can write

$$COP_{463} = 2.28, \tag{5.160}$$

$$P_{\mathrm{c},463}^\mathrm{max} = 2310\,\mathrm{W}. \tag{5.161}$$

Heating with coolant as a heat source

Tab. 5.6: VCRS operating conditions for heating with ambient air as a heat source

Condensing pressure	p_c	$15\,\mathrm{bar}$
Evaporating pressure	p_e	$2.5\,\mathrm{bar}$
Compressor inlet density	ρ_1	$14.1\,\mathrm{kg\,m^{-3}}$
Refrigerant mass flow rate	$\dot{m}_\mathrm{c}$	$0.055\,78\,\mathrm{kg\,s^{-1}}$
Coefficient of performance - heating	COP_h	2.816
Compressor maximal power	$P_\mathrm{c}^\mathrm{max}$	$2925\,\mathrm{W}$
Condenser maximal heat flow rate	$\dot{Q}_\mathrm{cond}^\mathrm{max}$	$8235\,\mathrm{J\,s^{-1}}$
Evaporator maximal heat flow rate	$\dot{Q}_\mathrm{evap}^\mathrm{max}$	$5311\,\mathrm{J\,s^{-1}}$

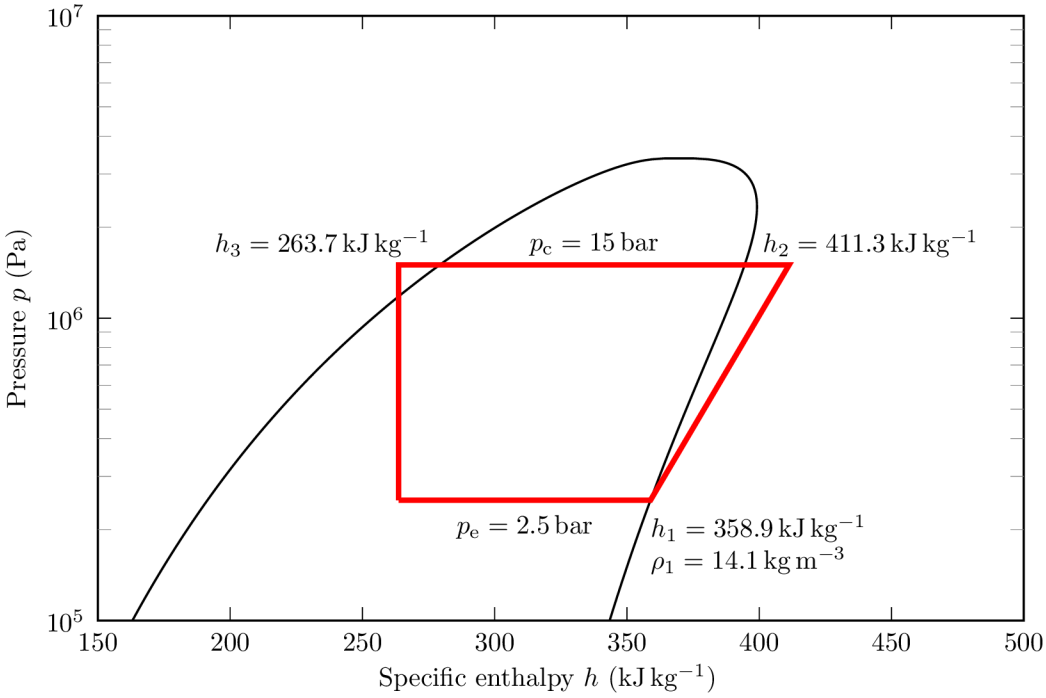

Fig. 5.15: ph diagram for heating with coolant as a heat source

This VCRS mode is active for OTF 373, thus we can write

$$COP_{373} = 2.816, \tag{5.162}$$

$$P_{\mathrm{c},373}^\mathrm{max} = 2925\,\mathrm{W}. \tag{5.163}$$

VTMS PWA model

The PWA model of VTMS energy flows was assembled in a general form as shown in Fig. 5.16 and it can be described by following set of equations

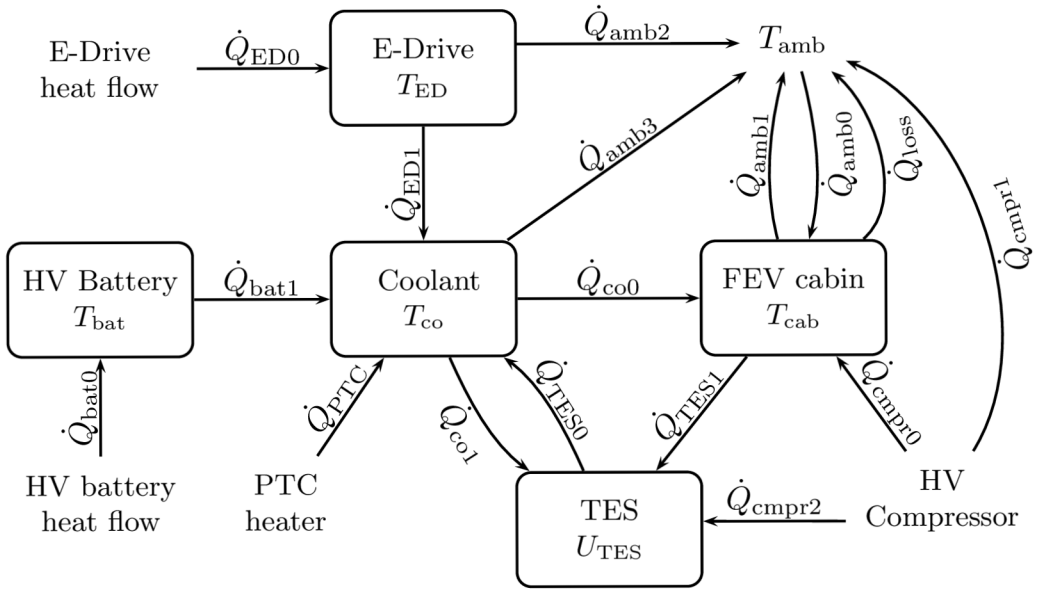

Fig. 5.16: Diagram of FEV simplified heat flows

$$C_{\mathrm{cab}}\frac{\mathrm{d}T_{\mathrm{cab}}}{\mathrm{d}t} = \dot{Q}_{\mathrm{amb0}} - \dot{Q}_{\mathrm{loss}} - \dot{Q}_{\mathrm{amb1}} + \dot{Q}_{\mathrm{cmpr0}} - \dot{Q}_{\mathrm{TES1}} + \dot{Q}_{\mathrm{co0}}, \tag{5.164}$$

$$C_{\mathrm{co}}\frac{\mathrm{d}T_{\mathrm{co}}}{\mathrm{d}t} = -\dot{Q}_{\mathrm{co0}} + \dot{Q}_{\mathrm{TES0}} - \dot{Q}_{\mathrm{co1}} + \dot{Q}_{\mathrm{PTC}} - \dot{Q}_{\mathrm{amb3}} + \dot{Q}_{\mathrm{ED1}} + \dot{Q}_{\mathrm{bat1}}, \tag{5.165}$$

$$C_{\mathrm{bat}}\frac{\mathrm{d}T_{\mathrm{bat}}}{\mathrm{d}t} = \dot{Q}_{\mathrm{bat0}} - \dot{Q}_{\mathrm{bat1}}, \tag{5.166}$$

$$C_{\mathrm{ED}}\frac{\mathrm{d}T_{\mathrm{ED}}}{\mathrm{d}t} = \dot{Q}_{\mathrm{ED0}} - \dot{Q}_{\mathrm{ED1}} - \dot{Q}_{\mathrm{amb2}}, \tag{5.167}$$

$$\frac{\mathrm{d}U_{\mathrm{TES}}}{\mathrm{d}t} = \dot{Q}_{\mathrm{TES1}} - \dot{Q}_{\mathrm{TES0}} + \dot{Q}_{\mathrm{co1}} + \dot{Q}_{\mathrm{cmpr2}}, \tag{5.168}$$

$$\frac{\mathrm{d}T_{\mathrm{amb}}}{\mathrm{d}t} = 0, \tag{5.169}$$

$$y_{\mathrm{cab}} = T_{\mathrm{cab}}, \tag{5.170}$$

$$y_{\mathrm{bat}} = T_{\mathrm{bat}}, \tag{5.171}$$

which can be simplified for each OTF, discretized and written in state-space form

$$\mathbf{x}^*_{k+1} = \mathbf{A}\mathbf{x}^*_k + \mathbf{B}^*\bar{\mathbf{u}}_k + \mathbf{f}^{\mathrm{c}}, \tag{5.172}$$

$$\mathbf{y}^*_k = \mathbf{C}\mathbf{x}^*_k + \mathbf{D}^*\bar{\mathbf{u}}_k + \mathbf{g}^{\mathrm{c}}, \tag{5.173}$$

where

$$\mathbf{x}^* = \begin{bmatrix} T_{\text{cab}} & T_{\text{co}} & T_{\text{bat}} & T_{\text{ED}} & U_{\text{TES}} & T_{\text{amb}} \end{bmatrix}^\intercal, \tag{5.174}$$

$$\bar{\mathbf{u}} = \begin{bmatrix} OTF & u_{\text{cmpr}} & u_{\text{hf}} & u_{\text{cc}} & u_{\text{cb}} & u_{\text{ptc}} \end{bmatrix}^\intercal, \tag{5.175}$$

$$\mathbf{y}^* = \begin{bmatrix} y_{\text{cab}} & y_{\text{bat}} \end{bmatrix}^\intercal. \tag{5.176}$$

For each operating mode (represented by OTF) a dynamic affine model with the common state, input, and output vector is being formulated by omitting and expressing the thermal flows taken from the general PWA model. The single OTF models are shown in Appendix G. The models are assembled in a continuous-time domain and then discretized (not shown within this text).

Here we remind that the PWA model does not aspire to be the exact representation of VTMS, it only serves as a high-level approximation for decision purposes. Also, the control vector obtained from the MPC controller should be discarded except the OTF indicator and the actuators need to be controlled by another set of low-level algorithms in the final implementation.

MPTDC implementation

MPTDC algorithms were tested only in simulations, as the demonstration vehicle was not finished. MPT toolbox [65] in combination with MATLAB and Simulink was used for hybrid MPC controller design, simulations and code generation. Also, Hybrid Toolbox [66] provides similar features and could be used for this purpose.

Firstly, Model in the Loop (MIL) simulations were performed with controllers in both the implicit and explicit form. MIL simulations were convenient in the early stages of controller development due to the fast cycle of deployment and verification.

Secondly, Software in the Loop (SIL) simulations were executed employing the generated C code of MPC controller in explicit form. This simulation was performed in MATLAB/Simulink environment.

Finally, the MPC algorithms were verified in Processor in the Loop (PIL) simulation. The generated code of controller was implemented into the Infineon AURIX Tricore TC299TF microcontroller unit (MCU), placed on AURIX Starter Kit TC299. The MCU contains three cores running at 300 MHz, 8 MB FLASH (4x2 MB) and 728 kB RAM. Due to FLASH memory limitation, it was possible to implement an MPC controller with a prediction horizon up to $N = 3$. It should not be an issue to prolong the prediction horizon with specifically designed PCB incorporating MCU and a bigger amount of FLASH memory.

There might be also some possibility of improvements in terms of exported code size and future research could improve the usability of this approach. Moreover, it could be feasible to run the optimization in real-time (implicit or online MPC),

which is not covered in this work. Successful MCU implementation of the B&B algorithm was reported in [67], thus real-time decision algorithm could also be the possible direction in this field.

For the demonstration, three results of MIL simulation and one PIL simulation result were selected. In Fig. 5.17 there is a result of MPTDC simulation under winter condition with charged TES. The MPC algorithm selects the appropriate OTF based on constraints and references compliance. For the first approximately 2200 s, the OTF 373 is selected and waste heat and TES are fully utilized. After exhaustion of TES, the system switches between OTF 373e and 463, waste heat recovery function and heating with ambient air as heat source respectively.

The second example (Fig. 5.18) shows MPTDC decisions under hot (summer) conditions with empty TES. In the first 400 s, the OTF 221 is selected (cabin cooling with AC with ambient and TES as a heat sink, HV Battery cooled passively by ambient air). Then switching to other OTFs occurs (based on HV Battery temperature and TES status), the reasons for switching sequences are evident.

The third simulation results in Fig. 5.19 represents MPTDC under mild conditions. Firstly, the cabin is cooled by the AC system to defined temperature reference and then it is sufficient to cool the cabin by ambient air (without AC system). Here we point out the model of OTF 124 and its submodes in Appendix G.

The last result in Fig. 5.20 comes from MPTDC PIL simulation under winter condition. The result is slightly different compared to the MIL simulation under winter condition (Fig. 5.17). The inconsistency is caused by shorter prediction horizon ($N = 3$ vs $N = 5$) and other minor changes due to precision (single vs double) etc. However the overall performance is very similar - the TES and waste heat are fully utilized, thus the decisions are near to optimal.

It is noticeable that the PTC heater is occasionally requested to support the cabin heating by adding some heat to the coolant (power of up to 200 W). This helps to keep the system in the waste heat recovery mode (OTF 373 or 373e) and thus the overall power consumption is lower, than if the system falls into heat pump mode with ambient air as a heat source.

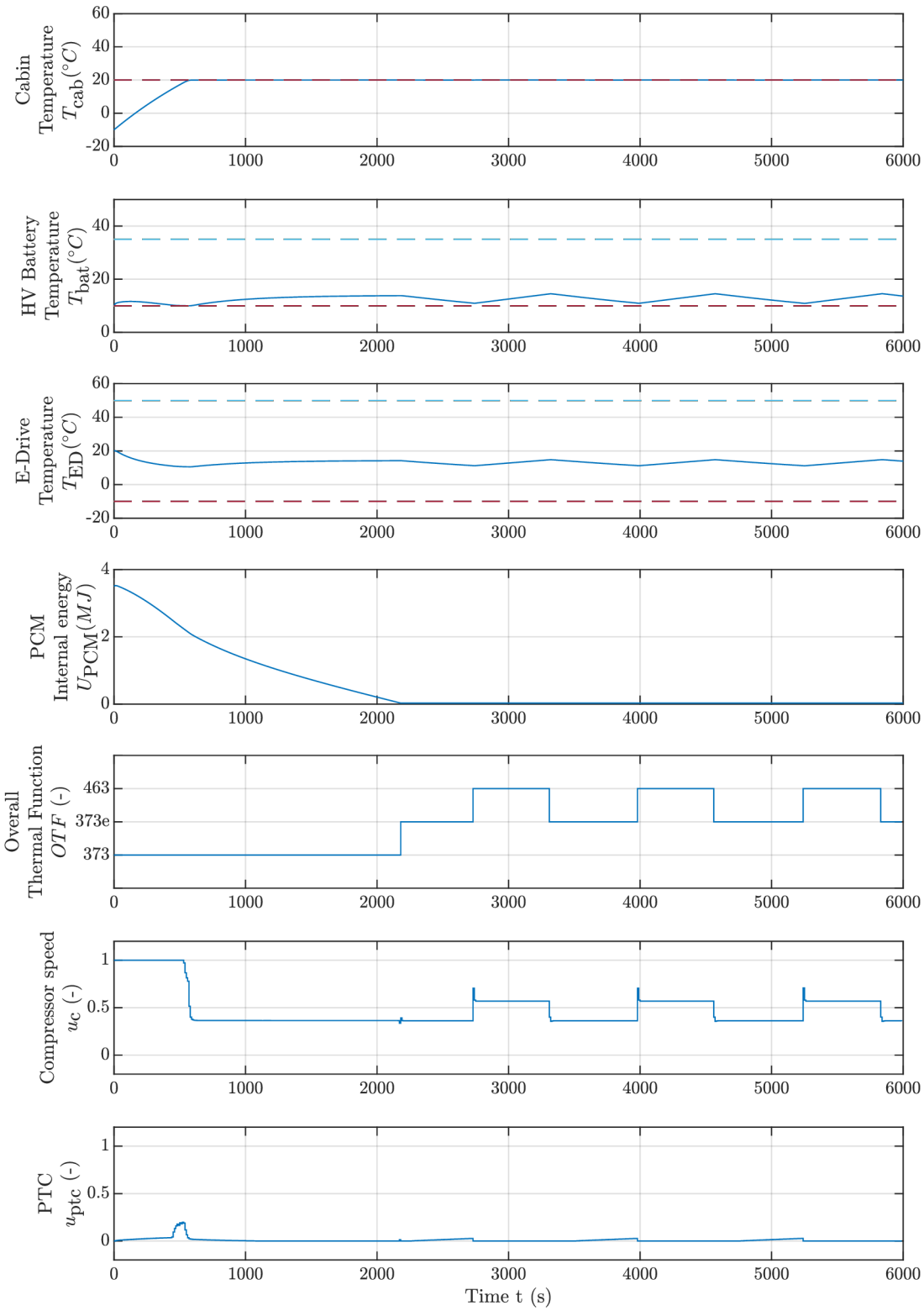

Fig. 5.17: MPTDC MIL simulation under winter condition with $T_{amb} = -10\,°C$, $\dot{Q}_{ED0} = 600\,W$ and $\dot{Q}_{bat0} = 400\,W$

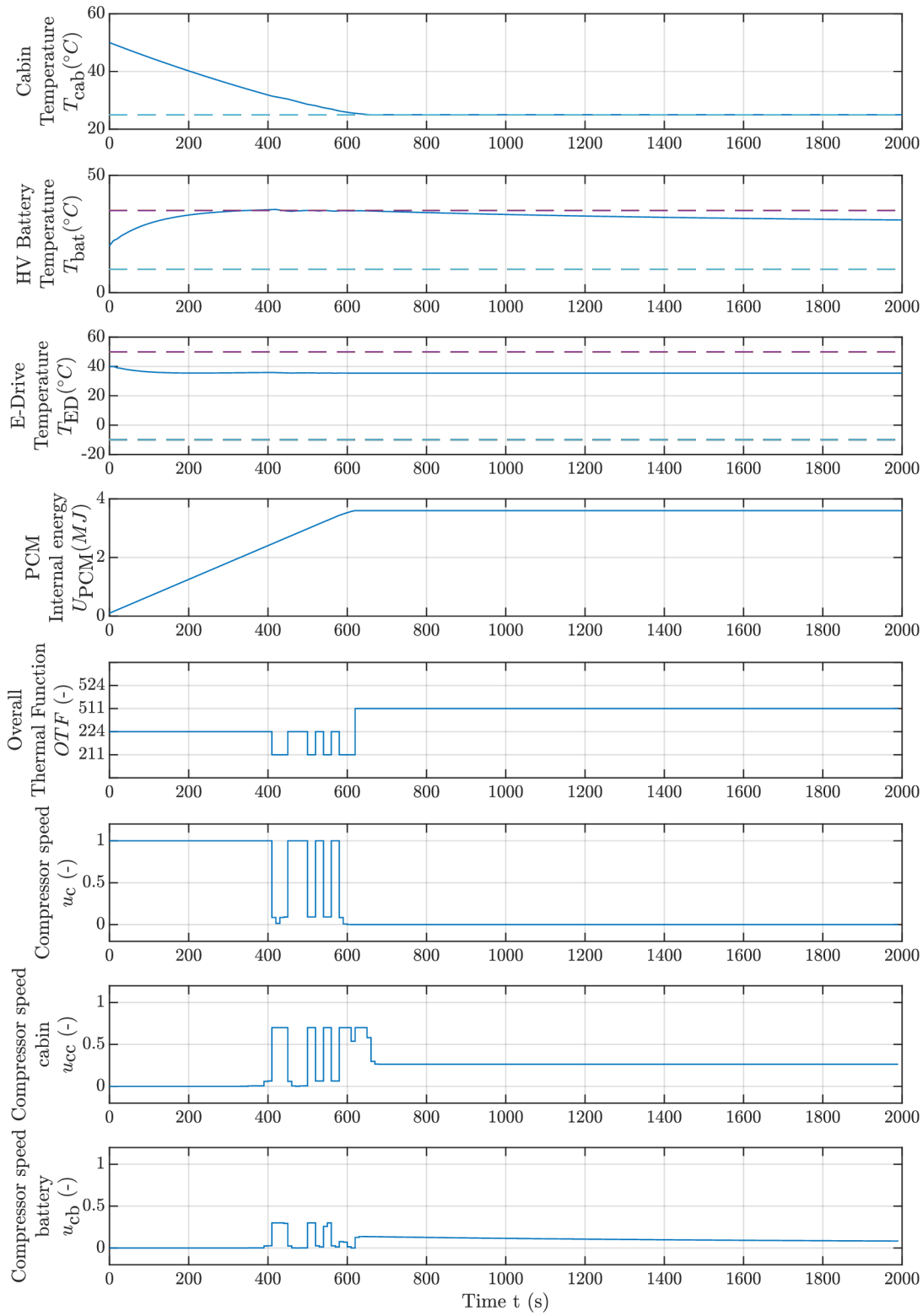

Fig. 5.18: MPTDC MIL simulation under summer condition with $T_{amb} = 35\,°C$, $\dot{Q}_{ED0} = 600\,W$ and $\dot{Q}_{bat0} = 400\,W$

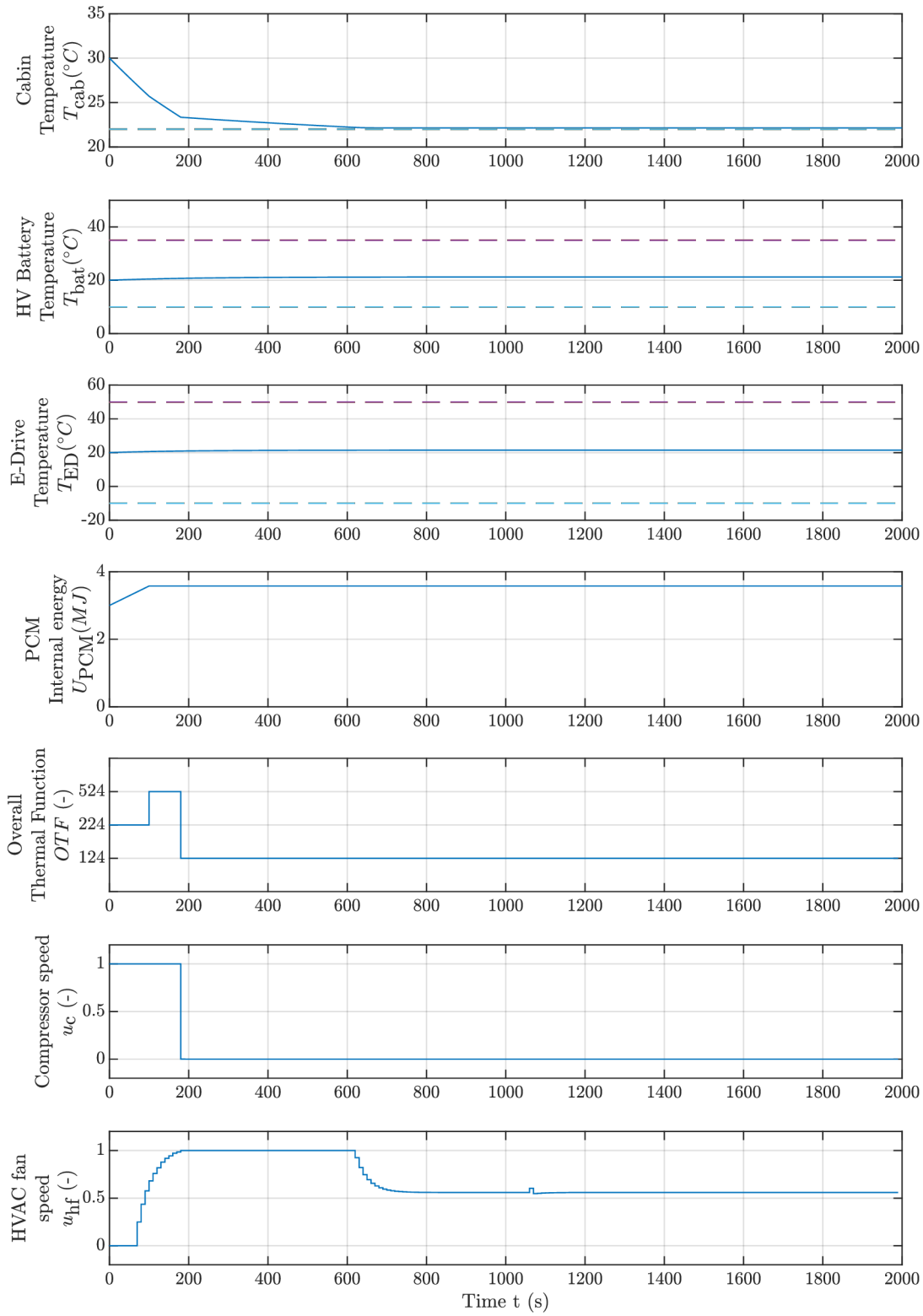

Fig. 5.19: MPTDC MIL simulation under mild condition with $T_{amb} = 20\,°C$, $\dot{Q}_{ED0} = 600\,W$ and $\dot{Q}_{bat0} = 400\,W$

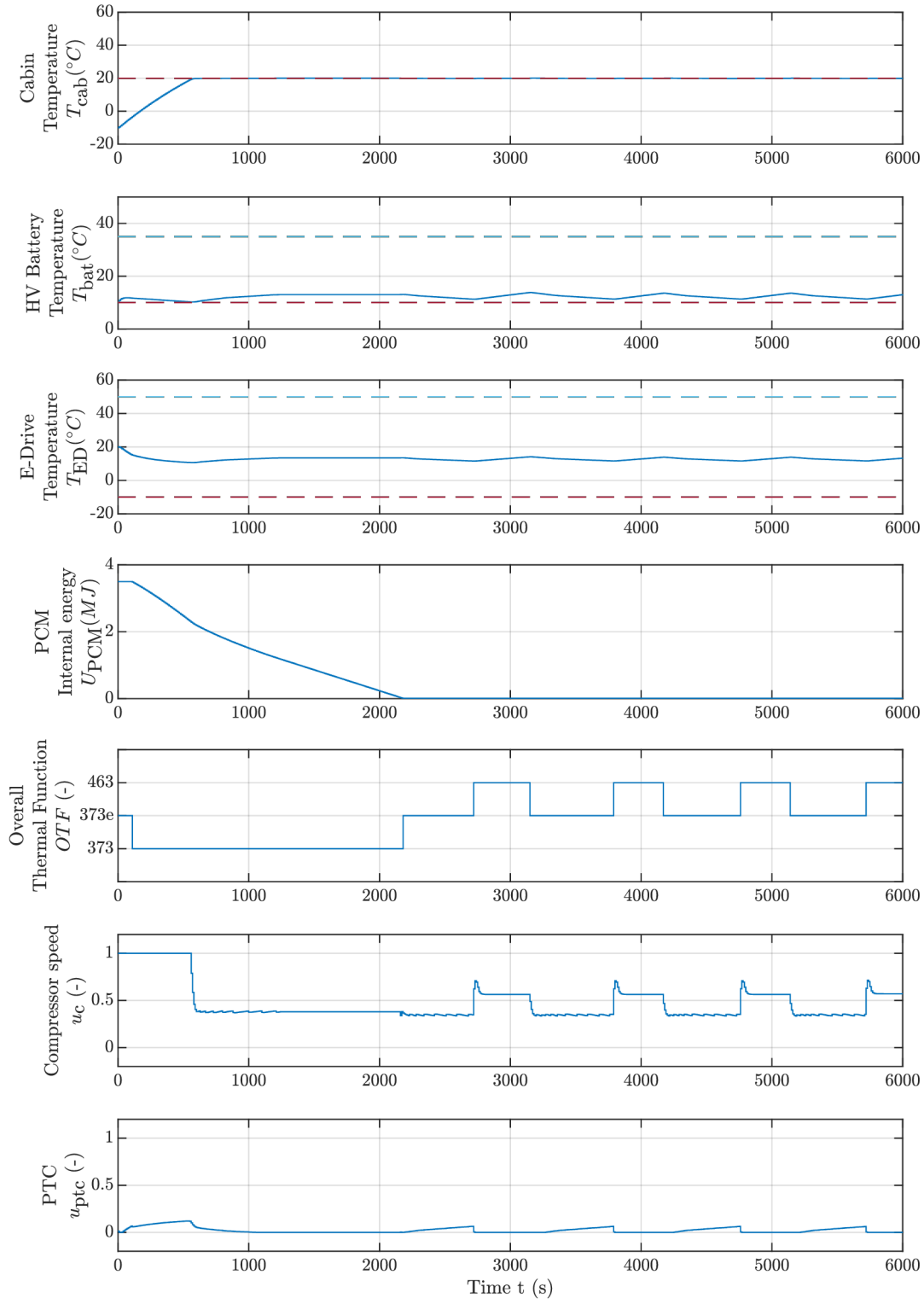

Fig. 5.20: MPTDC PIL simulation under winter condition with $T_{amb} = -10\,°C$, $\dot{Q}_{ED0} = 600\,W$ and $\dot{Q}_{bat0} = 400\,W$

6 Algorithms implementation and developed tools

This chapter describes the implementation of control algorithms and developed tools, which support the main parts of this work.

6.1 TEMCU software implementation

Erika Enterprise RTOS is used as an operating system for TEMCU. It is an open-source hard real-time operating system (RTOS), which was certified as OSEK/VDX compliant for use with Infineon AURIX [68]. Erika instance configuration is realized using an OIL configuration file (which uses OIL language standardized by OSEK/VDX consortium). In that file, tasks, events, and alarms are defined (and it also contains other RTOS settings). The OIL file was created for the implementation of TEMCU and its functionalities.

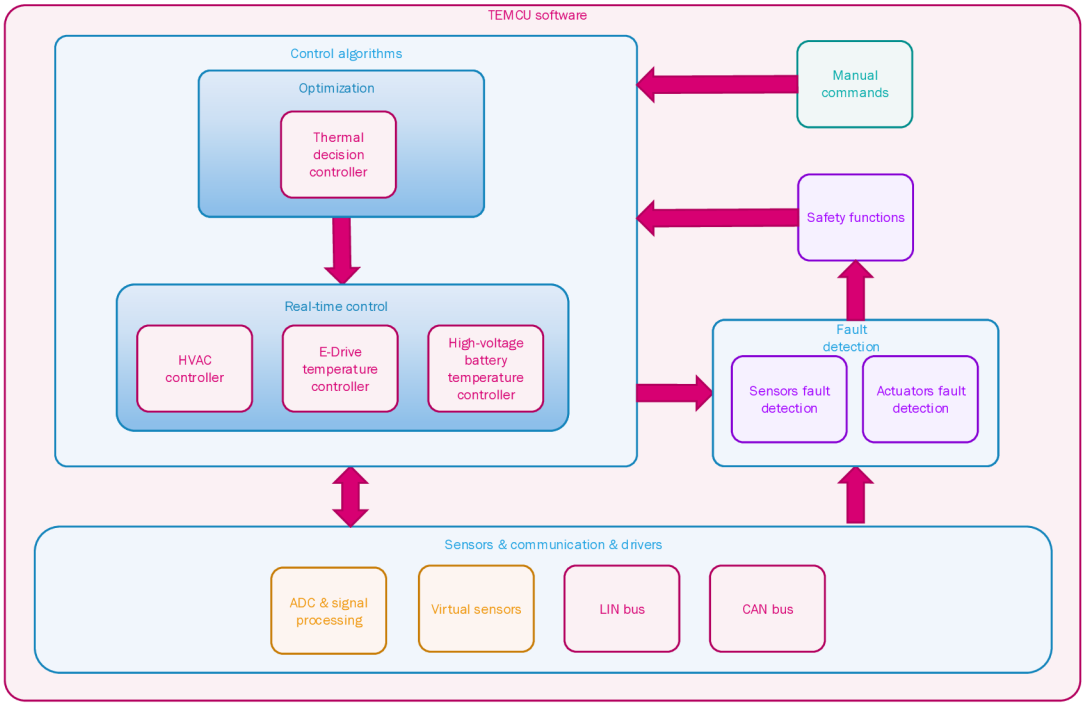

Fig. 6.1: TEMCU SW overview

In Figure 6.1, an overview of the TEMCU software structure is presented. Every block stands for a separate task of OS (eventually multiple tasks).

To allow error-free data sharing between TEMCU tasks, non-virtual buses were defined in MATLAB Simulink. This approach forces the generated code to use structures as block interfaces with a one-to-one mapping to the defined buses. That enables automatic signal name and data type checking in MATLAB Simulink and quite a comfortable and understandable interface for non-MATLAB parts of TEMCU code. The buses are defined in MATLAB Data Dictionary and after code generation, the bus-structure definition is placed to an automatically generated header file. Afterward, it can be used by other parts of the TEMCU code. This approach minimizes the possibility of code errors and substantially improves the readability of both the generated and manually-written code.

6.2 Matlab VCRS support

A utility called RefToolbox for MATLAB/Simulink was developed to enable the preparation of lookup tables and visualization of refrigeration states and properties. RefToolbox is based on CoolProp [23] and the communication is realized using its Python interface. The example of the RefToolbox screen is shown in Fig. 6.2, this

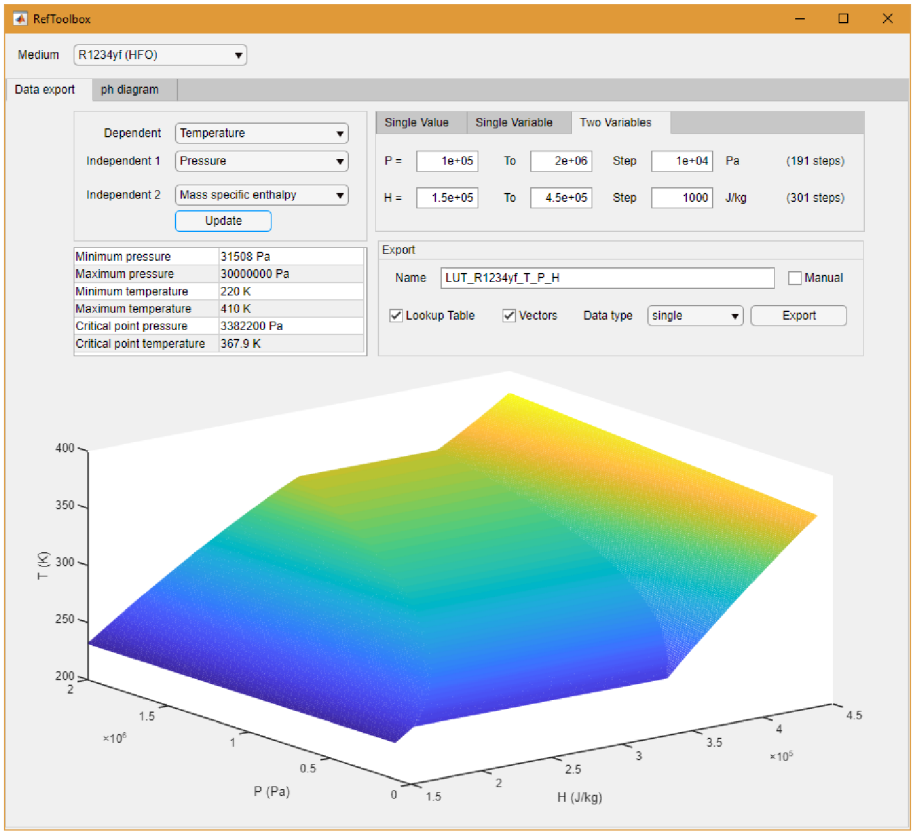

Fig. 6.2: RefToolbox for MATLAB/Simulink

part of the tool provides visualization of refrigerant state properties and allows the export of the lookup table.

The second main part of RefToolbox is intended for the export of the ph diagram into a MATLAB figure or general graphic file. A ph diagram is a very useful tool for analysis and control of VCRS. Since all the TEMCU control algorithms, as well as TEMCU GUI, were developed in MATLAB/Simulink, it was beneficial to enable ph diagram drawing under this environment.

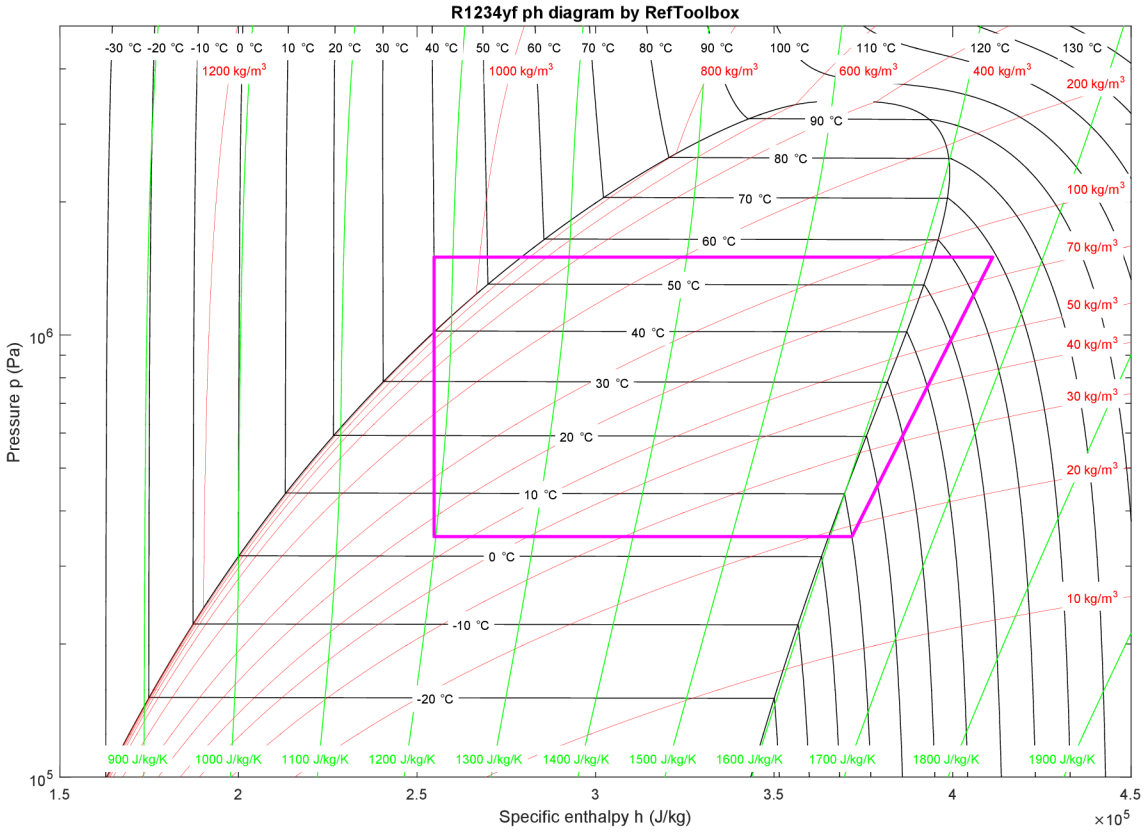

Fig. 6.3: MATLAB/Simulink ph diagram example

An example of a ph diagram printed in MATLAB/Simulink is in Fig. 6.3. The ph diagram tool supports different refrigerants (tested for R1234yf, R744 and R134a), allows cycle shape update during simulation or measurement and can be used with different input data (pressure and enthalpy/subcooling & superheat/refrigerant temperatures).

6.3 Virtual sensors

6.3.1 Thermal energy storage status estimator

The thermal energy storage (TES) is based on phase change material (PCM). This technology uses latent heat for storing thermal energy. Since the temperature is constant during the phase change (see Fig. 6.4), the temperature sensor does not provide enough information about the current TES state of charge. TES status estimator was developed to allow TES status monitoring and decisions making based on its status.

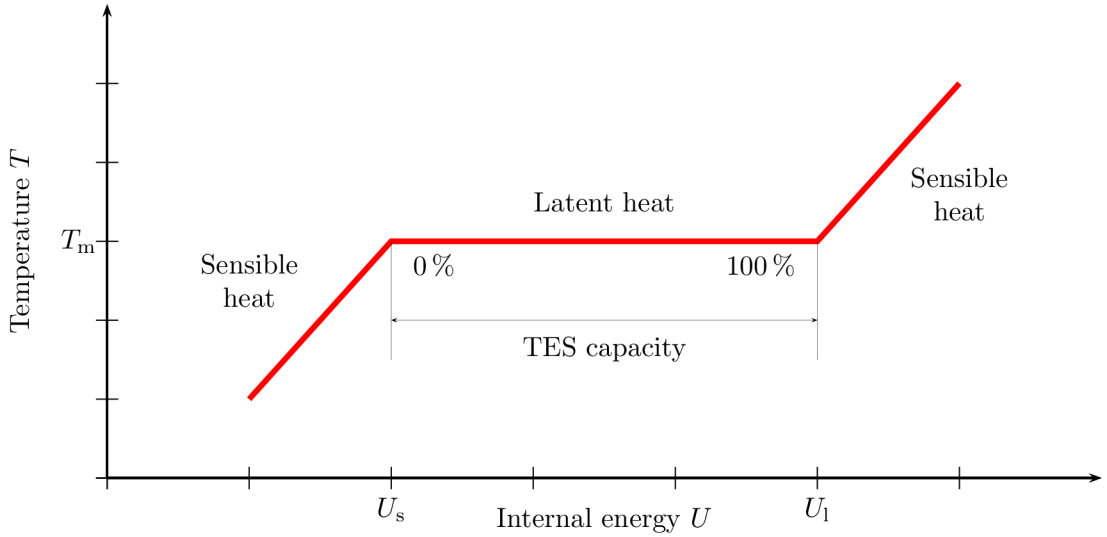

Fig. 6.4: TES temperature dependency on internal energy

In Fig. 6.4 there is a dependency of TES temperature on its internal energy. The heat storage capacity is based on latent heat of fusion (also known as enthalpy of fusion)

$$Q_\mathrm{L} = mL, \tag{6.1}$$

the sensible heat

$$Q_\mathrm{s} = mc\Delta T \tag{6.2}$$

does not significantly influence the capacity. Q_L and Q_s denote the latent and sensible heat, m is the TES mass, L stands for specific latent heat. c stands for specific heat capacity and ΔT is the temperature difference.

If the TES was based on water (only for an example), the specific latent heat would be $334\,\mathrm{kJ\,kg^{-1}}$ and the specific heat capacity would be $4.1855\,\mathrm{kJ\,kg^{-1}\,K^{-1}}$. Then it is evident that the same energy can be stored in latent heat of fusion or

sensible heat with a temperature difference of 80 K. This value is quite high and practically hard to achieve, thus it is preferable to employ primarily the latent heat.

The TES status estimator equations are based on (E.17) and the heat flow rate is summarized by time. We define current TES status as

$$S(k) = \frac{U(k) - U_\mathrm{s}}{mL}, \tag{6.3}$$

where $U(k)$ is current TES internal energy and U_s is TES internal energy in solid state at fusion start (index s stands for solid). For current internal energy $U(k)$ of TES we can write

$$U(k) = U(0) + \sum_{j=1}^{k-1} T_\mathrm{s}\dot{Q}, \tag{6.4}$$

$$U(k) = U(0) + \sum_{j=1}^{k-1} T_\mathrm{s}\dot{m}(j)c_p\left[T_\mathrm{in}(j) - T_\mathrm{out}(j)\right] \tag{6.5}$$

and after substituting into (6.3) we get

$$S(k) = \frac{U(0) + \sum_{j=1}^{k-1} T_\mathrm{s}\dot{m}(j)c_p\left[T_\mathrm{in}(j) - T_\mathrm{out}(j)\right] - U_\mathrm{s}}{mL}, \tag{6.6}$$

which can be rewritten using $\frac{U(0)-U_\mathrm{s}}{mL} = S(0)$ as

$$S(k) = S(0) + \frac{\sum_{j=1}^{k-1} T_\mathrm{s}\dot{m}(j)c_p\left[T_\mathrm{in}(j) - T_\mathrm{out}(j)\right]}{mL}. \tag{6.7}$$

Then we add the equations for fully charged and discharged TES and the resulting equation is

$$S(k) = \begin{cases} 0 & \text{if } T_\mathrm{hs} < T_\mathrm{m} \\ S(0) + \frac{c_\mathrm{p}}{mL}\sum_{j=1}^{k-1} T_\mathrm{s}\dot{m}(j)\left[T_\mathrm{in}(j) - T_\mathrm{out}(j)\right] & \text{if } T_\mathrm{hs} = T_\mathrm{m} \\ 100 & \text{if } T_\mathrm{hs} > T_\mathrm{m} \end{cases}, \tag{6.8}$$

where T_m is TES melting temperature. As the TES virtual sensor algorithm is expected to be implemented and triggered in TEMCU, it was necessary to adjust the algorithm to fit the real-time computation requirements. Specifically, the sum in (6.8) was changed to incremental expression and thus the sum is not evaluated in every algorithm step, only the increment of the stored heat is calculated and added

$$S(k) = \begin{cases} 0 & \text{if } T_\mathrm{hs} < T_\mathrm{m} \\ S(k-1) + \frac{T_\mathrm{s}\dot{m}(k-1)c_\mathrm{p}[T_\mathrm{in}(k-1) - T_\mathrm{out}(k-1)]}{mL} & \text{if } T_\mathrm{hs} = T_\mathrm{m} \\ 100 & \text{if } T_\mathrm{hs} > T_\mathrm{m} \end{cases}. \tag{6.9}$$

The TES status estimator algorithm is suitable for the estimation of heat stored in TES heat storage. Nevertheless, the algorithm has some constraints and disadvantages. Firstly, the algorithm starting state needs to be defined. This means that it needs to be started from a fully charged or fully discharged condition, or it needs to have information from previous estimations. Secondly, the algorithm precision depends on accurate knowledge of coolant mass flow rate $\dot{m}$. In laboratory conditions, it can be measured, but in real vehicle operation, it has to be guessed based on coolant pump speed and combination of coolant shut-off valves.

6.3.2 Superheat and subcooling virtual sensors

Superheat and subcooling are quantities (see Fig. 6.5), which can not be directly measured. Thus a virtual sensor was developed to allow superheat and subcooling measurement. The superheat (usually at evaporator outlet or compressor suction) is defined as a difference of refrigerant temperature and saturated temperature for defined pressure.

We define refrigerant saturated temperature as

$$\mathrm{T}_{\mathrm{sat}}(p) = \mathrm{T}(p, \xi), \tag{6.10}$$

where $T_{\mathrm{sat}}(p)$ denotes saturated temperature for defined pressure, $\mathrm{T}(p, \xi)$ stands for a function returning temperature based on pressure and quality, p is refrigerant pressure and ξ is refrigerant vapor quality in interval $\langle 0; 1 \rangle$.

Then we can compute superheat (SH) as

$$SH = T_{\mathrm{ref}} - \mathrm{T}_{\mathrm{sat}}(p), \tag{6.11}$$

$$SH = T_{\mathrm{ref}} - \mathrm{T}(p, \xi), \tag{6.12}$$

$$SH = T_{\mathrm{ref}} - \mathrm{T}(p, 1), \tag{6.13}$$

where T_{ref} denotes the measured refrigerant temperature.

Analogously the subcooling (SC) is possible. We recall saturated temperature from (6.10) and computation is similar to SH

$$SC = \mathrm{T}_{\mathrm{sat}}(p) - T_{\mathrm{ref}}, \tag{6.14}$$

$$SC = \mathrm{T}(p, \xi) - T_{ref}, \tag{6.15}$$

$$SC = \mathrm{T}(p, 0) - T_{ref}. \tag{6.16}$$

6.3.3 Compressor refrigerant mass flow rate virtual sensor

The measurement of the mass flow rate through the compressor is useful for EXV control and computations of performance, COP, etc.

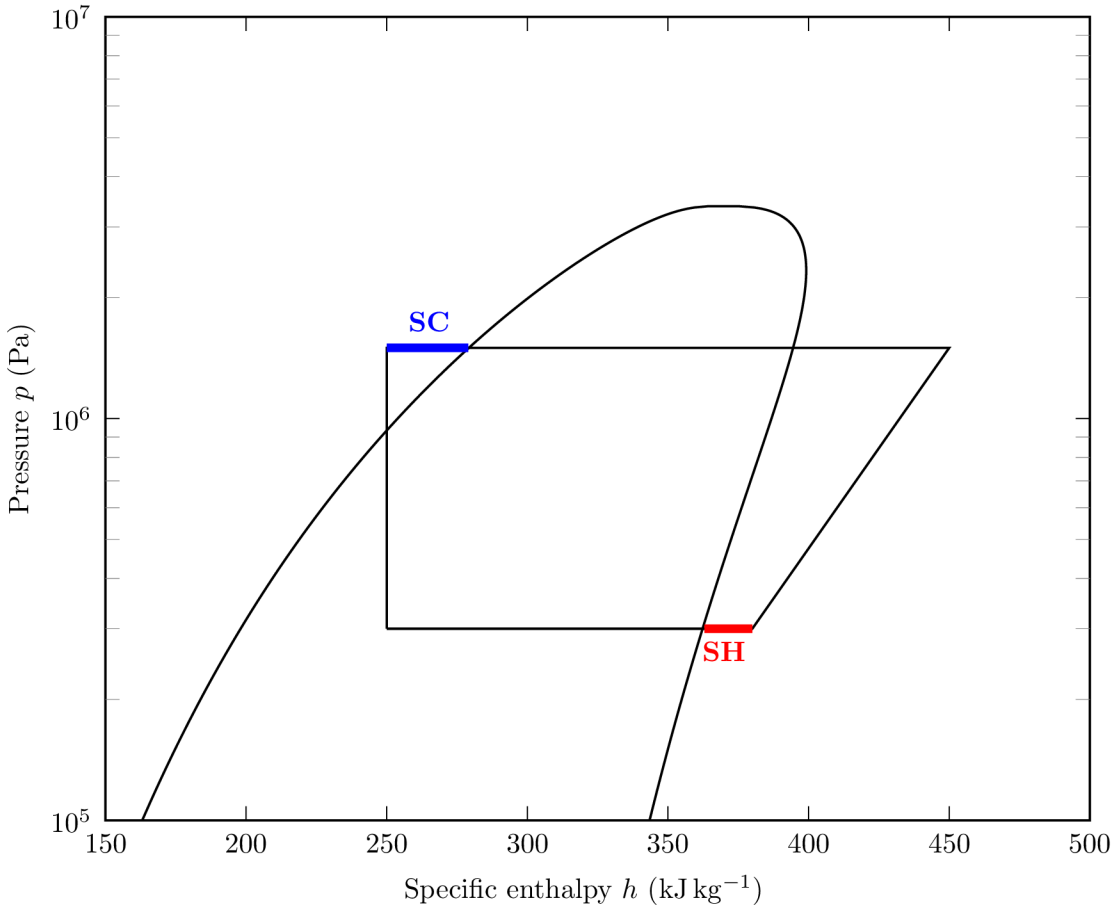

Fig. 6.5: Superheat and subcooling illustration

Recalling (F.1) and substituting $\omega = 2\pi n/60$ we get the compressor mass flow rate

$$\dot{m} = \frac{n}{60}\rho V \eta_{\text{vol}}, \tag{6.17}$$

where n is compressor speed in revolutions per minute (rpm). The current compressor speed is reported via LIN bus, displacement V is fixed and volumetric efficiency η_{vol} is expected to be very high (approx. 98 %). Thus only inlet refrigerant density is not known, but it can be computed from other refrigerant properties.

Assuming the suction accumulator, the refrigerant mass fraction ξ (quality) of 1 is anticipated (neglecting superheating in the suction line between accumulator and compressor). Then the refrigerant density can be obtained from

$$\rho = \mathsf{\rho}(p, \xi), \tag{6.18}$$

where $\mathsf{\rho}(p, \xi)$ is a function returning refrigerant density based on its pressure p and mass fraction ξ, where $\xi = 1$.

In VCRS employing liquid receiver, the superheat is usually measured and the refrigerant density can be computed as

$$\rho = \mathrm{\rho}(p, \mathrm{h}(p, T)), \tag{6.19}$$

where $\mathrm{\rho}(p, h)$ is a function returning refrigerant density based on its pressure and specific enthalpy, which is computed by function $\mathrm{h}(\cdot)$ based on refrigerant pressure p and temperature T.

6.3.4 COP virtual sensor

Coefficient of performance is defined for cooling and heating respectively as

$$COP_{\mathrm{c}} = \frac{\dot{Q}_{\mathrm{evap}}}{P_{\mathrm{cmpr}}}, \tag{6.20}$$

$$COP_{\mathrm{h}} = \frac{\dot{Q}_{\mathrm{cond}}}{P_{\mathrm{cmpr}}}, \tag{6.21}$$

where $\dot{Q}_{\mathrm{evap}}$ and $\dot{Q}_{\mathrm{cond}}$ are evaporator and condenser heat flow rates respectively and P_{cmpr} is the compressor power. Depending on available sensors it is possible to compute COP using different formulas.

As the most appropriate approach of heat flow rate estimation the condenser enthalpy difference was chosen. The reason for this choice is the availability of temperature sensors (inside refrigerant pipes) in combination with measurement reliability (points 2 and 3 in Fig. 6.6 are always single-phase). The evaporator heat flow rate can be reformulated using the condenser heat flow rate as

$$\dot{Q}_{\mathrm{evap}} = \dot{Q}_{\mathrm{cond}} - P_{\mathrm{cmpr}} \tag{6.22}$$

or using $\dot{Q} = \dot{m}\Delta h$ as

$$\dot{m}\Delta h_{\mathrm{evap}} = \dot{m}\Delta h_{\mathrm{cond}} - \dot{m}\Delta h_{\mathrm{cmpr}}, \tag{6.23}$$

with the assumption of a system in steady-state, i.e. refrigerant mass flow rate $\dot{m}$ is equal for all the components. We can rewrite the equations above as

$$COP_{\mathrm{c}} = \frac{\dot{m}\Delta h_{\mathrm{cond}} - P_{\mathrm{cmpr}}}{P_{\mathrm{cmpr}}}, \tag{6.24}$$

$$COP_{\mathrm{h}} = \frac{\dot{m}\Delta h_{\mathrm{cond}}}{P_{\mathrm{cmpr}}}, \tag{6.25}$$

where the condenser enthalpy difference

$$\Delta h_{\mathrm{cond}} = h_2 - h_3 \tag{6.26}$$

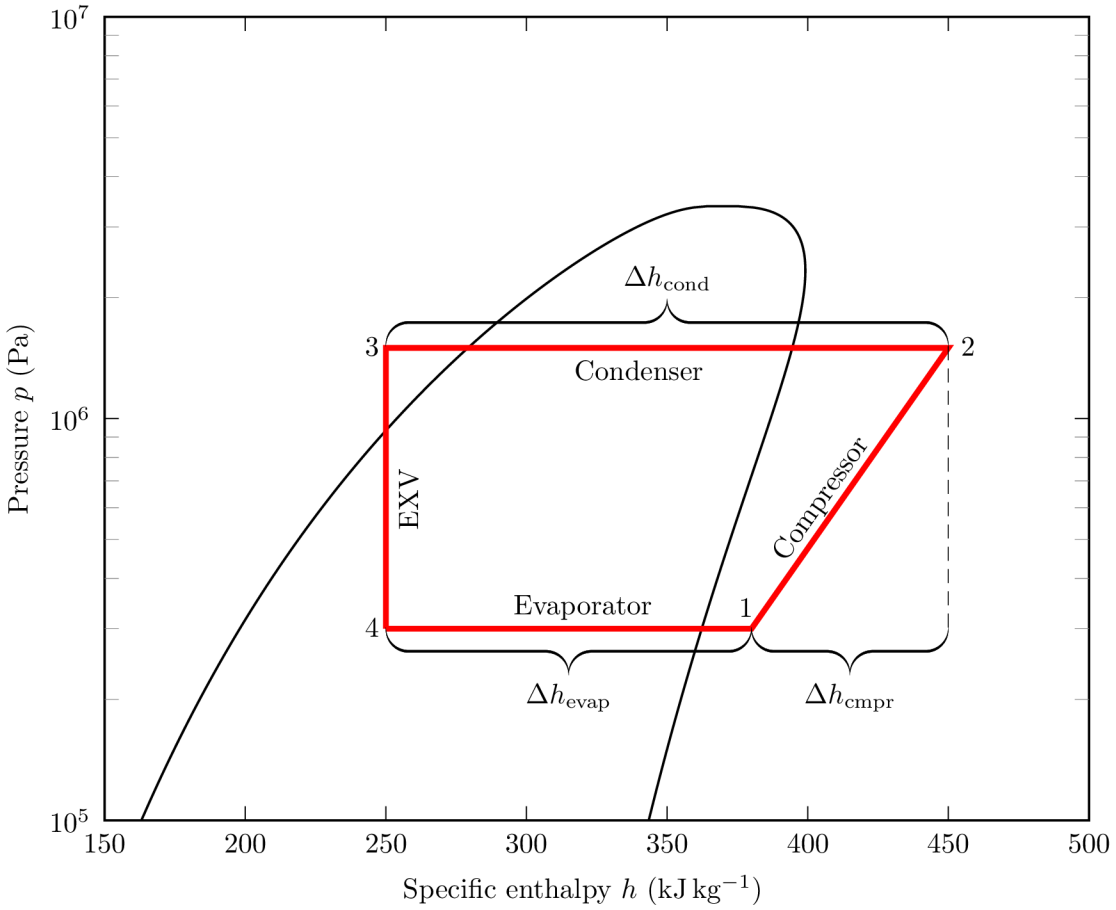

Fig. 6.6: ph diagram for COP virtual sensor

can be computed from pressure and temperature measurements

$$h_2 = \mathrm{h}(p_2, T_2), \tag{6.27}$$

$$h_3 = \mathrm{h}(p_3, T_3), \tag{6.28}$$

where $\mathrm{h}(p, T)$ is a function returning specific enthalpy based on pressure p and temperature T.

Then we define *Overall COP*, which reflects also the power consumption of VCRS auxiliaries (fans, pumps, etc.)

$$COP_{\mathrm{c}}^{\mathrm{oa}} = \frac{\dot{m}\Delta h_{\mathrm{cond}} - P_{\mathrm{cmpr}}}{P_{\mathrm{VCRS}}}, \tag{6.29}$$

$$COP_{\mathrm{h}}^{\mathrm{oa}} = \frac{\dot{m}\Delta h_{\mathrm{cond}}}{P_{\mathrm{VCRS}}}, \tag{6.30}$$

where the power consumption of the whole VCRS system is defined as

$$P_{\mathrm{VCRS}} = P_{\mathrm{cmpr}} + P_{\mathrm{hf}} + P_{\mathrm{mf}} + P_{\mathrm{pumps}} + \ldots, \tag{6.31}$$

where P_{hf} is the power consumption of HVAC fan, P_{mf} is the power consumption of Main Fan and P_{pumps} is the power consumption of all the coolant pumps together.

The dots (. . .) stand for power consumption of other devices (control units, valves, etc.), which can be neglected for simplicity.

6.4 TEMCU Graphical User Interface

TEMCU Graphical User Interface (GUI) was developed to allow a user to control the HVAC system and to enable monitoring and manual control of TEMCU. As TEMCU should operate as a standard automotive control unit, it was equipped with Controller Area Network (CAN bus) communication protocol. The TEMCU GUI uses this CAN bus interface to monitor and control the TEMCU signals. All the sensors' current values (including virtual sensors) are shown in GUI and for each actuator the possibility to switch it to manual control is possible.

The GUI was developed in MATLAB/Simulink using Vehicle Network Toolbox, which employs National Instruments cDAQ-9174 equipped with NI-9862 CAN module for connection to TEMCU CAN interface.

The screenshots of developed GUI are presented in Appendix C.

6.5 LIN automatic code generation

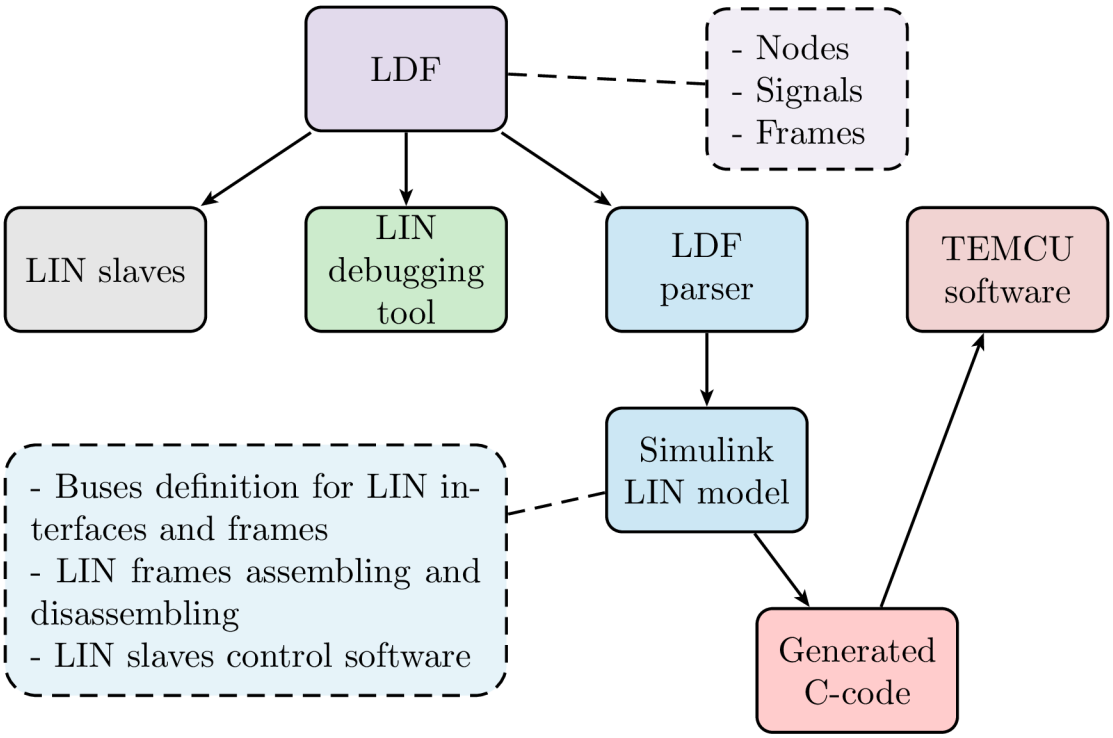

Fig. 6.7: LIN automatic code generation schematics

Since the LIN clusters are quite extensive (see Fig. 2.2), it was inefficient to manually write the code for LIN frames assembling and disassembling. Thus MATLAB Simulink code generation features were conveniently used in combination with self-developed parts of this solution. An overview of the LIN automatic code generation approach is shown in Fig. 6.7.

The first part is a LIN Description File (LDF) parser, which loads LDF and extracts signals, frames and signal encodings into Matlab structures with appropriate connections (each signal belongs to some frame and has some encoding). Based on these structures corresponding buses are created with a one-to-one mapping between frames and buses. The signals are assigned to the appropriate frame (represented by bus) as bus members with data type defined by the signal length (number of bits) and its encoding.

A Simulink subsystem is created for each LIN node and the buses are employed as subsystem input and output ports. An example of a LIN Simulink subsystem is shown in Fig. 6.8.

The frames are grouped based on the LIN interface and the direction (transmit or receive) and assigned to a parent bus. For three LIN clusters, we get three receive parent buses and three transmit parent buses. The data from these buses (structures in C) are utilized in transmit and receive tasks without the need for any further data manipulation.

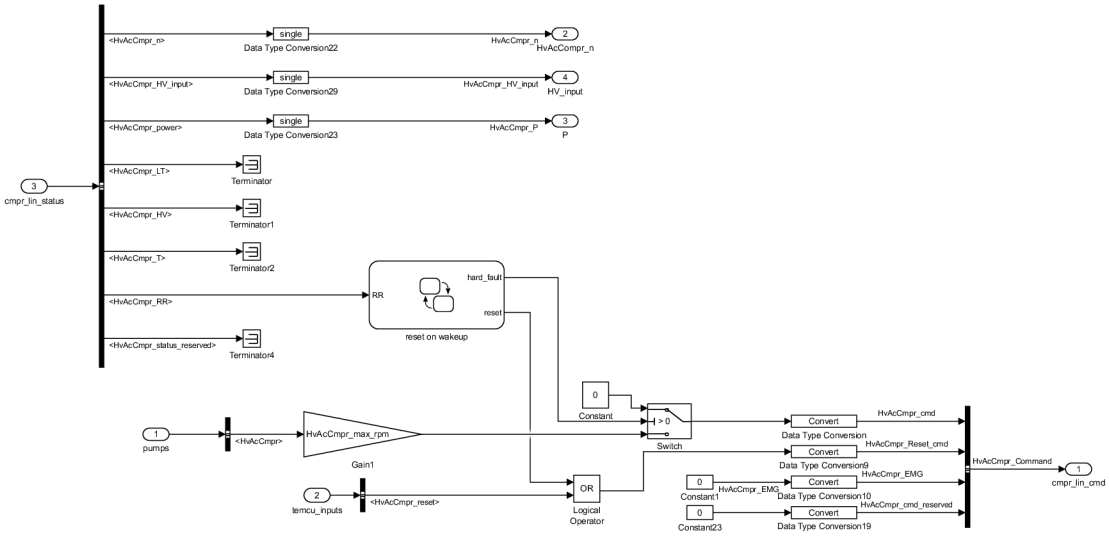

Fig. 6.8: HV compressor LIN Simulink model for automatic code generation

7 Demonstration and exploitation

The results of this work were presented at several conferences and meetings, for instance, TRA 2018, IEEE ICIT 2017, IEEE ISIE 2017 and others. Moreover, the part of the algorithms and approaches is applied to an assembled test bench, which is used to demonstrate the possibilities of advanced control in the field of VTMS and VCRS.

The overview of the test bench is shown in Fig. 7.1 and it is slightly different compared to the proposed OSEM-EV circuit (Fig. 2.1) as it was not possible to bring all the components to our laboratory. The E-Drive, Charger, HV Battery and DC/DC converter are emulated by PTC heater and this configuration allows testing almost all of the operating modes. The electric wiring of the test bench is placed in

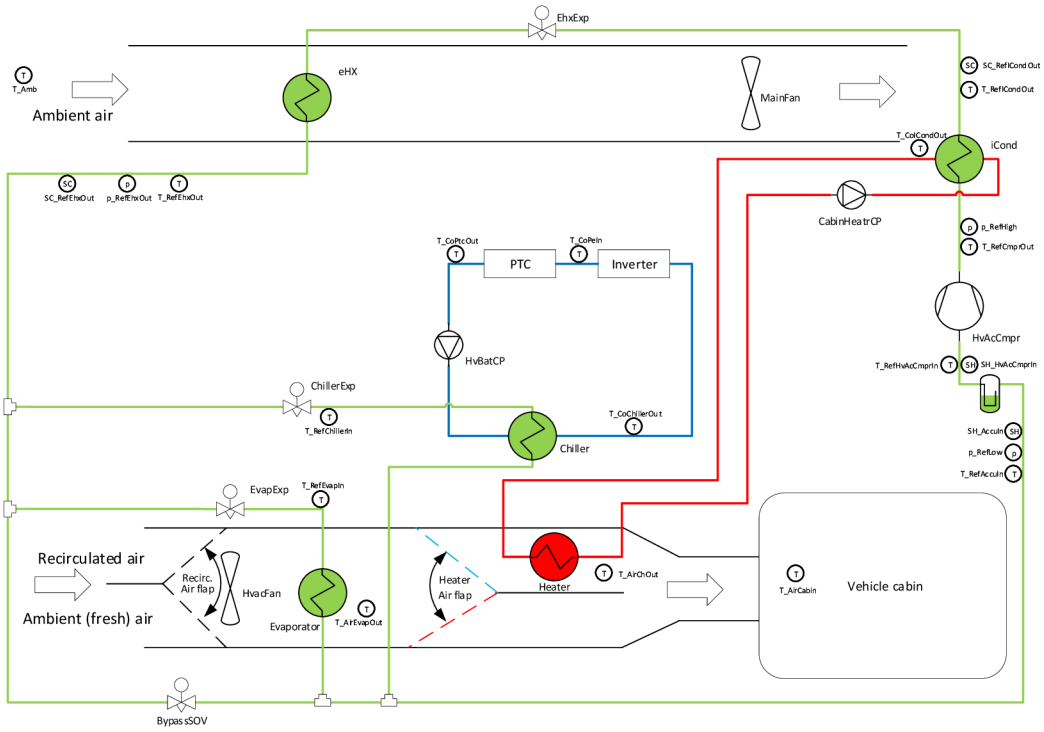

Fig. 7.1: OSEM-EV test bench schematics

Appendix A and the photos are attached in Appendix B.

A bachelor's thesis [69] with a scope on the modeling of a general vehicle cabin was advised. The student assembled a dynamic model of the cabin, calibrated it against measurements in ICE vehicle and he implemented the model into the microcontroller. This implementation enables hardware in the loop (HIL) simulation verification of part of the control algorithms for cabin heating and cooling. The bachelor's thesis was successfully defended.

8 Conclusion

This thesis deals with modeling and control of the innovative Vehicle Thermal Management System (VTMS) for Fully Electric Vehicle (FEV). The topic is very interesting from the FEV range perspective, as it can help to avoid mileage decrease under adverse ambient conditions without losing the user comfort during driving. Moreover, if we consider other EV types (PHEV, FCEV) or even different modes of transportation, the optimization of energy consumption is important not only from the range point of view but also from the general energy-saving perspective.

The models and control algorithms were developed for an innovative VTMS layout, which enables many operating modes, including heat pump functionality with a different heat source and sink configurations. However, the methods and approaches can be applied to different VTMS layouts and are not even limited to automotive applications and could be used in other areas.

Within this thesis, several dynamic models of whole VTMS and its parts were assembled. Part of the models was used for control algorithms design, some of them served as a reference model of FEV for algorithms verification and some of them were used to gain deep knowledge of dynamic behavior of the VTMS subsystems.

As the proposed VTMS layout allows many operating modes ("Thermal Functions"), it was needed to develop an algorithm for real-time mode selection. Two different approaches were proposed. The first algorithm (called "Basic Thermal Decision Controller") employs a heuristic approach in combination with defined limits and references. As a result, three complicated state diagrams were assembled and the connections between them were introduced to ensure the selection of compatible Thermal Functions and emergency functionality.

The second algorithm ("Model Predictive Thermal Decision Controller") uses a Hybrid MPC approach modification, which was formally described as Decision Model Predictive Control. This method is based on a set of highly simplified FEV thermal flows dynamic models, with each representing one Overall Thermal Function. The models were united into a single piecewise affine model and Hybrid MPC is used to select the appropriate Overall Thermal Function. This approach is preferable over the first one, as it does not require heuristic knowledge and can be easily applied to different VTMS layout. Moreover, it natively ensures the fulfillment of the defined limits. On the other hand, the predictive approach requires a simple dynamic model of the system and the algorithm implementation is much more difficult.

Then within each Thermal Function, a set of control algorithms was designed to fulfill the requirements on defined references. That means VCRS control, cabin temperature control, HV Battery temperature control and E-Drive temperature control.

These algorithms were implemented into TEMCU HW and partially tested on the test bench. The parts, which could not be tested on the test bench, were successfully evaluated against FEV Dymola thermal model.

For selected control problems more advanced control algorithms were prepared. First of them is cabin temperature control in combination with cabin air quality control realized by Non-linear Model Predictive Control. This integrated approach brings convenient cabin air quality and temperature together with the minimization of electric power consumption. This control approach was tested using PIL simulation, as the real-world testing would require a vehicle cabin, which was not available on the test bench.

The model-based electronic expansion valve control algorithm was designed for Vapor Compression Refrigeration System (VCRS) subcooling control. This approach uses a compressor refrigerant mass flow rate estimator in combination with an expansion valve mass flow rate equation and predicts the valve steady-state opening degree. To reject the disturbances and inaccuracies of this approach the model-based EXV controller was complemented by the PI controller. The algorithm was tested on the test bench and it brings substantial improvement of VCRS performance especially during system start-up. This control method could be improved by including the condenser model, which could refine the refrigerant mass flow rate estimation.

The algorithms described above were complemented by several virtual sensors (for subcooling, superheat, refrigerant mass flow rate, coefficient of performance, heat storage status, etc.) and a couple of supportive software tools were developed (FMUtoolbox, refToolbox, etc.). Fault detection algorithms were introduced to ensure the safe operation of VTMS including the VCRS circuit. The fault detection is based on the constant limits of the measured variables and combinations of the actuators states. There is an opportunity for fault detection algorithms future research and development, as it could be improved using model-based fault detection or artificial neural networks.

This thesis required a multidisciplinary approach to achieve relevant and improving results. The non-exhausting list of touched disciplines contains control theory, thermodynamics, refrigeration and dynamic system modeling. The control algorithms implementation required knowledge of measurements & signal processing, electricity, automotive applications, control unit communication, and real-time operating systems.

Future research and development could focus on vehicle cabin air dehumidification as the proposed VTMS layout could allow energy-efficient operation within this mode. Also, we can see possible improvements in decisive hybrid MPC, for example, implicit implementation could bring longer prediction horizon (if considering large sampling times, which provide enough time for online optimizations).

Bibliography

[1] W. Adaileh and A. Alahmer, "Recovery of Exhaust Waste Heat for ICE Using the Beta Type Stirling Engine," *Journal of Energy*, vol. 2015, p. Article ID 495418, 2015.

[2] K. T. Chau and C. C. Chan, "Emerging Energy-Efficient Technologies for Hybrid Electric Vehicles," *Proceedings of the IEEE*, vol. 95, pp. 821–835, Apr. 2007.

[3] M. Åhman, "Primary energy efficiency of alternative powertrains in vehicles," *Energy*, vol. 26, pp. 973–989, Nov. 2001.

[4] Z. Zhang, J. Wang, X. Feng, L. Chang, Y. Chen, and X. Wang, "The solutions to electric vehicle air conditioning systems: A review," *Renewable and Sustainable Energy Reviews*, vol. 91, pp. 443–463, Aug. 2018.

[5] J. R. M. Delos Reyes, R. V. Parsons, and R. Hoemsen, "Winter Happens: The Effect of Ambient Temperature on the Travel Range of Electric Vehicles," *IEEE Transactions on Vehicular Technology*, vol. 65, pp. 4016–4022, June 2016.

[6] G. Mimberg and C. Massonet, "Battery concept to minimize the climate-related reduction of electric vehicles driving range," in *2017 12th International Conference on Ecological Vehicles and Renewable Energies, EVER 2017*, Institute of Electrical and Electronics Engineers Inc., May 2017.

[7] N. Meyer, I. Whittal, M. Christenson, and A. Loiselle-Lapointe, "The Impact of Driving Cycle and Climate on Electrical Consumption & Range of Fully Electric Passenger," in *EVS26 International Battery, Hybrid and Fuel Cell Electric Vehicle Symposium*, 2012.

[8] Z. Zhao and N. Yu, "The application of advanced control technologies in air conditioning system–a review," *Advances in Building Energy Research*, vol. 11, no. 1, pp. 52–66, 2017.

[9] O. Ekren, S. Sahin, and Y. Isler, "Comparison of different controllers for variable speed compressor and electronic expansion valve," *International Journal of Refrigeration*, vol. 33, pp. 1161–1168, Sept. 2010.

[10] X. Yin and S. Li, "Energy efficient predictive control for vapor compression refrigeration cycle systems," *IEEE/CAA Journal of Automatica Sinica*, vol. 5, pp. 953–960, Sept. 2018.

[11] M. Wallace, P. Mhaskar, J. House, and T. Salsbury, "Offset-free model predictive controller of a heat pump," in *2014 American Control Conference*, pp. 2247–2252, IEEE, June 2014.

[12] M. Gräber, C. Kirches, J. P. Schlöder, and W. Tegethoff, "Nonlinear Model Predictive Control of a Vapor Compression Cycle based on First Principle Models," *IFAC Proceedings Volumes*, vol. 45, no. 2, pp. 258–263, 2012.

[13] X. H. Yin and S. Y. Li, "Model Predictive Control for Vapor Compression Cycle of Refrigeration Process," *International Journal of Automation and Computing*, vol. 15, pp. 707–715, Dec. 2018.

[14] A. Goyal, M. A. Staedter, and S. Garimella, "A review of control methodologies for vapor compression and absorption heat pumps," *International Journal of Refrigeration*, vol. 97, pp. 1–20, Jan. 2019.

[15] Q. Zhang, S. E. Li, and K. Deng, *Automotive air conditioning: Optimization, control and diagnosis*. Springer International Publishing, Jan. 2016.

[16] G. Pottker, P. Hrnjak, and P. H. Pottker Gustavo, "Effect of Condenser Subcooling of the Performance of Vapor Compression Systems: Experimental and Numerical Investigation," in *International Refrigeration and Air Conditioning Conference*, vol. 50, pp. 1–10, 2012.

[17] L. Xu and P. Hrnjak, "Potential for Improving Efficiency by Controlling Subcooling in Residential A / C System," *International Refrigeration and Air Conditioning Conference*, pp. 1–10, 2014.

[18] M. Pitarch, E. Hervas-Blasco, E. Navarro-Peris, J. Gonzálvez-Maciá, and J. M. Corberán, "Evaluation of optimal subcooling in subcritical heat pump systems," *International Journal of Refrigeration*, vol. 78, pp. 18–31, June 2017.

[19] E. Hervas-Blasco, M. Pitarch, E. Navarro-Peris, and J. M. Corberán, "Study of different subcooling control strategies in order to enhance the performance of a heat pump," *International Journal of Refrigeration*, vol. 88, pp. 324–336, Apr. 2018.

[20] P. A. Scheff, V. K. Paulius, S. W. Huang, and L. M. Conroy, "Indoor Air Quality in a Middle School, Part I: Use of CO2 as a Tracer for Effective Ventilation," *Applied Occupational and Environmental Hygiene*, vol. 15, no. 11, pp. 824–834, 2000.

[21] J. Sundell, "On the history of indoor air quality and health," *Indoor air*, vol. 14 Suppl 7, pp. 51–58, 2004.

[22] R. FLETCHER and B. JONSON, "DEADSPACE AND THE SINGLE BREATH TEST FOR CARBON DIOXIDE DURING ANAESTHESIA AND ARTIFICIAL VENTILATION: Effects of tidal volume and frequency of respiration," *British Journal of Anaesthesia*, vol. 56, pp. 109–119, Feb. 1984.

[23] I. H. Bell, J. Wronski, S. Quoilin, and V. Lemort, "Pure and Pseudo-pure Fluid Thermophysical Property Evaluation and the Open-Source Thermophysical Property Library CoolProp," *Industrial & Engineering Chemistry Research*, vol. 53, no. 6, pp. 2498–2508, 2014.

[24] C. Goh, L. Kamarudin, S. Shukri, N. Abdullah, and A. Zakaria, "Monitoring of carbon dioxide (CO2) accumulation in vehicle cabin," in *2016 3rd International Conference on Electronic Design (ICED)*, pp. 427–432, IEEE, Aug. 2016.

[25] J. Lopez Sanz, C. Ocampo-Martinez, J. Alvarez-Florez, M. Moreno Eguilaz, R. Ruiz-Mansilla, J. Kalmus, M. Graber, and G. Lux, "Nonlinear Model Predictive Control for Thermal Management in Plug-in Hybrid Electric Vehicles," *IEEE Transactions on Vehicular Technology*, pp. 1–1, 2016.

[26] J. Lopez-Sanz, C. Ocampo-Martinez, J. Alvarez-Florez, M. Moreno-Eguilaz, R. Ruiz-Mansilla, J. Kalmus, M. Graeber, and G. Lux, "Thermal Management in Plug-In Hybrid Electric Vehicles: A Real-Time Nonlinear Model Predictive Control Implementation," *IEEE Transactions on Vehicular Technology*, vol. 66, pp. 7751–7760, Sept. 2017.

[27] S. S. Butt, R. Prabel, and H. Aschemann, "Model-predictive on-off control of a combustion-heating-system for vehicles," in *2013 European Control Conference (ECC)*, pp. 1988–1993, IEEE, July 2013.

[28] T. Fischer, T. Kraus, C. Kirches, and F. Gauterin, "Demonstration of a Nonlinear Model Predictive Control of a Thermal Management System for Electric Vehicles in Real-Time," in *2018 IEEE Conference on Control Technology and Applications (CCTA)*, pp. 676–682, IEEE, Aug. 2018.

[29] K. Galatsis, W. Wlodarski, Yongxiang Li, and K. Kalantar-zadeh, "Ventilation control for improved cabin air quality and vehicle safety," in *IEEE VTS 53rd Vehicular Technology Conference, Spring 2001. Proceedings (Cat. No.01CH37202)*, vol. 4, pp. 3018–3021, IEEE, 2001.

[30] Jinjing Yang, Yu Chen, Yimin Liu, O. Makke, J. Yeung, O. Gusikhin, and P. MacNeille, "The effectiveness of cloud-based smart in-vehicle air quality

management," in *2016 IEEE Advanced Information Management, Communicates, Electronic and Automation Control Conference (IMCEC)*, pp. 325–329, IEEE, Oct. 2016.

[31] D. Kolokotsa, A. Pouliezos, G. Stavrakakis, and C. Lazos, "Predictive control techniques for energy and indoor environmental quality management in buildings," *Building and Environment*, vol. 44, pp. 1850–1863, Sept. 2009.

[32] J. Eckstein, C. Lüke, F. Brunstein, P. Friedel, and U. Köhler, "A Novel Approach Using Model Predictive Control to Enhance the Range of Electric Vehicles," *Procedia Technology*, vol. 26, pp. 177–184, Jan. 2016.

[33] S. Uebel, N. Murgovski, B. Bäker, and J. Sjöberg, "A Two-Level MPC for Energy Management Including Velocity Control of Hybrid Electric Vehicles," *IEEE Transactions on Vehicular Technology*, vol. 68, pp. 5494–5505, June 2019.

[34] M. Salazar, C. Balerna, P. Elbert, F. P. Grando, and C. H. Onder, "Real-time control algorithms for a hybrid electric race car using a two-level model predictive control scheme," *IEEE Transactions on Vehicular Technology*, vol. 66, pp. 10911–10922, Dec. 2017.

[35] H. Wang, Y. Huang, A. Soltani, A. Khajepour, and D. Cao, "Cyber-Physical Predictive Energy Management for Through-the-Road Hybrid Vehicles," *IEEE Transactions on Vehicular Technology*, vol. 68, pp. 3246–3256, Apr. 2019.

[36] D. M. Wu, Y. Li, C. Q. Du, H. T. Ding, Y. Li, X. B. Yang, and X. Y. Lu, "Fast velocity trajectory planning and control algorithm of intelligent 4WD electric vehicle for energy saving using time-based MPC," *IET Intelligent Transport Systems*, vol. 13, pp. 153–159, Jan. 2019.

[37] C. Sun, X. Zhang, Q. Zhou, and Y. Tian, "A Model Predictive Controller with Switched Tracking Error for Autonomous Vehicle Path Tracking," *IEEE Access*, vol. 7, pp. 53103–53114, 2019.

[38] H. Wang, B. Liu, X. Ping, and Q. An, "Path Tracking Control for Autonomous Vehicles Based on an Improved MPC," *IEEE Access*, pp. 1–1, Oct. 2019.

[39] J. Felez, C. Garcia-Sanchez, and J. A. Lozano, "Control Design for an Articulated Truck with Autonomous Driving in an Electrified Highway," *IEEE Access*, vol. 6, pp. 60171–60186, 2018.

[40] B. Sakhdari and N. L. Azad, "Adaptive Tube-Based Nonlinear MPC for Economic Autonomous Cruise Control of Plug-In Hybrid Electric Vehicles," *IEEE Transactions on Vehicular Technology*, vol. 67, pp. 11390–11401, Dec. 2018.

[41] D. Moser, R. Schmied, H. Waschl, and L. Del Re, "Flexible Spacing Adaptive Cruise Control Using Stochastic Model Predictive Control," *IEEE Transactions on Control Systems Technology*, vol. 26, pp. 114–127, Jan. 2018.

[42] L. Grüne and J. Pannek, *Nonlinear Model Predictive Control: Theory and Algorithms*. 2011.

[43] M. A. Stephens, C. Manzie, and M. C. Good, "Model predictive control for reference tracking on an industrial machine tool servo drive," *IEEE Transactions on Industrial Informatics*, vol. 9, no. 2, pp. 808–816, 2013.

[44] D. Ariens, B. Houska, H. Ferreau, and F. Logist, "ACADO: Toolkit for Automatic Control and Dynamic Optimization." `http://www.acadotoolkit.org/`.

[45] H. Bock and K. Plitt, "A Multiple Shooting Algorithm for Direct Solution of Optimal Control Problems," *IFAC Proceedings Volumes*, vol. 17, pp. 1603–1608, July 1984.

[46] H. J. Ferreau, C. Kirches, A. Potschka, H. G. Bock, and M. Diehl, "qpOASES: A parametric active-set algorithm for quadratic programming," *Mathematical Programming Computation*, vol. 6, no. 4, pp. 327–363, 2014.

[47] H. J. Ferreau, H. G. Bock, and M. Diehl, "An online active set strategy to overcome the limitations of explicit MPC," *International Journal of Robust and Nonlinear Control*, vol. 18, pp. 816–830, May 2008.

[48] G. Welch and G. Bishop, "An Introduction to the Kalman Filter," tech. rep., University of North Carolina at Chapel Hill, 1995.

[49] J. B. Rawlings and D. Q. Mayne, *Model predictive control : theory and design*. Nob Hill Pub, 2009.

[50] J. A. Rossiter, *Model-based predictive control: A practical approach*. CRC Press, Jan. 2017.

[51] N. Karmarkar, "A new polynomial-time algorithm for linear programming," *Combinatorica*, vol. 4, pp. 373–395, Dec. 1984.

[52] P. T. Boggs and J. W. Tolle, "Sequential Quadratic Programming," *Acta Numerica*, vol. 4, pp. 1–51, Jan. 1995.

[53] W. Heemels, B. De Schutter, and A. Bemporad, "Equivalence of hybrid dynamical models," *Automatica*, vol. 37, pp. 1085–1091, July 2001.

[54] M. Morari, "Hybrid system analysis and control via mixed integer optimization," *IFAC Proceedings Volumes*, vol. 34, pp. 1–12, June 2001.

[55] A. Bemporad and M. Morari, "Control of systems integrating logic, dynamics, and constraints," *Automatica*, vol. 35, pp. 407–427, Mar. 1999.

[56] E. Sontag, "Nonlinear regulation: The piecewise linear approach," *IEEE Transactions on Automatic Control*, vol. 26, pp. 346–358, Apr. 1981.

[57] F. Borrelli, M. Baotic, A. Bemporad, and M. Morari, "An efficient algorithm for computing the state feedback optimal control law for discrete time hybrid systems," in *Proceedings of the 2003 American Control Conference, 2003.*, vol. 6, pp. 4717–4722, IEEE, 2003.

[58] A. H. Land and A. G. Doig, "An automatic method for solving discrete programming problems," *ECONOMETRICA*, vol. 28, no. 3, pp. 497—-520, 1960.

[59] R. J. Dakin, "A tree-search algorithm for mixed integer programming problems," *The Computer Journal*, vol. 8, pp. 250–255, Mar. 1965.

[60] A. Bemporad, D. Mignone, and M. Morari, "An efficient branch and bound algorithm for state estimation and control of hybrid systems," in *1999 European Control Conference (ECC)*, pp. 557–562, IEEE, Aug. 1999.

[61] Y. Zhao and S. Liu, "Global optimization algorithm for mixed integer quadratically constrained quadratic program," *Journal of Computational and Applied Mathematics*, vol. 319, pp. 159–169, Aug. 2017.

[62] D. Axehill, T. Besselmann, D. M. Raimondo, and M. Morari, "A parametric branch and bound approach to suboptimal explicit hybrid MPC," *Automatica*, vol. 50, pp. 240–246, Jan. 2014.

[63] A. Bemporad, F. Borrelli, and M. Morari, "Piecewise linear optimal controllers for hybrid systems," in *Proceedings of the 2000 American Control Conference. ACC (IEEE Cat. No.00CH36334)*, pp. 1190–1194 vol.2, IEEE, 2000.

[64] M. Herceg, C. N. Jones, M. Kvasnica, and M. Morari, "Enumeration-based approach to solving parametric linear complementarity problems," *Automatica*, vol. 62, pp. 243–248, Dec. 2015.

[65] M. Herceg, M. Kvasnica, C. N. Jones, and M. Morari, "Multi-Parametric Toolbox 3.0," in *2013 European Control Conference (ECC)*, pp. 502–510, IEEE, July 2013.

[66] A. Bemporad, "Hybrid Toolbox - User's Guide." Available at: http://cse.lab.imtlucca.it/~bemporad/hybrid/toolbox, 2004.

[67] J. Novak and P. Chalupa, "Implementation of Mixed-integer Programming on Embedded System," *Procedia Engineering*, vol. 100, pp. 1649–1656, Jan. 2015.

[68] "OSEK/VDX Certification Approval Document: Infineon TriCore TC26x," 2014.

[69] M. Chromiak, "Tepelný model kabiny automobilu pro HIL simulaci," bakalářská práce, Vysoké učení technické v Brně, Brno, 2018.

[70] Y. A. Cengel and M. A. Boles, *Thermodynamics: an Engineering Approach 8th Edition*. McGraw-Hill Education, 2015.

[71] C. Borgnakke, R. E. Sonntag, G. J. V. Wylen, and R. E. Sonntag, *Fundamentals of thermodynamics*. Hoboken, NJ: Wiley, 7th ed ed., 2009.

[72] Z. S. Spakovszky, "Thermodynamics and Propulsion: Control volume form of the conservation laws," 2009.

[73] Z. S. Spakovszky, "Thermodynamics and Propulsion: Axiomatic Statements of the Laws of Thermodynamics," 2009.

[74] L. A. Incropera Frank P., Dewitt D.P., Bergman T. L., *Fundamentals of Heat and Mass Transfer*. John Wiley & Sons, 2011.

[75] D. Halliday, R. Resnick, and J. Walker, *Fundamentals of Physics*. John Wiley & Sons, Inc., 2013.

[76] Z. Dvořák, J. Petrák, and L. Klazar, *Tepelná čerpadla*. Praha: Státní nakladatelství technické literatury, 1987.

[77] Y. Shang, A. Wu, X. Fang, and Y. You, "Dynamic simulation of electronic expansion valve controlled refrigeration system under different heat transfer conditions," *International Journal of Refrigeration*, vol. 72, pp. 41–52, Dec. 2016.

[78] Q. Zhang and M. Canova, "Modeling and output feedback control of automotive air conditioning system," *International Journal of Refrigeration*, vol. 58, pp. 207–218, Oct. 2015.

[79] P. Deutsch and A. Harris, "Thermodynamic model of electric vehicle A/C system with single evaporator," in *Institution of Mechanical Engineers - VTMS*

2011, Vehicle Thermal Management Systems Conference Proceedings, pp. 241–249, Woodhead Publishing Limited, 2013.

[80] N. Park, J. Shin, and B. Chung, "A new dynamic heat pump simulation model with variable speed compressors under frosting conditions," in *Institution of Mechanical Engineers - 8th International Conference on Compressors and Their Systems*, pp. 681–696, Woodhead Publishing Limited, 2013.

[81] I. W. Eames, A. Milazzo, and G. G. Maidment, "Modelling thermostatic expansion valves," *International Journal of Refrigeration*, vol. 38, pp. 189–197, Feb. 2014.

Published papers

[82] J. Glos, P. Václavek, and P. Blaha, "Energy efficient control of a heat pump in fully electric vehicle," in *Proceedings of the 7th European Transport Research Arena 2018*, (Wien), 2018.

[83] J. Glos, "FMUtoolbox cross check implementation and FMI Standard compliance results," in *Proceedings of the 24th Conference STUDENT EEICT 2018*, (Brno), pp. 403–407, Vysoké učení technické v Brně, Fakulta elektrotechniky a komunikačních technologií, 2018.

[84] M. Hütter, M. Nica, E. Sumann, J. Tao, J. Glos, M. Gepp, M. Helwig, H.-F. D. C. Garcia, A. Bacar, and N. De-Guyenro, "Impact of thermal-electric networks on the usability of EVs based on a study with a C-segment car," in *Proceedings of the 7th European Transport Research Arena 2018*, 2018.

[85] J. Glos and F. Šolc, "Determination of optimum high-side pressure of R744 automotive heat pump using Fibonacci search method," in *Proceedings of the 2017 IEEE International Symposium on Industrial Electronics*, pp. 448–453, IEEE, 2017.

[86] J. Glos and P. Václavek, "Efficient control of automotive R744 heat pump using Nelder-Mead simplex method," in *Proceedings of the 2017 IEEE International Conference on Industrial Technology*, pp. 785–790, IEEE, 2017.

[87] J. Glos and P. Václavek, "Nelder-Mead algorithm based control strategy for CO2 heat pump," in *Book of Abstracts CEITEC PhD Retreat II.*, (Brno), pp. 70–70, Masaryk University, 2017.

[88] J. Glos, "FMU Toolbox for Matlab/Simulink," in *Proceedings of the 22st Conference STUDENT EEICT 2016*, pp. 426–430, Vysoké učení technické v Brně, Fakulta elektrotechniky a komunikačních technologií, 2016.

[89] J. Glos, "Využití modelů v jazyce Modelica v prostředí Matlab-Simulink," in *Proceedings of the 21st Conference STUDENT EEICT 2015*, (Brno), pp. 310–312, Vysoké učení technické v Brně, Fakulta elektrotechniky a komunikačních technologií, 2015.

[90] J. Glos, "RefToolbox - refrigeration toolbox for MATLAB/Simulink," in *Proceedings of the 25th Conference STUDENT EEICT 2019*, (Brno), pp. 551–555, Vysoké učení technické v Brně, Fakulta elektrotechniky a komunikačních technologií, 2019.

List of symbols, physical constants, and abbreviations

4WV	Four-way valve
AC	Air conditioning
AGS	Air grill shutter
BEV	Battery electric vehicle
BnB	Branch and bound
BTM	Battery thermal management
BUT	Brno University of Technology
CAN	Controller Area Network (bus)
COP	Coefficient of performance
DMPC	Decision Model Predictive Control
ECU	Electronic control unit
ED	E-Drive, Electric Drive
EKF	Extended Kalman Filter
ELC	extended linear complementarity (system)
EM	Electric motor
EV	Electric vehicle
ESC	Extremum-seeking control
EXV	Electric (electronic) expansion valve
FCEV	Fuel cell electric vehicle
FEV	Fully electric vehicle
GUI	Graphical user interface
GWP	Global warming potential
HEV	Hybrid Electric Vehicle
HV	High Voltage
HVAC	Heating, ventilation and air conditioning
HVAC&R	HVAC & Refrigeration
HvBat	High Voltage Battery
HX	Heat exchanger
HW	Hardware
ICE	Internal combustion engine
LC	linear complementarity (system)
LDF	LIN description file
LIN	Local Interconnect Network
LP	linear programming
LTI	Linear Time-Invariant

MAC	Mobile air conditioning
MIL	Model in the Loop
MIMO	Multi-input multi-output
MIQP	Mixed integer quadratic programming
MIQCP	Mixed integer quadratic constrained programming
MLD	mixed logical dynamical (system)
MMPS	max-min-plus-scaling (system)
MPC	Model predictive control
MPTDC	Model Predictive Thermal Decision Controller
NMPC	Non-linear model predictive control
OS	Operating system
OSEM-EV	Optimised and Systematic Energy Management in Electric Vehicles
OTF	Overall Thermal Function
NTC	Negative temperature coefficient (thermistor)
PCM	Phase change material
PE	Power electronics
PHEV	Plug-in hybrid electric vehicle
PIL	Processor in the Loop
PTC	Positive temperature coefficient (heater)
PWA	Piecewise Affine
QP	Quadratic Programming
RHC	Receding Horizon Control
SIL	Software in the Loop
SOA	State-of-the-Art
SOC	State of charge
SOV	Shut-off valve
SP	Setpoint
TEMCU	Thermo-Electric Management Control Unit
TES	Thermal Energy Storage
TF	Thermal Function
TXV	Thermostatic (thermal) expansion valve
VCRS	Vapor compression refrigeration system
VS	Virtual sensor
VTMS	Vehicle thermal management system
WLTC	Worldwide Harmonized Light Vehicles Test Cycle
A	Area
c	Specific heat capacity
C	Heat capacity
e	Specific energy

E	Energy
f	Frequency
g	Gravitational acceleration
G	Thermal conductance
h	Specific enthalpy
H	Enthalpy
I	Current
L	Specific latent heat
m	Mass
$\dot{m}$	Mass flow rate
M	Mass
n	Rotational speed - revolutions per minute
p	Pressure
P	Power consumption
q	Specific heat
Q	Heat
$\dot{Q}$	Heat flow rate
R	Ideal gas constant
S	Area OR Entropy
s	Specific entropy
SC	Subcooling
SH	Superheat
SHR	Sensible heat ratio
t	Time
T	Temperature
$T_{\mathbf{s}}$	Sampling period
u	Specific internal energy
U	Internal energy
v	Velocity OR Specific volume
V	Volume
$\dot{V}$	Volume flow rate
w	Specific work
W	Work
$\dot{W}$	Work rate
η	Efficiency
κ	Air quality
ξ	Mass fraction (refrigerant quality)
ρ	Volumetric mass density
ϕ	Relative humidity

χ	Specific humidity
ω	Angular velocity

List of appendices

A Test bench electric wiring

OSEM-EV test bench wiring

	OSEM-EV test bench wiring	
	Front page	
	CEITEC BUT	Glos Jan (125430)
C:\Users\jangl_000\ownCloud\projekty\OSEM-EV\testbench\osem_testbench_wiring.vsdx	2020-04-16 08:20	Page 1/12

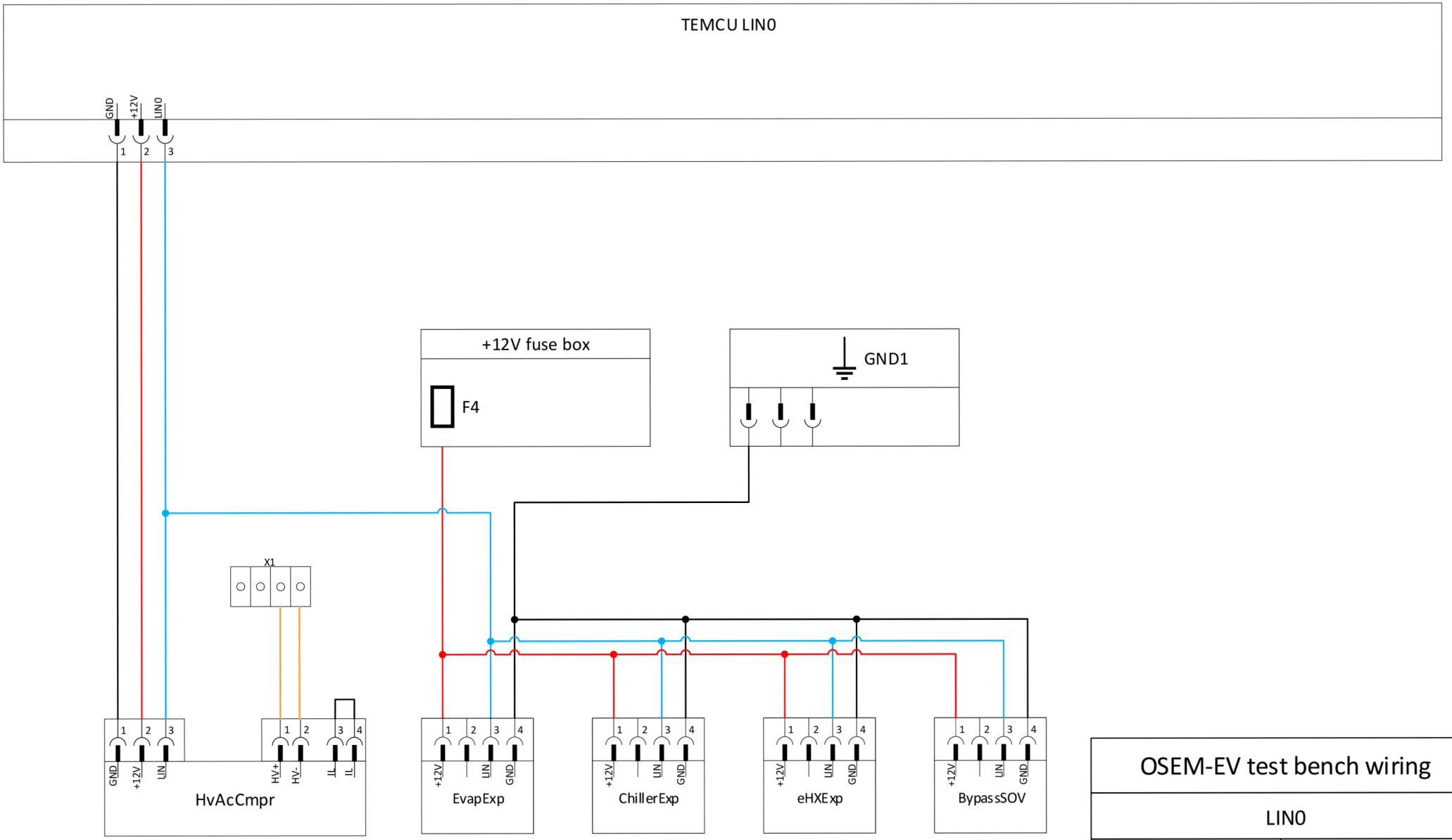

OSEM-EV test bench wiring	
LIN0	
CEITEC BUT	Glos Jan (125430)
2020-04-16 08:20	Page 2/12

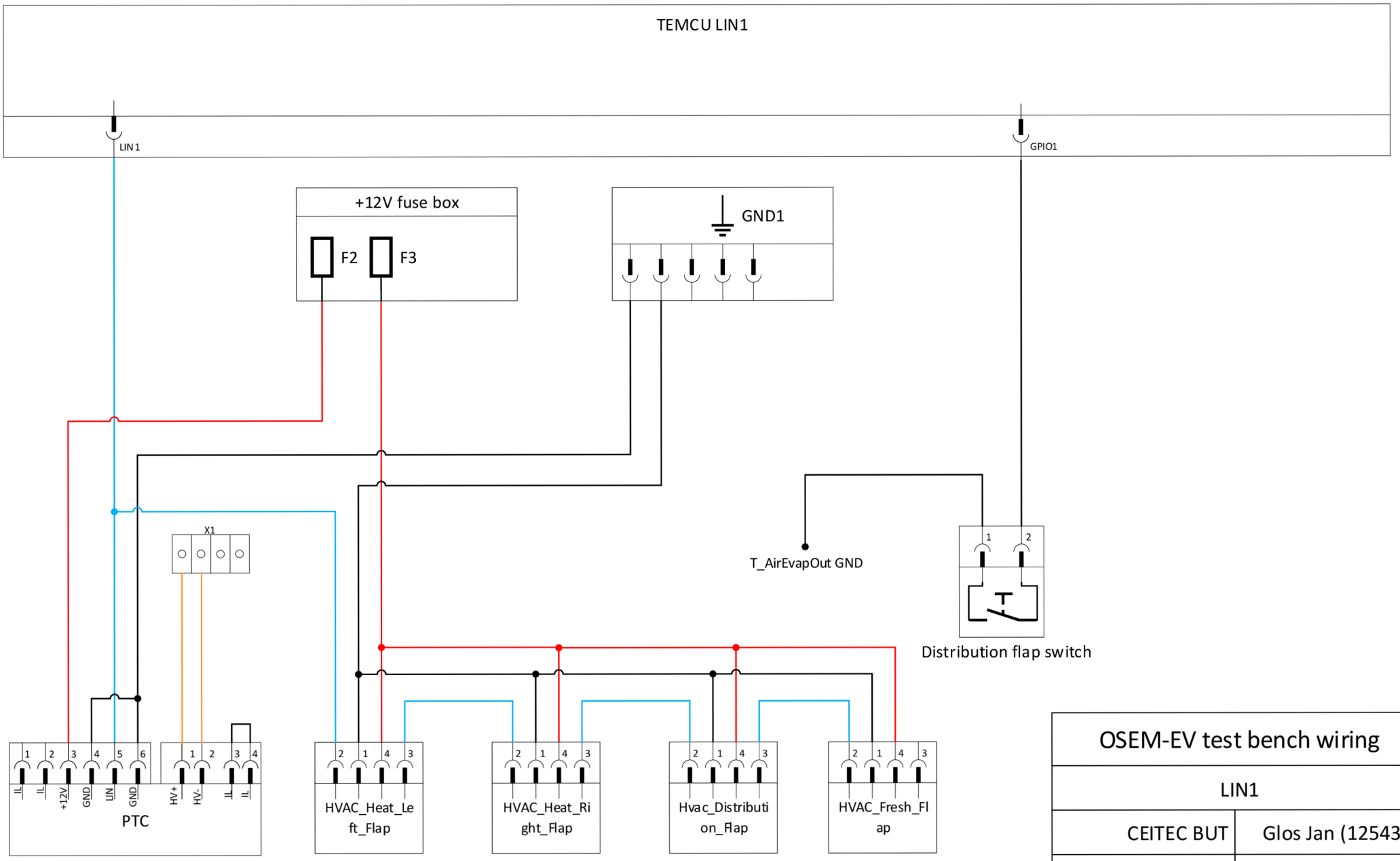

OSEM-EV test bench wiring	
LIN1	
CEITEC BUT	Glos Jan (125430)
2020-04-16 08:20	Page 3/12

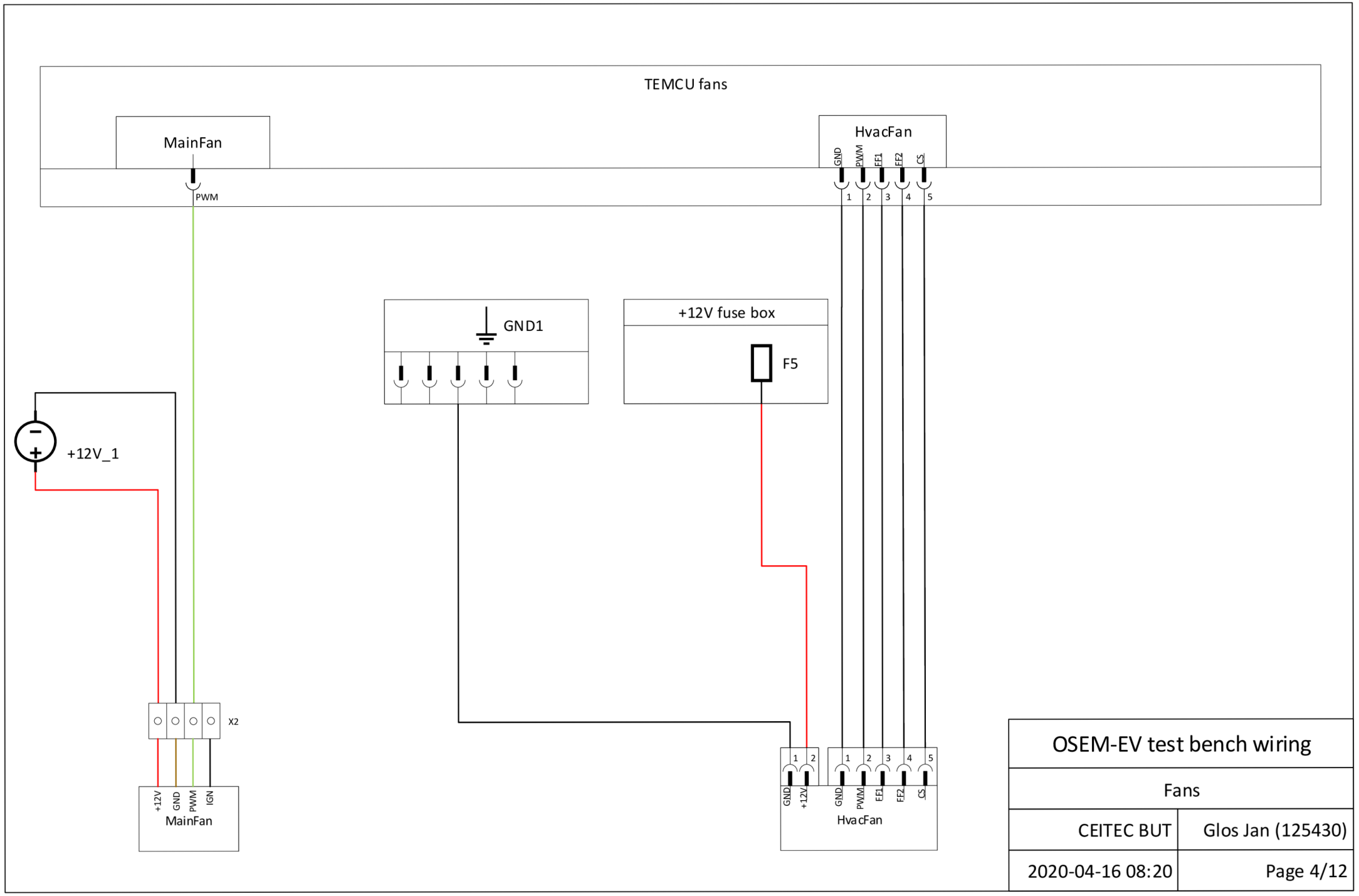
TEMCU fans
MainFan
PWM
HvacFan
GND
PWM
EF1
EF2
CS
1
2
3
4
5
GND1
+12V fuse box
F5
+12V_1
X2
+12V
GND
PWM
IGN
MainFan
1
2
GND
+12V
HvacFan
OSEM-EV test bench wiring
Fans
CEITEC BUT
Glos Jan (125430)
2020-04-16 08:20
Page 4/12

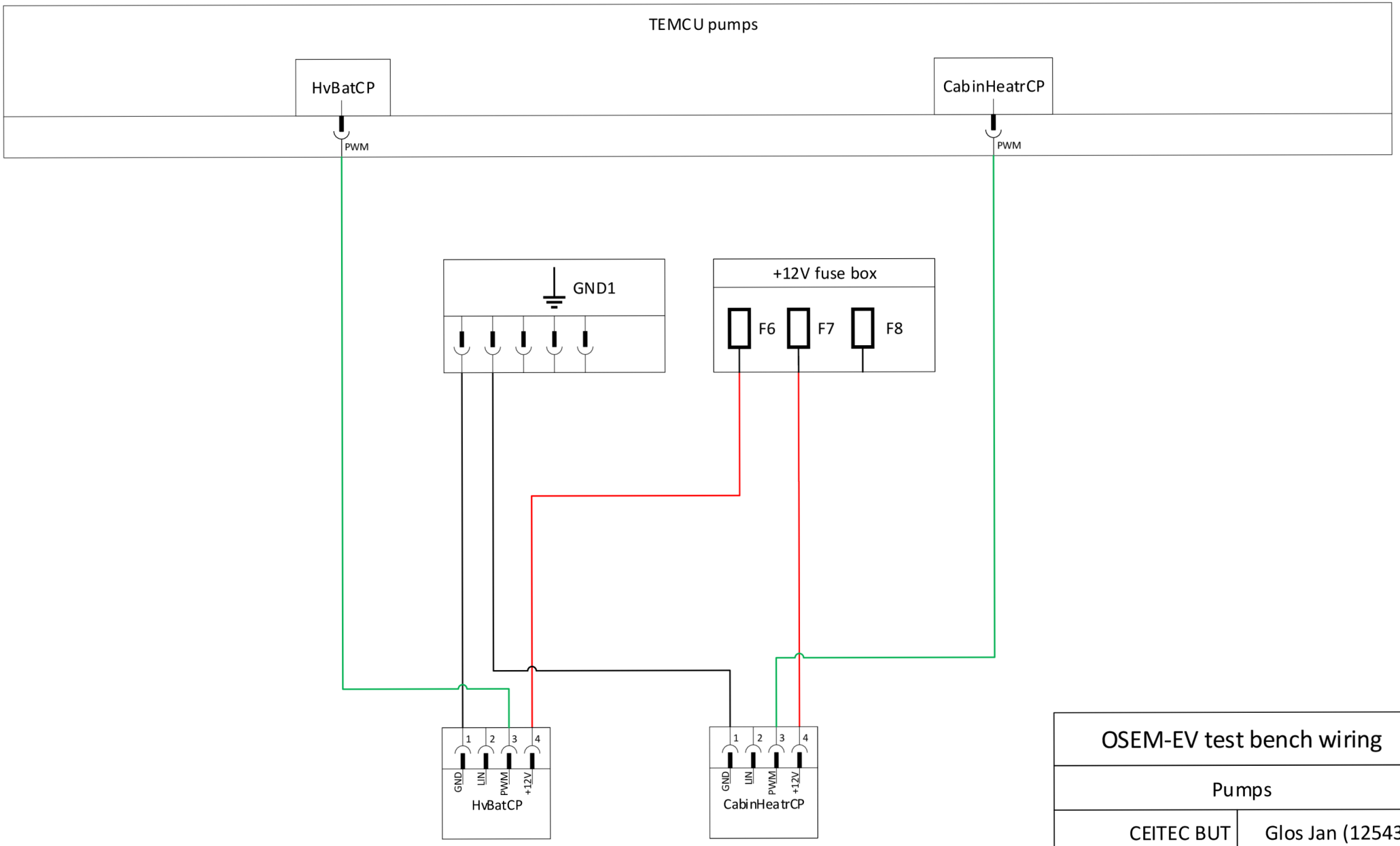

OSEM-EV test bench wiring	
Pumps	
CEITEC BUT	Glos Jan (125430)
2020-04-16 08:20	Page 5/12

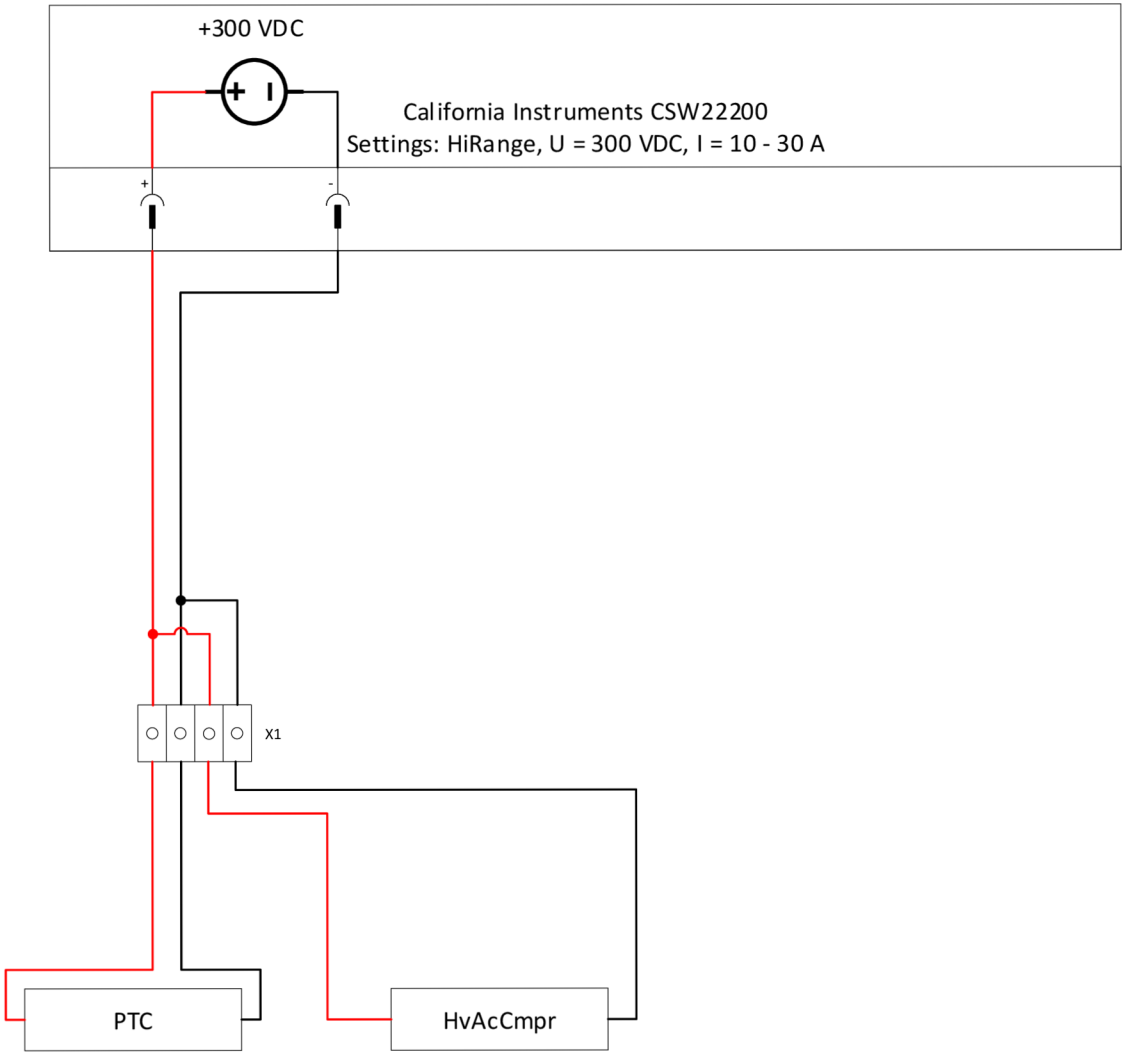

OSEM-EV test bench wiring	
Power HV	
CEITEC BUT	Glos Jan (125430)
2020-04-16 08:20	Page 6/12

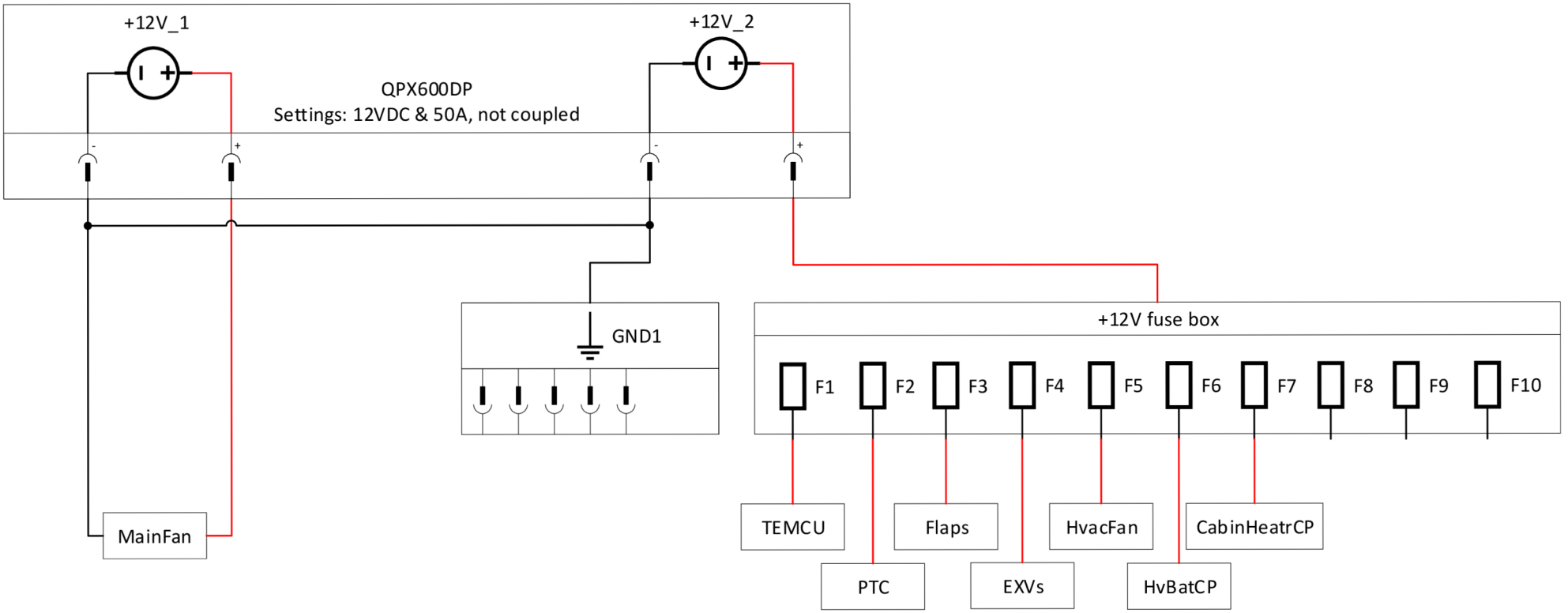

OSEM-EV test bench wiring	
Power 12V	
CEITEC BUT	Glos Jan (125430)
2020-04-16 08:20	Page 7/12

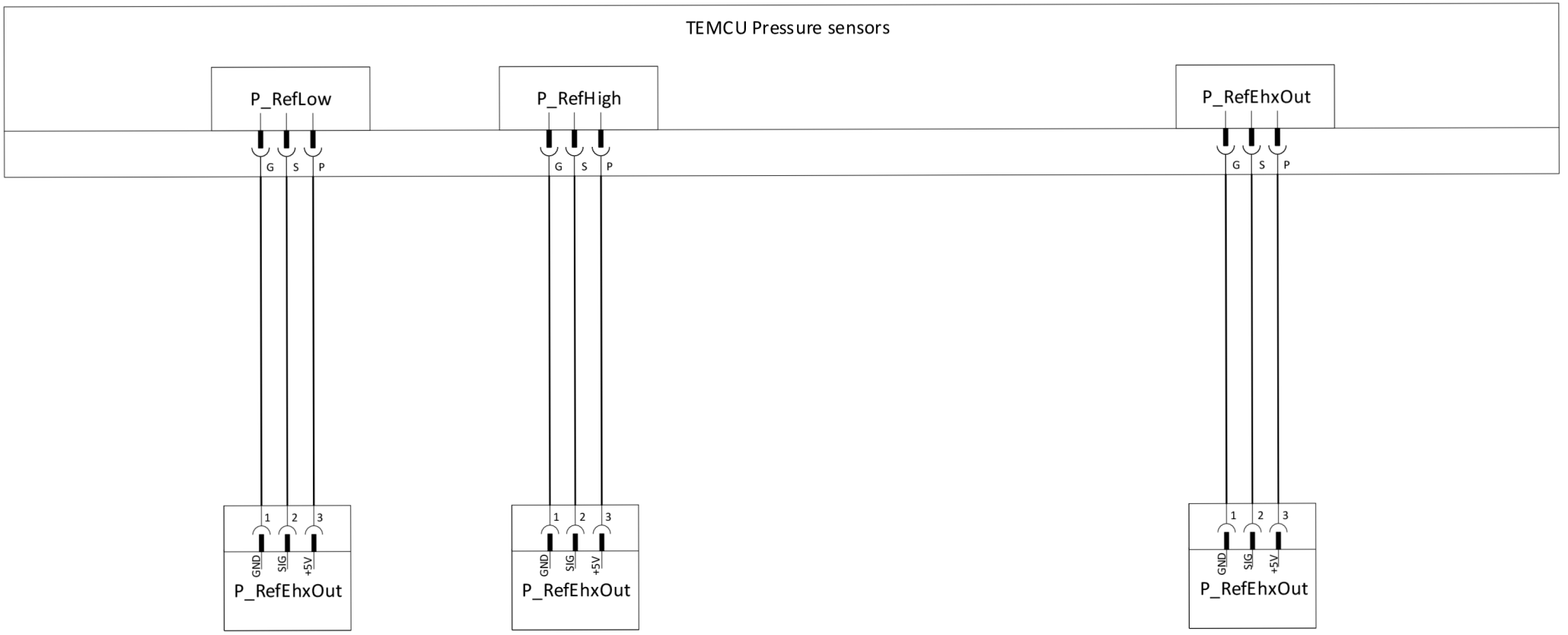

OSEM-EV test bench wiring	
Sensors - pressure	
CEITEC BUT	Glos Jan (125430)
2020-04-16 08:20	Page 8/12

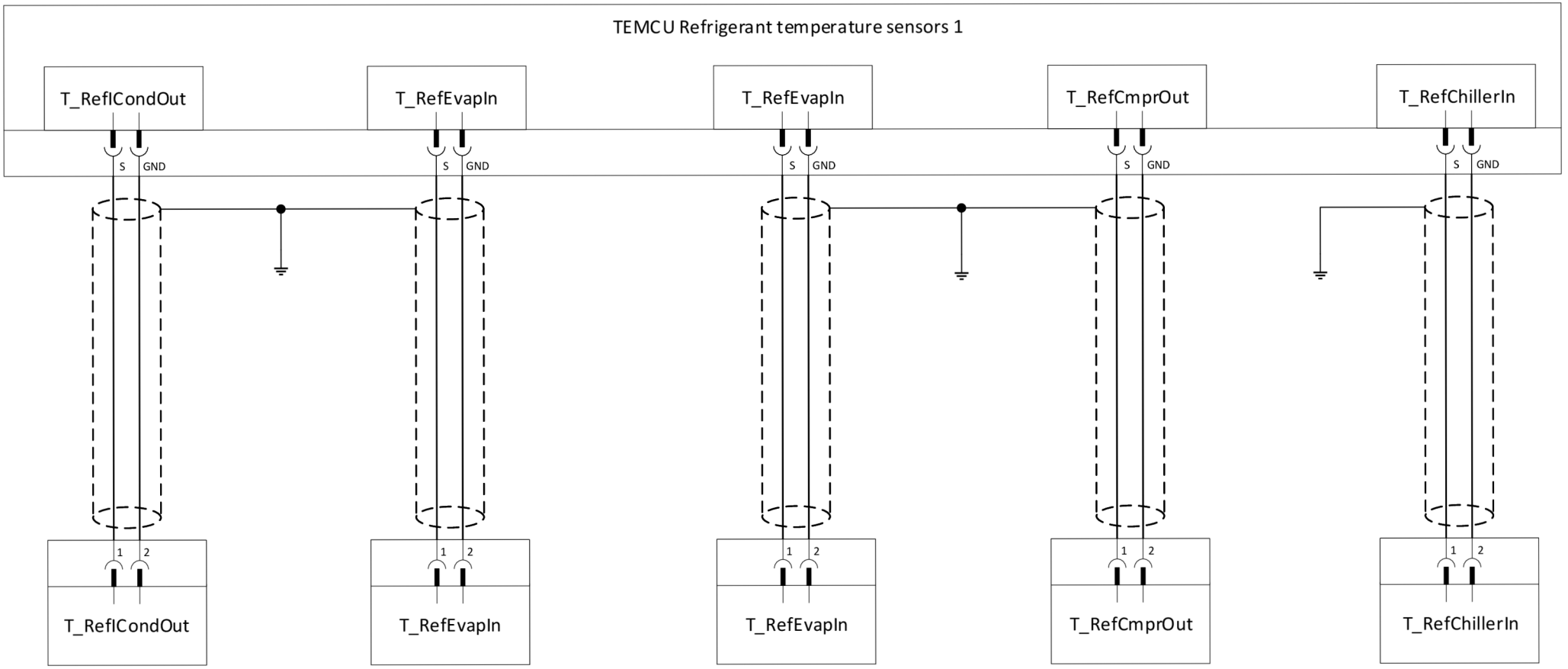

OSEM-EV test bench wiring	
Sensors - refrigerant temperature 1	
CEITEC BUT	Glos Jan (125430)
2020-04-16 08:20	Page 9/12

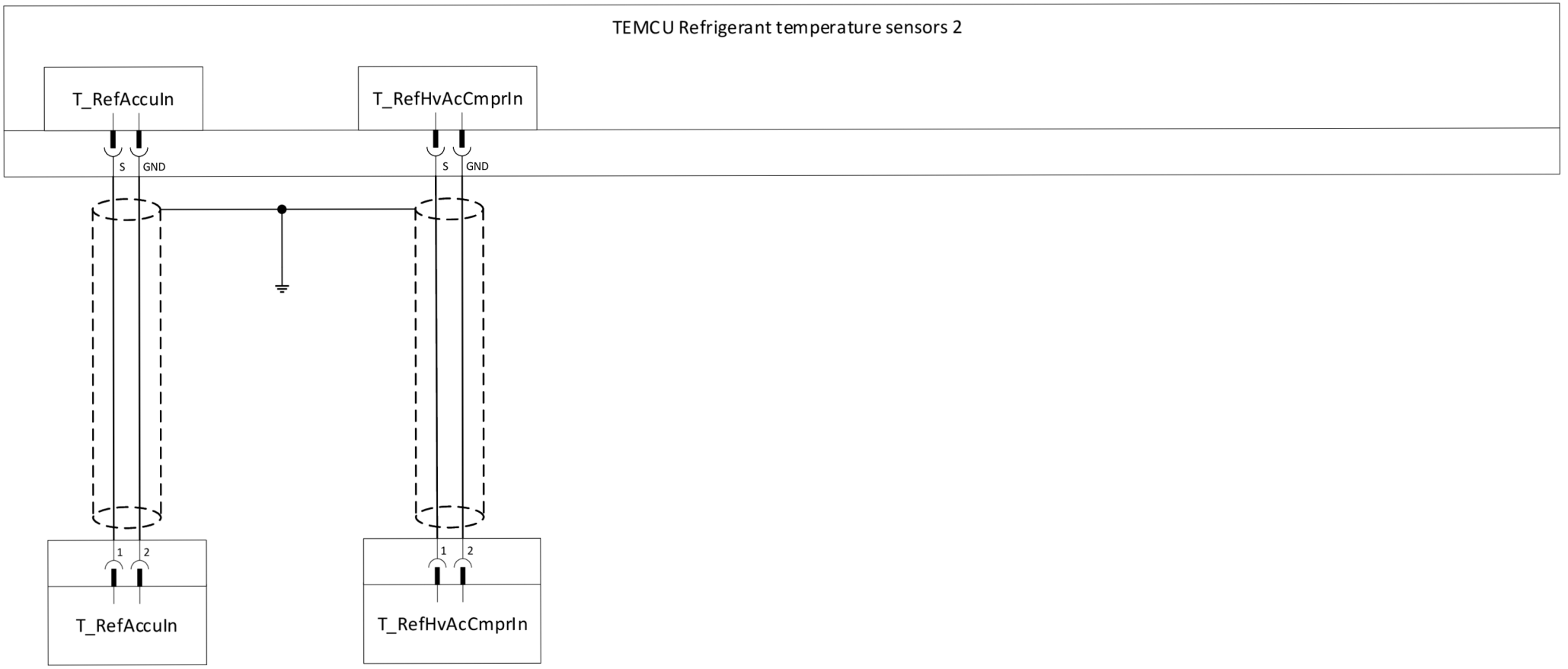

OSEM-EV test bench wiring	
Sensors - refrigerant temperature 2	
CEITEC BUT	Glos Jan (125430)
2020-04-16 08:20	Page 10/12

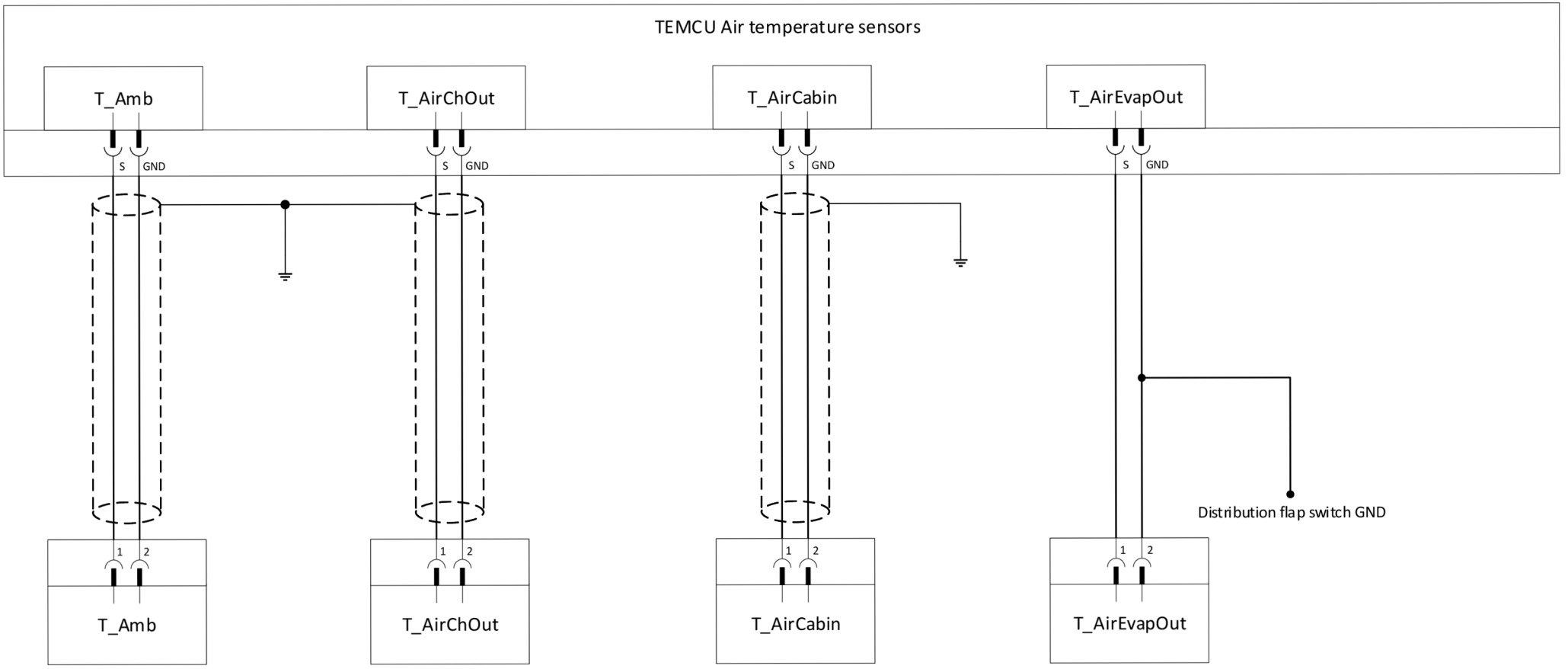

OSEM-EV test bench wiring	
Sensors - air temperature	
CEITEC BUT	Glos Jan (125430)
2020-04-16 08:20	Page 11/12

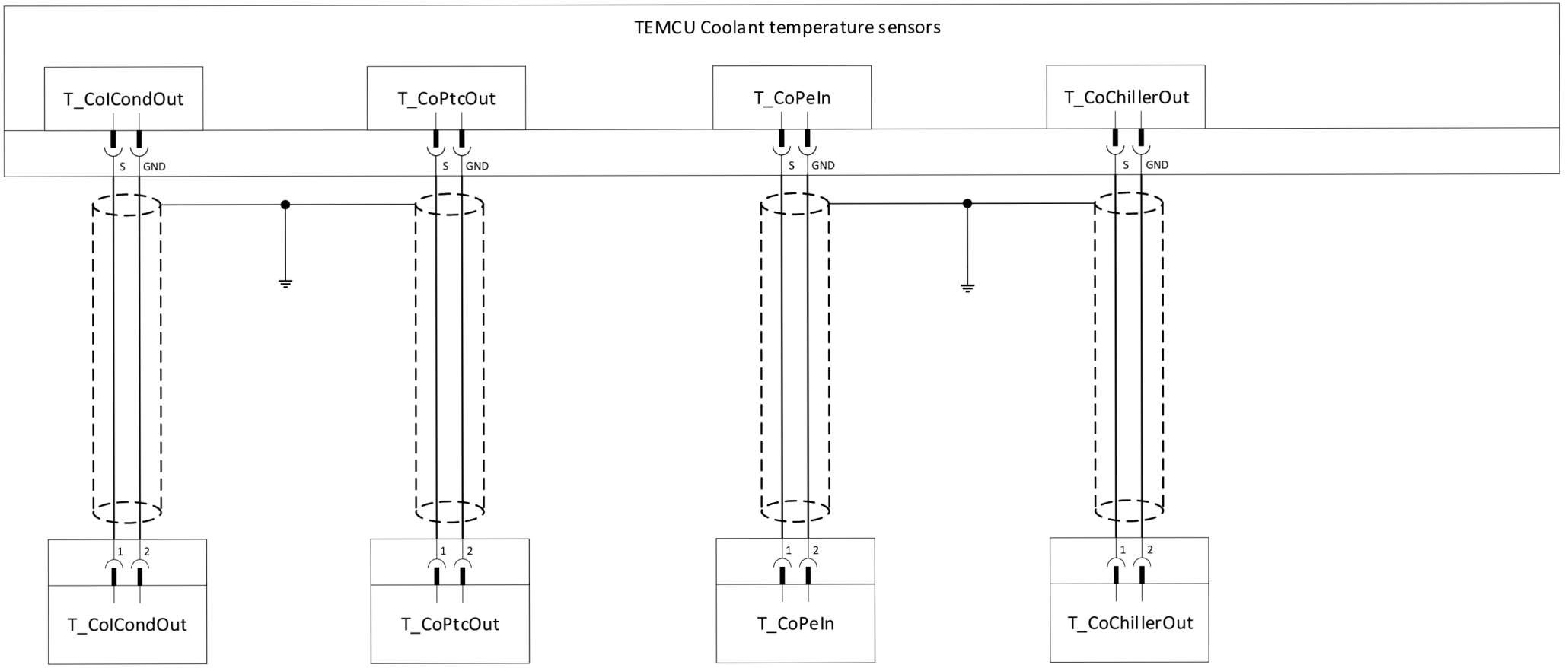

OSEM-EV test bench wiring	
Sensors - coolant temperature	
CEITEC BUT	Glos Jan (125430)
2020-04-16 08:20	Page 12/12

B Test bench pictures

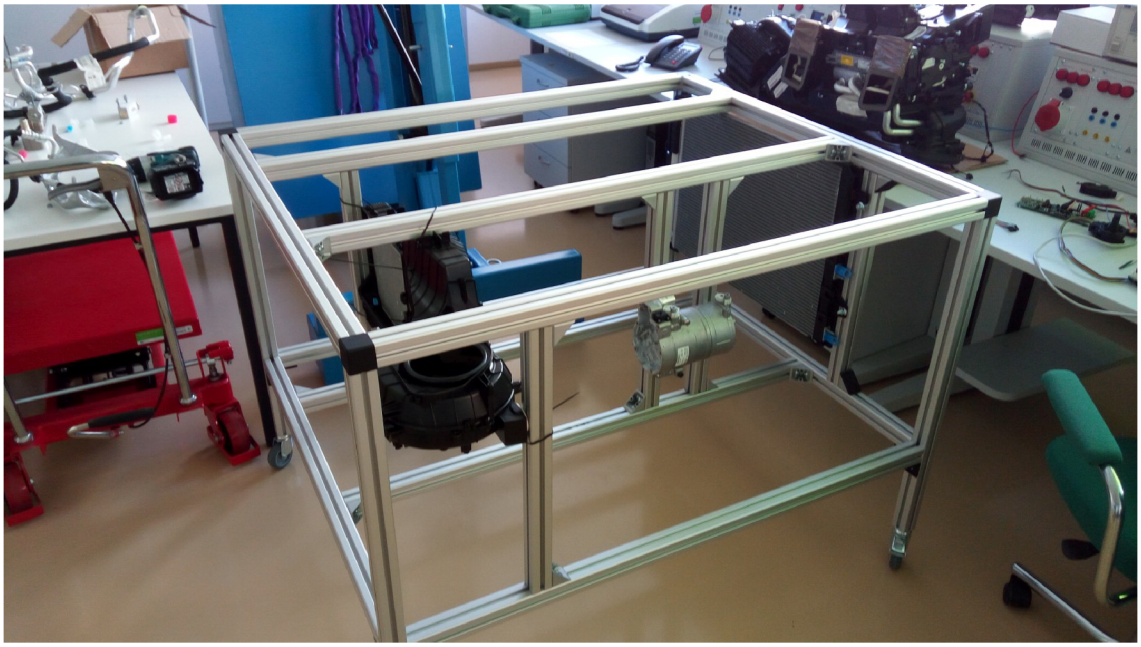

Fig. B.1: Test bench assembly - first components

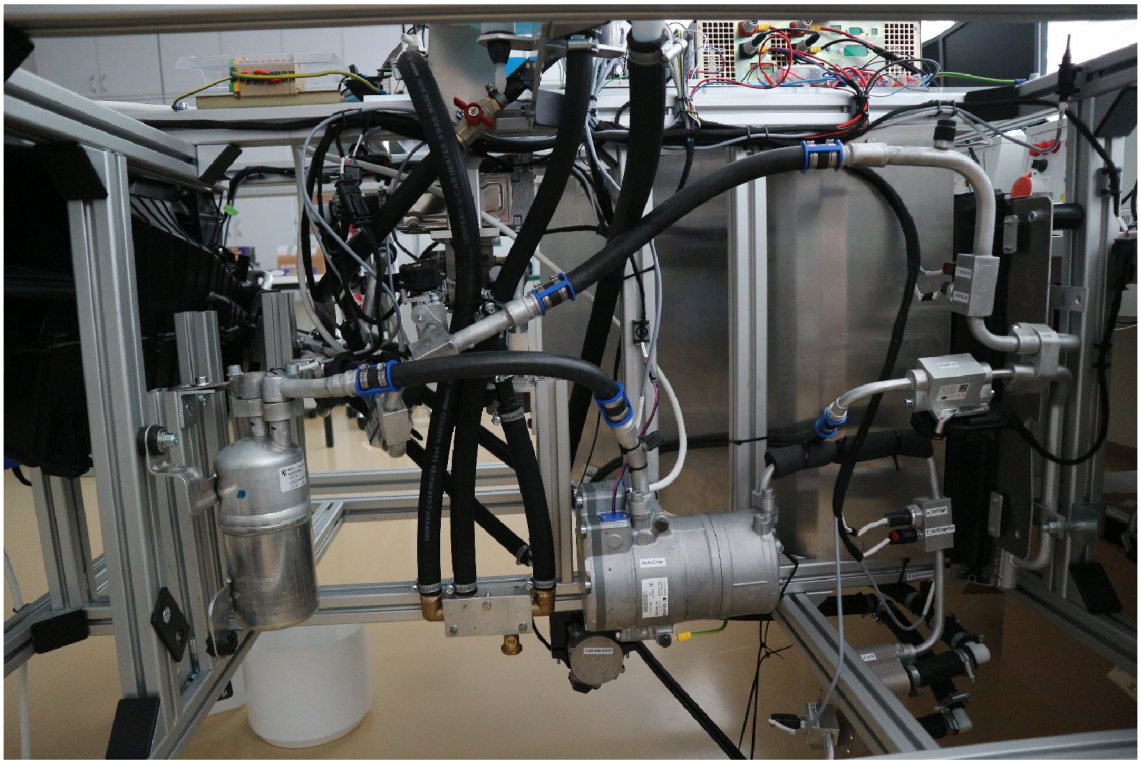

Fig. B.2: Finished test bench - right side view

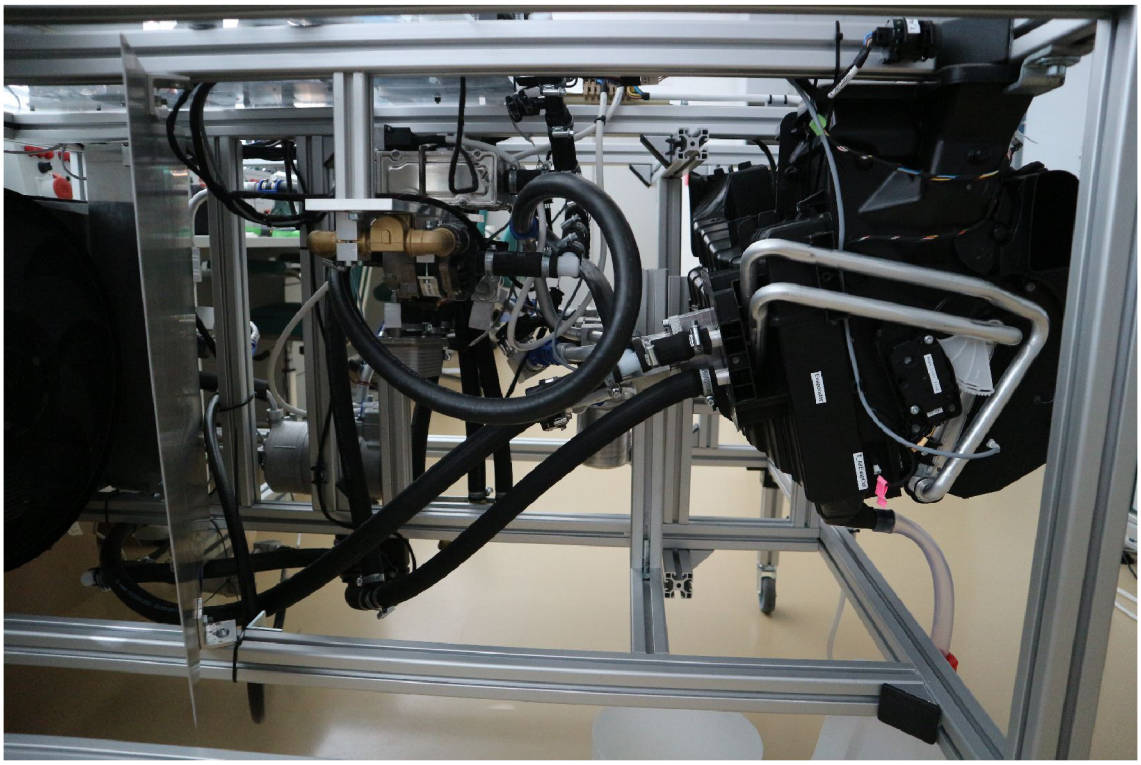

Fig. B.3: Finished test bench - left side view

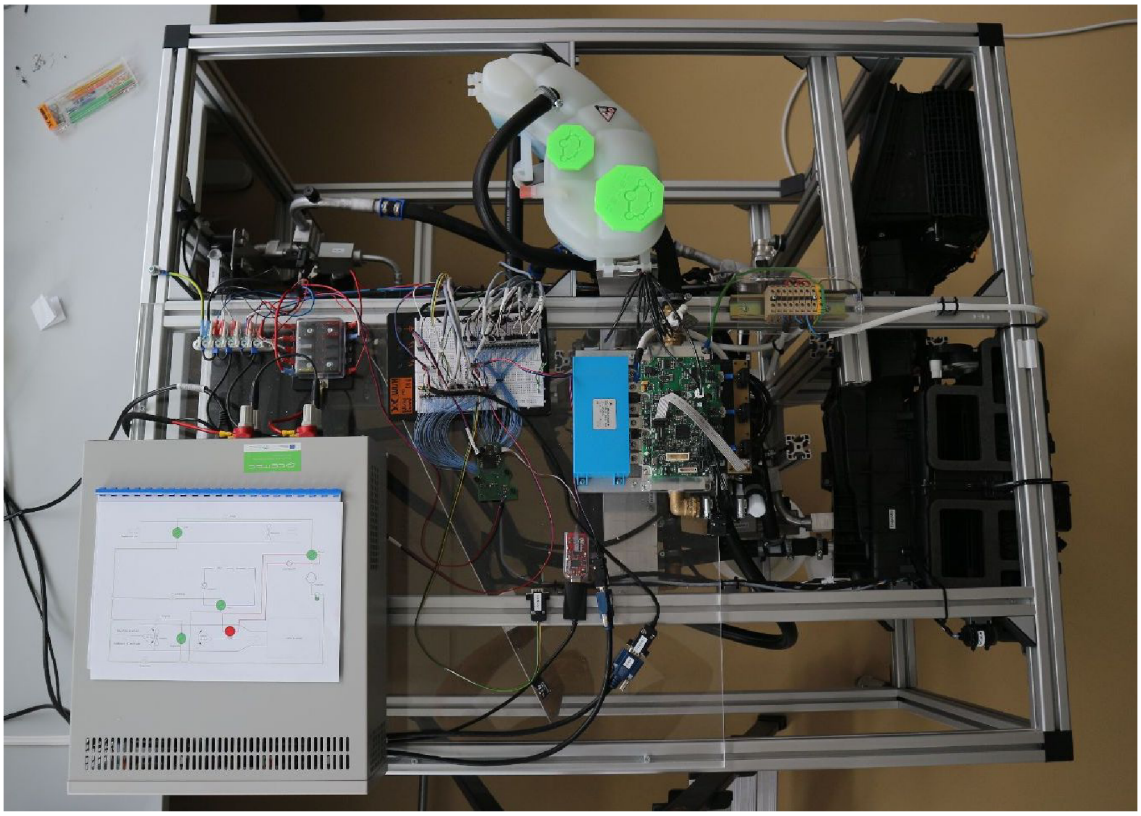

Fig. B.4: Finished test bench - top view

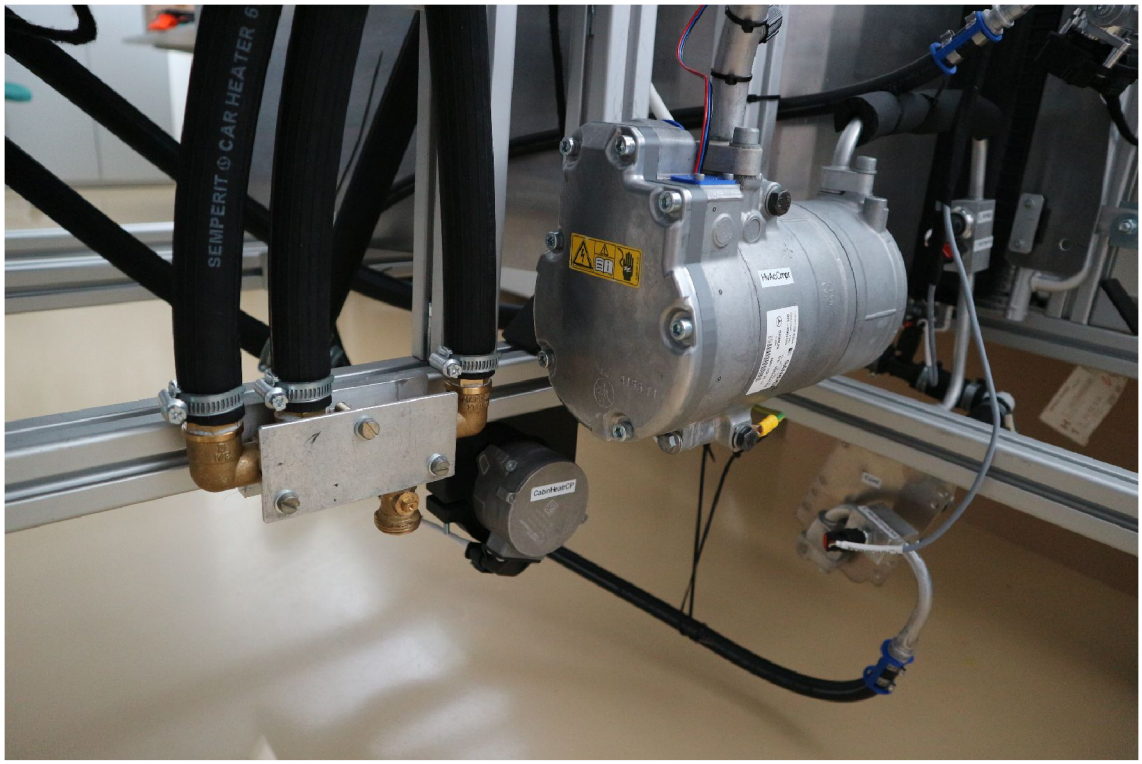

Fig. B.5: HV compressor and coolant pump

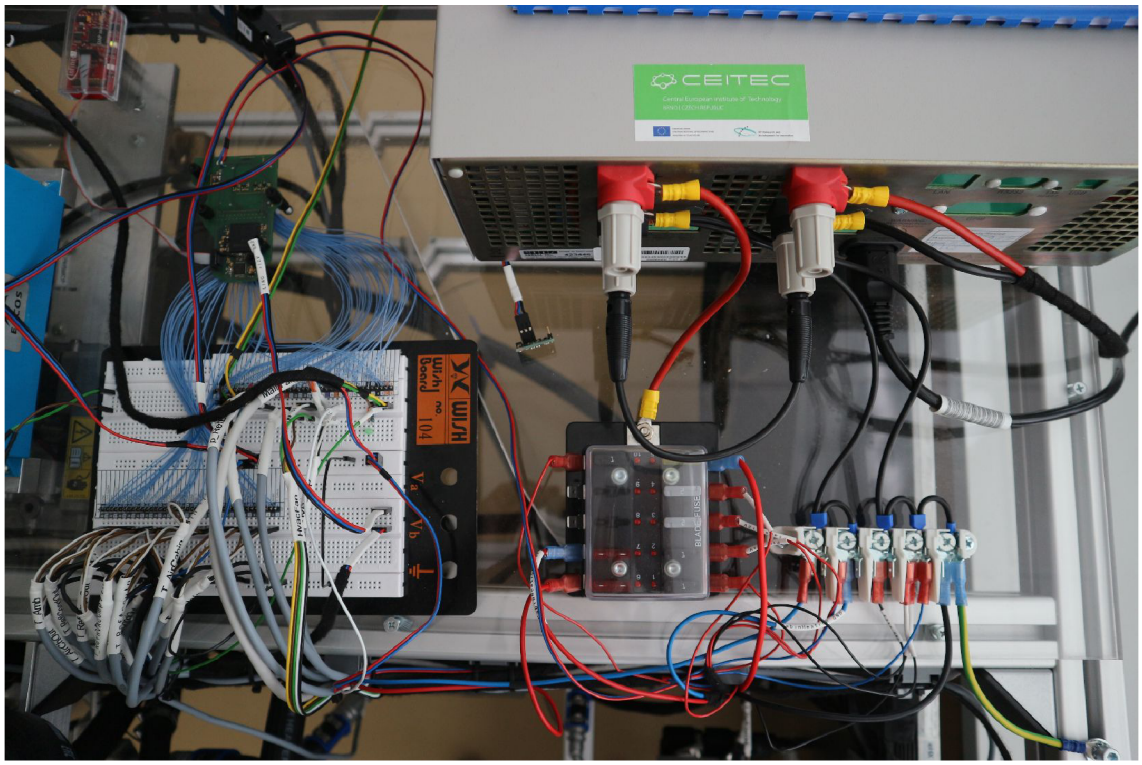

Fig. B.6: TEMCU, debug breadboard and 12 V power supply and fuse box

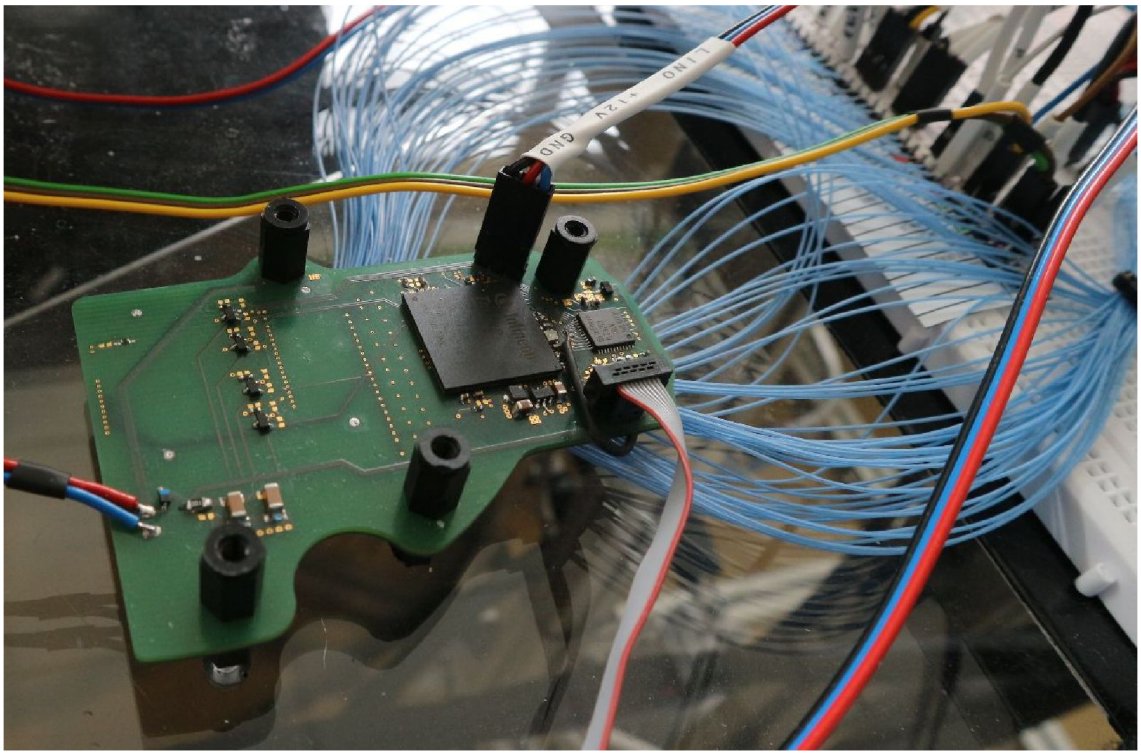

Fig. B.7: TEMCU PCB

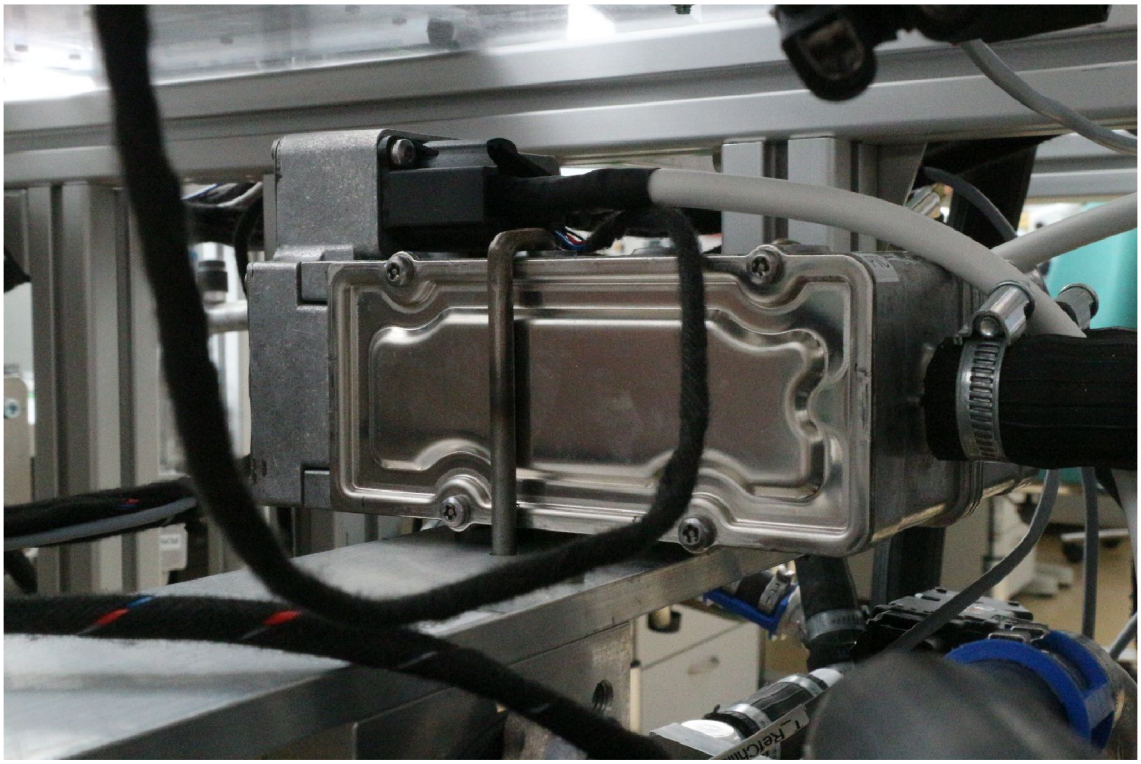

Fig. B.8: HV PTC heater

Fig. B.9: Refrigerant temperature and pressure sensors

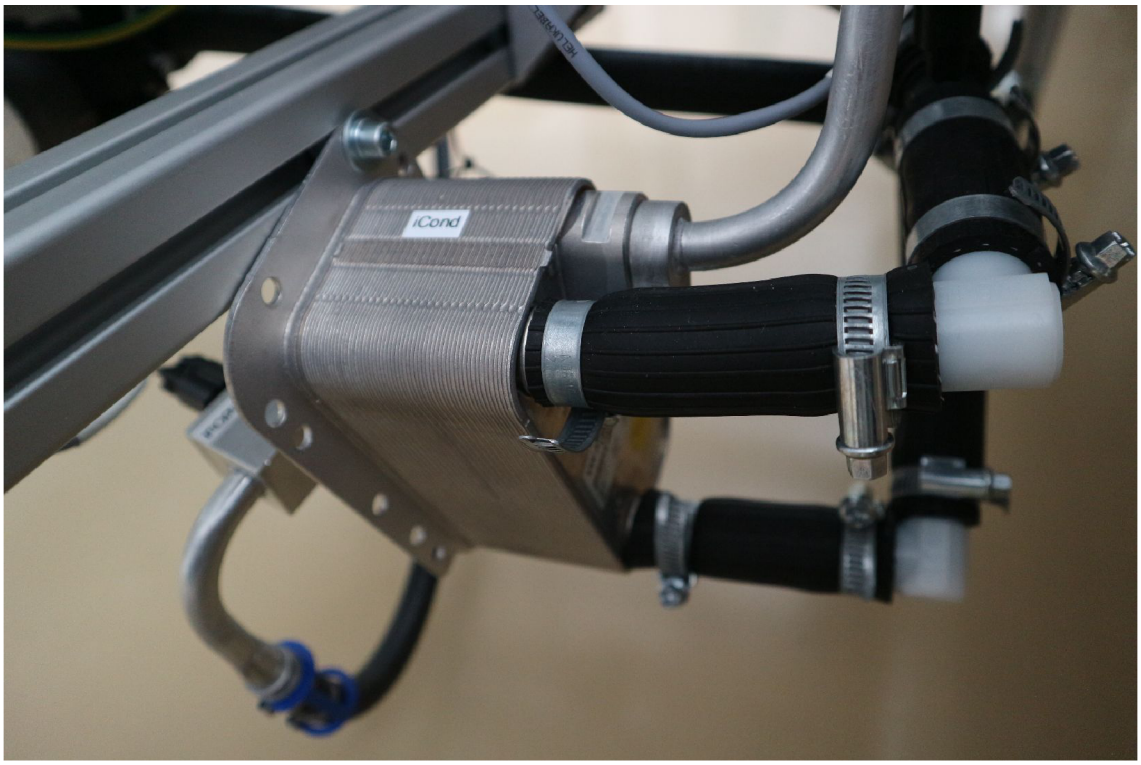

Fig. B.10: Internal condenser - iCond

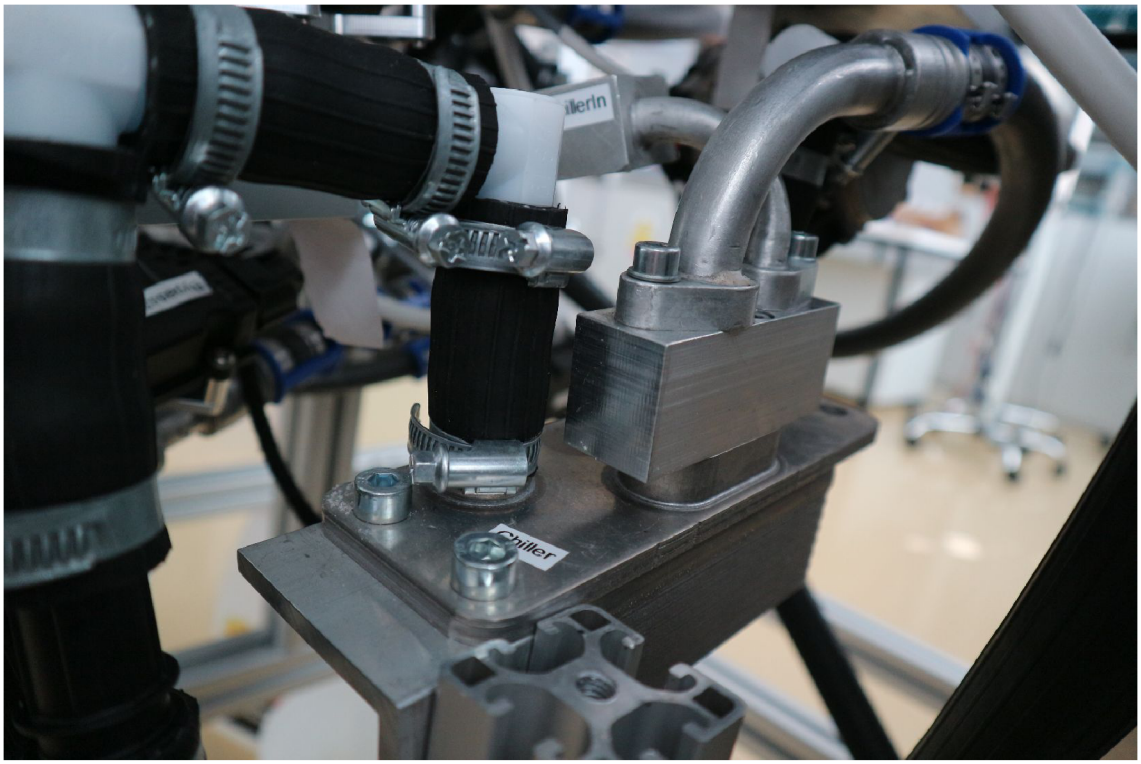

Fig. B.11: Chiller

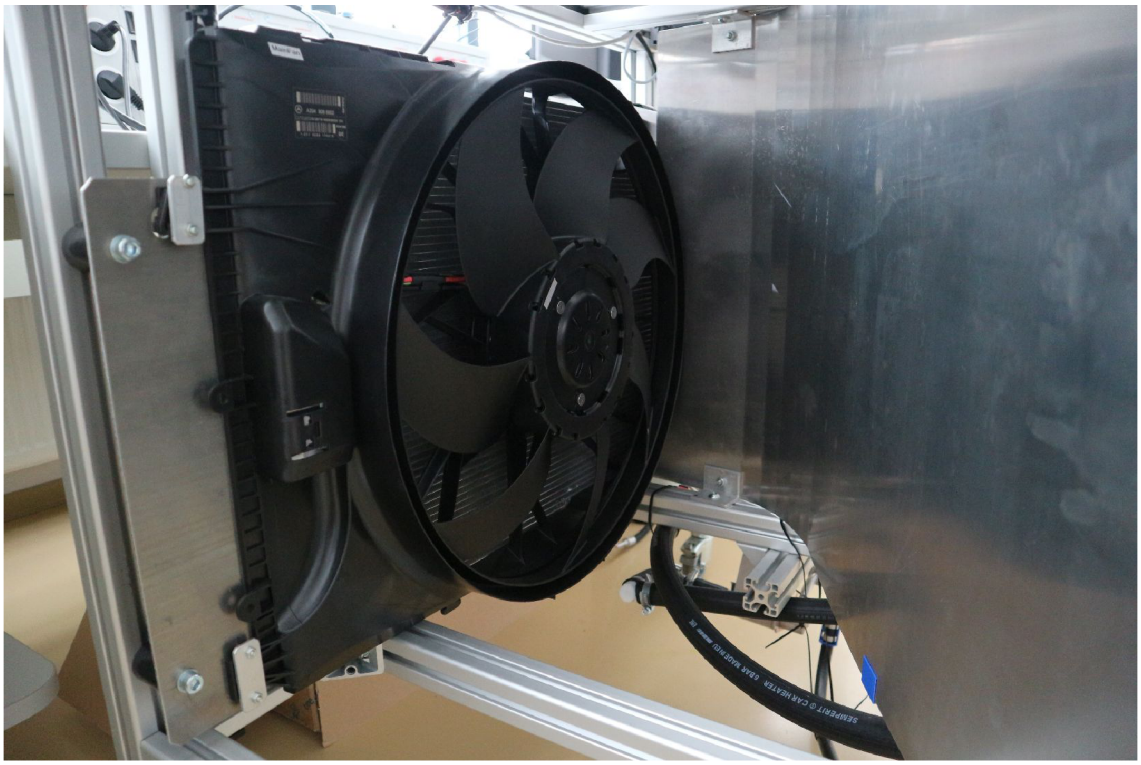

Fig. B.12: Main Fan

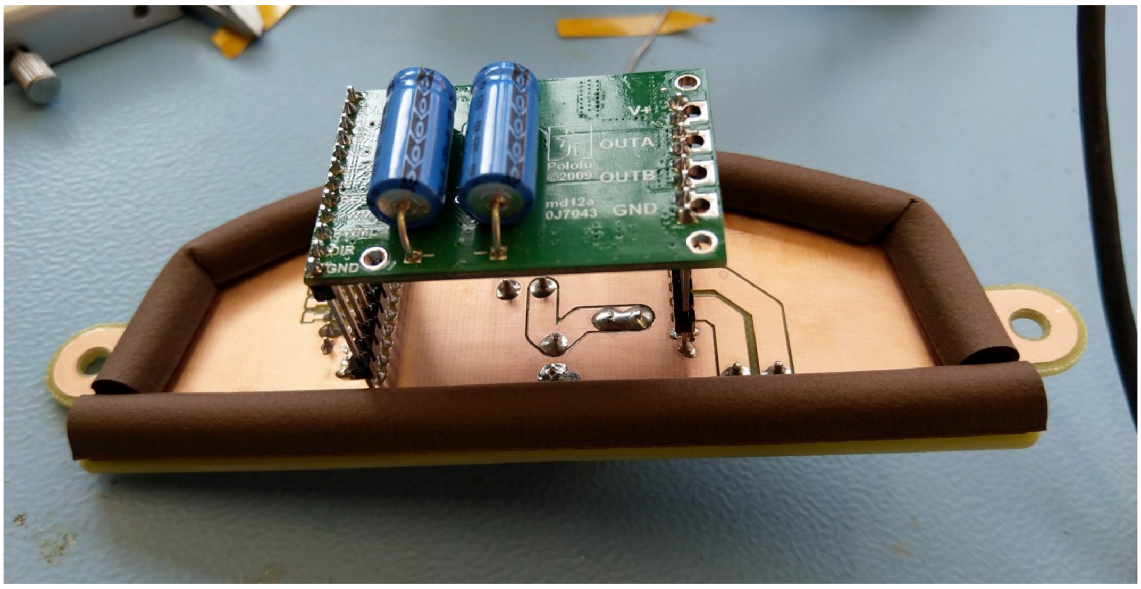

Fig. B.13: HVAC fan speed control PCB

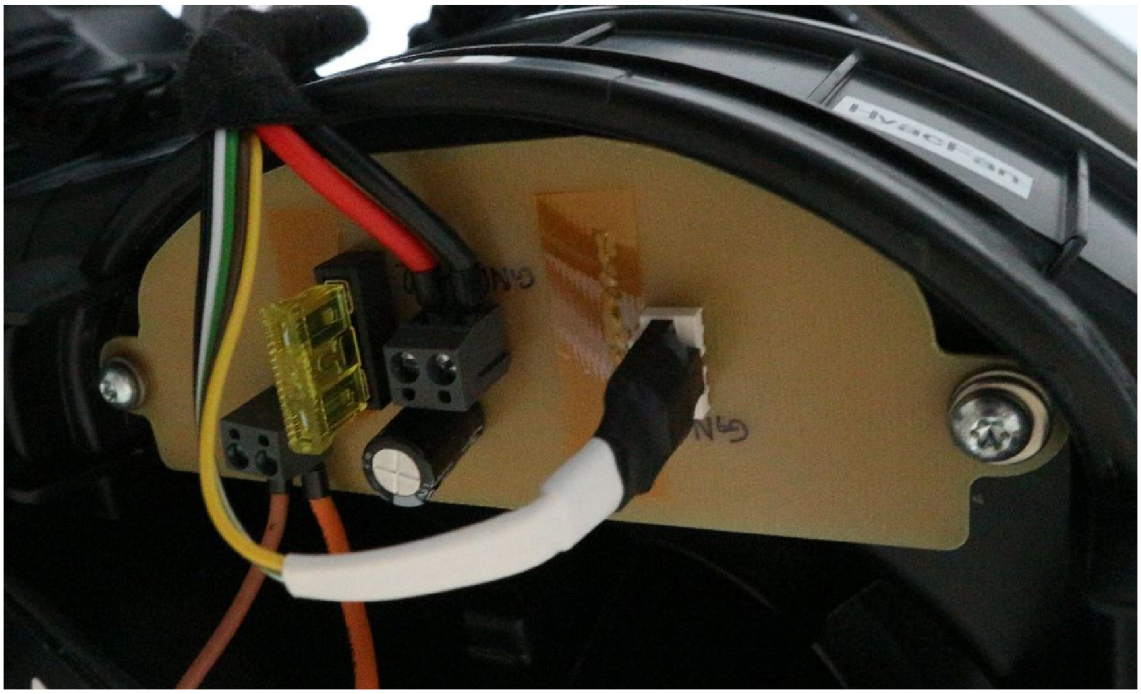

Fig. B.14: HVAC fan speed control PCB - installed

Fig. B.15: External heat exchanger (eHX) and Main Fan

C TEMCU dashboard

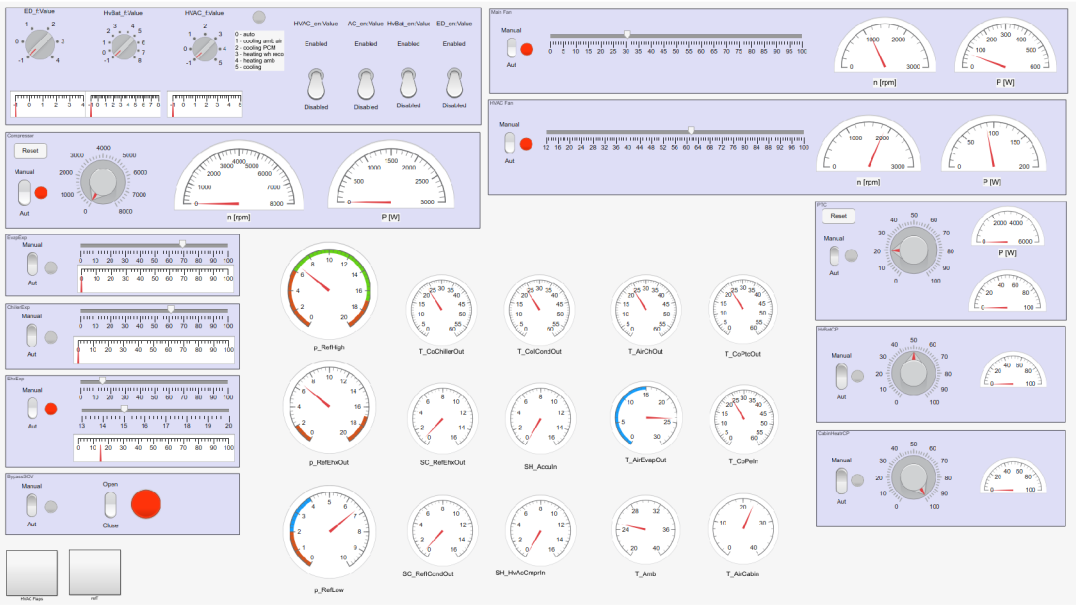

Fig. C.1: TEMCU dashboard - debug interface

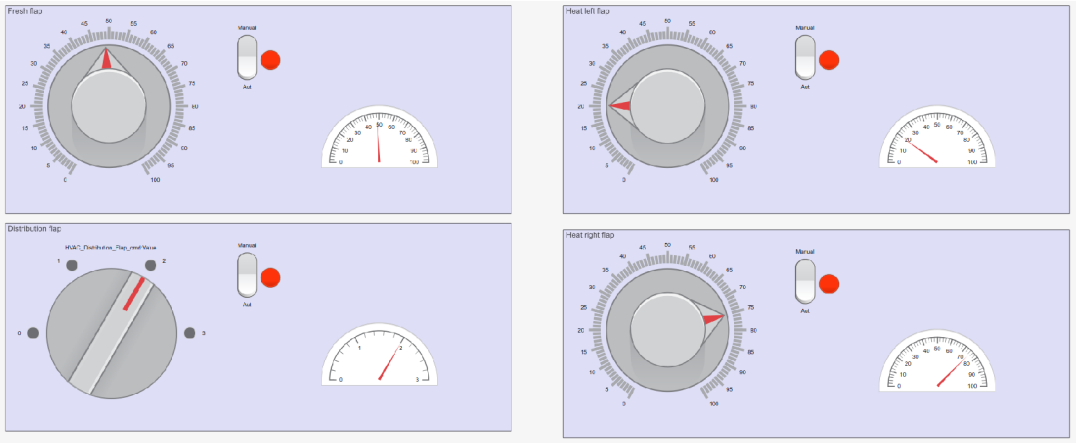

Fig. C.2: TEMCU dashboard - HVAC flaps interface

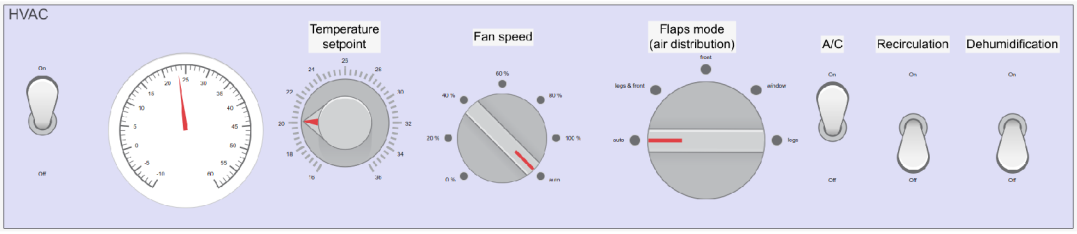

Fig. C.3: TEMCU dashboard - HMI

D Basic Thermal Decision Controller

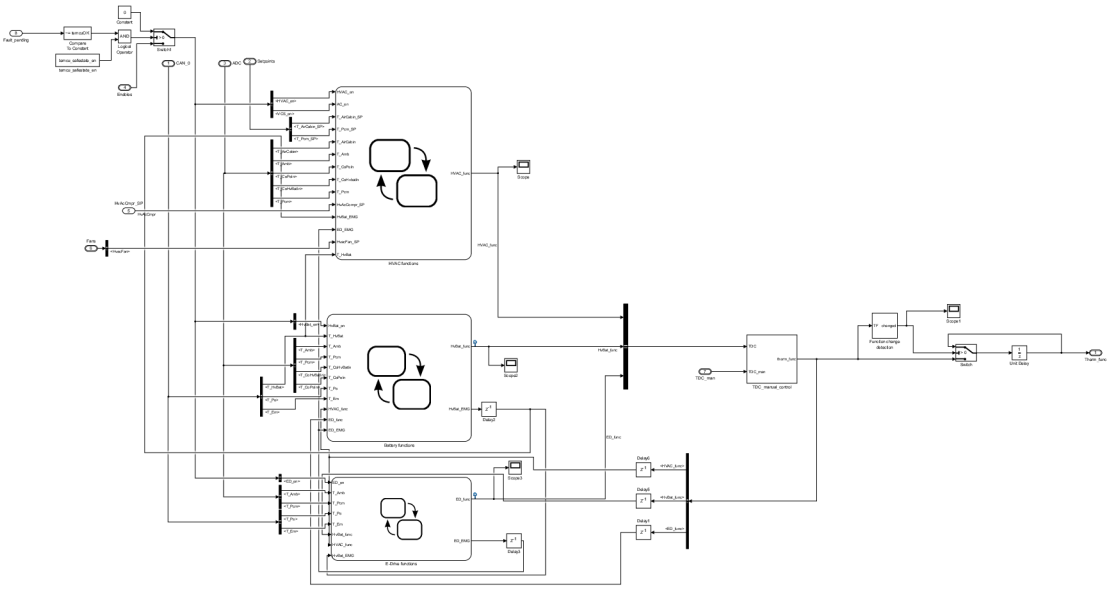

Fig. D.1: BTDC - top level schematics

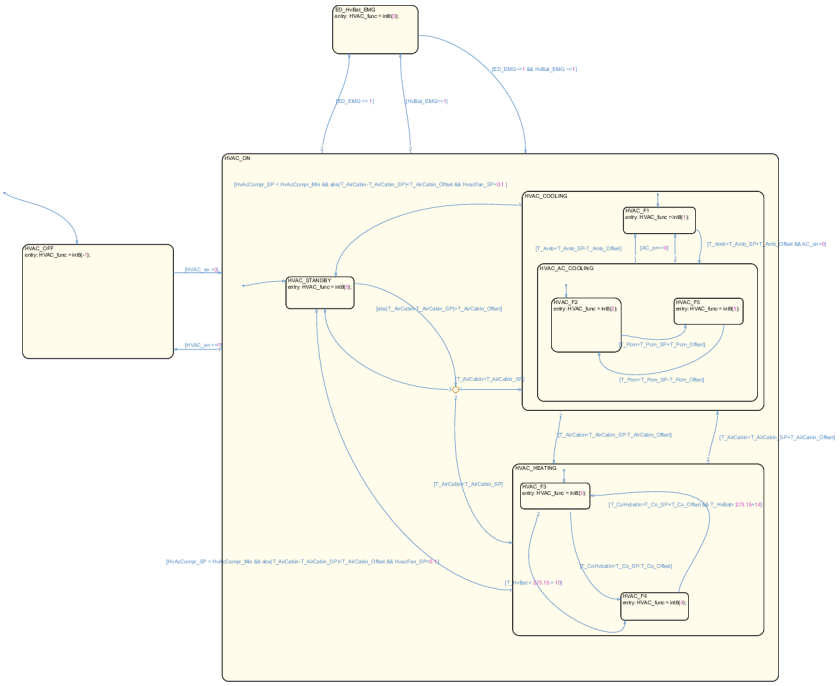

Fig. D.2: BTDC - HVAC TF selection chart

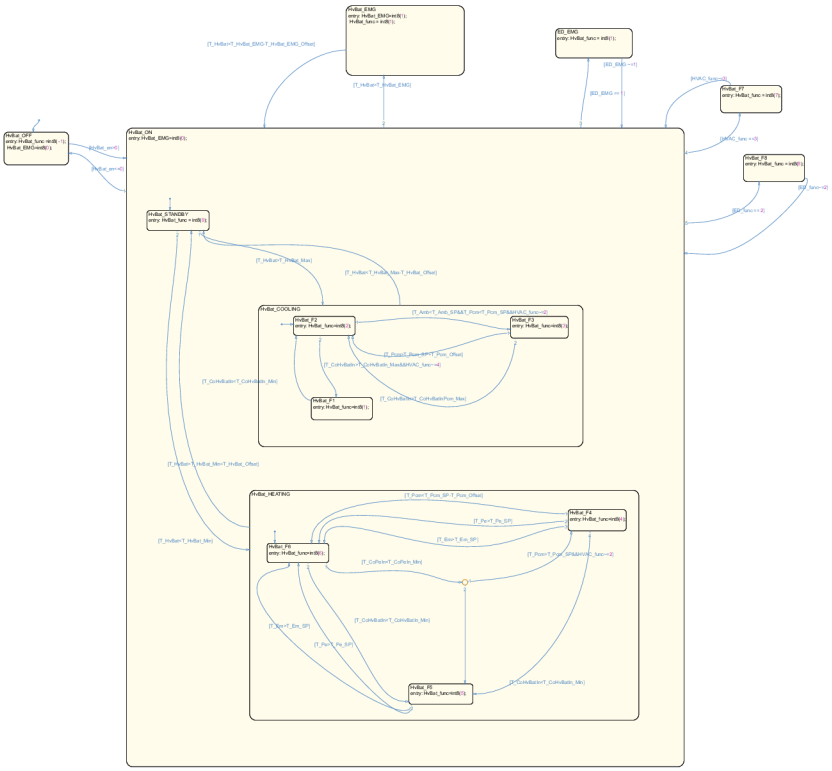

Fig. D.3: BTDC - HV Battery TF selection chart

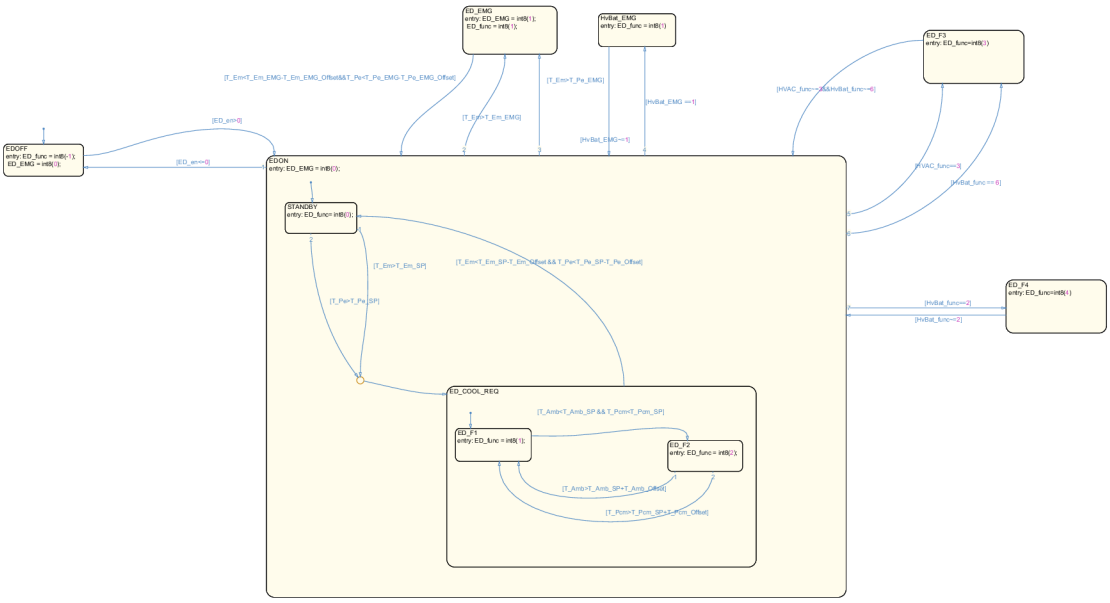

Fig. D.4: BTDC - ED TF selection chart

E Commonly used equations

This section describes the basic and commonly known equations, which were used during dynamic models assembly. These equations were taken from cited literature and all the model's equations were derived using them.

E.1 Zeroth thermodynamics law

"If two bodies are in thermal equilibrium with some third body, they are also in thermal equilibrium with each other." [70]

E.2 First thermodynamics law

From [71] we can write the First thermodynamics law as

$$\mathrm{d}E = \delta Q - \delta W, \tag{E.1}$$

$$\Delta E = Q - W, \tag{E.2}$$

where E is system energy (internal, kinetic, potential ...), Q is heat input to the system and W is work done by the system.

$$\Delta e = q - w \tag{E.3}$$

means the same as above, but is expressed in a specific form (($\mathrm{J\,kg^{-1}}$) instead of (J)). We can express the internal energy as

$$\mathrm{d}U = \delta Q - \delta W, \tag{E.4}$$

$$\mathrm{d}u = \delta q - \delta w, \tag{E.5}$$

if we can neglect changes in potential and kinetic energy. "d" stands for total differential and "δ" denotes path-dependent change.

First thermodynamic law can be also written using rate terms [72]

$$\frac{\mathrm{d}E}{\mathrm{d}t} = \dot{Q} - \dot{W}, \tag{E.6}$$

where

$$\dot{Q} = \lim_{\mathrm{d}t \to 0} \left(\frac{\delta Q}{\mathrm{d}t} \right) \tag{E.7}$$

is total heat transfer rate and

$$\dot{W} = \lim_{\mathrm{d}t \to 0} \left(\frac{\delta W}{\mathrm{d}t} \right) \tag{E.8}$$

is the total work rate done by the system.

E.3 Second thermodynamics law

E.3.1 Kelvin-Planck Statement

"It is impossible for any device that operates on a cycle to receive heat from a single reservoir and produce a net amount of work." [70]

E.3.2 Clausius statement

"It is impossible to construct a device that operates in a cycle and produces no effect other than the transfer of heat from a lower-temperature body to a higher-temperature body." [70]

E.3.3 Entropy statement

"There exists for every thermodynamic system in equilibrium an extensive scalar property called the entropy, S, such that in an infinitesimal reversible change of state of the system, $\mathrm{d}S = \mathrm{d}Q/T$, where T is the absolute temperature and $\mathrm{d}Q$ is the amount of heat received by the system. The entropy of a thermally insulated system cannot decrease and is constant if and only if all processes are reversible." [73]

E.4 Enthalpy definition

From [70] we can write enthalpy as

$$H = U + pV, \tag{E.9}$$

$$h = u + pv, \tag{E.10}$$

$$h = u + p/\rho, \tag{E.11}$$

where H is enthalpy, U is internal energy, p is pressure, V is volume. And then h is specific enthalpy, u is specific internal energy, and ρ is the volumetric mass density.

E.5 Conservation of mass

For control volume with one flow in and one flow out, we can write

$$\frac{\mathrm{d}m_{\mathrm{cv}}}{\mathrm{d}t} = \dot{m}_{\mathrm{i}} - \dot{m}_{\mathrm{o}}, \tag{E.12}$$

where m_{cv} is the mass of the control volume, $\dot{m}_{\mathrm{i}}$ and $\dot{m}_{\mathrm{o}}$ are inlet and outlet mass flow rates respectively [70].

E.6 Moist air

E.6.1 Dalton's law

In a mixture of non-reacting gases, the total pressure exerted is equal to the sum of the partial pressures of the individual gases [70]

$$p = \sum_{i=1}^{n} p_i. \tag{E.13}$$

According to Dalton's law (E.13), the pressure of moist air can be written as

$$p = p_{\mathrm{A}} + p_{\mathrm{V}}, \tag{E.14}$$

where p is the pressure of moist air, p_{A} stands for dry Air pressure and p_{V} is water Vapor pressure.

E.6.2 Clausius-Clapeyron relation

From [70] we can write the Clausius-Clapeyron relation

$$\frac{\mathrm{d}p_{\mathrm{V}}}{\mathrm{d}T} = \frac{h_{\mathrm{fg}}}{T(v_{\mathrm{g}} - v_{\mathrm{f}})}, \tag{E.15}$$

where p_{V} is the vapor pressure, T is temperature, h_{fg} is specific enthalpy needed for vaporization (specific latent heat) and v_{g} and v_{f} are specific volumes of gas and fluid respectively. The term $\frac{\mathrm{d}p_{\mathrm{V}}}{\mathrm{d}T}$ represents the slope of $p = \mathrm{p}(T)$ curves.

E.7 Steady-flow energy equation

Steady-flow energy equation (SFEE)[74]

$$\dot{m}(u + pv + \frac{1}{2}V^2 + gz)_{\mathrm{in}} - \dot{m}(u + pv + \frac{1}{2}V^2 + gz)_{\mathrm{out}} + \dot{Q} - \dot{W} = 0 \tag{E.16}$$

can be written for incompressible liquids as simplified SFEE (SSFEE)[74]

$$\dot{Q} = \dot{m}c_p(T_{\mathrm{out}} - T_{\mathrm{in}}). \tag{E.17}$$

E.8 Bernoulli's equation (principle)

Bernoulli's equation [75] can be written as

$$p_1 + \frac{1}{2}\rho v_1^2 + \rho g y_1 = p_2 + \frac{1}{2}\rho v_2^2 + \rho g y_2, \tag{E.18}$$

or

$$\frac{p_1}{\rho} + \frac{v_1^2}{2} + g y_1 = \frac{p_2}{\rho} + \frac{v_2^2}{2} + g y_2, \tag{E.19}$$

where y is the fluid elevation above a reference plane, g is the acceleration due to gravity, v is the fluid speed, p is the fluid pressure and ρ is the density of the fluid. Moreover, indexes 1 and 2 are designed for two pipe parts with different flow areas.

F VCRS model derivation

This appendix describes the derivation of the simplified VCRS model, which then serves as a basis for other parts of this thesis. This text covers only very basic implementation of the VCRS model, which could be improved e.g. by modeling heat exchangers with several cells of refrigerant and air, by adding liquid receiver/ accumulator, complementing the model with refrigeration pipes, etc. However these improvements substantially complicate the model and it gets confusing, thus the model is reported in its simplest form.

F.1 Compressor model

The compressor model was assembled based on equations from [76, 77]. For compressor mass flow rate we can write

$$\dot{m} = \frac{\omega}{2\pi}\rho V \eta_{\mathrm{vol}}, \tag{F.1}$$

where $\dot{m}$ is the mass flow rate of the compressor, ω is compressor shaft angular velocity, ρ is the refrigerant volumetric mass density at the compressor inlet, V is compressor displacement and η_{vol} is compressor volumetric efficiency.

To calculate compressor discharge enthalpy h_{o} we use isentropic efficiency coefficient

$$\eta_{\mathrm{ie}} = \frac{h_{\mathrm{o,ie}} - h_{\mathrm{i}}}{h_{\mathrm{o}} - h_{\mathrm{i}}}, \tag{F.2}$$

with $h_{\mathrm{o,ie}}$ as compressor discharge isentropic enthalpy, h_{i} compressor inlet enthalpy. Compressor discharge enthalpy we can then write as

$$h_{\mathrm{o}} = h_{\mathrm{i}} + \frac{h_{\mathrm{o,ie}} - h_{\mathrm{i}}}{\eta_{\mathrm{ie}}}. \tag{F.3}$$

If the compressor motor and power electronics are cooled by the refrigerant, (F.3) needs to be modified to

$$h_{\mathrm{o}} = h_{\mathrm{i}} + \frac{h_{\mathrm{o,ie}} - h_{\mathrm{i}}}{\eta_{\mathrm{ie}}\eta_{\mathrm{m}}\eta_{\mathrm{mot}}}, \tag{F.4}$$

where η_{m} and η_{mot} are mechanical and motor efficiencies respectively. Isentropic enthalpy can be obtained from tables as $h_{\mathrm{o,ie}} = \mathrm{h}(p_{\mathrm{o}}, s)$, where $s = \mathrm{s}(p_{\mathrm{i}}, h_{\mathrm{i}})$.

Compressor power can be also estimated from its model considering overall efficiency

$$P = \frac{P_{\mathrm{ie}}}{\eta_{\mathrm{o}}}, \tag{F.5}$$

where P_{ie} is compressor isentropic power and η_{o} stands for compressor overall efficiency

$$\eta_{\text{o}} = \eta_{\text{ie}}\eta_{\text{m}}\eta_{\text{mot}}, \tag{F.6}$$

where η_{ie} is isentropic efficiency, η_{m} mechanical efficiency and η_{mot} is motor efficiency (considering motor and inverter losses). Then we can write the shaft power as

$$P_{\text{shaft}} = \frac{P_{\text{ie}}}{\eta_{\text{ie}}} = P\eta_{\text{mot}}\eta_{\text{m}}. \tag{F.7}$$

The isentropic compressor power can be written as

$$P_{\text{ie}} = \dot{m}\Delta h_{\text{ie}}, \tag{F.8}$$

where h_{ie} is isentropic specific enthalpy difference of compressor inlet and outlet

$$h_{\text{ie}} = h_{\text{o,ie}} - h_i, \tag{F.9}$$

with $h_{2,\text{ie}}$ being the isentropic specific enthalpy at the compressor outlet. Using thermodynamic functions we can express it as

$$h_{\text{o,ie}} = \text{h}(p_{\text{o}}, \text{s}(p_{\text{i}}, T)), \tag{F.10}$$

where $h = \text{h}(p, s)$ is a thermodynamic function returning specific enthalpy based on pressure and specific entropy and $s = \text{s}(p, T)$ is a function returning specific entropy based on pressure and temperature.

F.2 EXV model

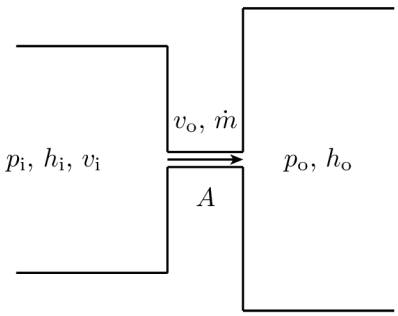

Fig. F.1: Expansion valve

Energy balance (isoenthalpic expansion):

$$h_{\text{i}} = h_{\text{o}} \tag{F.11}$$

Mass balance:

$$\dot{m}_{\mathrm{i}} + \dot{m}_{\mathrm{o}} = 0 \tag{F.12}$$

where $\dot{m}_{\mathrm{i}}$ and $\dot{m}_{\mathrm{o}}$ are mass flow rates into valve through inlet and outlet respectively.

From Bernoulli equation (E.19)

$$\frac{p_{\mathrm{i}}}{\rho} + \frac{v_{\mathrm{i}}^2}{2} + g y_{\mathrm{i}} = \frac{p_{\mathrm{o}}}{\rho} + \frac{v_{\mathrm{o}}^2}{2} + g y_{\mathrm{o}} \tag{F.13}$$

an equation for outlet fluid velocity v_{o} can be obtained. We can neglect the fluid elevation terms as valve inlet and outlet have approx. the same elevation

$$\frac{p_{\mathrm{i}}}{\rho} + \frac{v_{\mathrm{i}}^2}{2} = \frac{p_{\mathrm{o}}}{\rho} + \frac{v_{\mathrm{o}}^2}{2} \tag{F.14}$$

and after trivial modifications we get

$$v_{\mathrm{o}} = \sqrt{v_{\mathrm{i}}^2 + \frac{2}{\rho}\left(p_{\mathrm{i}} - p_{\mathrm{o}}\right)}. \tag{F.15}$$

For mass flow rate $\dot{m}$ we can write

$$\dot{m} = \dot{V}\rho = vA\rho, \tag{F.16}$$

where A stands for flow area. Then we get

$$\dot{m} = vA\rho = A\rho\sqrt{v_{\mathrm{i}}^2 + \frac{2}{\rho}\left(p_{\mathrm{i}} - p_{\mathrm{o}}\right)} \tag{F.17}$$

and by neglecting v_{i} (as it is very very small compared to other terms) we finally get

$$\dot{m} = A\sqrt{2\rho\left(p_{\mathrm{i}} - p_{\mathrm{o}}\right)}. \tag{F.18}$$

This equation can be completed by C_{d} term, which denotes the discharge coefficient. Its value is usually empirical or semi-empirical and depends on flow type (laminar, turbulent) and also on the pressure difference

$$\dot{m} = C_{\mathrm{d}} A\sqrt{2\rho\left(p_{\mathrm{i}} - p_{\mathrm{o}}\right)}. \tag{F.19}$$

Here we need to mention that the general Bernoulli equation is not fully valid for compressible flow, which usually occurs at the expansion valve outlet. However, the aim of this model is not to perfectly describe the expansion valve characteristics, but to bring some estimation of its performance. Moreover, a lot of neglect were made during the model derivation, thus it needs to be considered as the simplest approximation of expansion valve behavior. Furthermore, this equation is commonly used for expansion valve mass flow rate computation [78, 15, 79, 80, 81].

F.3 Heat exchanger model

The dynamic model of the heat exchanger consists of three main parts, the air cell, refrigerant cell and the thermal flow between them. Firstly we derive equations for moist air, as they will be needed in the air cell and then we develop the heat exchanger model.

Specific humidity

Specific humidity is defined as

$$\chi \equiv \frac{m_{\mathrm{V}}}{m_{\mathrm{A}}} = \frac{V\rho_{\mathrm{V}}}{V\rho_{\mathrm{A}}}. \tag{F.20}$$

We can write the ideal gas state equation as

$$pV = nRT, \tag{F.21}$$

with $n = \frac{m}{M}$, where m is gas mass and M is the molar mass

$$pV = \frac{m}{M}RT, \tag{F.22}$$

$$p = \rho r T, \tag{F.23}$$

where ρ is volumetric mass density and r is the specific gas constant.

Then we can substitute in (F.20) and we get

$$\chi = \frac{\rho_{\mathrm{V}}}{\rho_{\mathrm{A}}} = \frac{\frac{p_{\mathrm{V}}}{r_{\mathrm{V}}T}}{\frac{p_{\mathrm{A}}}{r_{\mathrm{A}}T}} = \frac{r_{\mathrm{A}}}{r_{\mathrm{V}}}\frac{p_{\mathrm{V}}}{p_{\mathrm{A}}}, \tag{F.24}$$

with $r_{\mathrm{A}} = 287.05\,\mathrm{J\,kg^{-1}\,K}$ and $r_{\mathrm{V}} = 461.52\,\mathrm{J\,kg^{-1}\,K}$. Finally, we can write

$$\chi = 0.622\frac{p_{\mathrm{V}}}{p_{\mathrm{A}}}. \tag{F.25}$$

Using (E.14) we get

$$\chi = 0.622\frac{p_{\mathrm{V}}}{p - p_{\mathrm{V}}}, \tag{F.26}$$

where the pressure of moist air p needs to be measured or estimated and partial pressure of water vapor can be computed using (F.37) and (F.36).

Dewpoint temperature calculation

With the following assumptions:

- latent heat is not temperature-dependent: $h_{\mathrm{fg}} \approx \mathrm{const}$
- vapor is ideal gas: $pV \approx nRT \Rightarrow v \approx \frac{RT}{p}$

- the specific volume of the liquid is negligible compared to the specific volume of the gas: $v_\mathrm{f} \ll v_\mathrm{g}$

we can write (E.15) as

$$\frac{\mathrm{d}p}{\mathrm{d}T} \approx \frac{p h_\mathrm{fg}}{R T^2} \tag{F.27}$$

or

$$\frac{\mathrm{d}p}{p} = \frac{h_\mathrm{fg}}{R} \frac{\mathrm{d}T}{T^2} \tag{F.28}$$

and after integrating

$$\int \frac{\mathrm{d}p}{p} = \frac{h_\mathrm{fg}}{R} \int \frac{\mathrm{d}T}{T^2} \tag{F.29}$$

we obtain

$$\ln p = -\frac{h_\mathrm{fg}}{R} \frac{1}{T} + \ln C. \tag{F.30}$$

Moreover, if we use definite integral, we obtain a more useful equation

$$\int_{p_1}^{p_2} \frac{\mathrm{d}p}{p} = \frac{h_\mathrm{fg}}{R} \int_{T_1}^{T_2} \frac{\mathrm{d}T}{T^2}, \tag{F.31}$$

$$\ln\left(\frac{p_2}{p_1}\right) = \frac{h_\mathrm{fg}}{R} \left(\frac{1}{T_1} - \frac{1}{T_2}\right). \tag{F.32}$$

The relative humidity is defined as the ratio of the partial pressure of water vapor to water equilibrium vapor pressure for a given temperature

$$\phi = \frac{p_\mathrm{V}}{p_\mathrm{V}^*} \cdot 100 \qquad [\%]. \tag{F.33}$$

If the relative humidity and the temperature is known, we can compute equilibrium vapor pressure p_V^*

$$\frac{p_2}{p_1} = \exp\left\{\left[\frac{h_\mathrm{fg}}{R}\left(\frac{1}{T_1} - \frac{1}{T_2}\right)\right]\right\}, \tag{F.34}$$

$$p_2 = p_1 \exp\left\{\left[\frac{h_\mathrm{fg}}{R}\left(\frac{1}{T_1} - \frac{1}{T_2}\right)\right]\right\}, \tag{F.35}$$

with p_1 and T_1 describing the reference state at triple point ($T_0 = 273.13\,\mathrm{K}, p_0 = 6.11\,\mathrm{mbar}$)

$$p_\mathrm{V}^* = p_0 \exp\left\{\left[\frac{h_\mathrm{fg}}{R}\left(\frac{1}{T_0} - \frac{1}{T}\right)\right]\right\}, \tag{F.36}$$

then the partial pressure

$$p_\mathrm{V} = p_\mathrm{V}^* \phi \tag{F.37}$$

and also the dew point temperature T_d

$$\ln\left(\frac{p_2}{p_1}\right) = \frac{h_\mathrm{fg}}{R}\left(\frac{1}{T_1} - \frac{1}{T_2}\right), \tag{F.38}$$

$$T_\mathrm{d} = \frac{1}{\frac{1}{T_0} - \frac{R}{h_\mathrm{fg}} \ln\left(\frac{p_\mathrm{V}}{p_0}\right)}. \tag{F.39}$$

F.3.1 Refrigerant cell

First of all, we derive the equations for a closed-cell with constant volume.

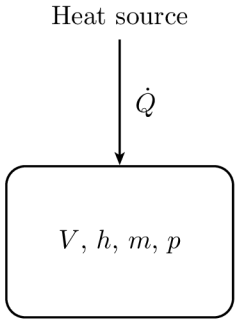

Fig. F.2: Closed and constant volume

For closed and constant volume V we can write enthalpy from (E.9) as:

$$H = U + pV \tag{F.40}$$

and in derivative form

$$\frac{\mathrm{d}H}{\mathrm{d}t} = \frac{\mathrm{d}U}{\mathrm{d}t} + \frac{\mathrm{d}(pV)}{\mathrm{d}t}, \tag{F.41}$$

$\mathrm{d}U$ we can substitute according to (E.4) and volume in term $\mathrm{d}(pV)$ is constant. As there is no work done by refrigerant, $\delta W = 0$

$$\frac{\mathrm{d}H}{\mathrm{d}t} = \frac{\delta Q - \delta W}{\mathrm{d}t} + \frac{V\,\mathrm{d}p}{\mathrm{d}t}, \tag{F.42}$$

$$\frac{\mathrm{d}H}{\mathrm{d}t} = \frac{\delta Q}{\mathrm{d}t} + \frac{V\,\mathrm{d}p}{\mathrm{d}t}. \tag{F.43}$$

For the term $\frac{\delta Q}{\mathrm{d}t}$ we will use the abbreviation $\dot{Q}$ (heat flow rate)

$$\frac{\mathrm{d}H}{\mathrm{d}t} = \dot{Q} + V\frac{\mathrm{d}p}{\mathrm{d}t}. \tag{F.44}$$

A volume enthalpy we can write as $H = m \cdot h$, where m is volume mass and h is volume specific enthalpy. After inserting into (F.44) we get

$$\frac{\mathrm{d}(hm)}{\mathrm{d}t} = \dot{Q} + V\frac{\mathrm{d}p}{\mathrm{d}t}, \tag{F.45}$$

$$\frac{h\,\mathrm{d}m + m\,\mathrm{d}h}{\mathrm{d}t} = \dot{Q} + V\frac{\mathrm{d}p}{\mathrm{d}t} \tag{F.46}$$

and finally for closed ($\mathrm{d}m = 0$) and constant volume we have

$$\frac{\mathrm{d}h}{\mathrm{d}t} = \frac{1}{m}\left(\dot{Q} + V\frac{\mathrm{d}p}{\mathrm{d}t}\right). \tag{F.47}$$

As the heat exchanger is not closed, the inlet and outlet of the refrigerant cell were introduced in Fig. F.3 and we will derive the equations for an open cell with constant volume.

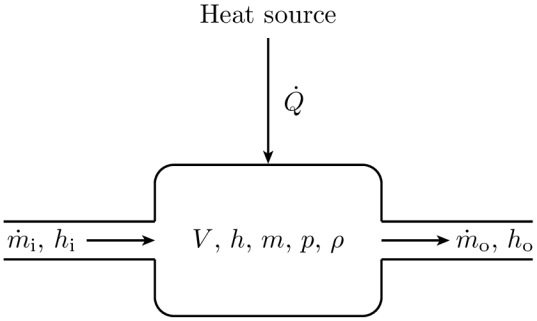

Fig. F.3: Open and constant volume

For open and constant volume V, we use (F.46) and move the term $\frac{h\mathrm{d}m}{\mathrm{d}t}$ to the right side of the equation

$$m\frac{\mathrm{d}h}{\mathrm{d}t} = \dot{Q} + V\frac{\mathrm{d}p}{\mathrm{d}t} - h\frac{\mathrm{d}m}{\mathrm{d}t} \tag{F.48}$$

and we will use modified first law equation

$$\mathrm{d}U = \delta Q - \delta W + \mathrm{d}U_\mathrm{in} - \mathrm{d}U_\mathrm{out} \tag{F.49}$$

and it can be shown that energy flow is $\dot{m}h$ (particularly $\dot{m}(u+pv)$ where pv is flow work). Then we obtain a new equation (by simply adding flow terms)

$$m\frac{\mathrm{d}h}{\mathrm{d}t} = \dot{Q} + \dot{m}_\mathrm{i}h_\mathrm{i} - \dot{m}_\mathrm{o}h_\mathrm{o} + V\frac{\mathrm{d}p}{\mathrm{d}t} - h\frac{\mathrm{d}m}{\mathrm{d}t}, \tag{F.50}$$

where we can substitute $\frac{\mathrm{d}m}{\mathrm{d}t} = \dot{m}_\mathrm{i} - \dot{m}_\mathrm{o}$ and get

$$m\frac{\mathrm{d}h}{\mathrm{d}t} = \dot{Q} + \dot{m}_\mathrm{i}h_\mathrm{i} - \dot{m}_\mathrm{o}h_\mathrm{o} + V\frac{\mathrm{d}p}{\mathrm{d}t} - h\dot{m}_\mathrm{i} + h\dot{m}_\mathrm{o}. \tag{F.51}$$

As we consider the control volume with lumped variables, $h_\mathrm{o} = h$, thus we have

$$\frac{\mathrm{d}h_\mathrm{o}}{\mathrm{d}t} = \frac{1}{m}\left(\dot{Q} + \dot{m}_\mathrm{i}(h_\mathrm{i} - h_\mathrm{o}) + V\frac{\mathrm{d}p}{\mathrm{d}t}\right). \tag{F.52}$$

For mass conservation, we can write

$$\dot{m}_\mathrm{i} - \dot{m}_\mathrm{o} = \frac{\mathrm{d}m}{\mathrm{d}t} = \frac{\mathrm{d}(\rho V)}{\mathrm{d}t} = V\left[\left(\frac{\partial\rho}{\partial p}\right)_h\frac{\mathrm{d}p}{\mathrm{d}t} + \left(\frac{\partial\rho}{\partial h}\right)_p\frac{\mathrm{d}h}{\mathrm{d}t}\right]. \tag{F.53}$$

For both the closed and open volume the pressure can be obtained using equation

$$p = \mathrm{p}(h, \rho), \tag{F.54}$$

which is dependent on refrigerant and can be solved using refrigerant tables, approximate functions, etc.

It is also necessary to use some trivial equations to make the problem clear

$$m = V\rho, \tag{F.55}$$

$$\Delta p = p_\mathrm{i} - p_\mathrm{o}, \tag{F.56}$$

where Δp is control volume pressure drop and p_i and p_o are pressures at control volume inlet and outlet respectively.

Resulting equations of refrigerant control volume are

$$\frac{\mathrm{d}h_\mathrm{o}}{\mathrm{d}t} = \frac{1}{m}\left(\dot{Q} + \dot{m}_\mathrm{i}(h_\mathrm{i} - h_\mathrm{o}) + V\frac{\mathrm{d}p_\mathrm{o}}{\mathrm{d}t}\right), \tag{F.57}$$

$$\dot{m}_\mathrm{i} - \dot{m}_\mathrm{o} = V\frac{\mathrm{d}\rho}{\mathrm{d}t} = V\left[\left(\frac{\partial\rho}{\partial p}\right)_h \frac{\mathrm{d}p_\mathrm{o}}{\mathrm{d}t} + \left(\frac{\partial\rho}{\partial h}\right)_p \frac{\mathrm{d}h}{\mathrm{d}t}\right], \tag{F.58}$$

$$\Delta p = p_\mathrm{i} - p_\mathrm{o}, \tag{F.59}$$

$$m = V\rho. \tag{F.60}$$

As this modeling approach requires a numeric calculation of pressure derivative, we assembled a second version of the refrigeration cell model, which eliminates this disadvantage. We reuse the energy conservation equation

$$\frac{\mathrm{d}h_\mathrm{o}}{\mathrm{d}t} = \frac{1}{m}\left(\dot{Q} + \dot{m}_\mathrm{i}(h_\mathrm{i} - h_\mathrm{o}) + V\frac{\mathrm{d}p_\mathrm{o}}{\mathrm{d}t}\right) \tag{F.61}$$

and then we reorder the mass conservation equation

$$\dot{m}_\mathrm{i} - \dot{m}_\mathrm{o} = V\left[\left(\frac{\partial\rho}{\partial p}\right)_h \frac{\mathrm{d}p_\mathrm{o}}{\mathrm{d}t} + \left(\frac{\partial\rho}{\partial h}\right)_p \frac{\mathrm{d}h}{\mathrm{d}t}\right], \tag{F.62}$$

$$\left(\frac{\partial\rho}{\partial p}\right)_h \frac{\mathrm{d}p_\mathrm{o}}{\mathrm{d}t} = \frac{\dot{m}_\mathrm{i} - \dot{m}_\mathrm{o}}{V} - \left(\frac{\partial\rho}{\partial h}\right)_p \frac{\mathrm{d}h}{\mathrm{d}t}, \tag{F.63}$$

$$\frac{\mathrm{d}p_\mathrm{o}}{\mathrm{d}t} = \frac{\frac{\dot{m}_\mathrm{i} - \dot{m}_\mathrm{o}}{V} - \left(\frac{\partial\rho}{\partial h}\right)_p \frac{\mathrm{d}h}{\mathrm{d}t}}{\left(\frac{\partial\rho}{\partial p}\right)_h}. \tag{F.64}$$

This approach is more preferable compared to the previous one, as it does not require the computation of pressure time derivative from its values. On the other hand, it needs partial derivatives of density, which can be prepared. The resulting equations

then are

$$\frac{\mathrm{d}h_\mathrm{o}}{\mathrm{d}t} = \frac{1}{m}\left(\dot{Q} + \dot{m}_\mathrm{i}(h_\mathrm{i} - h_\mathrm{o}) + V\frac{\mathrm{d}p_\mathrm{o}}{\mathrm{d}t}\right), \tag{F.65}$$

$$\frac{\mathrm{d}p_\mathrm{o}}{\mathrm{d}t} = \frac{\frac{\dot{m}_\mathrm{i}-\dot{m}_\mathrm{o}}{V} - \left(\frac{\partial\rho}{\partial h}\right)_p \frac{\mathrm{d}h}{\mathrm{d}t}}{\left(\frac{\partial\rho}{\partial p}\right)_h}, \tag{F.66}$$

$$\Delta p = p_\mathrm{i} - p_\mathrm{o}, \tag{F.67}$$

$$m = V\bar{\rho}, \tag{F.68}$$

$$\bar{\rho} = \mathsf{\rho}(\bar{h}, p). \tag{F.69}$$

This set of equations contains an algebraic loop (terms $\frac{\mathrm{d}p}{\mathrm{d}t}$ and $\frac{\mathrm{d}h}{\mathrm{d}t}$ in equations right-hand side). We reorder the equations to eliminate the algebraic loop with the following result

$$\frac{\mathrm{d}h}{\mathrm{d}t} = \frac{\left(\frac{\partial\rho}{\partial p}\right)_h \left(\dot{Q} + \dot{m}_\mathrm{i}(h_\mathrm{i} - h)\right) + \dot{m}_\mathrm{i} - \dot{m}_\mathrm{o}}{m\left(\frac{\partial\rho}{\partial p}\right)_h + V\left(\frac{\partial\rho}{\partial h}\right)_p}, \tag{F.70}$$

$$\frac{\mathrm{d}p}{\mathrm{d}t} = \frac{m(\dot{m}_\mathrm{i} - \dot{m}_\mathrm{o}) - V\left(\frac{\partial\rho}{\partial h}\right)_p \left(\dot{Q} + \dot{m}_\mathrm{i}(h_\mathrm{i} - h)\right)}{V\left(m\left(\frac{\partial\rho}{\partial p}\right)_h + V\left(\frac{\partial\rho}{\partial h}\right)_p\right)}, \tag{F.71}$$

which is more preferable for computations, but the native physical view of the cell behavior got lost.

F.3.2 Air cell

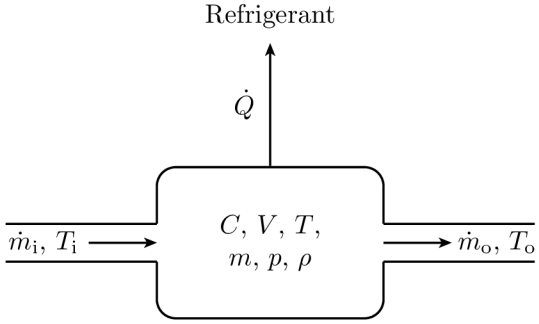

Fig. F.4: HX dry air side model

Firstly, we assemble an air cell model for dry air (with no humidity or with negligible water vapor condensation). The overview of the air cell is in Fig. F.4. The thermal behavior of dry air cell can be written as

$$C\frac{\mathrm{d}T_\mathrm{o}}{\mathrm{d}t} = \dot{m}_\mathrm{i}c_\mathrm{p,a}T_\mathrm{i} - \dot{m}_\mathrm{o}c_\mathrm{p,a}T_\mathrm{o} - \dot{Q}, \tag{F.72}$$

where C is air heat capacity, T_o is outlet air temperature, $\dot{m}_\mathrm{i}$ is inlet air mass flow rate, $\dot{m}_\mathrm{o}$ is the outlet air mass flow rate, T_i is the inlet air temperature and $c_\mathrm{p,a}$ is dry air specific heat capacity (under constant pressure). With $\dot{m}_\mathrm{i} = \dot{m}_\mathrm{o}$ and $\dot{Q} = UA\Delta T$ we can write

$$C\frac{\mathrm{d}T_\mathrm{o}}{\mathrm{d}t} = \dot{m}c_\mathrm{p,a}(T_\mathrm{i} - T_\mathrm{o}) - UA\Delta T, \tag{F.73}$$

where U is overall heat transfer coefficient, A is a heat transfer area and ΔT can be computed using LMTD, ϵ-NTU or another method.

If the air is not dry or if we can not neglect the water vapor condensation, we derive the equations for moist air cell as shown in Fig. F.5.

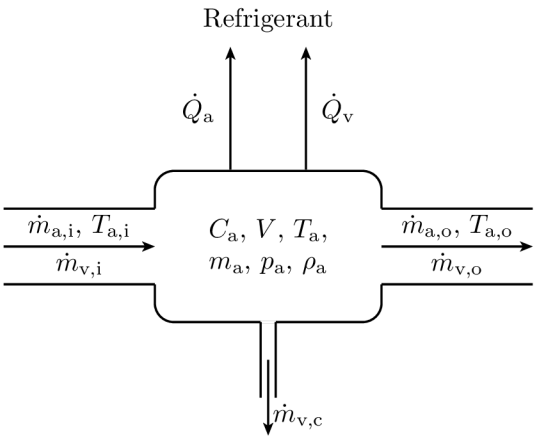

Fig. F.5: HX moist air side model

We recall eq. (F.73) and add additional terms for moist air

$$\dot{Q} = \dot{Q}_\mathrm{a} + \dot{Q}_\mathrm{v}, \tag{F.74}$$

where $\dot{Q}_\mathrm{a}$ is the heat flow rate between the refrigerant and dry air (sensible heat) and $\dot{Q}_\mathrm{v}$ is the heat flow rate caused by water vapor condensation (latent heat).

We can easily compute the HX inlet water vapor mass flow rate as

$$\dot{m}_\mathrm{v,i} = \dot{m}_\mathrm{a,i}\chi_\mathrm{a,i}(p_\mathrm{a}, T_\mathrm{a,i}, \phi_\mathrm{ai}), \tag{F.75}$$

where the symbols meaning is shown in Fig. F.5 and χ is the air specific humidity, see (F.20). Assuming that the refrigerant temperature is taken as a dew point (the excessive humidity is removed), we can compute the HX outlet water vapor flow rate as

$$\dot{m}_\mathrm{v,o} = \dot{m}_\mathrm{a,o}\chi_\mathrm{a,o}(p_a, \mathrm{T_r}(p_\mathrm{r}), \phi), \tag{F.76}$$

where $\phi = 100\,\%$ and $\mathrm{T_r}(p_\mathrm{r})$ is (evaporator) refrigerant temperature (superheating neglected).

The water condensate mass flow rate $\dot{m}_{\mathrm{v,c}}$ can be then computed as

$$\dot{m}_{\mathrm{v,c}} = \dot{m}_{\mathrm{v,i}} - \dot{m}_{\mathrm{v,o}}, \tag{F.77}$$

and this value can then be used for latent heat flow rate

$$\dot{Q}_\mathrm{v} = \dot{m}_{\mathrm{v,c}} L, \tag{F.78}$$

where L is the specific latent heat of water vaporization. The HX outlet air relative humidity can be computed using (F.37)

$$\phi = \frac{p_\mathrm{V}}{p^*_\mathrm{V}}, \tag{F.79}$$

where p_V was already used in (F.76) and p^*_V can be computed using (F.36) employing $T_{\mathrm{a,o}}$.

Resulting equations for HX moist air side can be then written as

$$\dot{Q}_\mathrm{v} = \dot{m}_{\mathrm{v,c}} L, \tag{F.80}$$

$$\begin{aligned}\dot{Q}_\mathrm{v} = \Bigg[& \dot{m}_{\mathrm{a,i}} 0.622 \frac{\phi_\mathrm{i} p_0 \exp\left\{\left[\frac{h_\mathrm{fg}}{R}\left(\frac{1}{T_0} - \frac{1}{T_{\mathrm{a,i}}}\right)\right]\right\}}{p - \phi_\mathrm{i} p_0 \exp\left\{\left[\frac{h_\mathrm{fg}}{R}\left(\frac{1}{T_0} - \frac{1}{T_{\mathrm{a,i}}}\right)\right]\right\}} \\ & - \dot{m}_{\mathrm{a,o}} 0.622 \frac{p_0 \exp\left\{\left[\frac{h_\mathrm{fg}}{R}\left(\frac{1}{T_0} - \frac{1}{T_\mathrm{r}}\right)\right]\right\}}{p - p_0 \exp\left\{\left[\frac{h_\mathrm{fg}}{R}\left(\frac{1}{T_0} - \frac{1}{T_\mathrm{r}}\right)\right]\right\}} \Bigg] L.\end{aligned} \tag{F.81}$$

Assuming $\dot{m}_{\mathrm{a,i}} = \dot{m}_{\mathrm{a,o}}$ we can write

$$\dot{Q}_\mathrm{v} = 0.622 \dot{m}_{\mathrm{a,i}} L \left[\frac{p^*_{\mathrm{V,i}} \phi_\mathrm{i}}{p - p^*_{\mathrm{V,i}} \phi_\mathrm{i}} - \frac{p^*_{\mathrm{V,r}}}{p - p^*_{\mathrm{V,r}}}\right]. \tag{F.82}$$

F.3.3 Heat exchanger thermal flow

Computation of sensible heat flow rate in a heat exchanger ($\dot{Q}_\mathrm{a}$ in (F.74)) can be realized using multiple approaches. All of them employ a basic equation

$$\dot{Q}_\mathrm{a} = UA\Delta T, \tag{F.83}$$

where U is the overall heat transfer coefficient and A is the heat exchanger surface area. The approaches differ in the calculation of the term ΔT, which stands for the temperature difference.

The most simple (and most inaccurate) method involves an algebraic difference of heat exchanger (HX) outlet temperatures. This approach could work properly

only if the temperature change within each medium across the HX can be neglected. As this condition is not fulfilled for refrigerant-air HX, this approach is not used.

The second possibility is the logarithmic mean temperature difference (LMTD), derived and clearly described in [74], chapter 11.3. This approach uses the difference of temperatures at both ends of HX and an equation

$$\Delta T_{\mathrm{LMTD}} = \frac{\Delta T_2 - \Delta T_1}{\ln \frac{\Delta T_2}{\Delta T_1}}, \tag{F.84}$$

where the endpoint temperatures ΔT_1 and ΔT_2 need to be defined according to HX arrangement (parallel flow, cross flow, etc.).

The third option of temperature difference computation is ϵ-NTU method based on the determination of maximal HX heat flow rate and then computation of HX effectiveness. The reader is referred to chapter 11.4 in [74] for further details on this method.

G OTF models

OTF 124: Cooling with ambient air

Within this OTF the VCRS is not used, the cabin is cooled by ambient air (which needs to be of lower temperature compared to vehicle cabin temperature).

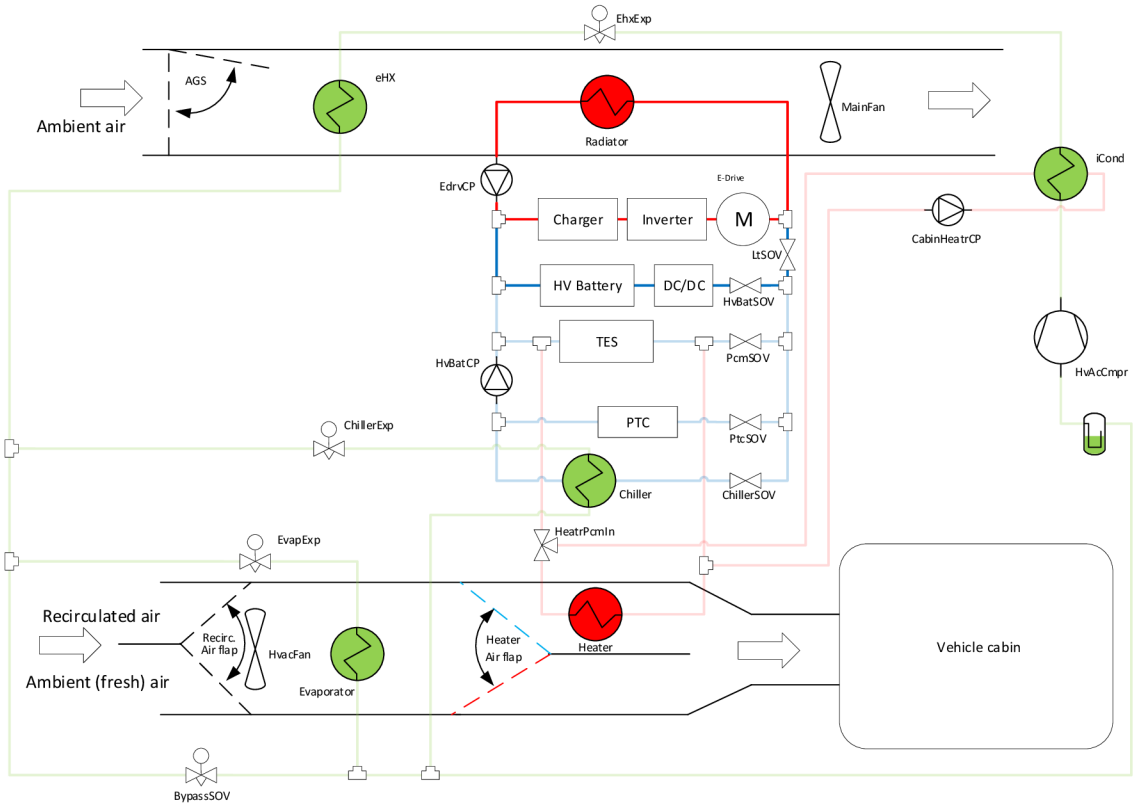

Fig. G.1: VTMS configuration under OTF 124

$$C_{\text{cab}}\frac{\mathrm{d}T_{\text{cab}}}{\mathrm{d}t} = -\dot{Q}_{\text{loss}} - \dot{Q}_{\text{amb1}}, \tag{G.1}$$

$$C_{\text{co}}\frac{\mathrm{d}T_{\text{co}}}{\mathrm{d}t} = -\dot{Q}_{\text{amb3}} + \dot{Q}_{\text{ED1}} + \dot{Q}_{\text{bat1}}, \tag{G.2}$$

$$C_{\text{bat}}\frac{\mathrm{d}T_{\text{bat}}}{\mathrm{d}t} = \dot{Q}_{\text{bat0}} - \dot{Q}_{\text{bat1}}, \tag{G.3}$$

$$C_{\text{ED}}\frac{\mathrm{d}T_{\text{ED}}}{\mathrm{d}t} = \dot{Q}_{\text{ED0}} - \dot{Q}_{\text{ED1}}, \tag{G.4}$$

$$\frac{\mathrm{d}U_{\text{TES}}}{\mathrm{d}t} = 0, \tag{G.5}$$

$$\frac{\mathrm{d}T_{\text{amb}}}{\mathrm{d}t} = 0. \tag{G.6}$$

This OTF is suitable only during mild ambient conditions. We assume $T_{\text{amb}} \in \langle 10, 20\rangle$ (°C) and cabin temperature $T_{\text{cab}} \in \langle 20, 30\rangle$ (°C) with cabin air temperature

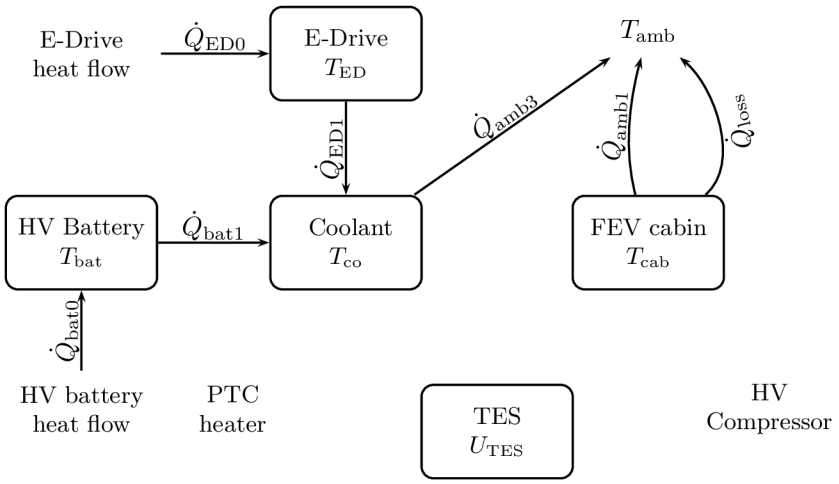

Fig. G.2: Simplified heat flows under OTF 124

Tab. G.1: Approximate heat flow rates for OTF124

T_{cab}	$\dot{Q}^{\mathrm{max}}_{\mathrm{amb1}}$
0..20 °C	0 W
20..22 °C	172 W
22..25 °C	601 W
25..30 °C	1288 W
30..35 °C	2146 W
35..40 °C	3005 W
40..60 °C	5151 W

reference $T^{\mathrm{ref}}_{\mathrm{cab}} = 22\,°\mathrm{C}$. Then the heat flow from cabin to ambient

$$\dot{Q}_{\mathrm{amb1}} = u_{\mathrm{hf}} \dot{m}_{\mathrm{a}} c_{\mathrm{a}} (T_{\mathrm{cab}} - T_{\mathrm{amb}}) \tag{G.7}$$

can be simplified to

$$\dot{Q}_{\mathrm{amb1}} = u_{\mathrm{hf}} \cdot 0.17 \cdot 1010 \cdot (30 - 20) = u_{\mathrm{hf}} \cdot 1717\ (\mathrm{J\,s^{-1}}) = u_{\mathrm{hf}} \cdot \dot{Q}^{\mathrm{max}}_{\mathrm{amb1}} \tag{G.8}$$

for an ambient temperature of 20 °C and cabin temperature of 30 °C. For other cabin temperatures and fixed ambient air temperature of 20 °C the approximate heat flow rates are in Tab. G.1.

We can write the heat flow from the coolant to ambient as

$$\dot{Q}_{\mathrm{amb3}} = \dot{m}_{\mathrm{co}} c_{\mathrm{co}} (T_{\mathrm{co}} - T_{\mathrm{amb}}). \tag{G.9}$$

Then we can write the heat flow from HV battery to coolant as

$$\dot{Q}_{\mathrm{bat1}} = \frac{\dot{m}_{\mathrm{co}}}{2} c_{\mathrm{co}} (T_{\mathrm{bat}} - T_{\mathrm{co}}) \tag{G.10}$$

and the heat flow from E-Drive to coolant as

$$\dot{Q}_{\mathrm{ED1}} = \frac{\dot{m}_{\mathrm{co}}}{2} c_{\mathrm{co}} (T_{\mathrm{ED}} - T_{\mathrm{co}}). \tag{G.11}$$

Remark. *The equations above hold only under defined conditions in combination with sufficient thermal conductivity of elements (heat exchangers, cooled devices, etc.). Specifically, it is supposed that the radiator (coolant to air HX) is capable to cool down the coolant to the ambient temperature, HV battery and E-Drive heat up the coolant to their internal temperatures. This simplification presents the heat flow rates above as maximal values, which are achievable within this OTF by neglecting the power consumption of the main fan and pump. However, the main fan should not be operated when the vehicle is moving (by above-defined speed) and the pump power consumption is quite low, thus the combined power consumption of these two devices will be substantially lower compared to VCRS cooling.*

Otherwise, the more precise model would bring additional dynamic states and generally higher model complexity, which is not desirable within this approach.

After installment we get

$$\frac{\mathrm{d}T_{\mathrm{cab}}}{\mathrm{d}t} = -\frac{G_{\mathrm{loss}}}{C_{\mathrm{cab}}} T_{\mathrm{cab}} + \frac{G_{\mathrm{loss}}}{C_{\mathrm{cab}}} T_{\mathrm{amb}} - \frac{\dot{Q}^{\mathrm{max}}_{\mathrm{amb1}}}{C_{\mathrm{cab}}} u_{\mathrm{hf}}, \tag{G.12}$$

$$\frac{\mathrm{d}T_{\mathrm{co}}}{\mathrm{d}t} = -\frac{2\dot{m}_{\mathrm{co}} c_{\mathrm{co}}}{C_{\mathrm{co}}} T_{\mathrm{co}} + \frac{\dot{m}_{\mathrm{co}} c_{\mathrm{co}}}{2C_{\mathrm{co}}} T_{\mathrm{bat}} + \frac{\dot{m}_{\mathrm{co}} c_{\mathrm{co}}}{2C_{\mathrm{co}}} T_{\mathrm{ED}} + \frac{\dot{m}_{\mathrm{co}} c_{\mathrm{co}}}{C_{\mathrm{co}}} T_{\mathrm{amb}}, \tag{G.13}$$

$$\frac{\mathrm{d}T_{\mathrm{bat}}}{\mathrm{d}t} = \frac{\dot{m}_{\mathrm{co}} c_{\mathrm{co}}}{2C_{\mathrm{bat}}} T_{\mathrm{co}} - \frac{\dot{m}_{\mathrm{co}} c_{\mathrm{co}}}{2C_{\mathrm{bat}}} T_{\mathrm{bat}} + \frac{\dot{Q}_{\mathrm{bat0}}}{C_{\mathrm{bat}}}, \tag{G.14}$$

$$\frac{\mathrm{d}T_{\mathrm{ED}}}{\mathrm{d}t} = \frac{\dot{m}_{\mathrm{co}} c_{\mathrm{co}}}{2C_{\mathrm{ED}}} T_{\mathrm{co}} - \frac{\dot{m}_{\mathrm{co}} c_{\mathrm{co}}}{2C_{\mathrm{ED}}} T_{\mathrm{ED}} + \frac{\dot{Q}_{\mathrm{ED0}}}{C_{\mathrm{ED}}}, \tag{G.15}$$

$$\frac{\mathrm{d}U_{\mathrm{TES}}}{\mathrm{d}t} = 0, \tag{G.16}$$

$$\frac{\mathrm{d}T_{\mathrm{amb}}}{\mathrm{d}t} = 0. \tag{G.17}$$

$$\mathbf{A}_{124} = \begin{bmatrix} -\frac{G_{\text{loss}}}{C_{\text{cab}}} & 0 & 0 & 0 & 0 & \frac{G_{\text{loss}}}{C_{\text{cab}}} \\ 0 & -\frac{2\dot{m}_{\text{co}}c_{\text{co}}}{C_{\text{co}}} & \frac{\dot{m}_{\text{co}}c_{\text{co}}}{2C_{\text{co}}} & \frac{\dot{m}_{\text{co}}c_{\text{co}}}{2C_{\text{co}}} & 0 & \frac{\dot{m}_{\text{co}}c_{\text{co}}}{C_{\text{co}}} \\ 0 & \frac{\dot{m}_{\text{co}}c_{\text{co}}}{2C_{\text{bat}}} & -\frac{\dot{m}_{\text{co}}c_{\text{co}}}{2C_{\text{bat}}} & 0 & 0 & 0 \\ 0 & \frac{\dot{m}_{\text{co}}c_{\text{co}}}{2C_{\text{ED}}} & 0 & -\frac{\dot{m}_{\text{co}}c_{\text{co}}}{2C_{\text{ED}}} & 0 & 0 \\ 0 & 0 & 0 & 0 & 0 & 0 \\ 0 & 0 & 0 & 0 & 0 & 0 \end{bmatrix}, \tag{G.18}$$

$$\mathbf{B}^*_{124} = \begin{bmatrix} 0 & 0 & -\frac{\dot{Q}^{\max}_{\text{amb1}}}{C_{\text{cab}}} & 0 & 0 & 0 \\ 0 & 0 & 0 & 0 & 0 & 0 \\ 0 & 0 & 0 & 0 & 0 & 0 \\ 0 & 0 & 0 & 0 & 0 & 0 \\ 0 & 0 & 0 & 0 & 0 & 0 \\ 0 & 0 & 0 & 0 & 0 & 0 \end{bmatrix}, \tag{G.19}$$

$$\mathbf{f}^{\text{c}} = \begin{bmatrix} 0 \\ 0 \\ \frac{\dot{Q}_{\text{bat0}}}{C_{\text{bat}}} \\ \frac{\dot{Q}_{\text{ED0}}}{C_{\text{ED}}} \\ 0 \\ 0 \end{bmatrix}. \tag{G.20}$$

As there are several values of $\dot{Q}^{\max}_{\text{amb1}}$, we found operating submodes within this operating mode (OTF 124). All the submodes are transformed into PWA system modes. The distinction between them is based on T_{cab} value.

OTF 211: VCRS cooling of cabin and battery with ambient and TES as a heat sink

This OTF utilizes VCRS for vehicle cabin and HV battery cooling with ambient air and TES as heat sinks. The VCRS is operated under conditions defined in Table 5.4 and illustrated in Fig. 5.13.

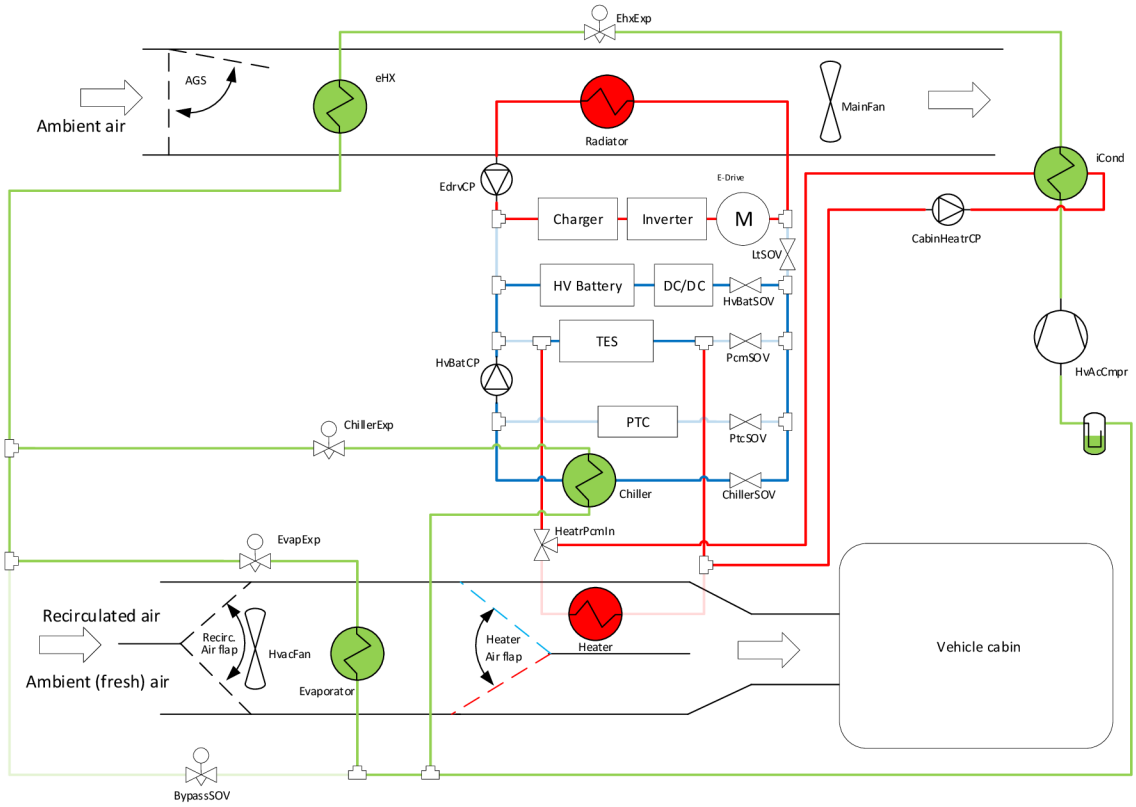

Fig. G.3: VTMS configuration under OTF 211

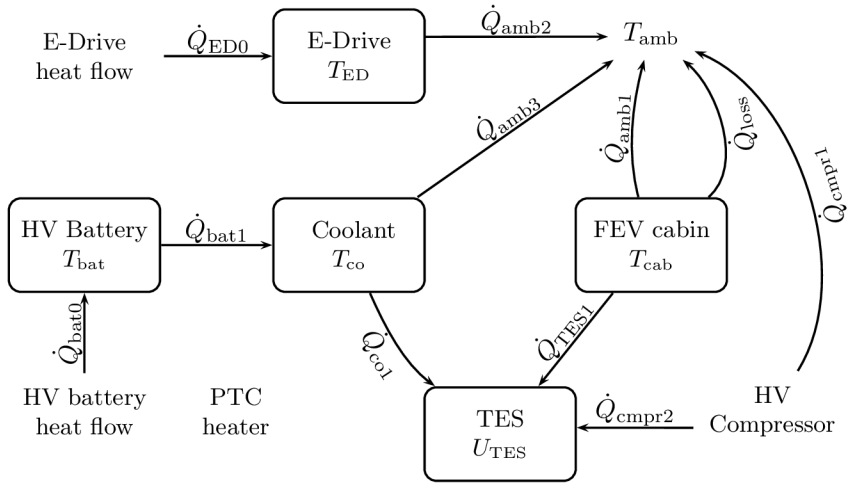

Fig. G.4: Simplified heat flows under OTF 211

$$C_{\mathrm{cab}}\frac{\mathrm{d}T_{\mathrm{cab}}}{\mathrm{d}t} = -\dot{Q}_{\mathrm{loss}} - SHR\cdot\dot{Q}_{\mathrm{amb1}} - SHR\cdot\dot{Q}_{\mathrm{TES1}}, \tag{G.21}$$

$$C_{\mathrm{co}}\frac{\mathrm{d}T_{\mathrm{co}}}{\mathrm{d}t} = -\dot{Q}_{\mathrm{co1}} - \dot{Q}_{\mathrm{amb3}} + \dot{Q}_{\mathrm{bat1}}, \tag{G.22}$$

$$C_{\mathrm{bat}}\frac{\mathrm{d}T_{\mathrm{bat}}}{\mathrm{d}t} = \dot{Q}_{\mathrm{bat0}} - \dot{Q}_{\mathrm{bat1}}, \tag{G.23}$$

$$C_{\mathrm{ED}}\frac{\mathrm{d}T_{\mathrm{ED}}}{\mathrm{d}t} = \dot{Q}_{\mathrm{ED0}} - \dot{Q}_{\mathrm{amb2}}, \tag{G.24}$$

$$\frac{\mathrm{d}U_{\mathrm{TES}}}{\mathrm{d}t} = \dot{Q}_{\mathrm{TES1}} + \dot{Q}_{\mathrm{co1}} + \dot{Q}_{\mathrm{cmpr2}}, \tag{G.25}$$

$$\frac{\mathrm{d}T_{\mathrm{amb}}}{\mathrm{d}t} = 0. \tag{G.26}$$

We consider ambient temperature (at condenser inlet) of $T_{\mathrm{amb}} = 30\,°\mathrm{C}$. Then if we use both the ambient and TES as heat sinks, the heat flow through the eHX can be lower and thus the condensing pressure can be also lower.

For $p_{\mathrm{c}} = 20\,\mathrm{bar}$, the saturation temperature $T_{\mathrm{c}} = 69\,°\mathrm{C}$ and thus temperature difference of 39 K. If we divide the thermal flow into eHX and TES with $T_{\mathrm{TES}} = 15\,°\mathrm{C}$, the temperature difference can be also divided to approx. half and a half (the TES has a capacity of 1 kW h and can be used for approx. 10 min (holds only for cooling modes), leading to $\dot{Q} = 6\,\mathrm{kW}$, which is approx. half of the condenser heat flow). Then the new condensing temperature is $T_{\mathrm{c}} = 50\,°\mathrm{C}$ with corresponding $p_{\mathrm{c}} = 13\,\mathrm{bar}$.

We suppose that the ratio of cabin and HV battery cooling as 70 % and 30 % of maximal available heat flow. Each heat flow needs to be controlled separately, so we divide the compressor control input u_{c} to two control inputs u_{cc} and u_{cb} (with respect to defined constraints).

$$\dot{Q}_{\mathrm{amb1}} = 0.5u_{\mathrm{cc}}P^{\mathrm{max}}_{\mathrm{c},211}\cdot COP_{211}, \tag{G.27}$$

$$\dot{Q}_{\mathrm{TES1}} = 0.5u_{\mathrm{cc}}P^{\mathrm{max}}_{\mathrm{c},211}\cdot COP_{211}, \tag{G.28}$$

$$\dot{Q}_{\mathrm{co1}} = 0.5u_{\mathrm{cb}}P^{\mathrm{max}}_{\mathrm{c},211}\cdot COP_{211}, \tag{G.29}$$

$$\dot{Q}_{\mathrm{amb3}} = 0.5u_{\mathrm{cb}}P^{\mathrm{max}}_{\mathrm{c},211}\cdot COP_{211}, \tag{G.30}$$

$$\dot{Q}_{\mathrm{cmpr2}} = 0.5(u_{\mathrm{cc}} + u_{\mathrm{cb}})P^{\mathrm{max}}_{\mathrm{c},211}. \tag{G.31}$$

The thermal flow from E-Drive to ambient air can be written as

$$\dot{Q}_{\mathrm{amb2}} = \dot{m}_{\mathrm{co}}c_{\mathrm{co}}(T_{\mathrm{ED}} - T_{\mathrm{amb}}) \tag{G.32}$$

and the final equations for OTF 211 are

$$\frac{\mathrm{d}T_{\mathrm{cab}}}{\mathrm{d}t} = -\frac{G_{\mathrm{loss}}}{C_{\mathrm{cab}}}T_{\mathrm{cab}} + \frac{G_{\mathrm{loss}}}{C_{\mathrm{cab}}}T_{\mathrm{amb}} - \frac{SHR \cdot P^{\max}_{\mathrm{c},211} \cdot COP_{211}}{C_{\mathrm{cab}}}u_{\mathrm{cc}}, \tag{G.33}$$

$$\frac{\mathrm{d}T_{\mathrm{co}}}{\mathrm{d}t} = -\frac{\dot{m}_{\mathrm{co}}c_{\mathrm{co}}}{C_{\mathrm{co}}}T_{\mathrm{co}} + \frac{\dot{m}_{\mathrm{co}}c_{\mathrm{co}}}{C_{\mathrm{co}}}T_{\mathrm{bat}} - \frac{P^{\max}_{\mathrm{c},211} \cdot COP_{211}}{C_{\mathrm{co}}}u_{\mathrm{cb}}, \tag{G.34}$$

$$\frac{\mathrm{d}T_{\mathrm{bat}}}{\mathrm{d}t} = \frac{\dot{m}_{\mathrm{co}}c_{\mathrm{co}}}{C_{\mathrm{bat}}}T_{\mathrm{co}} - \frac{\dot{m}_{\mathrm{co}}c_{\mathrm{co}}}{C_{\mathrm{bat}}}T_{\mathrm{bat}} + \frac{\dot{Q}_{\mathrm{bat0}}}{C_{\mathrm{bat}}}, \tag{G.35}$$

$$\frac{\mathrm{d}T_{\mathrm{ED}}}{\mathrm{d}t} = -\frac{\dot{m}_{\mathrm{co}}c_{\mathrm{co}}}{C_{\mathrm{ED}}}T_{\mathrm{ED}} + \frac{\dot{m}_{\mathrm{co}}c_{\mathrm{co}}}{C_{\mathrm{ED}}}T_{\mathrm{amb}} + \frac{\dot{Q}_{\mathrm{ED0}}}{C_{\mathrm{ED}}}, \tag{G.36}$$

$$\frac{\mathrm{d}U_{\mathrm{TES}}}{\mathrm{d}t} = 0.5P^{\max}_{\mathrm{c},211}(COP_{211}+1)u_{\mathrm{cc}} + 0.5P^{\max}_{\mathrm{c},211}(COP_{211}+1)u_{\mathrm{cb}}, \tag{G.37}$$

$$\frac{\mathrm{d}T_{\mathrm{amb}}}{\mathrm{d}t} = 0. \tag{G.38}$$

$$\mathbf{A}_{211} = \begin{bmatrix} -\frac{G_{\mathrm{loss}}}{C_{\mathrm{cab}}} & 0 & 0 & 0 & 0 & \frac{G_{\mathrm{loss}}}{C_{\mathrm{cab}}} \\ 0 & -\frac{\dot{m}_{\mathrm{co}}c_{\mathrm{co}}}{C_{\mathrm{co}}} & \frac{\dot{m}_{\mathrm{co}}c_{\mathrm{co}}}{C_{\mathrm{co}}} & 0 & 0 & 0 \\ 0 & \frac{\dot{m}_{\mathrm{co}}c_{\mathrm{co}}}{C_{\mathrm{bat}}} & -\frac{\dot{m}_{\mathrm{co}}c_{\mathrm{co}}}{C_{\mathrm{bat}}} & 0 & 0 & 0 \\ 0 & 0 & 0 & -\frac{\dot{m}_{\mathrm{co}}c_{\mathrm{co}}}{C_{\mathrm{ED}}} & 0 & \frac{\dot{m}_{\mathrm{co}}c_{\mathrm{co}}}{C_{\mathrm{ED}}} \\ 0 & 0 & 0 & 0 & 0 & 0 \\ 0 & 0 & 0 & 0 & 0 & 0 \end{bmatrix}, \tag{G.39}$$

$$\mathbf{B}^{*}_{211} = \begin{bmatrix} 0 & 0 & 0 & -\frac{SHR \cdot P^{\max}_{\mathrm{c},211} \cdot COP_{211}}{C_{\mathrm{cab}}} & 0 & 0 \\ 0 & 0 & 0 & 0 & -\frac{P^{\max}_{\mathrm{c},211} \cdot COP_{211}}{C_{\mathrm{co}}} & 0 \\ 0 & 0 & 0 & 0 & 0 & 0 \\ 0 & 0 & 0 & 0 & 0 & 0 \\ 0 & 0 & 0 & \frac{P^{\max}_{\mathrm{c},211}(COP_{211}+1)}{2} & \frac{P^{\max}_{\mathrm{c},211}(COP_{211}+1)}{2} & 0 \\ 0 & 0 & 0 & 0 & 0 & 0 \end{bmatrix}, \tag{G.40}$$

$$\mathbf{f}^{\mathrm{c}} = \begin{bmatrix} 0 \\ 0 \\ \frac{\dot{Q}_{\mathrm{bat0}}}{C_{\mathrm{bat}}} \\ \frac{\dot{Q}_{\mathrm{ED0}}}{C_{\mathrm{ED}}} \\ 0 \\ 0 \end{bmatrix}. \tag{G.41}$$

OTF 224: VCRS cooling of the cabin with ambient and TES as heat sinks, battery cooled by ambient air

This OTF utilizes VCRS for vehicle cabin cooling with ambient air and TES as heat sinks. The VCRS is operated under conditions defined in Table 5.4 and illustrated in Fig. 5.13.

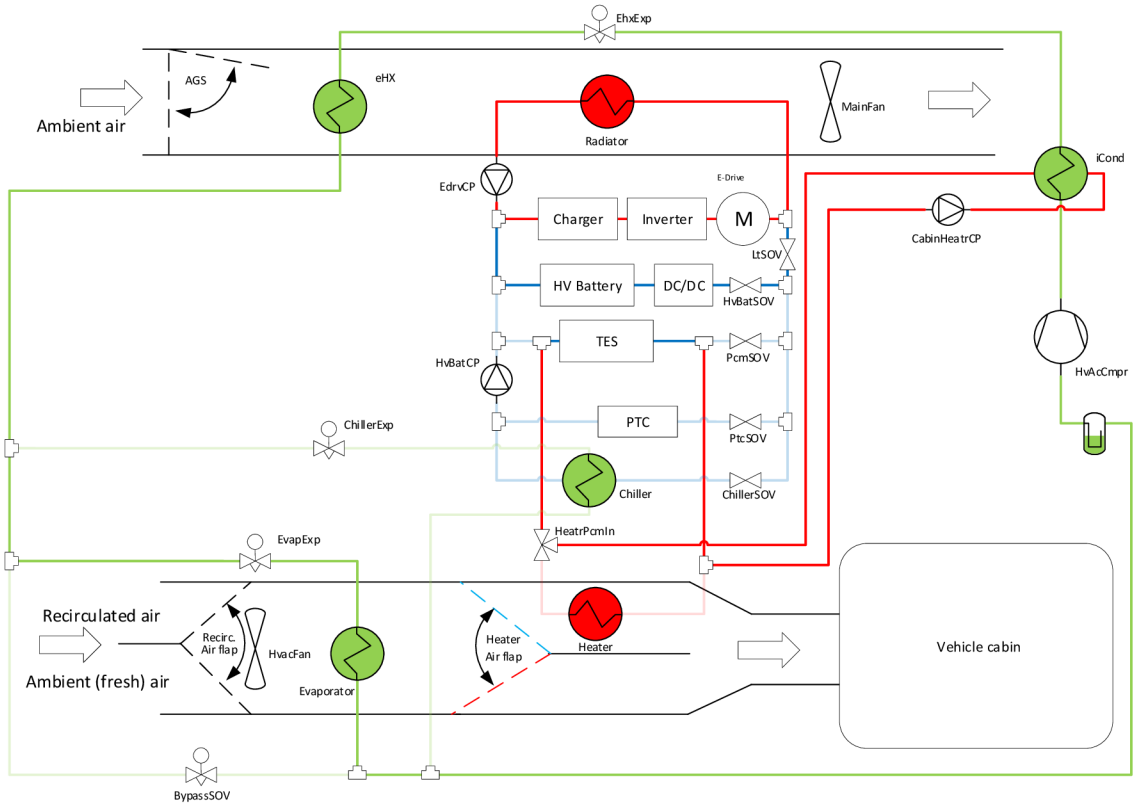

Fig. G.5: VTMS configuration under OTF 224

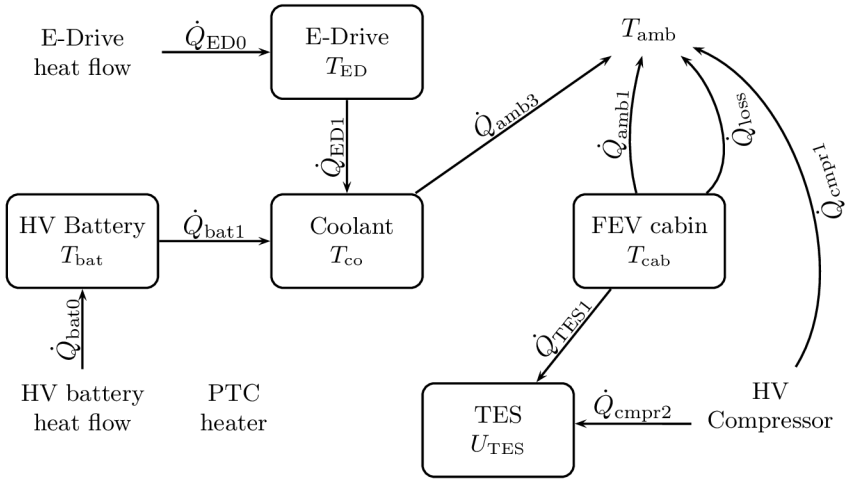

Fig. G.6: Simplified heat flows under OTF 224

$$C_{\text{cab}}\frac{\mathrm{d}T_{\text{cab}}}{\mathrm{d}t} = -\dot{Q}_{\text{loss}} - SHR \cdot \dot{Q}_{\text{amb1}} - SHR \cdot \dot{Q}_{\text{TES1}}, \tag{G.42}$$

$$C_{\text{co}}\frac{\mathrm{d}T_{\text{co}}}{\mathrm{d}t} = -\dot{Q}_{\text{amb3}} + \dot{Q}_{\text{ED1}} + \dot{Q}_{\text{bat1}}, \tag{G.43}$$

$$C_{\text{bat}}\frac{\mathrm{d}T_{\text{bat}}}{\mathrm{d}t} = \dot{Q}_{\text{bat0}} - \dot{Q}_{\text{bat1}}, \tag{G.44}$$

$$C_{\text{ED}}\frac{\mathrm{d}T_{\text{ED}}}{\mathrm{d}t} = \dot{Q}_{\text{ED0}} - \dot{Q}_{\text{ED1}} - \dot{Q}_{\text{amb2}}, \tag{G.45}$$

$$\frac{\mathrm{d}U_{\text{TES}}}{\mathrm{d}t} = \dot{Q}_{\text{TES1}} + \dot{Q}_{\text{cmpr2}}, \tag{G.46}$$

$$\frac{\mathrm{d}T_{\text{amb}}}{\mathrm{d}t} = 0. \tag{G.47}$$

$$\dot{Q}_{\text{amb1}} = 0.5u_{\text{c}} \cdot P^{\max}_{\text{c,224}} \cdot COP_{224}, \tag{G.48}$$

$$\dot{Q}_{\text{TES1}} = 0.5u_{\text{c}} \cdot P^{\max}_{\text{c,224}} \cdot COP_{224}, \tag{G.49}$$

$$\dot{Q}_{\text{cmpr2}} = 0.5u_{\text{c}} \cdot P^{\max}_{\text{c,224}}. \tag{G.50}$$

The heat flow from the coolant to ambient is

$$\dot{Q}_{\text{amb3}} = \dot{m}_{\text{co}} c_{\text{co}} (T_{\text{co}} - T_{\text{amb}}) \tag{G.51}$$

and after plugging in we get the final equations for OTF 224

$$\begin{aligned} C_{\text{cab}}\frac{\mathrm{d}T_{\text{cab}}}{\mathrm{d}t} &= -G_{\text{loss}}(T_{\text{cab}} - T_{\text{amb}}) - 0.5u_{\text{c}} \cdot SHR \cdot P^{\max}_{\text{c,224}} \cdot COP_{224} \\ &\quad - 0.5u_{\text{c}} \cdot SHR \cdot P^{\max}_{\text{c,224}} \cdot COP_{224}, \end{aligned} \tag{G.52}$$

$$\begin{aligned} C_{\text{co}}\frac{\mathrm{d}T_{\text{co}}}{\mathrm{d}t} &= -\dot{m}_{\text{co}} c_{\text{co}} (T_{\text{co}} - T_{\text{amb}}) + \frac{\dot{m}_{\text{co}}}{2} c_{\text{co}} (T_{\text{ED}} - T_{\text{co}}) \\ &\quad + \frac{\dot{m}_{\text{co}}}{2} c_{\text{co}} (T_{\text{bat}} - T_{\text{co}}), \end{aligned} \tag{G.53}$$

$$C_{\text{bat}}\frac{\mathrm{d}T_{\text{bat}}}{\mathrm{d}t} = \dot{Q}_{\text{bat0}} - \frac{\dot{m}_{\text{co}}}{2} c_{\text{co}} (T_{\text{bat}} - T_{\text{co}}), \tag{G.54}$$

$$C_{\text{ED}}\frac{\mathrm{d}T_{\text{ED}}}{\mathrm{d}t} = \dot{Q}_{\text{ED0}} - \frac{\dot{m}_{\text{co}}}{2} c_{\text{co}} (T_{\text{ED}} - T_{\text{co}}), \tag{G.55}$$

$$\frac{\mathrm{d}U_{\text{TES}}}{\mathrm{d}t} = 0.5u_{\text{c}} \cdot P^{\max}_{\text{c,224}} \cdot COP_{224} + 0.5u_{\text{c}} \cdot P^{\max}_{\text{c,224}}, \tag{G.56}$$

$$\frac{\mathrm{d}T_{\text{amb}}}{\mathrm{d}t} = 0. \tag{G.57}$$

$$\mathbf{A}_{224} = \begin{bmatrix} -\frac{G_{\text{loss}}}{C_{\text{cab}}} & 0 & 0 & 0 & 0 & \frac{G_{\text{loss}}}{C_{\text{cab}}} \\ 0 & -\frac{2\dot{m}_{\text{co}}c_{\text{co}}}{C_{\text{co}}} & \frac{\dot{m}_{\text{co}}c_{\text{co}}}{2C_{\text{co}}} & \frac{\dot{m}_{\text{co}}c_{\text{co}}}{2C_{\text{co}}} & 0 & \frac{\dot{m}_{\text{co}}c_{\text{co}}}{C_{\text{co}}} \\ 0 & \frac{\dot{m}_{\text{co}}c_{\text{co}}}{2C_{\text{bat}}} & -\frac{\dot{m}_{\text{co}}c_{\text{co}}}{2C_{\text{bat}}} & 0 & 0 & 0 \\ 0 & \frac{\dot{m}_{\text{co}}c_{\text{co}}}{2C_{\text{ED}}} & 0 & -\frac{\dot{m}_{\text{co}}c_{\text{co}}}{2C_{\text{ED}}} & 0 & 0 \\ 0 & 0 & 0 & 0 & 0 & 0 \\ 0 & 0 & 0 & 0 & 0 & 0 \end{bmatrix}, \tag{G.58}$$

$$\mathbf{B}^{*}_{224} = \begin{bmatrix} 0 & -\frac{SHR\cdot P^{\max}_{\text{c},224}\cdot COP_{224}}{C_{\text{cab}}} & 0 & 0 & 0 & 0 \\ 0 & 0 & 0 & 0 & 0 & 0 \\ 0 & 0 & 0 & 0 & 0 & 0 \\ 0 & 0 & 0 & 0 & 0 & 0 \\ 0 & \frac{P^{\max}_{\text{c},224}(COP_{224}+1)}{2} & 0 & 0 & 0 & 0 \\ 0 & 0 & 0 & 0 & 0 & 0 \end{bmatrix}, \tag{G.59}$$

$$\mathbf{f}^{\text{c}} = \begin{bmatrix} 0 \\ 0 \\ \frac{\dot{Q}_{\text{bat0}}}{C_{\text{bat}}} \\ \frac{\dot{Q}_{\text{ED0}}}{C_{\text{ED}}} \\ 0 \\ 0 \end{bmatrix}. \tag{G.60}$$

OTF 373: Heating with coolant as a heat source

This OTF utilizes VCRS for vehicle cabin heating with coolant as a heat source. The VCRS is operated under conditions defined in Table 5.6 and illustrated in Fig. 5.15.

$$C_{\text{cab}}\frac{\mathrm{d}T_{\text{cab}}}{\mathrm{d}t} = -\dot{Q}_{\text{loss}} + \dot{Q}_{\text{cmpr0}} + \dot{Q}_{\text{co0}}, \tag{G.61}$$

$$C_{\text{co}}\frac{\mathrm{d}T_{\text{co}}}{\mathrm{d}t} = -\dot{Q}_{\text{co0}} + \dot{Q}_{\text{TES0}} + \dot{Q}_{\text{PTC}} + \dot{Q}_{\text{ED1}} + \dot{Q}_{\text{bat1}}, \tag{G.62}$$

$$C_{\text{bat}}\frac{\mathrm{d}T_{\text{bat}}}{\mathrm{d}t} = \dot{Q}_{\text{bat0}} - \dot{Q}_{\text{bat1}}, \tag{G.63}$$

$$C_{\text{ED}}\frac{\mathrm{d}T_{\text{ED}}}{\mathrm{d}t} = \dot{Q}_{\text{ED0}} - \dot{Q}_{\text{ED1}}, \tag{G.64}$$

$$\frac{\mathrm{d}U_{\text{TES}}}{\mathrm{d}t} = -\dot{Q}_{\text{TES0}}, \tag{G.65}$$

$$\frac{\mathrm{d}T_{\text{amb}}}{\mathrm{d}t} = 0. \tag{G.66}$$

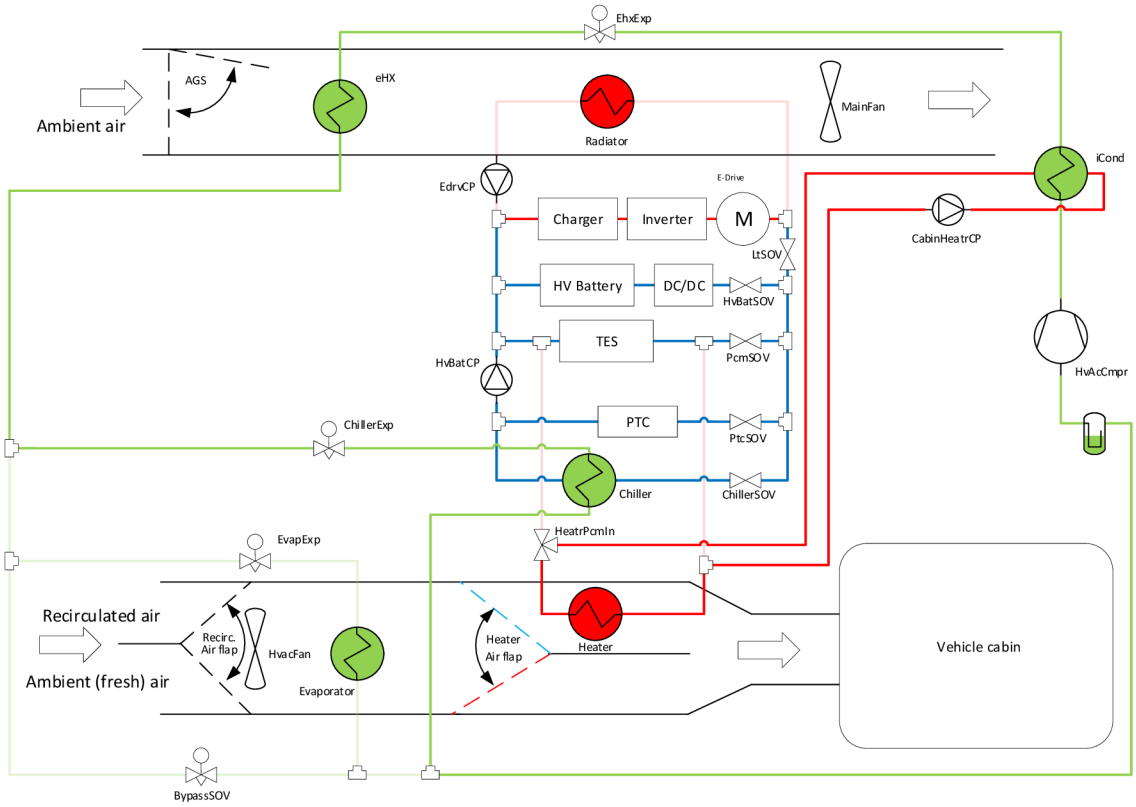

Fig. G.7: VTMS configuration under OTF 373

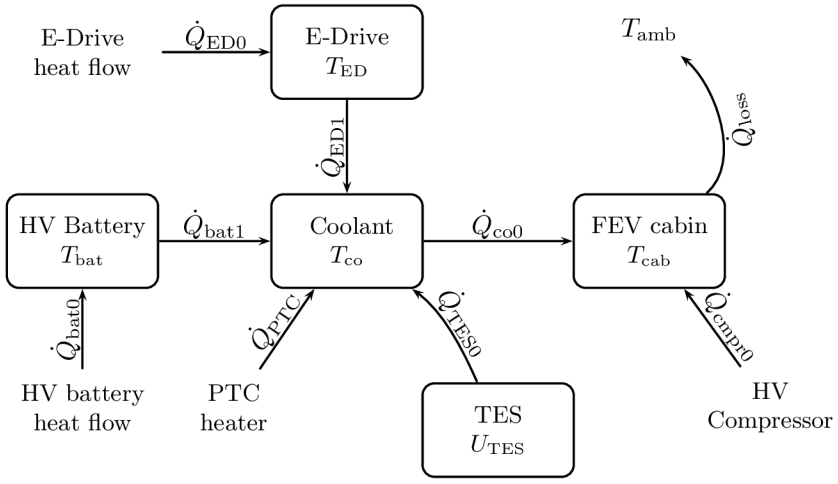

Fig. G.8: Simplified heat flows under OTF 373

The heat flow rates can be written as

$$\dot{Q}_{\mathrm{cmpr0}} = u_{\mathrm{c}} \cdot P^{\max}_{\mathrm{c},373}, \tag{G.67}$$

$$\dot{Q}_{\mathrm{co0}} = (COP_{373} - 1) u_{\mathrm{c}} \cdot P^{\max}_{\mathrm{c},373}, \tag{G.68}$$

$$\dot{Q}_{\mathrm{TES0}} = \frac{\dot{m}_{\mathrm{co}}}{3} c_{\mathrm{co}} (T_{\mathrm{TES}} - T_{\mathrm{co}}), \tag{G.69}$$

$$\dot{Q}_{\mathrm{PTC}} = \dot{Q}^{\max}_{\mathrm{PTC}} \cdot u_{\mathrm{ptc}} \tag{G.70}$$

and after installment we get

$$\frac{\mathrm{d}T_{\mathrm{cab}}}{\mathrm{d}t} = -\frac{G_{\mathrm{loss}}}{C_{\mathrm{cab}}} T_{\mathrm{cab}} + \frac{G_{\mathrm{loss}}}{C_{\mathrm{cab}}} T_{\mathrm{amb}} + \frac{COP_{373} \cdot P^{\max}_{\mathrm{c},373}}{C_{\mathrm{cab}}} u_{\mathrm{c}}, \tag{G.71}$$

$$\begin{aligned} \frac{\mathrm{d}T_{\mathrm{co}}}{\mathrm{d}t} = &-\frac{\dot{m}_{\mathrm{co}} c_{\mathrm{co}}}{C_{\mathrm{co}}} T_{\mathrm{co}} + \frac{\dot{m}_{\mathrm{co}} c_{\mathrm{co}}}{3C_{\mathrm{co}}} T_{\mathrm{bat}} + \frac{\dot{m}_{\mathrm{co}} c_{\mathrm{co}}}{3C_{\mathrm{co}}} T_{\mathrm{ED}} - \frac{(COP_{373} - 1) P^{\max}_{\mathrm{c},373}}{C_{\mathrm{co}}} u_{\mathrm{c}} \\ &+ \frac{\dot{Q}^{\max}_{\mathrm{PTC}}}{C_{\mathrm{co}}} u_{\mathrm{ptc}} + \frac{\dot{m}_{\mathrm{co}} c_{\mathrm{co}}}{3C_{\mathrm{co}}} T_{\mathrm{TES}}, \end{aligned} \tag{G.72}$$

$$\frac{\mathrm{d}T_{\mathrm{bat}}}{\mathrm{d}t} = \frac{\dot{m}_{\mathrm{co}} c_{\mathrm{co}}}{3C_{\mathrm{bat}}} T_{\mathrm{co}} - \frac{\dot{m}_{\mathrm{co}} c_{\mathrm{co}}}{3C_{\mathrm{bat}}} T_{\mathrm{bat}} + \frac{\dot{Q}_{\mathrm{bat0}}}{C_{\mathrm{bat}}}, \tag{G.73}$$

$$\frac{\mathrm{d}T_{\mathrm{ED}}}{\mathrm{d}t} = \frac{\dot{m}_{\mathrm{co}} c_{\mathrm{co}}}{3C_{\mathrm{ED}}} T_{\mathrm{co}} - \frac{\dot{m}_{\mathrm{co}} c_{\mathrm{co}}}{3C_{\mathrm{ED}}} T_{\mathrm{ED}} + \frac{\dot{Q}_{\mathrm{ED0}}}{C_{\mathrm{ED}}}, \tag{G.74}$$

$$\frac{\mathrm{d}U_{\mathrm{TES}}}{\mathrm{d}t} = \frac{\dot{m}_{\mathrm{co}} c_{\mathrm{co}}}{3} T_{\mathrm{co}} - \frac{\dot{m}_{\mathrm{co}} c_{\mathrm{co}}}{3} T_{\mathrm{TES}}, \tag{G.75}$$

$$\frac{\mathrm{d}T_{\mathrm{amb}}}{\mathrm{d}t} = 0. \tag{G.76}$$

$$\mathbf{A}_{373} = \begin{bmatrix} -\frac{G_{\text{loss}}}{C_{\text{cab}}} & 0 & 0 & 0 & 0 & \frac{G_{\text{loss}}}{C_{\text{cab}}} \\ 0 & -\frac{\dot{m}_{\text{co}}c_{\text{co}}}{C_{\text{co}}} & \frac{\dot{m}_{\text{co}}c_{\text{co}}}{3C_{\text{co}}} & \frac{\dot{m}_{\text{co}}c_{\text{co}}}{3C_{\text{co}}} & 0 & 0 \\ 0 & \frac{\dot{m}_{\text{co}}c_{\text{co}}}{3C_{\text{bat}}} & -\frac{\dot{m}_{\text{co}}c_{\text{co}}}{3C_{\text{bat}}} & 0 & 0 & 0 \\ 0 & \frac{\dot{m}_{\text{co}}c_{\text{co}}}{3C_{\text{ED}}} & 0 & -\frac{\dot{m}_{\text{co}}c_{\text{co}}}{3C_{\text{ED}}} & 0 & 0 \\ 0 & \frac{\dot{m}_{\text{co}}c_{\text{co}}}{3} & 0 & 0 & 0 & 0 \\ 0 & 0 & 0 & 0 & 0 & 0 \end{bmatrix}, \tag{G.77}$$

$$\mathbf{B}^{*}_{373} = \begin{bmatrix} 0 & \frac{P^{\max}_{\text{c},373} \cdot COP_{373}}{C_{\text{cab}}} & 0 & 0 & 0 & 0 \\ 0 & -\frac{(COP_{373}-1)P^{\max}_{\text{c},373}}{C_{\text{co}}} & 0 & 0 & 0 & \frac{\dot{Q}^{\max}_{\text{PTC}}}{C_{\text{co}}} \\ 0 & 0 & 0 & 0 & 0 & 0 \\ 0 & 0 & 0 & 0 & 0 & 0 \\ 0 & 0 & 0 & 0 & 0 & 0 \\ 0 & 0 & 0 & 0 & 0 & 0 \end{bmatrix}, \tag{G.78}$$

$$\mathbf{f}^{\text{c}}_{373} = \begin{bmatrix} 0 \\ \frac{\dot{m}_{\text{co}}c_{\text{co}}}{3C_{\text{co}}}T_{\text{TES}} \\ \frac{\dot{Q}_{\text{bat0}}}{C_{\text{bat}}} \\ \frac{\dot{Q}_{\text{ED0}}}{C_{\text{ED}}} \\ -\frac{\dot{m}_{\text{co}}c_{\text{co}}}{3}T_{\text{TES}} \\ 0 \end{bmatrix}. \tag{G.79}$$

OTF 373e: Heating with coolant as a heat source (with "empty" TES)

This OTF utilizes VCRS for vehicle cabin heating with coolant as a heat source. The VCRS is operated under conditions defined in Table 5.6 and illustrated in Fig. 5.15. This OTF is based on OTF 373 and the only difference is closed valve PcmSOV, which is useful when all the latent heat is removed from TES. Thus OTF 373e can be used to reuse waste heat from E-Drive and HV Battery, which is beneficially from a power consumption perspective.

$$C_{\text{cab}}\frac{\mathrm{d}T_{\text{cab}}}{\mathrm{d}t} = -\dot{Q}_{\text{loss}} + \dot{Q}_{\text{cmpr0}} + \dot{Q}_{\text{co0}}, \tag{G.80}$$

$$C_{\text{co}}\frac{\mathrm{d}T_{\text{co}}}{\mathrm{d}t} = -\dot{Q}_{\text{co0}} + \dot{Q}_{\text{PTC}} + \dot{Q}_{\text{ED1}} + \dot{Q}_{\text{bat1}}, \tag{G.81}$$

$$C_{\text{bat}}\frac{\mathrm{d}T_{\text{bat}}}{\mathrm{d}t} = \dot{Q}_{\text{bat0}} - \dot{Q}_{\text{bat1}}, \tag{G.82}$$

$$C_{\text{ED}}\frac{\mathrm{d}T_{\text{ED}}}{\mathrm{d}t} = \dot{Q}_{\text{ED0}} - \dot{Q}_{\text{ED1}}, \tag{G.83}$$

$$\frac{\mathrm{d}U_{\text{TES}}}{\mathrm{d}t} = 0, \tag{G.84}$$

$$\frac{\mathrm{d}T_{\text{amb}}}{\mathrm{d}t} = 0. \tag{G.85}$$

$$\mathbf{A}_{373\mathrm{e}} = \begin{bmatrix} -\frac{G_{\mathrm{loss}}}{C_{\mathrm{cab}}} & 0 & 0 & 0 & 0 & \frac{G_{\mathrm{loss}}}{C_{\mathrm{cab}}} \\ 0 & -\frac{\dot{m}_{\mathrm{co}} c_{\mathrm{co}}}{C_{\mathrm{co}}} & \frac{\dot{m}_{\mathrm{co}} c_{\mathrm{co}}}{2C_{\mathrm{co}}} & \frac{\dot{m}_{\mathrm{co}} c_{\mathrm{co}}}{2C_{\mathrm{co}}} & 0 & 0 \\ 0 & \frac{\dot{m}_{\mathrm{co}} c_{\mathrm{co}}}{2C_{\mathrm{bat}}} & -\frac{\dot{m}_{\mathrm{co}} c_{\mathrm{co}}}{2C_{\mathrm{bat}}} & 0 & 0 & 0 \\ 0 & \frac{\dot{m}_{\mathrm{co}} c_{\mathrm{co}}}{2C_{\mathrm{ED}}} & 0 & -\frac{\dot{m}_{\mathrm{co}} c_{\mathrm{co}}}{2C_{\mathrm{ED}}} & 0 & 0 \\ 0 & 0 & 0 & 0 & 0 & 0 \\ 0 & 0 & 0 & 0 & 0 & 0 \end{bmatrix}, \tag{G.86}$$

$$\mathbf{B}^{*}_{373\mathrm{e}} = \begin{bmatrix} 0 & \frac{P^{\max}_{\mathrm{c},373\mathrm{e}} \cdot COP_{373\mathrm{e}}}{C_{\mathrm{cab}}} & 0 & 0 & 0 & 0 \\ 0 & -\frac{(COP_{373\mathrm{e}}-1) P^{\max}_{\mathrm{c},373\mathrm{e}}}{C_{\mathrm{co}}} & 0 & 0 & 0 & \frac{\dot{Q}^{\max}_{\mathrm{PTC}}}{C_{\mathrm{co}}} \\ 0 & 0 & 0 & 0 & 0 & 0 \\ 0 & 0 & 0 & 0 & 0 & 0 \\ 0 & 0 & 0 & 0 & 0 & 0 \\ 0 & 0 & 0 & 0 & 0 & 0 \end{bmatrix}, \tag{G.87}$$

$$\mathbf{f}^{\mathrm{c}}_{373\mathrm{e}} = \begin{bmatrix} 0 \\ 0 \\ \frac{\dot{Q}_{\mathrm{bat0}}}{C_{\mathrm{bat}}} \\ \frac{\dot{Q}_{\mathrm{ED0}}}{C_{\mathrm{ED}}} \\ 0 \\ 0 \end{bmatrix}. \tag{G.88}$$

OTF 463: Heating with ambient as a heat source

This OTF utilizes VCRS for vehicle cabin heating with ambient air as a heat source. The VCRS is operated under conditions defined in Table 5.5 and illustrated in Fig. 5.14.

$$C_{\mathrm{cab}} \frac{\mathrm{d}T_{\mathrm{cab}}}{\mathrm{d}t} = \dot{Q}_{\mathrm{amb0}} - \dot{Q}_{\mathrm{loss}} + \dot{Q}_{\mathrm{cmpr0}}, \tag{G.89}$$

$$C_{\mathrm{co}} \frac{\mathrm{d}T_{\mathrm{co}}}{\mathrm{d}t} = \dot{Q}_{\mathrm{ED1}} + \dot{Q}_{\mathrm{bat1}}, \tag{G.90}$$

$$C_{\mathrm{bat}} \frac{\mathrm{d}T_{\mathrm{bat}}}{\mathrm{d}t} = \dot{Q}_{\mathrm{bat0}} - \dot{Q}_{\mathrm{bat1}}, \tag{G.91}$$

$$C_{\mathrm{ED}} \frac{\mathrm{d}T_{\mathrm{ED}}}{\mathrm{d}t} = \dot{Q}_{\mathrm{ED0}} - \dot{Q}_{\mathrm{ED1}}, \tag{G.92}$$

$$\frac{\mathrm{d}U_{\mathrm{TES}}}{\mathrm{d}t} = 0, \tag{G.93}$$

$$\frac{\mathrm{d}T_{\mathrm{amb}}}{\mathrm{d}t} = 0. \tag{G.94}$$

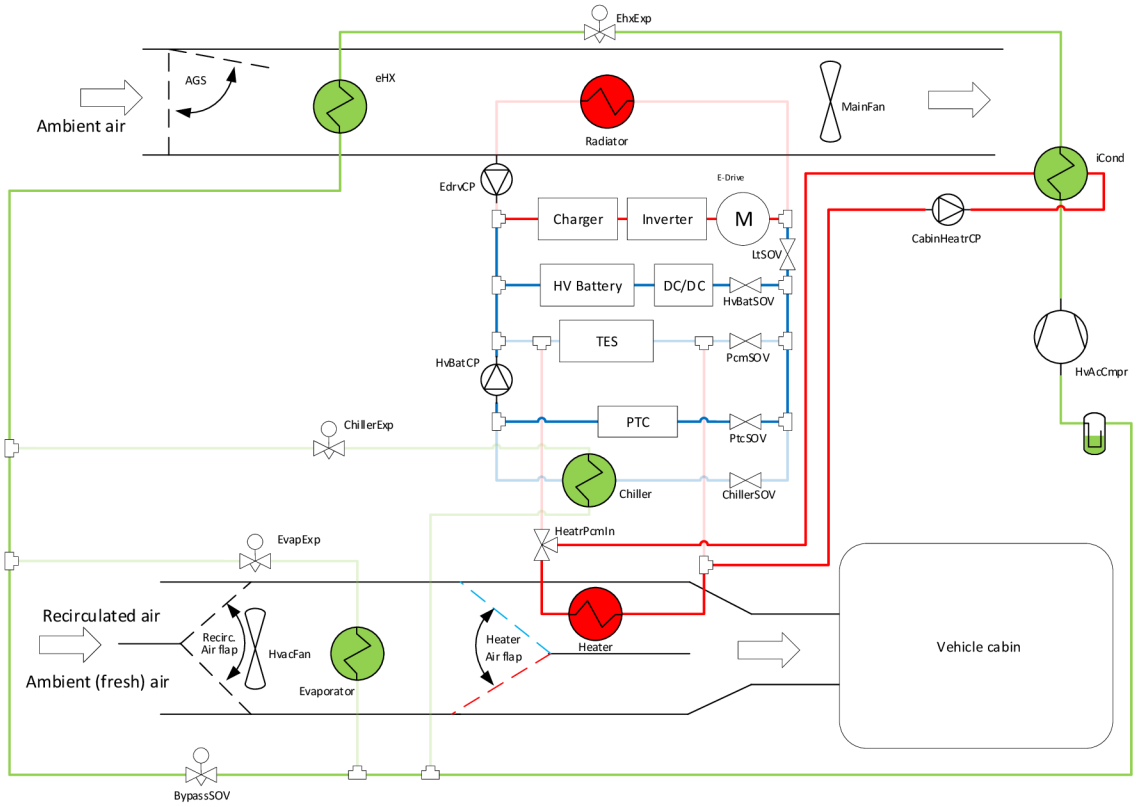

Fig. G.9: VTMS configuration under OTF 463

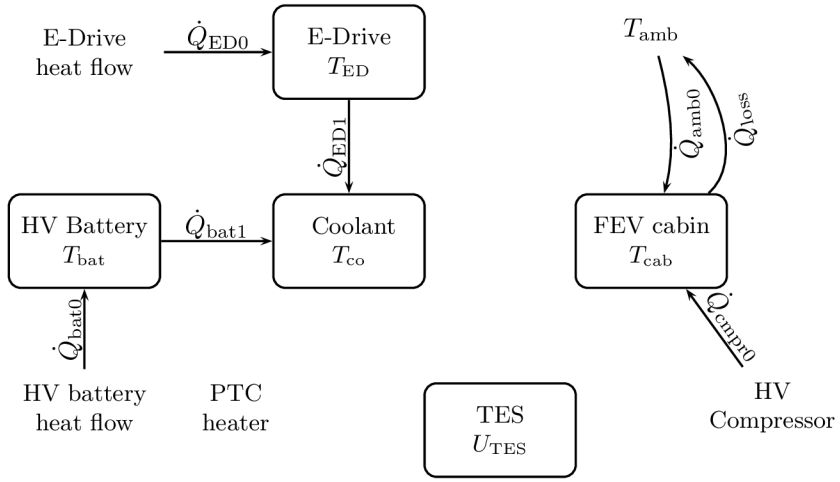

Fig. G.10: Simplified heat flows under OTF 463

The thermal flows from ambient to cabin and from the compressor to the cabin are described by their rates, respectively

$$\dot{Q}_{\mathrm{amb0}} = P^{\max}_{\mathrm{c},463}(COP_{463} - 1)u_{\mathrm{c}}, \tag{G.95}$$
$$\dot{Q}_{\mathrm{cmpr0}} = P^{\max}_{\mathrm{c},463} \cdot u_{\mathrm{c}} \tag{G.96}$$

and after plugging in general equations we get

$$\frac{\mathrm{d}T_{\mathrm{cab}}}{\mathrm{d}t} = -\frac{G_{\mathrm{loss}}}{C_{\mathrm{cab}}}T_{\mathrm{cab}} + \frac{G_{\mathrm{loss}}}{C_{\mathrm{cab}}}T_{\mathrm{amb}} + \frac{P^{\max}_{\mathrm{c},463} \cdot COP_{463}}{C_{\mathrm{cab}}}u_{\mathrm{c}}, \tag{G.97}$$
$$\frac{\mathrm{d}T_{\mathrm{co}}}{\mathrm{d}t} = -\frac{\dot{m}_{\mathrm{co}}c_{\mathrm{co}}}{C_{\mathrm{co}}}T_{\mathrm{co}} + \frac{\dot{m}_{\mathrm{co}}c_{\mathrm{co}}}{2C_{\mathrm{co}}}T_{\mathrm{bat}} + \frac{\dot{m}_{\mathrm{co}}c_{\mathrm{co}}}{2C_{\mathrm{co}}}T_{\mathrm{ED}}, \tag{G.98}$$
$$\frac{\mathrm{d}T_{\mathrm{bat}}}{\mathrm{d}t} = \frac{\dot{m}_{\mathrm{co}}c_{\mathrm{co}}}{2C_{\mathrm{bat}}}T_{\mathrm{co}} - \frac{\dot{m}_{\mathrm{co}}c_{\mathrm{co}}}{2C_{\mathrm{bat}}}T_{\mathrm{bat}} + \frac{\dot{Q}_{\mathrm{bat0}}}{C_{\mathrm{bat}}}, \tag{G.99}$$
$$\frac{\mathrm{d}T_{\mathrm{ED}}}{\mathrm{d}t} = \frac{\dot{m}_{\mathrm{co}}c_{\mathrm{co}}}{2C_{\mathrm{ED}}}T_{\mathrm{co}} - \frac{\dot{m}_{\mathrm{co}}c_{\mathrm{co}}}{2C_{\mathrm{ED}}}T_{\mathrm{ED}} + \frac{\dot{Q}_{\mathrm{ED0}}}{C_{\mathrm{ED}}}, \tag{G.100}$$
$$\frac{\mathrm{d}U_{\mathrm{TES}}}{\mathrm{d}t} = 0, \tag{G.101}$$
$$\frac{\mathrm{d}T_{\mathrm{amb}}}{\mathrm{d}t} = 0. \tag{G.102}$$

$$\mathbf{A}_{463} = \begin{bmatrix} -\frac{G_{\mathrm{loss}}}{C_{\mathrm{cab}}} & 0 & 0 & 0 & 0 & \frac{G_{\mathrm{loss}}}{C_{\mathrm{cab}}} \\ 0 & -\frac{\dot{m}_{\mathrm{co}}c_{\mathrm{co}}}{C_{\mathrm{co}}} & \frac{\dot{m}_{\mathrm{co}}c_{\mathrm{co}}}{2C_{\mathrm{co}}} & \frac{\dot{m}_{\mathrm{co}}c_{\mathrm{co}}}{2C_{\mathrm{co}}} & 0 & 0 \\ 0 & \frac{\dot{m}_{\mathrm{co}}c_{\mathrm{co}}}{2C_{\mathrm{bat}}} & -\frac{\dot{m}_{\mathrm{co}}c_{\mathrm{co}}}{2C_{\mathrm{bat}}} & 0 & 0 & 0 \\ 0 & \frac{\dot{m}_{\mathrm{co}}c_{\mathrm{co}}}{2C_{\mathrm{ED}}} & 0 & -\frac{\dot{m}_{\mathrm{co}}c_{\mathrm{co}}}{2C_{\mathrm{ED}}} & 0 & 0 \\ 0 & 0 & 0 & 0 & 0 & 0 \\ 0 & 0 & 0 & 0 & 0 & 0 \end{bmatrix}, \tag{G.103}$$

$$\mathbf{B}^{*}_{463} = \begin{bmatrix} 0 & \frac{P^{\max}_{\mathrm{c},463} \cdot COP_{463}}{C_{\mathrm{cab}}} & 0 & 0 & 0 & 0 \\ 0 & 0 & 0 & 0 & 0 & 0 \\ 0 & 0 & 0 & 0 & 0 & 0 \\ 0 & 0 & 0 & 0 & 0 & 0 \\ 0 & 0 & 0 & 0 & 0 & 0 \\ 0 & 0 & 0 & 0 & 0 & 0 \end{bmatrix}, \tag{G.104}$$

$$\mathbf{f}^{\mathrm{c}}_{463} = \begin{bmatrix} 0 \\ 0 \\ \frac{\dot{Q}_{\mathrm{bat0}}}{C_{\mathrm{bat}}} \\ \frac{\dot{Q}_{\mathrm{ED0}}}{C_{\mathrm{ED}}} \\ 0 \\ 0 \end{bmatrix}. \tag{G.105}$$

OTF 511: VCRS cooling of cabin and battery with ambient as a heat sink

This OTF utilizes VCRS for vehicle cabin and HV battery cooling with ambient air as a heat sink. The VCRS is operated under conditions defined in Table 5.3 and illustrated in Fig. 5.12.

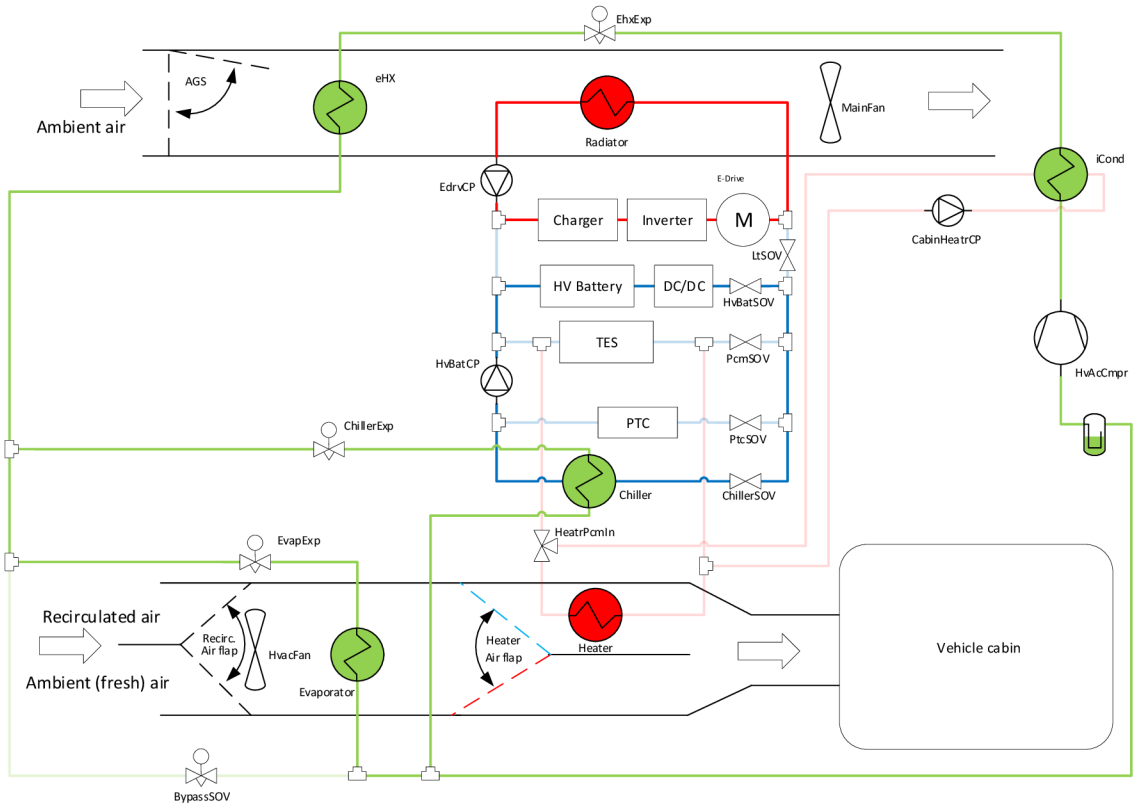

Fig. G.11: VTMS configuration under OTF 511

$$C_{\mathrm{cab}}\frac{\mathrm{d}T_{\mathrm{cab}}}{\mathrm{d}t} = -\dot{Q}_{\mathrm{loss}} - SHR \cdot \dot{Q}_{\mathrm{amb1}}, \tag{G.106}$$

$$C_{\mathrm{co}}\frac{\mathrm{d}T_{\mathrm{co}}}{\mathrm{d}t} = -\dot{Q}_{\mathrm{amb3}} + \dot{Q}_{\mathrm{bat1}}, \tag{G.107}$$

$$C_{\mathrm{bat}}\frac{\mathrm{d}T_{\mathrm{bat}}}{\mathrm{d}t} = \dot{Q}_{\mathrm{bat0}} - \dot{Q}_{\mathrm{bat1}}, \tag{G.108}$$

$$C_{\mathrm{ED}}\frac{\mathrm{d}T_{\mathrm{ED}}}{\mathrm{d}t} = \dot{Q}_{\mathrm{ED0}} - \dot{Q}_{\mathrm{amb2}}, \tag{G.109}$$

$$\frac{\mathrm{d}U_{\mathrm{TES}}}{\mathrm{d}t} = 0, \tag{G.110}$$

$$\frac{\mathrm{d}T_{\mathrm{amb}}}{\mathrm{d}t} = 0. \tag{G.111}$$

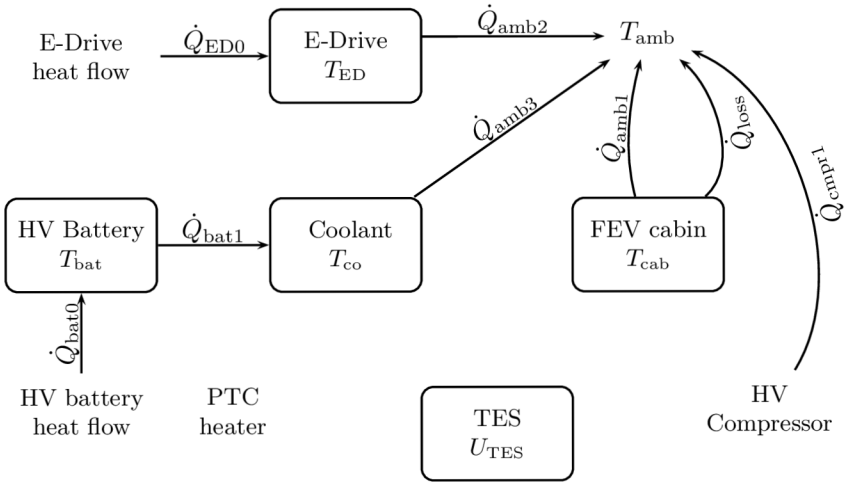

Fig. G.12: Simplified heat flows under OTF 511

$$\mathbf{A}_{511} = \begin{bmatrix} -\frac{G_{\mathrm{loss}}}{C_{\mathrm{cab}}} & 0 & 0 & 0 & 0 & \frac{G_{\mathrm{loss}}}{C_{\mathrm{cab}}} \\ 0 & -\frac{\dot{m}_{\mathrm{co}} c_{\mathrm{co}}}{C_{\mathrm{co}}} & \frac{\dot{m}_{\mathrm{co}} c_{\mathrm{co}}}{C_{\mathrm{co}}} & 0 & 0 & 0 \\ 0 & \frac{\dot{m}_{\mathrm{co}} c_{\mathrm{co}}}{C_{\mathrm{bat}}} & -\frac{\dot{m}_{\mathrm{co}} c_{\mathrm{co}}}{C_{\mathrm{bat}}} & 0 & 0 & 0 \\ 0 & 0 & 0 & -\frac{\dot{m}_{\mathrm{co}} c_{\mathrm{co}}}{C_{\mathrm{ED}}} & 0 & \frac{\dot{m}_{\mathrm{co}} c_{\mathrm{co}}}{C_{\mathrm{ED}}} \\ 0 & 0 & 0 & 0 & 0 & 0 \\ 0 & 0 & 0 & 0 & 0 & 0 \end{bmatrix}, \tag{G.112}$$

$$\mathbf{B}^{*}_{511} = \begin{bmatrix} 0 & 0 & 0 & -\frac{SHR \cdot P^{\max}_{\mathrm{c},511} \cdot COP_{511}}{C_{\mathrm{cab}}} & 0 & 0 \\ 0 & 0 & 0 & 0 & -\frac{P^{\max}_{\mathrm{c},511} \cdot COP_{511}}{C_{\mathrm{co}}} & 0 \\ 0 & 0 & 0 & 0 & 0 & 0 \\ 0 & 0 & 0 & 0 & 0 & 0 \\ 0 & 0 & 0 & 0 & 0 & 0 \\ 0 & 0 & 0 & 0 & 0 & 0 \end{bmatrix}, \tag{G.113}$$

$$\mathbf{f}^{\mathrm{c}}_{511} = \begin{bmatrix} 0 \\ 0 \\ \frac{\dot{Q}_{\mathrm{bat0}}}{C_{\mathrm{bat}}} \\ \frac{\dot{Q}_{\mathrm{ED0}}}{C_{\mathrm{ED}}} \\ 0 \\ 0 \end{bmatrix}. \tag{G.114}$$

OTF 524: VCRS cooling of the cabin with ambient as heat sink, battery cooled by ambient air

This OTF utilizes VCRS for vehicle cabin cooling with ambient air as a heat sink. The VCRS is operated under conditions defined in Table 5.3 and illustrated in

Fig. 5.12.

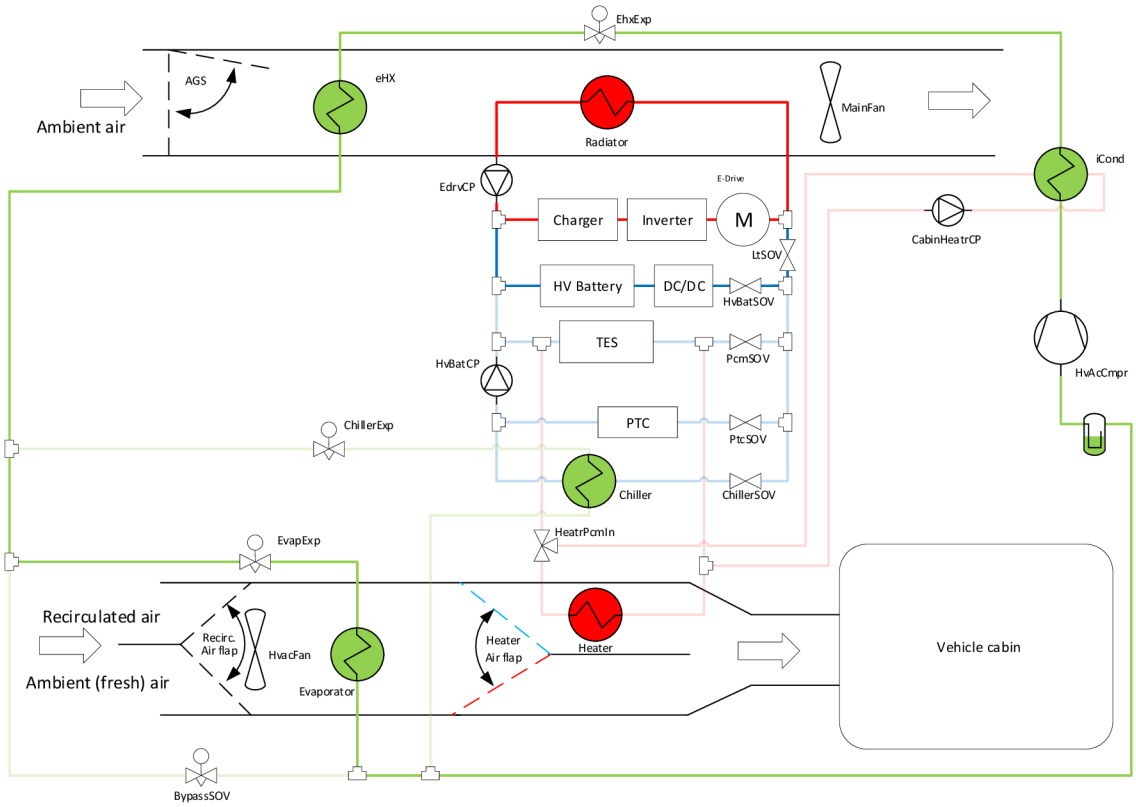

Fig. G.13: VTMS configuration under OTF 524

$$C_{\mathrm{cab}}\frac{\mathrm{d}T_{\mathrm{cab}}}{\mathrm{d}t} = -\dot{Q}_{\mathrm{loss}} - SHR \cdot \dot{Q}_{\mathrm{amb1}}, \tag{G.115}$$

$$C_{\mathrm{co}}\frac{\mathrm{d}T_{\mathrm{co}}}{\mathrm{d}t} = -\dot{Q}_{\mathrm{amb3}} + \dot{Q}_{\mathrm{ED1}} + \dot{Q}_{\mathrm{bat1}}, \tag{G.116}$$

$$C_{\mathrm{bat}}\frac{\mathrm{d}T_{\mathrm{bat}}}{\mathrm{d}t} = \dot{Q}_{\mathrm{bat0}} - \dot{Q}_{\mathrm{bat1}}, \tag{G.117}$$

$$C_{\mathrm{ED}}\frac{\mathrm{d}T_{\mathrm{ED}}}{\mathrm{d}t} = \dot{Q}_{\mathrm{ED0}} - \dot{Q}_{\mathrm{ED1}}, \tag{G.118}$$

$$\frac{\mathrm{d}U_{\mathrm{TES}}}{\mathrm{d}t} = 0, \tag{G.119}$$

$$\frac{\mathrm{d}T_{\mathrm{amb}}}{\mathrm{d}t} = 0. \tag{G.120}$$

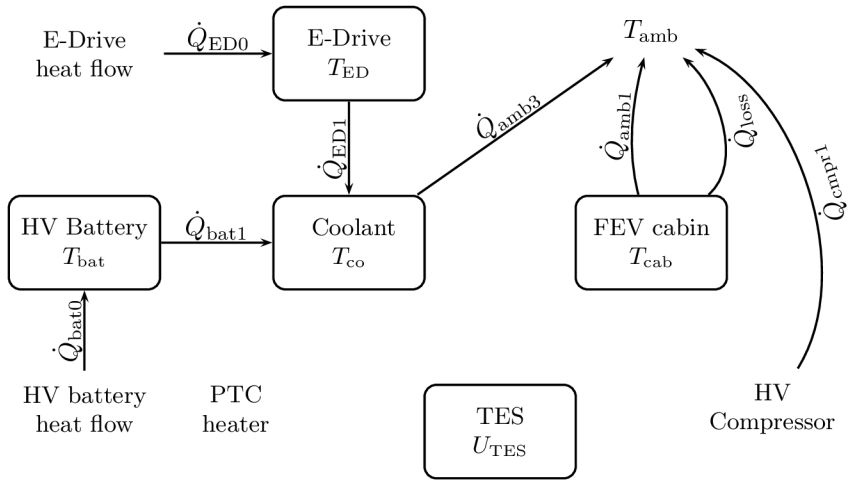

Fig. G.14: Simplified heat flows under OTF 524

$$\mathbf{A}_{524} = \begin{bmatrix} -\frac{G_{\mathrm{loss}}}{C_{\mathrm{cab}}} & 0 & 0 & 0 & 0 & \frac{G_{\mathrm{loss}}}{C_{\mathrm{cab}}} \\ 0 & -\frac{2\dot{m}_{\mathrm{co}}c_{\mathrm{co}}}{C_{\mathrm{co}}} & \frac{\dot{m}_{\mathrm{co}}c_{\mathrm{co}}}{2C_{\mathrm{co}}} & \frac{\dot{m}_{\mathrm{co}}c_{\mathrm{co}}}{2C_{\mathrm{co}}} & 0 & \frac{\dot{m}_{\mathrm{co}}c_{\mathrm{co}}}{C_{\mathrm{co}}} \\ 0 & \frac{\dot{m}_{\mathrm{co}}c_{\mathrm{co}}}{2C_{\mathrm{bat}}} & -\frac{\dot{m}_{\mathrm{co}}c_{\mathrm{co}}}{2C_{\mathrm{bat}}} & 0 & 0 & 0 \\ 0 & \frac{\dot{m}_{\mathrm{co}}c_{\mathrm{co}}}{2C_{\mathrm{bat}}} & 0 & -\frac{\dot{m}_{\mathrm{co}}c_{\mathrm{co}}}{2C_{\mathrm{bat}}} & 0 & 0 \\ 0 & 0 & 0 & 0 & 0 & 0 \\ 0 & 0 & 0 & 0 & 0 & 0 \end{bmatrix}, \tag{G.121}$$

$$\mathbf{B}^{*}_{524} = \begin{bmatrix} 0 & -\frac{SHR\cdot P^{\max}_{\mathrm{c},524}\cdot COP_{524}}{C_{\mathrm{cab}}} & 0 & 0 & 0 & 0 \\ 0 & 0 & 0 & 0 & 0 & 0 \\ 0 & 0 & 0 & 0 & 0 & 0 \\ 0 & 0 & 0 & 0 & 0 & 0 \\ 0 & 0 & 0 & 0 & 0 & 0 \\ 0 & 0 & 0 & 0 & 0 & 0 \end{bmatrix}, \tag{G.122}$$

$$\mathbf{f}^{\mathrm{c}}_{524} = \begin{bmatrix} 0 \\ 0 \\ \frac{\dot{Q}_{\mathrm{bat0}}}{C_{\mathrm{bat}}} \\ \frac{\dot{Q}_{\mathrm{ED0}}}{C_{\mathrm{ED}}} \\ 0 \\ 0 \end{bmatrix}. \tag{G.123}$$

H VTMS complex models

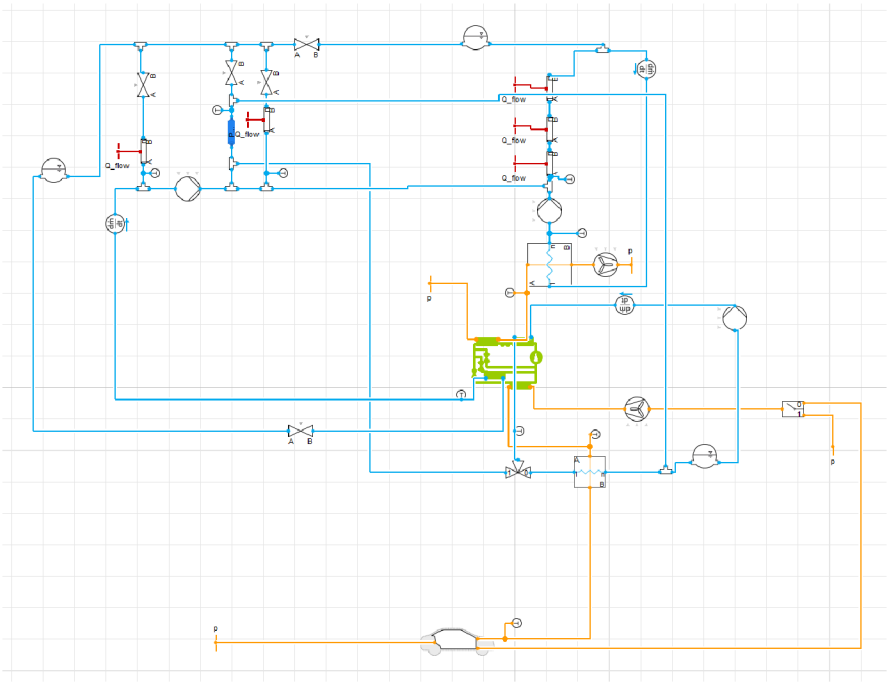

Fig. H.1: VTMS Dymola model

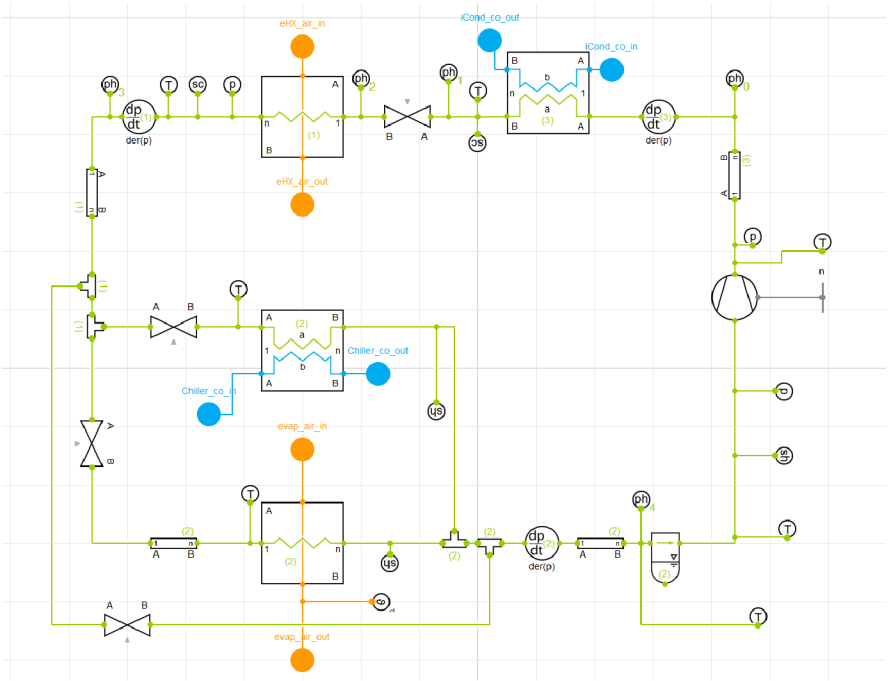

Fig. H.2: VCRS Dymola model